

FINAL REPORT

AUGUST 2025



Geomorphic and Ecological Impacts of Sand Mining in Large Rivers as revealed from high-resolution historical remote sensing data and drone surveys: Assessment, Analysis and Mitigation

Principal Investigator
Rajiv Sinha

Professor, Department of Earth Sciences
Indian Institute of Technology Kanpur
Email: rsinha@iitk.ac.in



Supported by
National Mission for Clean Ganga (NMCG)
Ministry of Jal Shakti, Government of India, New Delhi

Certificate

It is certified that the work presented in this report is based on the scientific study of sand mining-impacted areas in the Gaula, Damodar and Sone River basins during the period March 2021 and June 2025. The report is based on the data collected from drone surveys, bathymetric surveys and satellite images obtained from NRSC Hyderabad and Google Maps. We also certify that we have no conflict of interest whatsoever in this project or the matters related to this project.

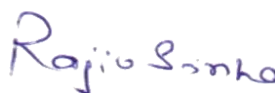


Rajiv Sinha
Professor
Department of Earth Sciences
IIT Kanpur

Acknowledgment

We gratefully acknowledge the National Mission for Clean Ganga (NMCG), Ministry of Jal Shakti, Government of India, for entrusting IIT Kanpur with this important and timely assignment and for providing the necessary financial support to undertake the project. This opportunity has allowed our team to engage deeply in the critical issue of sand mining in large river systems, and we believe the findings presented in this report will serve as an important step towards shaping a long-term, science-based policy for sustainable sand mining practices in the country.

We extend our sincere thanks to the Forest Department, Government of Uttarakhand, for their invaluable logistical support and for granting the necessary permissions to conduct the field surveys along the Gaula River. Their cooperation at every stage of the work, from planning to execution, was essential to the successful completion of field investigations. We also express our appreciation to Dr. S A. Hussain and his team at the Wildlife Institute of India, Dehradun, for their constructive discussions and valuable guidance. Finally, we would like to express our appreciation to the lab staff at IIT Kanpur for their assistance during the fieldwork.



Rajiv Sinha

Table of Contents

Certificate	1
Acknowledgment.....	2
Executive Summary	19
Chapter 1	22
1. Introduction	22
1.1. Background and motivation of the project.....	22
1.2. State of the Art and Knowledge Gaps.....	23
1.3. Major objectives of the project	28
1.4. Study area and methodology	28
1.4.1. Gaula River, Uttarakhand	28
1.4.2. Damodar River, West Bengal	31
1.4.3. Sone River, Bihar	32
1.4.4. Broad Methodology (Himalayan vs Peninsular rivers)	33
Chapter 2.....	35
2. Geomorphic impacts of sand mining: Himalayan River.....	35
2.1. The Gaula River: A Himalayan example	35
2.2. Datasets and Methodology	36
2.3. Spatio-temporal planform dynamics and characterisation of the reference state	39
2.4. Morphometric Indices	42
2.4.1. Channel belt width variability	42
2.4.2. Deviation from the reference state.....	44
2.4.3. Decadal-scale rate of morphometric parameters	46
2.4.4. Thalweg Shifts.....	49
2.4.5. SWAT-derived discharge and stream power distribution.....	50
2.5. Planform response to changes in flux boundary conditions.....	52
2.5.1. Geomorphic response, feedback and interaction.....	52
2.5.2. Spatio-temporal variability in morphological response	55
2.5.3. Controls of thalweg shifts	57

2.6.	Connecting the morphological response to evolutionary timelines.....	58
2.6.1.	Start of sand mining: Barren conditions (1976-1995).....	59
2.6.2.	Mobilization (1995 – 1999) followed by incision (1999 -2009).....	59
2.6.3.	Channel belt widening (2009 – 2014).....	60
2.6.4.	An underfit channel (2014 – 2021).....	60
2.7.	Process- Response framework.....	61
2.8.	Summary and conclusions	63
Chapter 3	64
3.	Geomorphic impacts of sand mining: Peninsular River.....	64
3.1.	General	64
3.2.	Mining footprints in high-resolution satellite imagery	65
3.3.	Mapping geomorphic impacts of sand mining	66
3.3.1.	Datasets and Methodology.....	66
3.3.2.	Results	72
3.4.	Sub-decadal Planform analysis using GEE.....	88
3.4.1.	Datasets and methodology	88
3.4.2.	Results	98
3.5.	Linking morphological changes to sand mining and flow regulation.....	125
3.5.1.	Hotspots of mining	125
3.5.2.	Impact of sand mining and flow regulation on river planform	128
3.5.3.	Geomorphic impacts of sand mining in peninsular rivers– a process response framework	131
3.6.	Summary and conclusions	133
Chapter 4	136
4.	Impact of sand mining on the sediment dynamics of the Gaula River using CASCADE modelling	136
4.1.	General	136
4.2.	Approach, data and methodology	136
4.2.1.	Drone-based granulometry	138
4.2.2.	SWAT modelling	140

4.2.3.	CASCADE model	142
4.3.	Network Scale GSD establishment with BASEGRAIN	143
4.4.	Hydrological response using the SWAT model.....	144
4.5.	Hydro-geomorphic controls: catchment slope, channel slope and stream power	145
4.6.	Sediment Flux estimation from the CASCADE model	146
4.6.1.	Sediment flux under mining scenario	147
4.6.2.	Sediment flux under no-mining scenario.....	148
4.6.3.	Net sediment delivery	149
4.7.	Reconstruction of hydrology for an ephemeral river.....	150
4.8.	River Behaviour with the ‘imposed’ boundary conditions	152
4.9.	River response to changes in ‘flux’ boundary conditions	153
4.9.1.	Bed coarsening due to sand mining.....	154
4.9.2.	Sediment connectivity in mining and no-mining scenarios	155
4.10.	Summary and conclusions	157
Chapter 5	158
5.	Measuring Erosion and Deposition in the Gaula River using UAV-based DEM of Difference .	158
5.1.	General	158
5.2.	Approach and Methodology	158
5.2.1.	UAV survey planning and Data Acquisition	159
5.2.2.	Photogrammetric Processing and DEM Generation	160
5.2.3.	DEM of Difference (DoD) Processing	162
5.2.4.	Volume Calculation of Erosion and Deposition.....	162
5.3.	Results	163
5.3.1.	Seasonal changes in planform morphology and bed topography as revealed from high-resolution UAV images	163
5.3.2.	Volumetric Analysis of Erosion and Deposition in the Gaula River	169
5.4.	Synthesis of results	171
5.5.	Episodic Recovery and Sustainable Mining Limits	172
5.6.	Summary, conclusions and limitations	173
Chapter 6	175

6. 'Hotspots' of sand mining and Policy recommendations	175
6.1. Himalayan River: The Gaula River	175
6.1.1. Methodology	175
6.1.2. Results	180
6.1.3. Discussion	182
6.2. Peninsular Rivers: Damodar and Sone	188
6.2.1. Methodology	188
6.2.2. Results	189
6.2.3. Discussion	195
6.3. Policy Implications for Sustainable Sand Mining in Himalayan and Peninsular Rivers	197
6.3.1. Himalayan River: Gaula	200
6.3.2. Peninsular Rivers: Damodar and Sone	203
6.4. Final remarks	208
S&T benefits accrued from this project	210
References	213

List of Figures

Figure 1.1 The Gaula River basin and the river network under study. The river network has been divided into 20 reaches, grouped into Upper Segment, Middle Segment and Lower Segment. The mining locations and other important sites used for this study are shown.....	30
Figure 1.2 (a) Location of the Damodar River Basin in India along with elevation ranges; (b) Study area within the Damodar River Basin; (c) Division of the study area into 25 reaches grouped into three zones for detailed analysis.....	31
Figure 1.3 (a) Location of the Sone River Basin in India along with elevation ranges; (b) Study area within the Sone River Basin; (c) three study windows for detailed analysis.	33
Figure 2.1: Flowchart illustrating the methodology used in this study. Pre-processed satellite data (30 m) was used for planform mapping. Planform data was further used for developing morphometric indices. Digital Elevation Model (DEM 30 m) coupled with planform data was used to develop the valley bottom confinement and longitudinal profile. LULC, soil data, weather input, Gaula barrage discharge data and DEM data were fed into SWAT to generate the total stream power. All datasets and results were used to develop a process-response framework for the Gaula river to understand the geomorphic impacts of sand mining.	37
Figure 2.2: (a) Different types of valley bottom confinement in the Gaula River, using the Copernicus DEM. Type A denotes bedrock and tectonics controlled partly confined valley bottom as seen in the upper segment (reaches 1 and 2). Type B denotes terrace-controlled partly confined valley bottom as seen in reaches 6 and 7 of the middle segment. Type C denotes the laterally unconfined reaches in the rest of the reaches of the middle segment and the whole lower segment. (b) The graph shows the valley bottom confinement in percentage across all the 20 reaches. Notably reaches 1 and 2 show 52.75 % and 11.27 % confinement respectively, influenced by bedrock, hillslope morphology, and tectonic activity. Reaches 6 and 7 are terrace-constrained, with reach 7 exhibiting the highest confinement (64.60 %), followed by reach 6 (27.73 %) where the terrace mainly confines the eastern bank. Other reaches are laterally unconfined.	40
Figure 2.3: Planform dynamics of the Gaula River, from 1976 (reference condition) to 2021. Representative reaches of the upper, middle and lower segments are shown. (a) The Gaula	

barrage is situated in reach 1 of the upper segment where its operation started in 1980. In the upper segment, vegetated bars began forming downstream of the barrage from 1995 showing a braided morphology. (b) The middle segment shows a significant narrowing of the channel belt, with a loss of vegetated bars and fresh deposits and a decline in geomorphic diversity. By 2021, a degraded, incised underfit channel was developed. (c) The lower segment exhibits a delayed response to mining, with gradual narrowing and a reduction in fresh deposits and vegetated bars.

.....42

Figure 2.4: (a) Channel belt width (CBW) of the Gaula River across 20 reaches from 1976 to 2021, with the most pronounced narrowing observed in mining-affected reaches (5, 6, and 7). (b) CBW variability and its mean, indicate the long-term response of the river to sand mining, with the middle segment (reaches 3 to 13) showing the highest variability and most significant narrowing. The black dashed line shows the mean value and the shaded grey area represents the standard deviation as variability. (c) Intra-seasonal differences in CBW between pre- and post-mining periods highlight dynamic fluctuations, with negative values indicating narrowing and positive values showing widening across different months (GBa — Gaula Barrage, GBr — Gaula Bridge, EC — Elephant Corridor).43

Figure 2.5: a) Wet Channel Difference Index (WCDI) shows the deviation of wet channels from the reference condition of 1976. Positive WCDI values indicate a reduction and negative WCDI values show expansion in the wet channel area. (b) Dry Channel Difference Index (DCDI) shows the deviation of dry channels (dry channel, fresh deposits and degraded channel) from the reference condition of 1976. Positive DCDI values indicate channel narrowing and negative DCDI values denote channel widening. (c) Vegetated Bar Difference Index (VBDI) across 20 reaches of the Gaula River from 1994 to 2021, showing the deviation of the vegetated bars from the reference condition of 1976. Positive VBDI suggests the decline of vegetated bars and negative VBDI suggests vegetated bar development in the subsequent years. (d) Spatio-temporal variability of VBDI, WCDI, and DCDI indices, depicting how the Gaula River's channel morphology has evolved in response to anthropogenic activities. Positive correlations are observed between dry channel and vegetated bars, while wet channel exhibits a negative correlation with both (GBa — Gaula Barrage, GBr — Gaula Bridge, EC — Elephant Corridor).45

Figure 2.6: (a) Decadal-scale change rate (m^2/year) in the Channel Belt area of the Gaula River from 1976 to 2021, showing periods of expansion and contraction. Positive values represent channel belt narrowing, while negative values indicate expansion. (b) Decadal change rate in the vegetated bar area, (c) wet channel area, and (d) dry channel area across different timeframes, revealing in-channel processes. The upper segment (reaches 1 and 2) shows initial expansion and stability, while the middle segment (reaches 3 to 13) exhibits significant contraction and degradation. The lower segment (reaches 14 to 20) displays moderate variability with alternating trends in wet channels, vegetated bars, and dry channels across decades.48

Figure 2.7: (a) Thalweg shifts across 20 reaches of the Gaula River at the seasonal scale (pre- and post-mining) with significant variability in reaches 2 to 12, and particularly pronounced in reaches 2 and 3. (b) Variability and average of seasonal thalweg shifts. (c) Thalweg shifts at the inter-decadal scale (1976–2021), showing long-term impacts of sand mining with higher mean shifts in reaches 2, 3, 19, and 20, and relatively consistent shifts in other reaches. (d) Variability and average of inter-decadal thalweg shifts (GBa — Gaula Barrage, GBr — Gaula Bridge, EC — Elephant Corridor).50

Figure 2.8: SWAT-derived hydrograph calculated at the Gaula catchment outlet from 1994 to 2020, showing low discharge before 2005, following a sharp increase in 2005, with particularly high discharge from 2010 to 2014.51

Figure 2.9: Longitudinal Profile of the Gaula River based on Copernicus DEM showing all 20 reaches used in this study, the black line represents the raw data and the red dashed line represents the fitted profile. Inset shows the Total Stream Power (W/m) distribution of the Gaula River with all the major locations such as the Gaula Barrage (GBa), Gaula Bridge (GBr) and the Elephant Corridor (EC) marked. The mining stretch is shown in the TSP plot.51

Figure 2.10: Field photographs showing the geomorphic impacts of sand mining in the Gaula River. (a) Mining is prohibited in the Elephant Corridor and a pilot channel has been created to facilitate water flow. Over time, sediment has accumulated in this corridor, raising the elevation of the deposited bar to match that of the riverbanks on both sides in recent years; (b) channel incision along the right bank of the Gaula River in reach 7 where the river terrace is approximately 11 m higher than the contemporary channel bed; (c) scouring of bridge piers as evidence of

channel incision at the Gaula bridge (reach 4) due to sand mining; (d) channel bed degradation as seen from UAV image. The entire channel bed has been excavated, with no geomorphic diversity remaining; (e) on-going sand mining and an armoured riverbed. Approximately, 7500 trucks and other carriers, such as horse carts, supported by 6500 labourers, are involved in this activity; (f) channel bed degradation and bed armouring; (g) the wet channel reappears as baseflow in the reaches of the lower segment, with sparse vegetation on either side of the channel. No sand mining activity is spotted here.....54

Figure 2.11: Geomorphic evolution of the Gaula River from 1976 to 2021, highlighting key phases of channel alteration due to sand mining and barrage influence. Alteration of the channel from (a) reference condition to (b) barren conditions (1976–1995) with the clearing of vegetated bars, controlled discharge from the upstream Gaula barrage. This was followed by (c) mobilization (1995–1999) and incision (1999–2009) phases, characterized by thalweg shift, sediment mobilization, and narrowing caused by channel incision and then, (d) channel belt widening (2009–2014), driven by high discharge events widening the channel belt. The Gaula River developed (d) underfit channel conditions (2014–2021), marked by bed armouring, low flow incised channel inset a macro-channel with vegetation encroachment on benches during periods of mining cessation (COVID-19).....61

Figure 2.12: A process-response framework of the Gaula River under the anthropogenic forcing of sand mining showcasing a positive feedback system.63

Figure 3.1: Google Earth imagery showing various sand mining features in the Damodar River. Red circles indicate examples of dry mining pits, typically located on exposed sandbars. Blue circles indicate wet mining pits, either situated directly within the wet channel or excavated deep enough for groundwater or channel water to accumulate. Yellow arrows point to bunds, which are temporary earthen roads constructed to facilitate the movement of trucks and equipment for sand transportation.65

Figure 3.2: Methodology workflow for feature extraction: (a) Pre-monsoon (April) false-color and monthly median composite; (b-d) Derived spectral indices: (b) NDWI (water bodies and wet mining pits), (c) NSI (sand deposits), and (d) NDVI (vegetation cover); (e-g) Threshold-classified

geomorphic features: (e) Active wet channel, (f) Sand deposits, and (g) Vegetated bars and floodplains.....69

Figure 3.3: (a) Spatiotemporal geomorphic map of the Damodar River (Zone 1) showing variations in morphological features and mining site distributions. (b) Temporal trends in total mining area for Zone 1 (2019-2024). (c) Mining intensity for Zone 1, calculated as the ratio of total mining area to total channel belt area.73

Figure 3.4: (a) Spatiotemporal geomorphic map of the Damodar River (Zone 2) showing variations in morphological features and mining site distributions. (b) Temporal trends in total mining area for Zone 2 (2019-2024). (c) Mining intensity for Zone 2, calculated as the ratio of total mining area to total channel belt area.76

Figure 3.5(a) Spatiotemporal geomorphic map of the Damodar River (Zone 3) showing variations in morphological features and mining site distributions. (b) Temporal trends in total mining area for Zone 3 (2019-2024). (c) Mining intensity for Zone 3, calculated as the ratio of total mining area to total channel belt area.78

Figure 3.6: Temporal evolution (2019–2024) of morphological features across the Damodar River: (a) Zone 1, (b) Zone 2, and (c) Zone 3.....79

Figure 3.7: Temporal variation in reach-wise mining intensity (mining area/channel belt area ratio) for the Damodar River (2019–2024). Red vertical dashed lines indicate barrage locations (Durgapur, Rondiha) and boundaries between the three zones, while red dashed rectangles highlight mining hotspots.....81

Figure 3.8: Geomorphic maps of the Sone River (Window-1) showing changes in river morphological features and mining pits over time, created using Landsat, Sentinel, and Google Earth imagery84

Figure 3.9: Geomorphic maps of the Sone River (Window-2) showing changes in river morphological features and mining pits over time, created using Landsat, Sentinel, and Google Earth imagery.85

Figure 3.10: Geomorphic maps of the Sone River (Window-3) showing changes in river morphological features and mining pits over time, created using Landsat, Sentinel, and Google Earth imagery.87

Figure 3.11: Spatiotemporal variation in area of mining pits: (W1) window 1, (W2) window 2, and (W3) window 3.	87
Figure 3.12: Mining intensity three zones calculated as the ratio of total mining area to total channel belt area: (W1) window 1, (W2) window 2, and (W3) window 3.	88
Figure 3.13: Showing the available satellite datasets and their revisit time and spatial resolution (Source: Nagel et al., 2023).	89
Figure 3.14: Methodology for extracting the binary mask of the active river channel and wet channel using Google Earth Engine.	92
Figure 3.15: Methodology for calculating Braiding and Sinuosity Index using RivGraph.	97
Figure 3.16: (a) Spatiotemporal planform maps of Zone 1 of the Damodar River, derived from Landsat imagery, (b) Changes in morphological classes, and (c) illustrating morphological changes in wet channels, sand deposits, and area of active river channel over time.....	99
Figure 3.17: (a) Spatiotemporal planform maps of Zone 2 of the Damodar River, derived from Landsat imagery. (b) Changes in morphological classes, and (c) illustrating morphological changes in wet channels, sand deposits, and the area of active river channel over time.	100
Figure 3.18: (a) Spatiotemporal planform maps of Zone 3 of the Damodar River, derived from Landsat imagery, (b) Changes in morphological classes, and (c) illustrating morphological changes in wet channels, sand deposits, and area of active river channel over time.....	102
Figure 3.19: (a) Reach-wise line plots depicting changes in wet channel area; (b) Percentage change in wet channel area relative to the reference year (1988); and (c) Percentage change from the previous year, illustrating periodic variability. The blue dashed lines in panels (b) and (c) indicate the locations of the Durgapur and Rondiha barrages.....	103
Figure 3.20: (a) Reach-wise line plots depicting changes in Sand deposit area; (b) Percentage change in sand deposit area relative to the reference year (1988); and (c) Percentage change from the previous year, illustrating periodic variability. The blue dashed lines in panels (b) and (c) indicate the locations of the Durgapur and Rondiha barrages.....	107
Figure 3.21: (a) Reach-wise line plots depicting changes in active river channel area; (b) Percentage change in active river channel area relative to the reference year (1988); and (c)	

Percentage change from the previous year, illustrating periodic variability. The blue dashed lines in panels (b) and (c) indicate the locations of the Durgapur and Rondiha barrages.	109
Figure 3.22: (a) Percentage change in Braiding index relative to the reference year 1988; (b) Spatial distribution of the braiding index. The blue dashed lines in panels (b) and (c) mark the locations of the Durgapur and Rondiha Barrages.	110
Figure 3.23: (a) Percentage change in sinuosity index relative to the reference year 1988; (b) Spatial distribution of the sinuosity index. The blue dashed lines in panels (b) and (c) mark the locations of the Durgapur and Rondiha Barrages.	113
Figure 3.24: Percentage change in BA/CA index relative to the reference year 1988. The blue dashed lines in panels mark the locations of the Durgapur and Rondiha Barrages.	114
Figure 3.25: (a) Spatiotemporal planform maps of window 1 of the Sone River, derived from Landsat imagery. Zone 1, (b) Changes in morphological classes, and (c) illustrating morphological changes in wet channels, sand deposits, and area of active River channel over time.	116
Figure 3.26: (a) Spatiotemporal planform maps of window 2 of the Sone River, derived from Landsat imagery. Zone 1, (b) Changes in morphological classes, and (c) illustrating morphological changes in wet channels, sand deposits, and the area of the active river channel over time. ...	118
Figure 3.27: (a) Spatiotemporal planform maps of the window 3 of the Sone River, derived from Landsat imagery. Zone 1, (b) Changes in morphological classes, and (c) illustrating morphological changes in wet channels, sand deposits, and the area of the active river channel over time. ...	119
Figure 3.28: Showing Braiding Index value across three study windows of the Sone River.....	122
Figure 3.29: Sinuosity Index value across three study windows of the Sone River.....	123
Figure 3.30: Bar area/ channel area Index value across three study windows of the Sone River.	125
Figure 3.31: High-resolution Google Earth imagery from post-monsoon periods (images a–e; year and month labelled) showing progressive pit capturing by the wet channel in a sand mining-impacted downstream reach of the river. Red circles highlight the location of mining pits being reoccupied by flow in subsequent years. The sequence illustrates how flow gradually reoccupies mining pits due to erosion and channel incision, driven by sediment-starved ("hungry") water. Over time, the wet channel widens laterally, encroaching into the former pit area. This process	

demonstrates the downstream geomorphic instability induced by intense sand mining activity.

.....129

Figure 3.32: The process-response framework of the river demonstrates a positive feedback system under the anthropogenic forcing of sand mining and flow regulation.132

Figure 4.1: Flowchart illustrating an integrated approach of hydrology, GSD size distribution at network scale and their integration with the sediment transport modelling (CASCADE).137

Figure 4.2: Overview of the Gaula River catchment showing key physical and hydrological features (a) Digital Elevation Model (DEM) of the Gaula catchment illustrating terrain variability, river network, and major tectonic structures, including mapped thrusts and faults. (b) Spatial distribution of average rainfall across the catchment with demarcated river reaches divided at 1 km intervals in the upper catchment and 2 km intervals in the lower catchment for hydrological and geomorphic analysis. (c) Land use and land cover map of the Gaula catchment, highlighting forested areas, agricultural zones, urban settlements, and riverine features relevant to sediment source and transport processes.138

Figure 4.3: Detailed methodology adopted for the GSD data collection using drone images and BASEGRAIN software, a MATLAB-based tool for optical granulometric analysis of top-view images of non-cohesive river deposits to evaluate D16, D50, and D84 grain distribution information. 139

Figure 4.4: SWAT generated 27 years (1994 to 2021) of hydrological simulation response of the Gaula River catchment, and the inset map shows validation for the limited years.144

Figure 4.5: (a) Slope map of the Gaula River catchment showing the topographic gradients and delineated river network; (b) Longitudinal variation in channel slope along the Gaula River, highlighting morphological transitions from the upper to lower catchment; and (c) Specific stream power distribution along the Gaula River, indicating zones of high energy and potential erosion linked to geomorphic activity and anthropogenic pressures.146

Figure 4.7: Gaula River's pristine upper catchment conditions demonstrate negligible impact on sediment delivery at the foothill zone in (a) mining and (b) no-mining scenarios (Yang's TCF). 147

Figure 4.8: Yang's TCF based sediment fluxes (deposited, transported and entrainment) in the lower catchment reaches in a) mining and b) no-mining scenarios. Net sediment delivery

highlighting sediment deposition and transport dominant river reaches in c) mining and d) no-mining scenarios.....148

Figure 5.1: Workflow illustrating the practical application of UAV-based photogrammetry and DEM of Difference (DoD) analysis for detecting and quantifying the geomorphic impacts of sand mining on riverbeds.....160

Figure 5.2: a) Orthomosaic image of Reach 2 in March (active mining period) and b) December (post-monsoon period). Inset images 1a and 1b from both the orthomosaics shows lateral erosion and inset images 2a and 2b shows remnant mining scars prevalent even after the monsoon; c) DTM of Reach 2 in March 2022 and d) December 2022; e) DEM of Difference (March DEM – December DEM), where positive values indicate erosion and negative values indicate deposition, and -0.16 to 0.16 indicates vertical uncertainty calculated from vertical Level of detection (LoD); f) Cross-sectional profile along AA' in Reach 2 derived from December and March DTM. Red indicates March profile, while blue indicates December profile; g) Longitudinal profile along BB' in reach 2 derived from December and March DTM. Red indicates the March profile, while blue indicates the December profile.164

Figure 5.3: a) Orthomosaic image of Reach 3 in March (active mining period) and b) December (post-monsoon period). Inset image 1 from both the orthomosaics shows vegetation regrowth post monsoon and inset image 2 shows lateral erosion along floodplain; c) DTM of Reach 3 in March 2022 and d) December 2022; e) DEM of Difference (March DEM – December DEM), where positive values indicate erosion and negative values indicate deposition, and -0.16 to 0.16 indicates vertical uncertainty calculated from vertical Level of detection (LoD); f) Cross-sectional profile along AA' in Reach 3 derived from December and March DTM. Red indicates March profile, while blue indicates December profile; g) Longitudinal profile along BB' in reach 3 derived from December and March DTM. Red indicates the March profile, while blue indicates the December profile.165

Figure 5.4: a) Orthomosaic image of Reach 7 in March (active mining period) and b) December (post-monsoon period). Inset image 1 from both the orthomosaics shows filling of mined pits and bar reshaping and inset image 2 shows vegetation recolonization; c) DTM of Reach 7 in March 2022 and d) December 2022; e) DEM of Difference (March DEM – December DEM), where

positive values indicate erosion and negative values indicate deposition, and -0.16 to 0.16 indicates vertical uncertainty calculated from vertical Level of detection (LoD); f) Cross-sectional profile along AA' in Reach 7 derived from December and March DTM. Red indicates March profile, while blue indicates December profile; g) Longitudinal profile along BB' in reach 7 derived from December and March DTM. Red indicates the March profile, while blue indicates the December profile.166

Figure 5.5: a) Orthomosaic image of Reach 12 in March (active mining period) and b) December (post-monsoon period); c) DTM of Reach 12 in March 2022 and d) December 2022; e) DEM of Difference (March DEM – December DEM), where positive values indicate erosion and negative values indicate deposition, and -0.16 to 0.16 indicates vertical uncertainty calculated from vertical Level of detection (LoD); f) Cross-sectional profile along AA' in Reach 12 derived from December and March DTM. Red indicates March profile, while blue indicates December profile; g) Longitudinal profile along BB' in reach 12 derived from December and March DTM. Red indicates the March profile, while blue indicates the December profile.167

Figure 5.6: a) Orthomosaic image of Reach 13 in March (active mining period) and b) December (post-monsoon period). Inset images 1a and 1b from both the orthomosaics shows filling of mined pits and inset images 2a and 2b shows lateral erosion along the floodplain; c) DTM of Reach 13 in March 2022 and d) December 2022; e) DEM of Difference (March DEM – December DEM), where positive values indicate erosion and negative values indicate deposition, and -0.16 to 0.16 indicates vertical uncertainty calculated from vertical Level of detection (LoD); f) Cross-sectional profile along AA' in Reach 13 derived from December and March DTM. Red indicates March profile, while blue indicates December profile; g) Longitudinal profile along BB' in reach 13 derived from December and March DTM. Red indicates the March profile, while blue indicates the December profile.168

Figure 6.1: Hotspot Index for the Gaula River187

Figure 6.2: Hotspot Index of Damodar River.195

Figure 6.3: Hotspot Index of the Sone River.....196

List of Tables

Table 2.1: Definition of the different geomorphic features mapped.	38
Table 3.1: Definition and mapping criteria for geomorphic feature	70
Table 3.2: Percent distribution of morphological units of Damodar River (zone-normalized to 100%).....	74
Table 3.3: Reach-wise temporal variations in mining intensity (mining area/channel belt area ratio) with annual and zonal mean values across Zones 1–3 (2019–2024).....	80
Table 3.4: Annual mining intensities with vulnerability classification for the Damodar River. Color coding: Critical (red), Very High (orange), High (yellow), Moderate (blue), Low (green), Protected (gray).	82
Table 3.5: Percent distribution of morphological features of Sone River (window-normalized to 100%): Mining-Impacted Wet Channel, Active Wet Channel, Mining-Affected Channel Belt, and Undisturbed Channel Belt (Windows 1–2); Active Wet Channel, Undisturbed Floodplain, and Mining-Impacted Floodplain (Window 3), showing temporal changes (2010–2023).	86
Table 3.6: Showing Braiding and Sinuosity Index value across three study windows of the Sone River.	121
Table 4.1: Thematic, weather, and discharge data used in the SWAT model setup.	140
Table 4.2: Grain size survey performed along the river for no-mining and mining periods.....	143
Table 5.1: UAV image count, data size, and spatial coverage for selected Gaula River reaches (March and December 2022)	160
Table 5.2: Summary of seasonal geomorphic changes between pre-monsoon (March 2022) and post-monsoon (December 2022) in selected Gaula River reaches, based on UAV-derived orthomosaics and topographic profiles.....	169
Table 5.3: Net aggradation/degradation, reported extraction volumes, and drone coverage for selected monitored reaches of the Gaula River.	172
Table 6.1: Tier-1 Long-term Geomorphic Impact(LGI) using planform dynamics indicators.....	177
Table 6.2: Tier-2 Connectivity Disruption Index (CDI) using CASCADE model.	178
Table 6.3: Tier-3 Short-Term / Seasonal Indicators.	179

Table 6.4: Computation of Long-term Geomorphic Impact (LGI) for tier 1 using morphometric indices from satellite-based planform dynamics (46 years data).....	180
Table 6.6: Computation of Tier 3 using Seasonal or short-term indicators.....	182
Table 6.7: Computation of Hotspot Index for the Gaula River	185
Table 6.8: Tier-1 parameters used for calculating the Hotspot Index for the Damodar and Sone rivers.....	189
Table 6.9: Computation of Hotspot Indices for Damodar River	190
Table 6.10: Computation of Hotspot Index for Sone River.....	194
Table 6.11: Structure of the District Survey Report and Mining Plan	200
Table 6.12: Policy recommendations for sand mining: Himalayan vs Peninsular rivers	207

Executive Summary

Instream sand mining, driven by rapid urbanization and economic growth, has surged in recent years, causing significant ecological and geomorphological damage to rivers. Unregulated extraction leads to channel incision, endangering infrastructure such as bridges and lowering water tables, while also triggering lateral instability, bank erosion, and channel shifts that increase flood risks. The loss of channel form and sediment balance disrupts aquatic and riparian habitats, degrades fisheries, and undermines biodiversity. In India, both Himalayan and peninsular rivers have been severely impacted, with the Damodar River experiencing lowered water levels, habitat loss, and chemical pollution, and the Sone River suffering from altered flow, habitat degradation, and groundwater decline. For the Himalayan setting, the Gaula river in Uttarakhand was selected as a prominent Himalayan river to document and analyse the impacts of sand mining.

In-channel sand mining in the Gaula River has altered the flux boundary conditions, creating an imbalance between driving and resisting forces. For example, the indiscriminate extraction of sand from the channel bed increases the local gradient and generates knickpoints that, in turn, increase the stream power and hence the energy available for sediment transport. We have documented channel narrowing and incision, thalweg fixing, bed armouring and a severe decline in geomorphic diversity as some of the major geomorphic impacts of sand mining in the Gaula River. We have identified four distinct evolutionary phases of the Gaula River at a historical time scale which reveal a fairly rapid degradation of the river in response to sand mining viz. (a) barren conditions (1976–1995), (b) mobilization followed by incision (1995–2009), (c) channel belt widening (2009–2014), and (d) underfit channel (2014–2021). Further, a process-response framework to characterize the geomorphic impacts of sand mining in the Gaula River reveals a positive feedback system. The major hydrogeomorphic processes shaping the channel morphology have been significantly altered by intensive sand mining activities manifested in terms of modified hydrological and sediment transport regimes.

Spatiotemporal sand mining hotspots along with their geomorphological association in both Damodar and Sone rivers suggest that most of the reaches in the identified hotspots have more

than 50% of their area occupied by sand mining activities. It emphasizes the urgent need to prioritize these hotspots for monitoring and initiate remediation measures for restoring the river. The severity of impacts from sand mining in both the Damodar and Sone Rivers is evident through extensive morphological degradation observed over time. In some reaches of the Damodar River, a mining intensity as high as 0.8 was documented in recent years (2024) indicating that 80% of its total area was covered by mining activities. A rapid increase in mining activities has been documented in the Damodar River between 2019 and 2024, with several reaches recording 3.5-fold increase in dry mining area and a 2.7-fold increase in wet mining pits, resulting in severe wet channel fragmentation. In the Sone River, major geomorphic impacts of sand mining include loss of channel belt and sand bar areas, and transformation from braided to a single-thread channel system. In some reaches, nearly 53% of sand bars have been lost, including the near-total disappearance of mid-channel bars. In both Damodar and Sone Rivers, widespread channel incision, bar erosion, and morphological simplification, which collectively reduce the river's flood buffering capacity, impair floodplain connectivity, and diminish groundwater recharge potential, rendering these reaches highly vulnerable to both hydrological extremes and long-term ecological degradation. The combined effects of sediment extraction through sand mining and sediment entrapment by flow regulation structures significantly reduce the sediment supply downstream. Flow-regulating structures like dams and barrages trap large amounts of sediment upstream, disrupting the natural sediment replenishment process. This sediment deficit is further exacerbated by sand mining, which directly removes sediment from the river system. Sand mining has reduced sediment availability in downstream reaches in two critical ways: firstly, by diminishing the initial sediment supply traveling downstream, and secondly, by creating deep mining pits that act as sediment traps where much of the transported sediment settles and is no longer available to replenish downstream reaches. As a result, downstream reaches become severely sediment-starved. Sediment starvation because of mining triggers the 'hungry water' effect, where sediment-depleted water has increased erosive power, causing channel incision, lowering riverbed levels, and increasing vertical channel space. This has led to significant morphological changes in both Damodar and Sone Rivers, including the loss of sediment bars (lateral erosion) that serve as flood buffers and groundwater aquifers. The

loss of these bars and the transformation from multichannel to single-channel morphology reduces channel belt area and degrades floodplain connectivity and ecosystem health.

To understand and manage these impacts, the CASCADE (Catchment Sediment Connectivity And Delivery) modelling framework was also set up for the Gaula river, which integrates graph theory with sediment transport equations to estimate grain-specific sediment flux and assess habitat availability. The upper and middle segments of the lower catchment exhibit high stream power due to higher discharge and moderate slopes, enabling active sediment transport and channel adjustments. These reaches function as sediment transport zones. As the river flows downstream, it transitions from a confined, high-energy system to a laterally unconfined meandering form, accompanied by declining stream power and reduced erosional capacity, promoting sediment deposition. Additionally, both discharge and tectonic forces act as dominant imposed boundary conditions shaping the river's form and function across different reaches. Sand mining leads to bed armouring, characterised by coarser surface grains that function as a 'blanket', shielding the riverbed from erosion and disrupting sediment connectivity. This creates a decoupled, transport-limited system, reducing transmission sensitivity and increasing locational sensitivity. This alters the flux boundary conditions. This armour layer increases critical shear stress thresholds, thereby reducing sediment entrainment, especially during low-flow events and contributing to spatially discontinuous sediment transport, akin to a 'jerky conveyor belt'. The integrated method (SWAT-based hydrology, GSD and CASCADE-based sediment transport) provides important insights into sediment flux and dynamics under no-mining and mining scenarios in a data-scarce river catchment.

Given their differing geomorphic settings—Himalayan rivers with high sediment loads driven by tectonic activity and monsoons, and sediment-limited peninsular rivers—management strategies must be river-specific: for Himalayan rivers, regulating extraction based on dynamic sediment budgets and maintaining connectivity; for peninsular rivers, restricting mining to low-sensitivity zones and favouring controlled, non-mechanised methods. Overall, science-based, data-driven policies, continuous monitoring, strict enforcement, and community engagement are essential to safeguard riverine ecosystems and preserve their ecological and societal benefits.

Chapter 1

1. Introduction

1.1. Background and motivation of the project

Sand plays a crucial role in fluvial geomorphology by supporting the dynamics and ecology of riverine networks. It acts as a reservoir, retaining water at shallow depths and extending residence time. Furthermore, sand provides essential breeding and hiding grounds for fish and microorganisms, thus nurturing and sustaining diverse riverine ecosystems and biotas. The rising demand and supply of sand, driven by rapid urbanisation and industrialisation, have severely affected river channels. Unsustainable sediment extraction has inflicted extensive damage on the entire river ecosystem, altering its morphology, ecology, and hydrology. Sediment transport and dynamics govern the supply of nutrients in large river systems, influencing the balance between morphological and biological processes. Excessive sand and gravel extraction from river channels and floodplains disrupts natural flow, impacting ecosystems and river stability. Globally, around 50 billion tonnes of sand (as per WWF estimates) are extracted annually, making it the world's largest natural resource industry.

In-channel sediment mining involves the extraction of sand and gravel directly from the river bed, point bars and braided bars, altering channel geometry and bed elevation (Rinaldi et al., 2005; Surian et al., 2009; Dufour et al., 2015). In-channel sediment mining comprises two main types: in-channel pit mining, excavating pits below the thalweg, and bar skimming, which entails scraping the upper layer of a gravel bar (Padmalal and Maya, 2014). In-channel pit mining is further categorised into dry-pit mining, where the groundwater table is unaffected or remains at greater depths as seen in ephemeral rivers (Calle et al., 2017; Akuria and Sinha, 2025), and wet-pit mining, which involves excavating pits below the surface water of perennial rivers or the alluvial groundwater table (Hackney et al., 2020, 2021; Ng and Park, 2021). Wet-pit mining often requires equipment such as draglines or hydraulic excavators to dredge sand and gravel from beneath the water surface. These practices significantly disrupt riverine processes, threatening the ecological and hydrological balance of river systems.

When the extraction of sand exceeds replenishment, severe on-site and off-site impacts occur on the hydrology and ecology of the river systems. Impacts include loss of floodplain habitat, alteration of channel form, and sediment distribution, affecting ecosystems. In-channel mining disrupts longitudinal river connectivity, leading to incision, instability, and bank erosion. These changes harm wildlife habitats and cause infrastructure damage. Rivers in India experiences sand mining exceeding their capacity, resulting in altered channels, habitats, and ecosystems. Scientific scrutiny of riverine sand mining has increased, and this project aimed to develop a comprehensive assessment of the geomorphic impacts of sand mining with a focus on the Himalayan and peninsular rivers. Addressing these issues is crucial to safeguard the river systems and their associated environments.

1.2. State of the Art and Knowledge Gaps

The geomorphic processes and resulting forms in rivers are driven by a balance between the driving forces such as water discharge (Q_w), channel slope (S), and resisting forces such as sediment discharge or sediment load (Q_s), and sediment bed grain size or particle diameter (D_s) (Lane, 1955). The imbalance of the driving and resisting forces causes the river to adjust in three dimensions: vertically, laterally and longitudinally which can further cause a wholesale adjustment in rivers (Fryirs and Brierley, 2005). Koehnken et al. (2020) reported that channel incision is the most widely reported geomorphic impact of riverine sand mining, followed by channel narrowing across the globe. Several Italian rivers have experienced bed incisions ranging from 2 m in the Piave River (Comiti et al., 2011), up to 4-5 m in the Lower Orba River from 1950 to 1970s (Mandarino, 2022) and as much as 10 m in certain reaches of the Panaro River, which occurred during or shortly after a period of extensive sediment mining (Gumiero et al., 2015). Isik et al. (2008) observed channel bed incision up to 7 m in the lower Sakarya River in Turkey during the 41-year period (1965–2006), which was mostly related to sand and gravel mining. In Spain, gravel extraction resulted in incision of over 5m in Gállego River (Martín-Vide et al., 2010), at least 3.5m in Rambla de la Viuda (Calle et al., 2017), and an average of 1.5m over the whole reach in lower Tordera, leading to damage to infrastructures and severely affecting the river ecosystem and groundwater (Rovira et al., 2005). Several sections in the Maipo River in Chile experienced very large incision up to 20 m, with an increase in the area affected by gravel mining from 86.62

to 368.13 ha from 1954 to 2015 (Arróspide et al., 2018). Sand mining is likely generating a net deficit in the Mekong and the Bassac channels in Cambodia, which showed significant bed material losses amounting to approximately 90 and 110 Million cubic meters, respectively, and an increase of mean depth by an excess of 1.3m over a period of 10 years (1998 and 2008) (Brunier et al., 2014). Binh et al. (2021) reported an increase in riverbed incision rate from 0.16 m/yr in 1998–2014 to 0.5 m/yr in 2014–2017, resulting in lowering of water levels in the Mekong River.

In planform view, the river changes often from a wide, braided channel to a straight, single thread and/or wandering narrow channel, causing a wholesale change in rivers (Fryirs and Brierley, 2005; Fryirs, 2017). This implies disruption of the pre-existing channel morphology and sediment deficiency. Such morphological changes have been documented in several rivers, including the Tagliamento, Brenta, Magra, Piave and Panaro rivers in Italy (Rinaldi et al., 2005, 2009; Surian and Cisotto, 2007; Comiti et al., 2011; Dufour et al., 2015; Gumiero et al., 2015; Ziliani and Surian, 2016), in Rambla de la Viuda and the Palancia River in Spain (Calle et al., 2017; Sanchis-Ibor et al., 2017) and the Maipo River, Chile (Arróspide et al., 2018). Some studies indicate a strong correlation between channel incision and channel narrowing/degradation (Rinaldi et al., 2005; Surian and Cisotto, 2007; Surian et al., 2009; Gumiero et al., 2015; Calle et al., 2017), though some suggested a weaker but still evident correlation (Comiti et al., 2011; Mandarino, 2022).

Channel incision induced by riverbed mining has also disrupted the lateral hydrological connectivity between river and wetland in the Vietnamese Mekong Delta as the connected days of the river and wetland decreased from 360 to 270 within about 15 years (after 2000) (Park et al., 2020). This decline in hydrological connectivity directly reduces available water resources for irrigation and local consumption. Comiti et al. (2011) revealed that bed incision due to gravel mining promotes vegetation encroachment, leading to channel narrowing, and only intense, infrequent flood events with a return period of 10–15 years can inundate the floodplains, thereby reducing lateral connectivity. Removal of fine sediments from riverbeds can lead to bed armour, resulting in a layer of coarser sediment that is more resistant to erosion (Kondolf, 1994; Rinaldi et al., 2005), eventually disrupting the longitudinal connectivity of the river.

The processes of sediment excavation and bed armouring decrease the sediment load within the river system. Channel excavation creates localised steep gradients, generating over-steepened knickpoints. The reduced bedload supply, along with the localised steep gradient, increases stream power because of the 'hungry water effect' (Kondolf, 1994, 1997), exacerbating bed and bank erosion (Hackney et al., 2020). This causes head-cutting that can propagate several kilometres upstream. A topographic survey of Cache Creek, California, conducted in 1992, documented a 3-meter-deep knickpoint resulting from excavation that created a 4-meter-high headwall, situated 1400 meters downstream of Capay Bridge. By 1993, the knickpoint had migrated 960 meters upstream. Subsequent flooding in 1995 exacerbated its progression, leading it beneath Capay Bridge and nearly causing its structural failure (Kondolf, 1997). Similarly, instream pit mining on the Russian River near Healdsburg, California, in the 1950s and 1960s led to channel incision of 3–6 m over an 11 km length of the river (Kondolf, 1997). The incision is so severe that some studies have documented bedrock exposure in certain rivers. In the Drac River, France, incision intensified as the channel rapidly eroded ancient fluvial-lacustrine clay deposits, increasing scouring rates (Brousse et al., 2021). Similarly, the impact of bedload particles eroding soft bedrock in the Bernesga River, Spain, led to the concentration of incisions in narrower segments, creating a positive feedback loop of further incision (Ferrer-Boix et al., 2023). In Austria's Johnsbach Valley, channel incision led to the exposure of talus-covered bedrock (Rascher et al., 2018). Channel incision can increase bank height and induce instability, threatening key infrastructure and communities on the river's banks (Hackney et al., 2020). On the other hand, bar skimming and undercutting can also cause bank failure, leading to the widening of the river channel, showcasing channel instability (Kondolf, 1994). Apart from in-channel mining, sand mining also occurs on floodplains and older terrace deposits of perennial rivers, as observed in the Amite River in the USA (Mossa and McLean, 1997) and the Cibi River floodplain in Romania (Costea, 2018). In the event of an avulsion or gradual migration, floodplain pits may integrate into the active channel, termed 'pit capturing', posing potential instream or in-channel implications over a time scale of decades (Padmalal and Maya, 2014).

The sand mining industry, crucial for construction and urbanization, is particularly prevalent in developing countries like India, where 61.6% of surveyed river reaches showed evidence of

mining (Dujardin et al., 2024). Due to reduced sediment supply, the Dwarkeswar and Mayurakshi Rivers in West Bengal have undergone significant narrowing and incision, transforming from multi-threaded to single-thread channels (Ghosh and Maiti, 2021; Ghosh, 2024). Channel incision has often triggered shifts in the thalweg, leading to substantial channel migration, instability and pool-riffle alterations in the Damodar and Kangsabati rivers (Ghosh et al., 2016; Bhattacharya et al., 2019a, 2019b; Ghosh and Jana, 2021). Channel incision has resulted in the destabilisation of engineering structures, increased bank erosion, and a lowering in the water table, as observed in the rivers of Kerala, South India (Padmalal et al., 2008; Sreebha and Padmalal, 2011). Research on Himalayan rivers has emerged in the past decade, highlighting similar trends, including severe channel narrowing and incision exposing bedrock, reduced channel bar areas and a shift from braided to single-thread sinuous channels (Tamang and Mandal, 2015; Wiejaczka et al., 2018; Mitra et al., 2023). Mitra et al. (2023) further emphasised that sediment extraction is the primary driver of channel degradation surpassing other anthropogenic factors like urbanization, vegetation removal, and channel embankments. Additionally, riverbed mining in the Himalayas exacerbates flood hazards by intensifying erosion, making floodplains more vulnerable to flooding, particularly in the monsoon season due to increased downstream transport of loose landmass (Singh and Sidhu, 2016). Vercruysse and Grabowski, (2021) associated with the impacts of sand mining with a timescale-dependent evolutionary trajectory, highlighting a pulse response in the Sutlej River in the Himalayas.

Geomorphic impacts of sand mining have often led to disrupting the ecological functioning of the rivers as the habitats of the aquatic life get severely damaged. Gravel mining from active channel beds and adjacent floodplains contributes to the fragmentation of riparian forests such as in the lower Eygues River in France (Kondolf et al., 2007). Human-induced channel bed incision disconnects the adjacent floodplains from the main channel causing a lowering of the groundwater table and impacting the surrounding ecology and riparian vegetation. Gumiero et al., (2015) reported that due to riverbed incision some reaches of the Panaro River in Italy, caused a decline of hygrophilous trees such as willows and poplars and an inclination towards xerophilous conditions. Some incised reaches also showed recolonization of the abandoned floodplains by vegetation. Skalski et al. (2016) reported that river incision reduced the species richness and

diversity of ground beetles on the lowest bench, which was frequently inundated, but increased them on the highest bench, which was rarely flooded. The abundance of small, predatory, macropterous, and spring-breeding species, which are adapted to dynamic habitats, was negatively affected by river incision, especially on the lowest bench. Conversely, the abundance of large, herbivorous, brachypterous, and autumn-breeding species, which are typical of stable habitats, was positively affected by river incision, especially on the highest bench (Skalski et al., 2016). Mingist and Gebremedhin (2016) revealed that sand mining interfered with the migratory routes of fish and resulted in the loss of their spawning grounds in the inflowing rivers to Lake Tana, Ethiopia. Gravel dredging in large rivers diminishes fish abundance, diversity, and trophic positions by altering habitats and nutrient pathways, reducing benthic primary production, and simplifying food webs. This poses a threat, particularly to native and specialist fish species, dependent on gravel and rock substrata for spawning, leading to potential biodiversity loss and shifts in community composition in the river (Freedman et al., 2013).

In India, sand mining and the laying of roads up to the riverbank have led to a reduction in the nesting sites of crocodiles, turtles, and birds in the Chambal River (Singh and Rao, 2017). A study of in-channel sand mining in the Ganga River near Haridwar has significantly altered the channel morphology over the past two decades, leading to the degradation of water quality and a decline in aquatic biodiversity (Kamboj and Kamboj, 2019). Meanwhile, floodplain mining has adversely affected the riparian vegetation along adjacent riverbanks. Prabhakar et al. (2019) further observed that sand mining activities increased turbidity and decreased the transparency of the water, which negatively affected the primary production and the feeding efficiency of zooplankton in the River Ganga in Bihar.

A comparative review of existing literature reveals critical gaps in the current understanding of sand mining impacts across both the Himalayan and Peninsular River systems. In the case of Himalayan rivers, there are limited systematic studies on sand mining despite their geomorphic sensitivity and high sediment flux. Few existing studies link sand mining impacts with fundamental geomorphic concepts such as channel evolution, connectivity, and hotspots, resulting in a fragmented understanding of river dynamics. Most studies fail to adopt a process-

response approach, which is crucial for capturing the dynamic feedback between sand extraction, channel morphology, and sediment transport. While Peninsular rivers have received more attention, there remains under utilization of automated platforms like Google Earth Engine (GEE) for geomorphic analysis. Manual methods dominate, introducing user bias and limiting reproducibility.

1.3. Major objectives of the project

Keeping in view the knowledge gaps, the following objectives were envisaged for this project:

1. Assessment of spatio-temporal geomorphic impacts of sand mining on rivers.
2. Spatio-temporal evaluation of the impact on longitudinal and sediment connectivity of rivers caused by sand mining.
3. Calculating volumes of erosion and deposition using a DEM created from UAV.
4. Assessment of associated hazards such as flash floods and bank erosion caused by indiscriminate sand mining, superimposed by hydrological changes.
5. Integration of data for identification of hotspots of degradation in rivers and suggestions for mitigation measures.
6. Formulation of region-specific policy guidelines for sand mining based on scientific understanding.

1.4. Study area and methodology

1.4.1. Gaula River, Uttarakhand

One of study sites for this project is the Gaula River, flowing in the Himalayan region in the Uttarakhand state of northwestern India (Fig. 1.1). The Gaula River has a catchment area of 740 Km², a drainage density of 2.28 km/km² and the studied stretch is approximately 40 Km long. The river originates in the Paharpani Village, Nainital District, Uttarakhand, in the Kumaun Lesser Himalaya. It then flows southward through Kathgodam and Haldwani before merging with Ramganga, a tributary of the Ganges. The elevation of the Gaula River catchment ranges from 2557 m to 139 m and is approximately bound between latitudes 28°54'47.51" N and 29°27'34.73" N and longitudes 79°32'46.12" E and 79°44'39.48" E. The upper part of the catchment comprises the Kumaun Lesser Himalayas, marked by rugged topography, steep slopes, deep gorges, and

narrow valleys. South of the Lesser Himalayas is the outer Himalayas or the Siwalik and is demarcated from the Lesser Himalayas by the Main Boundary Thrust (MBT). The southern boundary of the Siwalik zone is marked by a layer of gravel deposits from the foothill zone, referred to as the "Bhabar".

We have investigated the 40 Km ephemeral stretch of the Gaula River flowing from Kathgodam (29°16'43.89" N 79°32'44.38" E) to Kichha (28°56'08.66" N 79°32'15.74" E) (Fig. 1.1). This area falls under the sub-humid subtropical climate of the Terai belt, located in the foothills of the Himalayas. The Gaula River forms a blanket of sediments of mainly gravel and sand deposits from the piedmont zone, forming the Gaula fan. The Gaula fan exhibits a convex-up transverse profile, covering approximately 631 km² with a radial length of around 30 km and an average radial slope of 0.44° (Goswami, 2018). The area receives (80-90) % of the total annual rainfall in the monsoon season from mid-June to mid-September. The average annual precipitation is 1669 mm, whereas the average monsoonal rainfall (mid-June to mid-September) is 1750 mm. The average minimum-maximum temperature varies between 8 and 20 °C in winter to 25 and 38 °C in the summer. Some notable anthropogenic structures include the Gaula Barrage, constructed in the year 1980 for the diversion of water to the city of Haldwani for irrigation and domestic purposes, and the Gaula bridge for ease of transportation (Fig. 1.1).

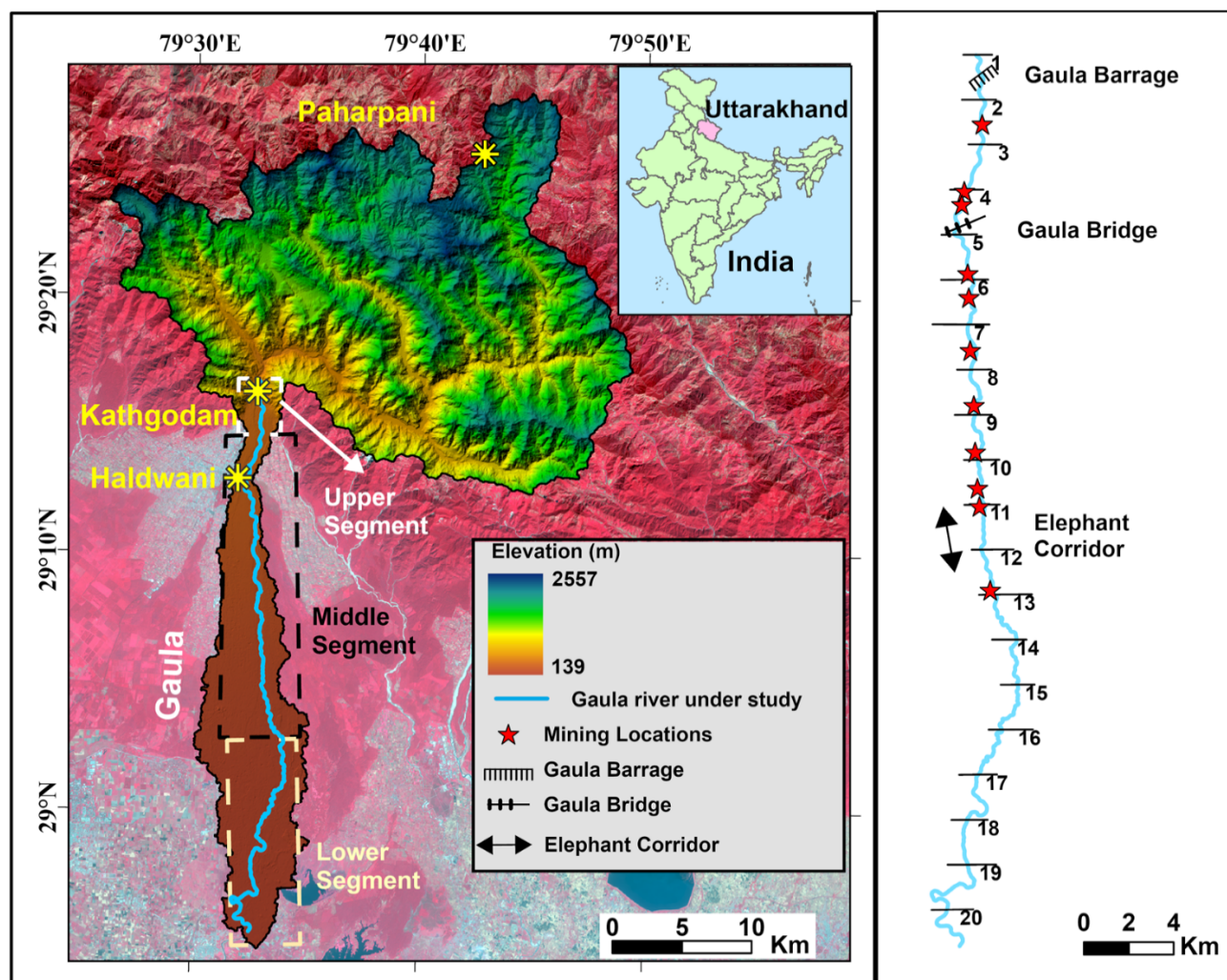


Figure 1.1 The Gaula River basin and the river network under study. The river network has been divided into 20 reaches, grouped into Upper Segment, Middle Segment and Lower Segment. The mining locations and other important sites used for this study are shown.

The Gaula River receives a high sediment flux from a tectonically active hinterland, which is transported downstream by monsoonal discharges to the lower reaches of the river. The ephemeral nature and high sediment flux make the Gaula River attractive for sand miners. The mining operations started in 1990 and now span a continuous 29 km stretch, excluding a 2.5 km 'no extraction zone' at the Elephant Corridor (Fig.1.1) to allow safe passage for elephants and other wildlife. Additionally, a 500-meter stretch both upstream and downstream of the Gaula bridge is also excluded from mining activities to protect the bridge piers from erosion. Sand mining operations are undertaken from 11 mining gates under the Haldwani and Terai East Forest Divisions between November and May each year, which utilise approximately 7,500 trucks and

other carriers, such as horse carts, supported by 6,500 mine workers. The Ministry of Environment and Forests (MoEF) has set the permissible limit for sand/boulder extraction at 6,500,000 cubic meters, and a 25-meter-wide area from both sides of the riverbank was designated for erosion control. According to the environmental clearance report prepared by the Uttarakhand Forest Development Corporation (UKFDC), the average annual extraction between 1990 and 2005 was 1,743,238 cubic meters, which increased to a maximum of 6,203,998 cubic meters between 2008 and 2009.

1.4.2. Damodar River, West Bengal

The Damodar River originates from the Chotanagpur Plateau in Jharkhand and flows eastward into West Bengal before joining the Hooghly River. The river is characterized by a multi-thread channel planform in certain reaches, with a complex interplay between sediment transport, flow regulation, and anthropogenic activities. The catchment of the basin is primarily composed of Precambrian metamorphic rocks in the upper reaches, transitioning into Quaternary alluvial deposits in the lower reaches. Due to its rich alluvial deposits, the lower Damodar River is highly

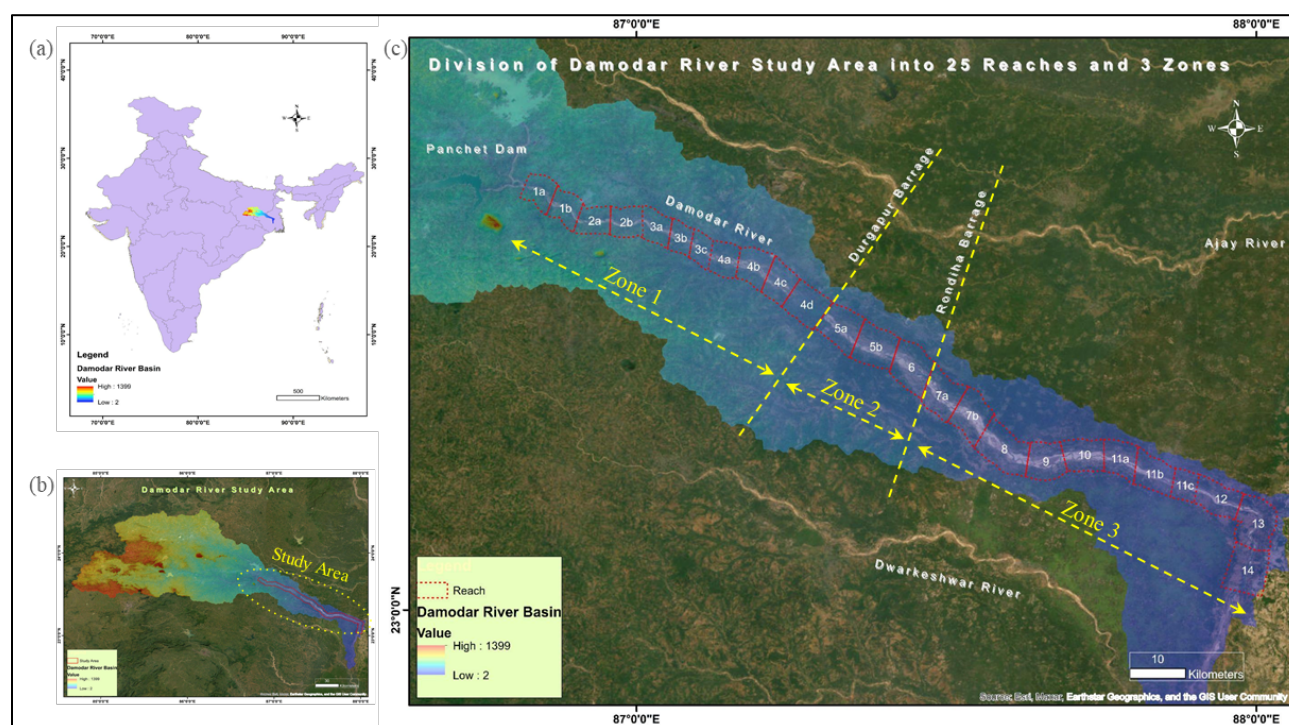


Figure 1.2 (a) Location of the Damodar River Basin in India along with elevation ranges; (b) Study area within the Damodar River Basin; (c) Division of the study area into 25 reaches grouped into three zones for detailed analysis.

vulnerable to extensive sand mining, which has significantly altered its morphology (Ghosh and Jana, 2021).

Additionally, flow regulation through barrages such as the Durgapur Barrage has altered sediment connectivity, leading to downstream sediment starvation and channel instability. The lower section of the Damodar River, from Hijuli, West Bengal, near the Jharkhand border to Jamalpur, West Bengal, has been selected as the study area. This section has been divided into 25 reaches and 3 zones (Fig.1.2) to investigate the effects of sand mining and flow regulation on various parts of the river.

- a) Zone 1: Between Panchet Dam (upstream) and Durgapur Barrage (downstream).
- b) Zone 2: Downstream of Durgapur barrage and upstream of Rondiha barrage.
- c) Zone 3: Downstream of Rondiha Barrage and most affected by sand mining.

1.4.3. Sone River, Bihar

The Sone River, a major right-bank tributary of the Ganga, originates from the Amarkantak Plateau in Madhya Pradesh and flows northward into Bihar before merging with the Ganga. The river is known for its wide alluvial channel and high sediment transport capacity. The upper reaches of the basin are dominated by Precambrian crystalline rocks, while the lower reaches consist of alluvial deposits. Excessive sediment extraction in this river has led to increased erosion, loss of mid-channel bars, and modifications in bank stability. The combination of mining activities and flow regulation through the Indrapuri Barrage has significantly altered the river's morphological dynamics. The Sone River is particularly important in understanding how large-scale sand mining and flow regulation interact to influence sediment dynamics in an alluvial river system.

For the geomorphic mapping of large peninsular rivers, the Sone River has been selected as the study area. Three windows (Window-1, Window-2, and Window-3) have been chosen to observe the planform dynamics and mining impacts (Fig.1.3).

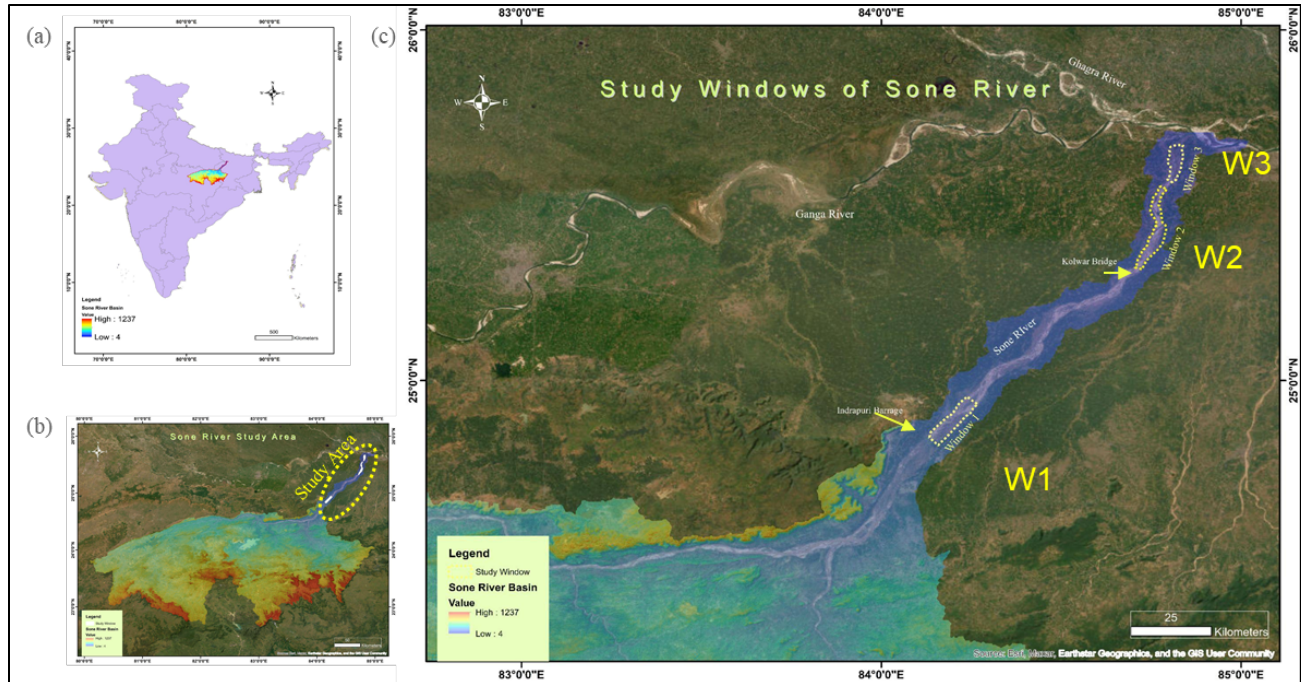


Figure 1.3 (a) Location of the Sone River Basin in India along with elevation ranges; (b) Study area within the Sone River Basin; (c) three study windows for detailed analysis.

- a) Window-1: Located in the downstream section of Indrapuri Barrage, extending from Indrapuri Barrage to Chainpur village, covering a length of 16.75 km with an area of 65 km².
- b) Window-2: Covers the middle stream section from Azimabad to the Old Koilwar Bridge, spanning 27.4 km with an area of 48 km².
- c) Window-3: Covers the lower stream section from the New Koilwar Bridge to Rampur Diara (near the confluence with the Ganga River), covering 11.7 km with an area of 36 km².

1.4.4. Broad Methodology (Himalayan vs Peninsular rivers)

Geomorphic mapping utilizing satellite-based remote sensing techniques has revolutionized our understanding of Earth's surface processes and landforms. By harnessing the capabilities of satellite imagery, such as high-resolution optical datasets, researchers can accurately identify and classify various landforms and geomorphic features over large spatial extents. From delineating river channels and identifying erosion hotspots to mapping the fluvial features, satellite-based remote sensing enables comprehensive and cost-effective analysis of geomorphic phenomena.

Furthermore, the integration of advanced data processing techniques, including automated mapping algorithms using GEE, UAV-based digital terrain analysis and orthomosaic data, enhances the accuracy and efficiency of geomorphic mapping efforts. Overall, satellite-based remote sensing serves as a powerful tool for studying Earth's dynamic landscapes, facilitating informed decision-making in river management and policy making.

The methodological approach for assessing the geomorphic impacts of sand mining in Himalayan and Peninsular rivers was tailored to the scale, setting, and data characteristics of each system. In the Himalayan context, the Gaula River is a relatively small ephemeral yet highly dynamic river draining a tectonically active hinterland requiring high-resolution, manual mapping to capture detailed geomorphic changes. This allowed for focused spatio-temporal planform analysis using historical satellite imagery, UAV-derived DEM of Difference for volumetric estimation, and sediment transport modelling to examine connectivity and sediment flux under varied mining scenarios. In contrast, the Peninsular rivers, such as the Sone and Damodar, are large rivers with more extensive channel networks, which necessitated an automated approach. Here, Google Earth Engine (GEE) was employed to map mining hotspots across longer temporal scales, supported by high-resolution Google Earth imagery. The emphasis was on detecting broad-scale morphological trends, associating them with anthropogenic drivers like sand mining and flow regulation. Thus, while the Gaula study prioritised detailed, manual analysis for fine-scale process-response understanding, the Peninsular case studies leveraged automated, large-scale mapping to capture systemic patterns and spatial variability in mining impacts.

Chapter 2

2. Geomorphic impacts of sand mining: Himalayan River

2.1. The Gaula River: A Himalayan example

Sand mining is a major anthropogenic intervention that alters the natural geomorphic functioning of river systems. In Himalayan rivers like the Gaula, which are characterised by high sediment flux, dynamic morphology, and monsoon-driven flow regimes, in-channel sand extraction has profound implications. To assess the river conditions, identifying the contemporary status of a river relative to a reference state is required; however, the ideal reference conditions against which measurements must be made are debatable (Rinaldi et al., 2013; Fryirs, 2015; Brierley and Fryirs, 2022). The expected reference state is determined by the specific characteristics and behaviour of a river within the existing catchment boundary conditions, aiming to represent the best conditions attainable by the river, including human-induced alterations to the catchment. Rinaldi et al. (2013) defined the reference state as when a river reach is in a state of dynamic equilibrium, performing the morphological functions characteristic of its specific morphological typology, with minimal anthropogenic interference that does not impact river dynamics at both the catchment and reach scales.

The major components of the methodological framework include (a) delineation of the valley bottom margin and assessment of the valley bottom confinement, (b) planform mapping, (c) measurement of various planform parameters for designing morphometric indices, (d) mapping thalweg shifts, (e) computing total stream power, and (f) field surveys for ground truth (Fig. 2.1). The delineation of valley bottom confinement helped us to study the contemporary range of processes that control river response on a reach scale (Fryirs et al., 2016). Anthropogenic margins, including embankments, levees, railway lines, roads, etc., can also contribute to confinement, restricting the lateral movement of rivers. In river segments where human-induced confinement surpasses natural valley bottom confinement, it is considered that anthropogenic activities are artificially regulating the river's inherent ability to adjust laterally (Fryirs et al., 2016).

2.2. Datasets and Methodology

We delineated the valley bottom margin using the 30 m Copernicus DEM (<https://spacedata.copernicus.eu/collections/copernicus-digital-elevation-model>) in ArcGIS environment using the fluvial corridor toolbox (Roux et al., 2015). Further, the valley bottom margin was manually edited in ArcGIS environment comprising the active channel (bankfull width) and contemporary active floodplain from the recent planform map of 2021 for understanding the contemporary river behaviour and morphology (Wheaton et al., 2015). We determined the channel confinement as the boundary between the valley bottom margin and the channel margin providing insights into the river's adjustment potential (Wheaton et al., 2015; Fryirs et al., 2016; O'Brien et al., 2019) using the formula:

$$C_{VB} = [(\sum_{DS}^{US} CL_{EB}@C_M)/RL],$$

where C_{VB} is the valley bottom confinement; $CL_{EB}@C_M$ is the length of the channel along either bank that abuts a confining margin within each reach, and RL is the reach length (Fryirs et al., 2016).

We used Landsat archives (MSS, TM, ETM, and OLI) from 1976 to 2021 for spatiotemporal assessment of the geomorphic impacts of sand mining on the Gaula River. The 1976 pre-monsoon Landsat image of 60 m spatial resolution was used as a reference for this study. For the period 1994-2021, the satellite image pairs (mostly 30 m spatial resolution) for the pre-mining (October to November of the preceding year) and post-mining (March to June of the succeeding year) scenarios were used to quantify short-term, seasonal scale response to mining. Satellite datasets were processed to generate modified Normalized Difference Water Index (mNDWI), Normalised Water Index (NDWI), Normalised Vegetation Index (NDVI), Normalised Water Index (NDWI), False Color Composite (FCC), and Pan-Sharpened FCC (Landsat 8) in the ArcGIS software. Major planform features and anthropogenic imprints suggestive of sand mining activities were mapped at a 1:6000 scale for the following years: 1976 (reference), 1994 & 1995, 1998 & 1999, 2008 & 2009, 2013 & 2014, and 2020 & 2021. The Gaula is an ephemeral and small piedmont river, with the planform features too subtle to be picked up by unsupervised and supervised classification. Hence, a manual mapping was carried out. We divided the 40 km long stretch of the Gaula River

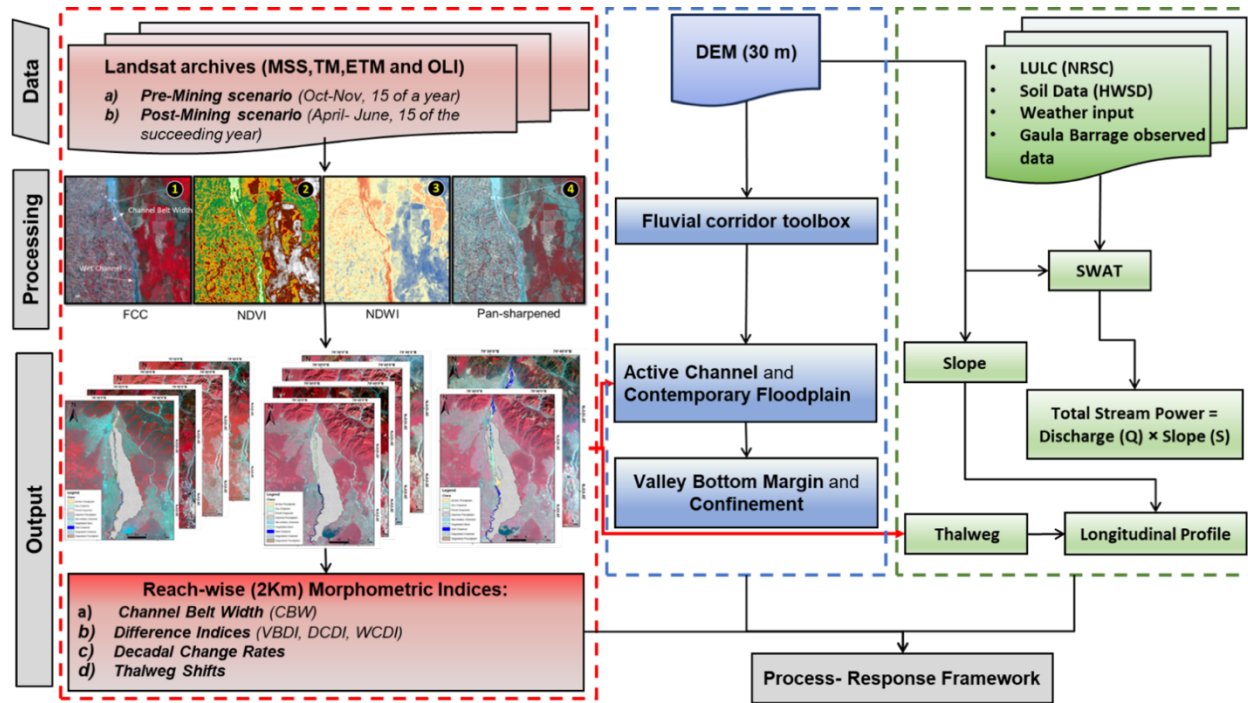


Figure 2.1: Flowchart illustrating the methodology used in this study. Pre-processed satellite data (30 m) was used for planform mapping. Planform data was further used for developing morphometric indices. Digital Elevation Model (DEM 30 m) coupled with planform data was used to develop the valley bottom confinement and longitudinal profile. LULC, soil data, weather input, Gaula barrage discharge data and DEM data were fed into SWAT to generate the total stream power. All datasets and results were used to develop a process-response framework for the Gaula river to understand the geomorphic impacts of sand mining.

into 20 reaches of 2 km length and in-channel geomorphic features such as wet channels, dry channels, fresh deposits, vegetated bars, sparsely vegetated bars and degraded channels were mapped (Table 2.1).

Channel belt width (CBW) was calculated by dividing the planform area of all in-channel geomorphic features by reach length. The difference in channel belt width between the post and pre-mining seasons was also calculated to assess the impact of mining for each season. We selected 1976 as the baseline or reference year, as sand mining practices did not begin until 1990, and the Gaula barrage was constructed in 1980. Then, difference indices (DI) were calculated as deviation from reference state/reach Length:

$$DI = (N_r - N_i)/RL,$$

where N_r is the area of a geomorphic unit in the reference state and N_i is the area of the geomorphic unit for the subsequent i^{th} years.

Table 2.1: Definition of the different geomorphic features mapped.

Feature	Definition and characteristics
Wet Channels	Channel like features carved by the active flow of water; includes major and minor active channels with visible water.
Dry Channels	Channel features without any water flow for most of the year.
Fresh Deposits	Fresh depositional features in and around river channel including mid-channel bars, point bars, and lateral bars.
Vegetated Bars	Stable depositional features formed due to low flow condition and vegetation cover.
Sparsely Vegetated Bars	Bars and depositional areas with incipient vegetation, mainly small shrubs and bushes which grow due to low flow conditions.
Degraded Channel	Scars and mining pits on the channel bed in active mining reaches.
Channel Belt	Encompassing all in-channel geomorphic features such as wet channel, dry channel, fresh deposits, vegetated and sparsely vegetated bar.

In particular, three DIs were computed such as (a) Vegetated Bar Difference Index (VBDI), (b) Wet Channel Difference Index (WCDI), and (c) Dry Channel Difference Index (DCDI). Further, the changes were documented at a decadal scale to understand the evolutionary trend, and the interdecadal Change Rate (CR) was calculated as:

$$CR = (N_o - N_f)/t,$$

where N_o is the area of a geomorphic unit in the initial year and N_f is the area of the geomorphic unit for the final year, t is the number of years between the initial year and final year of each timeframe concerned. Decadal change rates ($m^2/year$) were calculated for a) channel belt area, b) dry channel area, c) vegetated bar area, and d) wet channel area.

Additionally, we mapped the river's thalweg from the MNDWI map using the wettest pixel. For each reach, the interdecadal thalweg shift rate was calculated by dividing the area between thalwegs of successive years by the reach length and the time interval in years. The seasonal thalweg shift was calculated as the area between thalwegs of pre- and post-mining seasons divided by the reach length.

We generated the longitudinal profile of the river using the thalweg of Gaula of the year 2021 using the Copernicus DEM (30 m). An 11th-order polynomial curve was fitted to the profile, yielding an R^2 value of 0.99 following the methodology by Sarkar and Sinha (2024). We used the 27-year (1994 to 2020) averaged August discharge data from the SWAT model (Pipil et al., in prep) and combined it with the slope data from DEM (30 m) to estimate total stream power (TSP) values for each river segment (Kaushal et al., 2020). As Gaula is an ephemeral river, active primarily during the monsoon season, the bankfull discharge from August was used, as it represents the 'effective discharge' responsible for transporting the bulk of the annual coarse sediment load (Emmett and Wolman, 2001). Further, geomorphic field surveys were conducted for validation and ground truth.

2.3. Spatio-temporal planform dynamics and characterisation of the reference state

In the Gaula River, three distinct types of valley bottom confinement are observed (Fig. 2.2). Reach 1 is partly confined, showing 52.75 % confinement, and is primarily controlled by factors such as bedrock, hillslope morphology, and tectonic activity. Reaches 2, 6, and 7 are terrace-constrained partly confined reaches, with reach 7 exhibiting the highest confinement (64.60 %), followed by reach 6 (27.73 %) and reach 2 (11.27 %), where the terrace has formed predominantly on the left bank, and a railway line further constrains the right bank of reach 2. The remaining reaches are laterally unconfined, with minimal confinement, except for reach 8, which shows a 9.92 % confinement. Here, the river has greater freedom for channel adjustment and morphological changes.

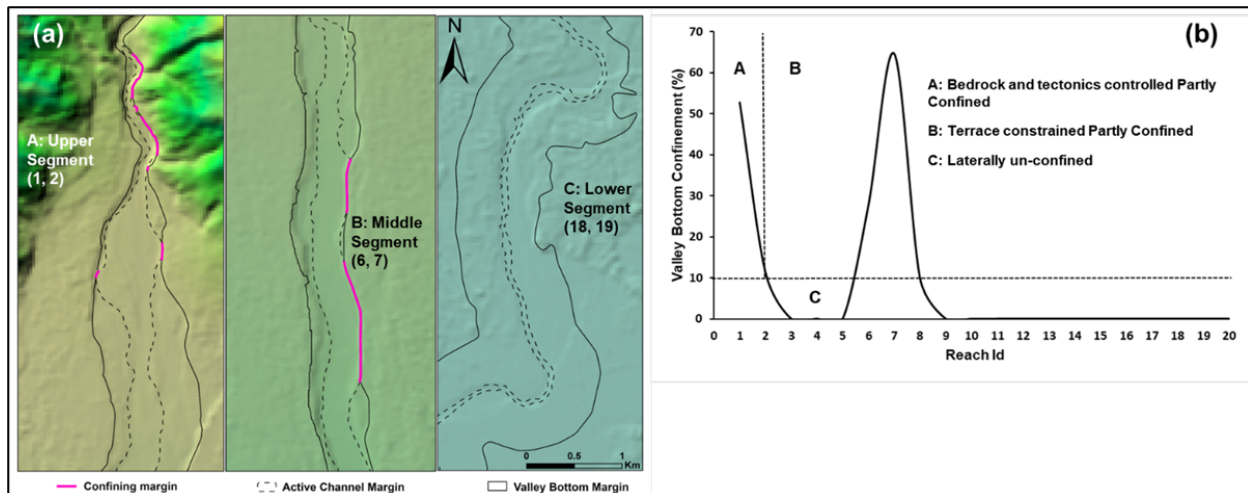


Figure 2.2: (a) Different types of valley bottom confinement in the Gaula River, using the Copernicus DEM. Type A denotes bedrock and tectonics controlled partly confined valley bottom as seen in the upper segment (reaches 1 and 2). Type B denotes terrace-controlled partly confined valley bottom as seen in reaches 6 and 7 of the middle segment. Type C denotes the laterally unconfined reaches in the rest of the reaches of the middle segment and the whole lower segment. (b) The graph shows the valley bottom confinement in percentage across all the 20 reaches. Notably reaches 1 and 2 show 52.75 % and 11.27 % confinement respectively, influenced by bedrock, hillslope morphology, and tectonic activity. Reaches 6 and 7 are terrace-constrained, with reach 7 exhibiting the highest confinement (64.60 %), followed by reach 6 (27.73 %) where the terrace mainly confines the eastern bank. Other reaches are laterally unconfined.

Planform maps of the 40 Km stretch of the Gaula River, divided into 20 reaches of 2 Km each, reveal notable spatio-temporal variability in channel belt width (CBW), wet channels, vegetated bars, and dry channels (Fig. 2.3). Based on the river's contemporary character, and to analyze its spatio-temporal morphodynamics, the river is categorized into (a) tectonics and bedrock-controlled upper segment (reaches 1 and 2), (b) middle segment (reaches 3 to 13) corresponding to the mining zone, and (c) unconfined lower segment (reaches 14-20). In the upper segment (reaches 1 and 2), the river shows a braided morphology. The vegetated bars started to form downstream of the barrage since its operation in 1980, with a consistent presence in the upper part of reach 2 since 1995 (Fig. 2.3a). Although wet channels have persisted due to controlled discharge from the barrage, they have declined in recent years. The middle segment (reaches 3 to 13) shows a consistent and substantial channel belt narrowing and loss of vegetated bars in response to sand mining (Fig. 2.3b). The wet channel emerged in 1995, followed by river fragmentation in 1999, and then a complete degradation was documented with little or no geomorphic diversity. By 2021, vegetation encroached upon the sidebars, resulting in a narrow,

incised dry channel within a macro channel, resembling an ‘underfit’ channel (Dury, 1964). In the lower segment (reaches 14 to 20), the river follows a meandering pattern (Fig. 2.3c). Since 2009, the planform response to sand mining has become prominent in these reaches as well, manifested as channel narrowing and a gradual decline in fresh sediment deposits and vegetated bars (Fig. 2.3c).

Based on the planform mapping and given that the Gaula barrage was constructed in 1980, and the mining activities did not begin until 1990, we have identified the reference state for the Gaula River corresponding to 1976. We presume that the imposed boundary conditions (geologic controls such as tectonics and lithology) have not undergone any significant alterations at the catchment scale since 1976. In the reaches of the upper segment (Fig. 2.3a), the river descends from a bedrock-controlled reach and enters the alluvial plains. There were fewer vegetated bars in 1976, signifying that these reaches got inundated during high flows and were prone to erosion. Moving downstream, reaches 3 and 4, had little to no vegetation, implying that they behaved mostly as transfer zones dominated by entrainment processes. In contrast, reaches 5 to 9 had large, densely vegetated bars in a braided channel (Fig. 2.3b), suggesting sediment retention by enhancing friction, which facilitates sediment deposition (Bull, 1997; Sandercock et al., 2007). This likely caused a notable decrease in wet channel width and expansion of islands and side bars as documented in previous studies (Graf, 1978). An increase in channel belt width and vegetated bars imply that these reaches were deposition-dominated zones. Reach 10 is again documented as an erosion-dominated zone in 1976, with no vegetation cover, while reach 11 had fewer vegetated bars, which increased in reaches 12 and 13. It is evident that in the reference state (1976), when the water was not regulated by a barrage, the river was ephemeral in the upper and middle segments (reaches 1 to 13) for most of the year, except in monsoons. From reach 14 downstream, the river was narrow, and wet channels appeared due to the intersection of the water table with surface topography. The river displayed a meandering pattern with fresh sand deposits as point bars in the downstream reaches (Fig. 2.3c). Vegetated bars were less common, implying that the areas were frequently inundated, ensuring good lateral connectivity.

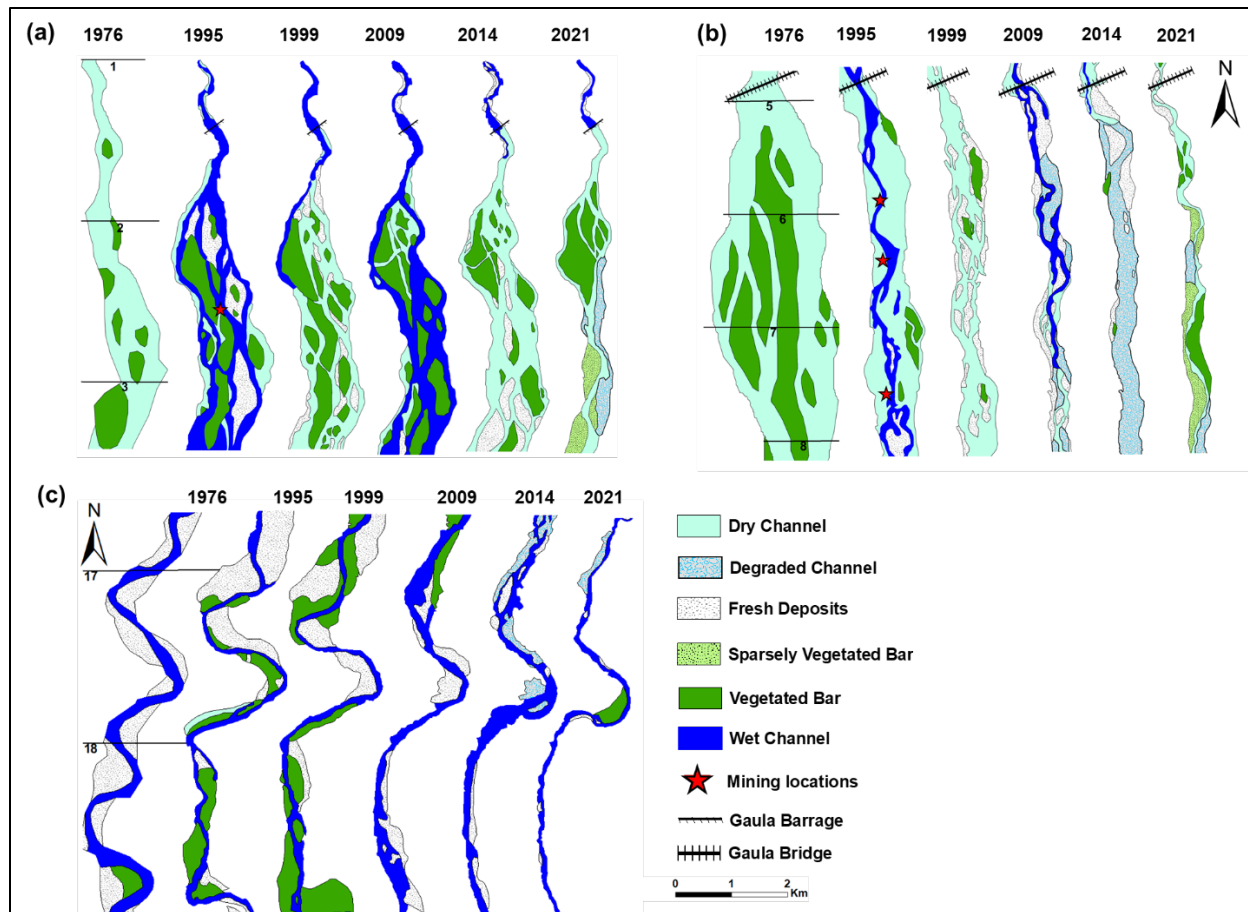


Figure 2.3: Planform dynamics of the Gaula River, from 1976 (reference condition) to 2021. Representative reaches of the upper, middle and lower segments are shown. (a) The Gaula barrage is situated in reach 1 of the upper segment where its operation started in 1980. In the upper segment, vegetated bars began forming downstream of the barrage from 1995 showing a braided morphology. (b) The middle segment shows a significant narrowing of the channel belt, with a loss of vegetated bars and fresh deposits and a decline in geomorphic diversity. By 2021, a degraded, incised underfit channel was developed. (c) The lower segment exhibits a delayed response to mining, with gradual narrowing and a reduction in fresh deposits and vegetated bars.

2.4. Morphometric Indices

2.4.1. Channel belt width variability

Figure 2.4a shows an overall decrease of 62.93% in CBW across all reaches between 1976 and 2021, the most significant decrease being in the mining reaches 5, 6 and 7. Spatially, the upper segment (reaches 1 and 2) show a decrease of 25.46%, while the middle segment (reaches 3 to 13) show 72%, and the lower segment (reaches 14 to 20) show a 61% decrease in channel belt width in 2021 compared to the reference state of 1976.

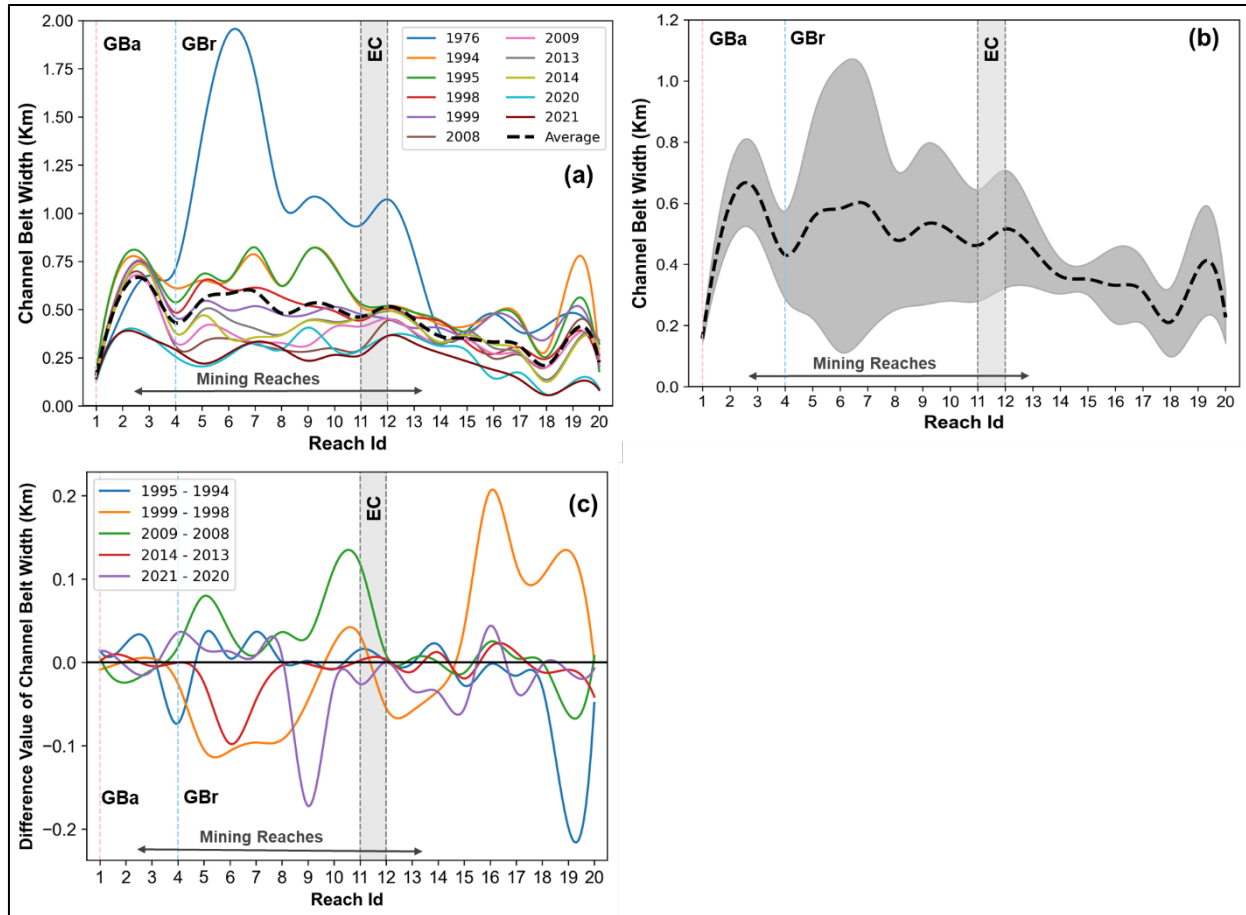


Figure 2.4: (a) Channel belt width (CBW) of the Gaula River across 20 reaches from 1976 to 2021, with the most pronounced narrowing observed in mining-affected reaches (5, 6, and 7). (b) CBW variability and its mean, indicate the long-term response of the river to sand mining, with the middle segment (reaches 3 to 13) showing the highest variability and most significant narrowing. The black dashed line shows the mean value and the shaded grey area represents the standard deviation as variability. (c) Intra-seasonal differences in CBW between pre- and post-mining periods highlight dynamic fluctuations, with negative values indicating narrowing and positive values showing widening across different months (GBa — Gaula Barrage, GBr — Gaula Bridge, EC — Elephant Corridor).

Figure 2.4b illustrates CBW variability concerning mean, showcasing the river's long-term response to sand mining activities. The reaches of the middle segment, being subjected to intensive mining, have been more prone to channel belt narrowing relative to the other reaches. Specifically, reaches 5 to 13 show extremely high variability in CBW, while a strong downward trend with lower variability is observed in reaches 14 and 15 (Fig. 2.4b). Reaches 16-20 show a slight increase in CBW variability, but not as much as in reaches 5 to 13. Figure 2.4c depicts the intra-seasonal difference in CBW between pre- and post-mining periods. The negative value in the figure corresponds to narrowing, while the positive value indicates widening. Figure 2.4c

shows that there is a large seasonal dynamicity in terms of CBW, and channel belt width across all the reaches can vary even within months, depending upon the nature of the excavation.

2.4.2. Deviation from the reference state

We have designed three indices, namely the Wet Channel Difference Index (WCDI), Dry Channel Difference Index (DCDI) and Vegetated Bar Difference Index (VBDI) to assess the reach-scale geomorphic condition of the river in terms of wet channel, dry channels/fresh deposits/degraded channels and vegetated bars, respectively, compared to the reference state (Fig. 2.5).

2.4.2.1. *Wet Channel Difference Index (WCDI)*

The WCDI quantifies the deviation of geomorphic conditions from the reference state in terms of the wet channel (Fig. 2.5a). Positive WCDI values narrowing of wet channels compared to reference state and vice versa. Reaches 1 to 13 show highly variable but mostly negative values of WCDI, implying the presence of wet channels in later years relative to the reference state. Since 2014, there has been a decline in the wet channel, and the WCDI value was close to zero in reaches 1-12 by 2021 (Fig. 6a). Reach 13 shows a significant trough in most years, suggesting the consistent presence of wet channels. Reaches 14 and 15 represent the transition from mining to non-mining reaches and display minimal deviation from the reference state. Further downstream, reaches 16 to 20 exhibit positive values, with notable peaks in Reach 16, 18, and 19, suggesting a reduction in wet channel area compared to the reference state.

2.4.2.2. *Dry Channel Difference Index (DCDI)*

The DCDI has been designed to assess the alteration of channel morphology caused by uneven siltation and channel abandonment/degradation relative to the reference state manifested as fresh deposits, degraded channels and dry channels (Fig. 2.5b). Positive DCDI values indicate channel narrowing and degradation, while negative DCDI values denote channel widening in the subsequent years. Across multiple years and all the reaches, we observe positive values indicative of channel narrowing. Reaches 1, 2 and 3 display minimal alteration from the reference state with slight positive DCDI values, implying limited channel narrowing. In the middle segment, particularly downstream of reach 4, the deviation from the reference state intensifies, forming pronounced peaks in reaches 5-7, followed by a sharp decline at reach 8. This deviation again

intensifies at reach 9, producing a strong peak at reach 10, before gradually tapering at reaches 11 and 12 and dropping at reach 13. This implies that reaches 5, 6, 7 and 10 have undergone intensive channel narrowing. Conversely, reaches 14 and 15 display minimal deviation, suggesting insignificant changes. The downstream reaches 16-20 also demonstrate positive but relatively smaller deviation from the reference state indicative of minor channel narrowing (Fig. 2.5b).

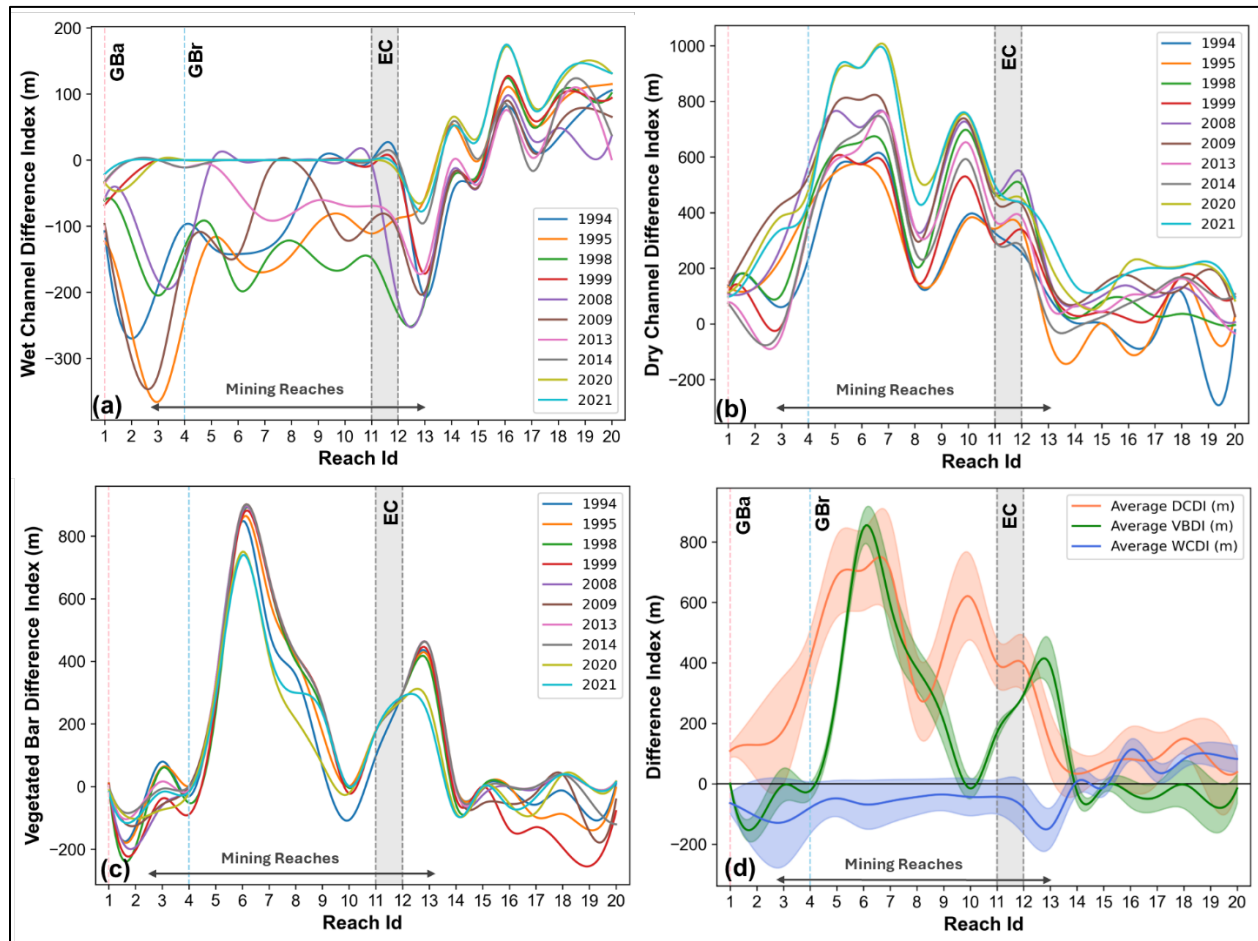


Figure 2.5: a) Wet Channel Difference Index (WCDI) shows the deviation of wet channels from the reference condition of 1976. Positive WCDI values indicate a reduction and negative WCDI values show expansion in the wet channel area. (b) Dry Channel Difference Index (DCDI) shows the deviation of dry channels (dry channel, fresh deposits and degraded channel) from the reference condition of 1976. Positive DCDI values indicate channel narrowing and negative DCDI values denote channel widening. (c) Vegetated Bar Difference Index (VBDI) across 20 reaches of the Gaula River from 1994 to 2021, showing the deviation of the vegetated bars from the reference condition of 1976. Positive VBDI suggests the decline of vegetated bars and negative VBDI suggests vegetated bar development in the subsequent years. (d) Spatio-temporal variability of VBDI, WCDI, and DCDI indices, depicting how the Gaula River's channel morphology has evolved in response to anthropogenic activities. Positive correlations are observed between dry channel and vegetated bars, while wet channel exhibits a negative correlation with both (GBa — Gaula Barrage, GBr — Gaula Bridge, EC — Elephant Corridor).

2.4.2.3. *Vegetated Bar Difference Index (VBDI)*

Positive VBDI values denote the decline of vegetated bars manifesting geomorphic degradation, and the negative values indicate vegetated bar development in the subsequent years, suggesting stabilization (Fig. 2.5c). Notably, reaches 6 and 7 exhibit the highest positive values, followed by reaches 12 and 13, indicating significant geomorphic degradation of these reaches. Reaches 5, 8, 9 and 11 have moderate to high VBDI values, whereas reach 3 initially shows slight positive values but gradually changes to negative values, suggesting vegetation growth in the later years. A few reaches, such as reach 2, 10 and 16-20, show slightly negative deviation from the reference state, implying the development of vegetated bars in the subsequent years. The remaining reaches show negligible difference values, suggesting insignificant alteration from the reference state (Fig. 2.5c).

Figure 2.5d depicts the spatiotemporal variability and mean values of three difference indices (VBDI, WCDI and DCDI) to reflect the overall character and behaviour of each reach in terms of river response to anthropogenic activities. The upper segment (reaches 1 and 2) shows a slight positive deviation in the average DCDI and negative but overlapping average values for VBDI and WCDI. This implies minor channel narrowing, vegetated bars and wet channels in the subsequent years from the reference state. The middle segment (reaches 3 to 13) shows significant changes in average VBDI and DCDI, with the positive values suggesting extensive channel degradation, even though the average WCDI values show a slight negative deviation from the reference state. The lower segment (reaches 14 to 20) depicts overlapping envelopes of the WCDI, VBDI and DCDI with values closely aligned to the reference state. Figure 6d also shows that the spatiotemporal variabilities of vegetated bars, wet channels, and dry channels are interrelated, suggesting a process linkage. For example, the Dry channel and Vegetated Bars show a strong positive correlation ($p = 0.70$). In contrast, the dry channel and wet channel show a moderately negative correlation ($p = -0.39$). Similarly, the vegetated bars and wet channel also show a moderately negative correlation ($p = -0.38$).

2.4.3. *Decadal-scale rate of morphometric parameters*

The change rate is calculated to quantify the dynamics of the morphometric parameters over a decadal scale. Figure 2.6a represents the overall change in the channel belt area, providing insight

into the rate of widening or narrowing within each timeframe. Positive values indicate channel belt narrowing, while negative values denote the expansion of the channel belt. Between 1976 and 1995, reaches 2 and 3 experienced channel belt expansions of 544,706 m² and 132,818 m², respectively, while significant narrowing occurred in reaches 6 and 7, with reductions of 2,557,621 m² and 1,800,098 m² in channel belt area resulting in highly positive change rate (Fig. 2.6a). Another notable event is the extensive channel narrowing in reaches 7, 9 and 10 of 610,871 m², 659,158 m², and 415,210 m², respectively, between 1995 and 1999 giving rise to a highly positive change rate. Conversely, during 2009–2014, channel expansion was recorded across all reaches with a negative change rate (Fig. 2.6a), with an aggregate increase of 50,460 m² along the whole channel.

Similarly, the decadal change rates for wet channels, dry channels, and vegetated bars have been calculated to understand in-channel processes within each timeframe (Fig. 2.6b, c and d). Positive values indicate a reduction in these features, whereas negative values denote expansion within each timeframe. Between 1976 and 1995, wet channel areas in reaches 2, 3, and 4 expanded by 516,510 m², 732,533 m², and 478,637 m², respectively resulting in a negative change rate (Fig. 2.6b). In contrast, from 1995 to 1999, these same reaches experienced significant reductions of 466,951 m², 732,532 m², and 478,637 m² resulting in change rates of >165,000 m²/yr (Fig. 2.6b). However, during the same period, reaches 13 and 14 showed an increase in wet channel areas by 228,694 m² and 157,265 m² with a change rate of -54,000 m²/yr. Between 1999 and 2009, wet channel expansion occurred across most reaches, with notable increases of 547,461 m² and 651,848 m² in reaches 2 and 3 as reflected in the negative change rate. This trend reversed during 2009–2014, with reductions of 597,019 m² and 651,848 m² in the wet channel areas of the same reaches 2 and 3, respectively (Fig. 2.6b).

The dry channel area showed a significant reduction across reaches 1 to 12 between 1976 and 1995, with notable decreases in reaches 5 (1,086,987 m²), 6 (1,148,232 m²), and 7 (932,749 m²) as reflected in widespread positive change rates (Fig. 2.6c). Between 1995 and 1999, alternating patterns of expansion and reduction were observed. The largest reductions occurred in 9 (299,145 m²), 10 (290,499 m²), 13 (363,368 m²), 14 (307,156 m²), 16 (244,384 m²), and 19 (291,452 m²). A notable expansion was recorded in reach 3, with an increase of 489,408 m².

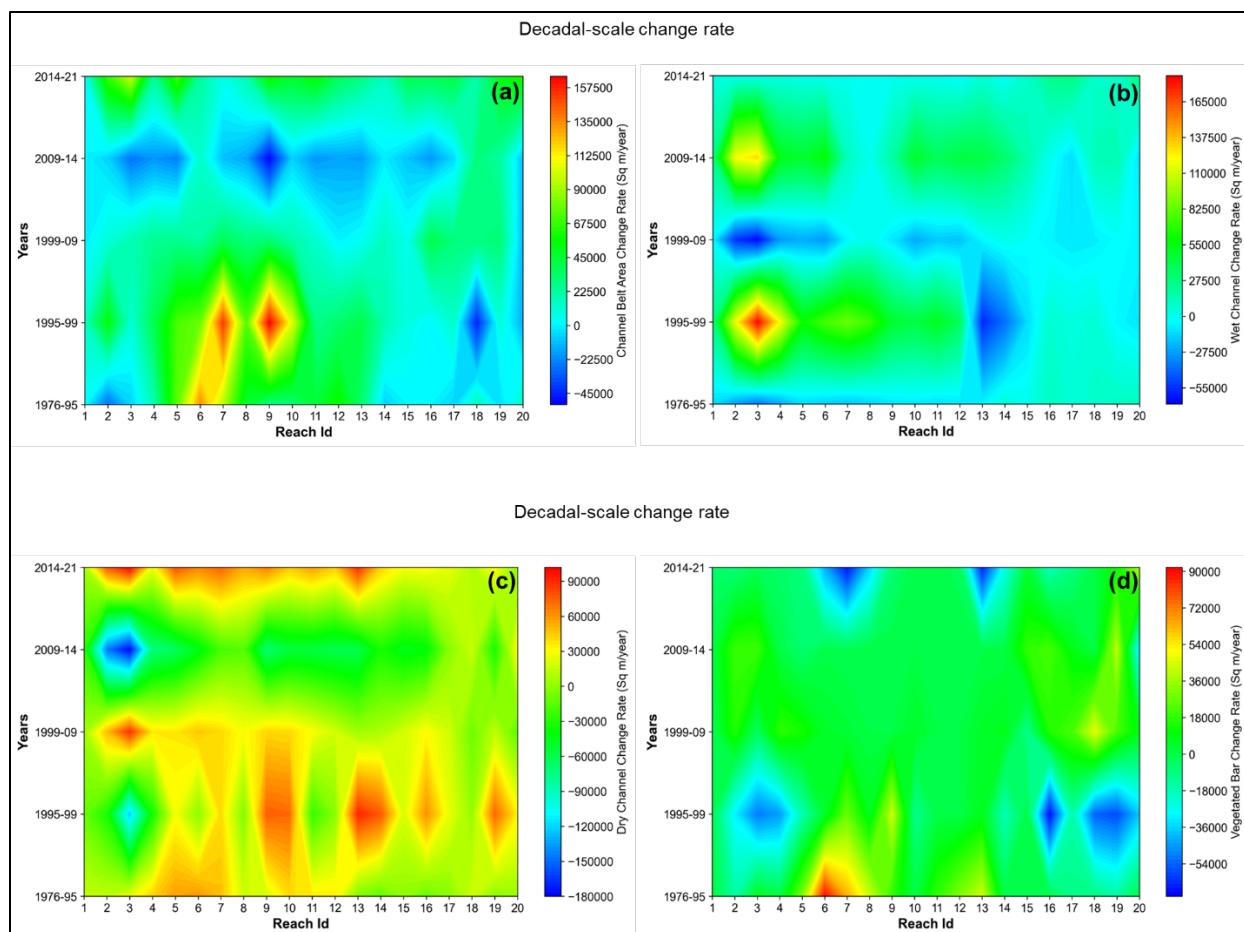


Figure 2.6: (a) Decadal-scale change rate ($m^2 / year$) in the Channel Belt area of the Gaula River from 1976 to 2021, showing periods of expansion and contraction. Positive values represent channel belt narrowing, while negative values indicate expansion. (b) Decadal change rate in the vegetated bar area, (c) wet channel area, and (d) dry channel area across different timeframes, revealing in-channel processes. The upper segment (reaches 1 and 2) shows initial expansion and stability, while the middle segment (reaches 3 to 13) exhibits significant contraction and degradation. The lower segment (reaches 14 to 20) displays moderate variability with alternating trends in wet channels, vegetated bars, and dry channels across decades.

Between 1999 and 2009, reductions in dry channel area occurred across all reaches, particularly in reach 3, which decreased by $874,612 m^2$. Conversely, from 2009 to 2014, significant but variable expansion was observed in all reaches (average $244,719 m^2$), with reach 2 increasing by $728,448 m^2$ and reach 3 by $888,568 m^2$. This trend reversed between 2014 and 2021, marked by a positive change rate (Fig. 2.6c) caused by substantial reductions in dry channel area, averaging $333,341 m^2$ across all the reaches with a significant reduction in reach 3 ($706,268 m^2$).

Figure 2.6d shows a significant decline in the vegetated bar area between 1976 and 1995, particularly in reaches 6 ($1,710,767 m^2$) and 7 ($1,206,671 m^2$) marked by a positive change rate.

From 1995 to 1999, vegetated bar expansion occurred in several reaches, including reach 2 (122,847 m²), reach 3 (199,927 m²), reach 4 (179,579 m²), reach 16 (273,025 m²), reach 18 (215,148 m²), and reach 19 (231,427 m²) (Fig. 7d). Another notable period of vegetated bar expansion was recorded between 2014 and 2021, with an average increase of 87,611 m² across all reaches. This was particularly prominent in reaches 6 (292,103 m²), 7 (468,783 m²), 8 (249,010 m²), and 13 (454,894 m²) all characterized by a negative change rate (Fig. 2.6d).

2.4.4. Thalweg Shifts

We have assessed thalweg shifts from pre- to post-mining periods at seasonal (1994-2021) and inter-decadal (1976- 2021) scales to investigate the impact of sand mining on the Guala River (Fig. 2.7). At the seasonal scale, reaches 2 to 12 exhibit significant variability in thalweg shift. Major peaks are observed at reaches 2 and 3, averaging 180 m and 191 m, respectively (Fig. 2.7a, b). Pronounced shifts in the reaches 4-12 are attributed to extensive mining activities. Average thalweg shift, as well as its seasonal variability, decreases downstream of reach 13. Further downstream, reaches 14 to 20 demonstrate minimal or no shift at the seasonal scale.

While the seasonal scale thalweg shift reflects the immediate impacts of sediment mining, the same at the inter-decadal scale helps in understanding long-term effects on river morphology in response to in-channel mining. At the inter-decadal scale, the river's average thalweg shift across all reaches was 14.94 m/year from 1976 to 1995, 36.90 m/year in 1999, declining to 15.12 m/year in 2009, and then slightly increasing to 26.37 m/year from 2009 to 2014, only to decrease again to 16.36 m/year from 2014 to 2021. At the inter-decadal scale, higher mean thalweg shift rates were observed in reaches 2 (56.9 m/year), 3 (38.7 m/year), 19 (37.9 m/year), and 20 (40.7 m/year), accompanied by the highest variability (Fig. 2.7c, d). Reach 1 exhibited the lowest shift rate (9.3 m/year), while the other reaches demonstrated relatively consistent lower average thalweg shift rates with comparatively reduced variability. A strong positive correlation ($p=0.90$) was noted between the average thalweg shift and its variability.

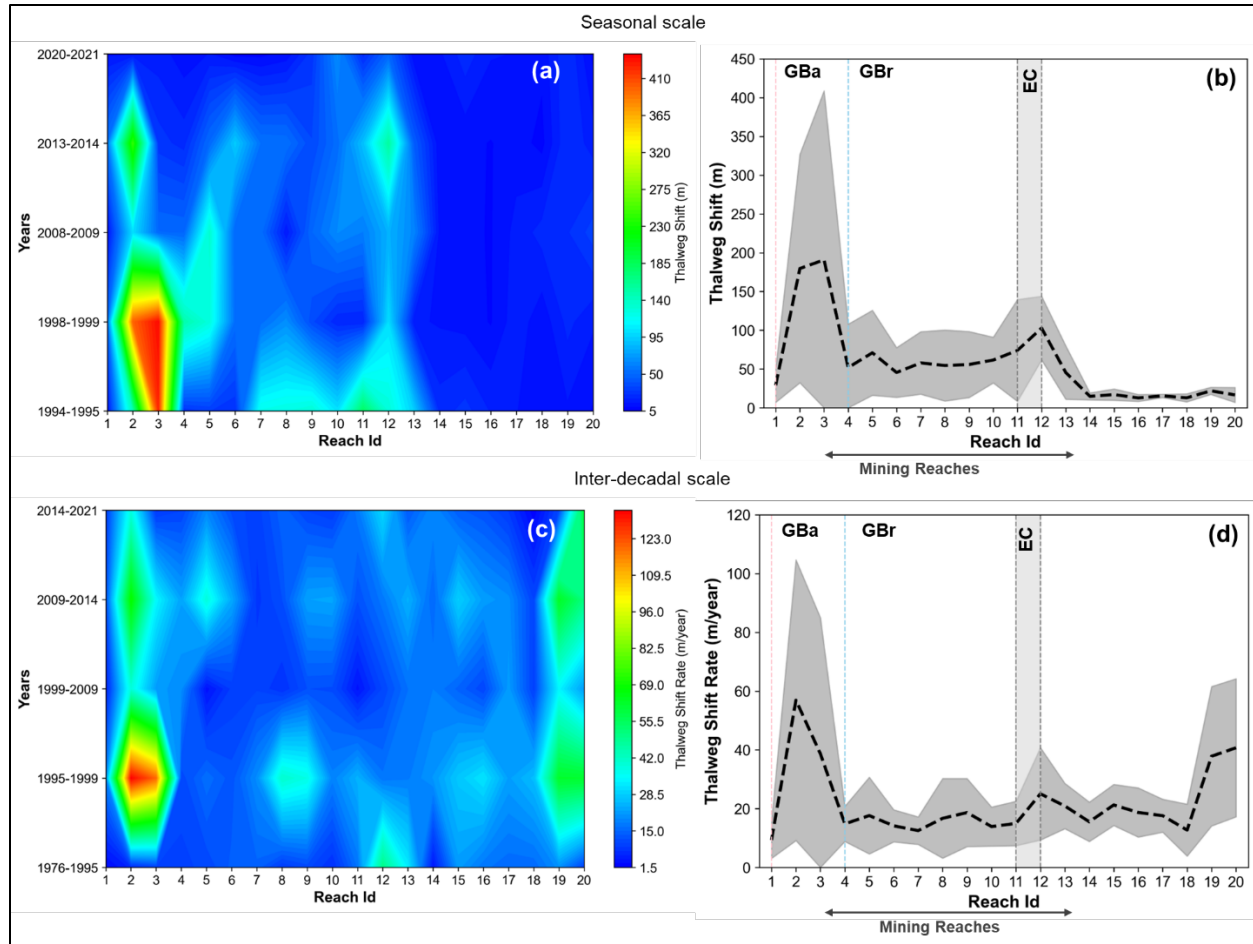


Figure 2.7: (a) Thalweg shifts across 20 reaches of the Gaula River at the seasonal scale (pre- and post-mining) with significant variability in reaches 2 to 12, and particularly pronounced in reaches 2 and 3. (b) Variability and average of seasonal thalweg shifts. (c) Thalweg shifts at the inter-decadal scale (1976–2021), showing long-term impacts of sand mining with higher mean shifts in reaches 2, 3, 19, and 20, and relatively consistent shifts in other reaches. (d) Variability and average of inter-decadal thalweg shifts (GBa — Gaula Barrage, GBr — Gaula Bridge, EC — Elephant Corridor).

2.4.5. SWAT-derived discharge and stream power distribution

A 27-year (1994 to 2020) hydrograph derived from the SWAT model (Pipil et al., in prep) is shown in Figure 2.8. Discharge data shows low discharge levels before 2006, followed by a surge from 2010 to 2014, which likely influenced channel morphology and river dynamics during this time. Figure 2.9 illustrates the reach-wise distribution of total stream power (TSP) along the long profile of the Gaula River based on the SWAT-derived discharge data. Stream power is very high in bedrock-controlled reach 1 and then declines in reach 2. There is a sharp rise in TSP from reach 2 to reach 3, marking the beginning of the mining zone. Stream power remains moderately high

and doesn't vary much till Reach 7 and then declines in reach 8. Reaches 9, 10, 11 and 12 show minor fluctuations in TSP, following which there is a sharp decline in reach 13. The elephant corridor lies within reaches 11 and 12. Stream power remains consistent from reach 14 to 16, declines slightly in reaches 17 to 19, and gently rises in reach 20. Notably, the knickpoints are located in reach 3, and at the transitions from reaches 7 to 8 and 12 to 13.

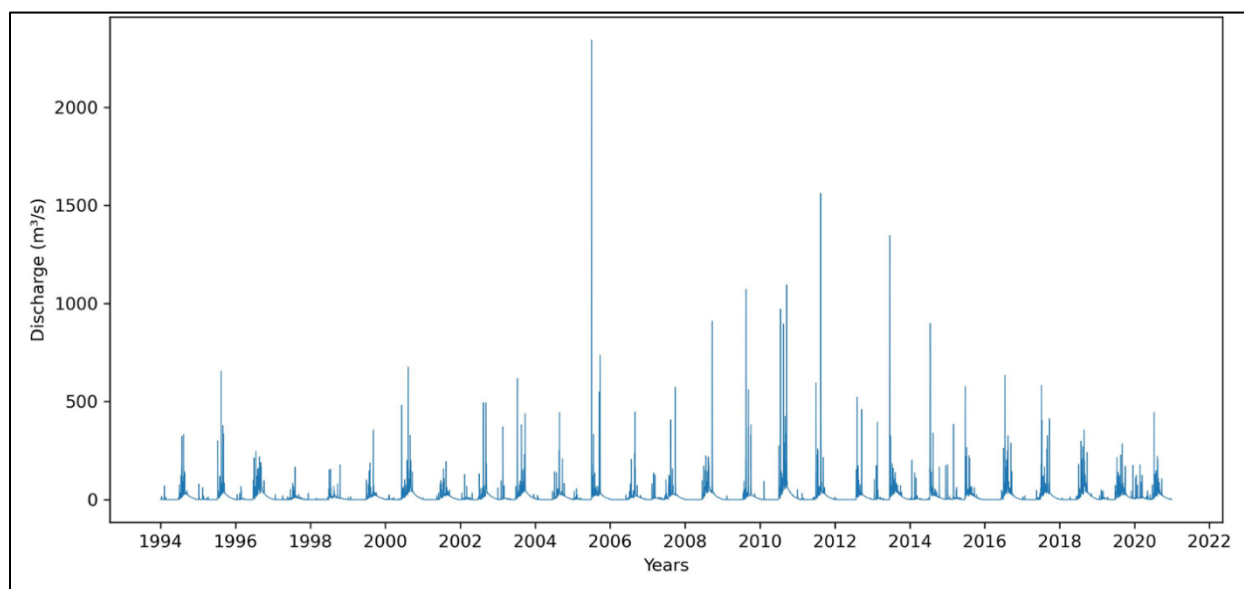


Figure 2.8: SWAT-derived hydrograph calculated at the Gaula catchment outlet from 1994 to 2020, showing low discharge before 2005, following a sharp increase in 2005, with particularly high discharge from 2010 to 2014.

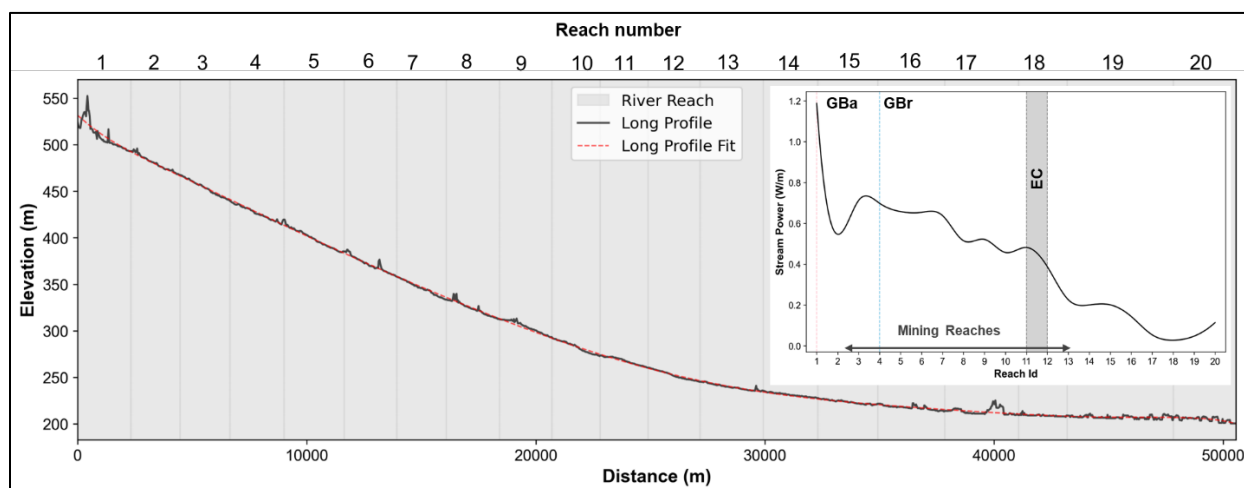


Figure 2.9: Longitudinal Profile of the Gaula River based on Copernicus DEM showing all 20 reaches used in this study, the black line represents the raw data and the red dashed line represents the fitted profile. Inset shows the Total Stream Power (W/m) distribution of the Gaula River with all the major locations such as the Gaula Barrage (GBa), Gaula Bridge (GBr) and the Elephant Corridor (EC) marked. The mining stretch is shown in the TSP plot.

2.5. Planform response to changes in flux boundary conditions

2.5.1. Geomorphic response, feedback and interaction

Geomorphic processes and the resulting river forms are governed by the interaction between driving forces, such as discharge and channel slope, and resisting forces, like vegetation and channel bed features, defining the flux boundary conditions. Flux boundary conditions are positioned within the imposed boundary conditions, directing the energy conditions that influence river behaviour (Fryirs, 2017). Valley bottom confinement serves as an imposed boundary condition that dictates the functioning of a contemporary river within the valley bottom or the "effective valley width", determining how flow energy is concentrated or dissipated, and shaping the patterns of sediment erosion and deposition (Brierley and Fryirs, 2005; Fryirs and Brierley, 2010; Fryirs et al., 2016). The natural capacity for adjustment refers to the river's ability to undergo morphological changes in response to alterations in flux boundary conditions. This enables the river to maintain a characteristic state, with morphology remaining relatively uniform on a reach-averaged scale, without bringing a wholesale change in river type (Fryirs and Brierley, 2005). Since in-channel sand mining involves the extraction of sediment from the channel bed, it creates an imbalance between driving and resisting forces, which is manifested in terms of alteration in the local gradient, creating knickpoints, leading to high stream power, thus altering the flux boundary conditions.

The imbalance of the driving and resisting forces causes the river to adjust or change in three dimensions: vertical, lateral and wholesale (Fryirs and Brierley, 2005). Gravel-bed rivers have been considered to possess seven degrees of freedom because they are free to adjust their average bankfull width, sinuosity, meander arc length, mean depth, maximum depth, slope and velocity (Hey and Thorne, 1986).

Our paper mainly focuses on the lateral adjustment of the river in planform. The Gaula River has undergone significant channel narrowing in mining reaches, often associated with channel incision (Yanites et al., 2010; Ylla Arbós et al., 2021). Being located in an active tectonic regime, the Gaula River has a natural tendency to incise (Goswami, 2018). However, our analysis of planform dynamics reveals that channel belt width decreased significantly after sand mining started in this region, and the variability is higher in the middle segment of the river (mining zone)

than in the upper or lower segments (Fig. 2.3, 2.4a and 2.4b). The reaches of the upper segment are partly confined due to bedrock and tectonics; hence the channel belt narrowing is not significant there (Fig. 2.2a, 2.2b, 2.3a, 2.4a and 2.4b). Further, since mining is prohibited in the elephant corridor (reach 11 and a part of reach 12), pilot channels have been created to provide a pathway for the flow of water (Fig. 2.10a). With continued sediment deposition in the elephant corridor, the pilot channels were further constrained, thereby limiting the lateral movement. Further downstream, the lower segment (reaches 14 to 20) show much less variability, as they are not significantly impacted by anthropogenic stress.

The independent variables controlling the regime dimensions of the channel regime are discharge, bed load discharge, bed material size, bank material characteristics, valley slope and bank vegetation (Hey and Thorne, 1986). In this work, the interaction and interplay among in-channel belt features such as vegetated bars, dry channels and wet channels help us to understand the processes within the channel belt. Our work demonstrates a feedback mechanism among vegetation, channel morphology and hydraulics, where changes in one component significantly impacted the others. For example, a decline in in-channel vegetation led to the convergence of sheet flow and initiation of channels, which further reduced vegetation cover, thus promoting channel entrenchment (Bull, 1997; Sandercock et al., 2007).

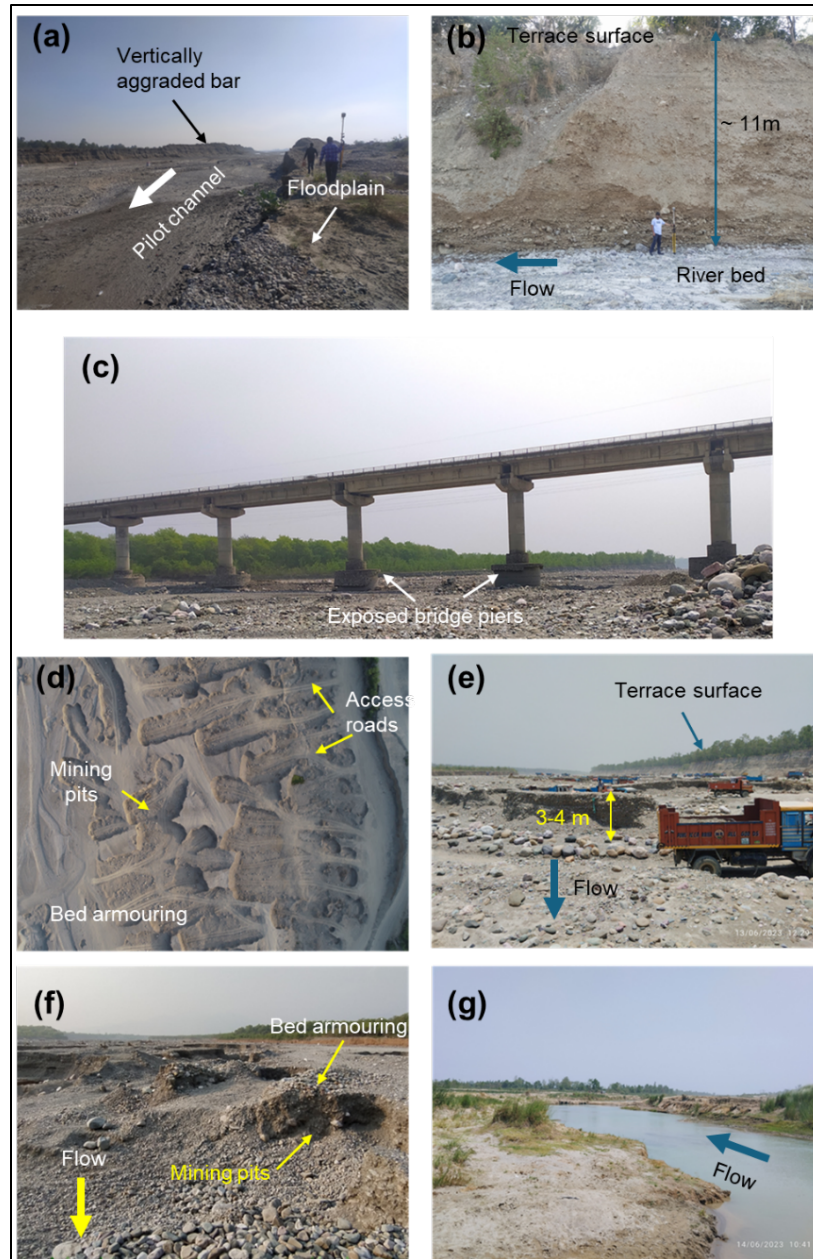


Figure 2.10: Field photographs showing the geomorphic impacts of sand mining in the Gaula River. (a) Mining is prohibited in the Elephant Corridor and a pilot channel has been created to facilitate water flow. Over time, sediment has accumulated in this corridor, raising the elevation of the deposited bar to match that of the riverbanks on both sides in recent years; (b) channel incision along the right bank of the Gaula River in reach 7 where the river terrace is approximately 11 m higher than the contemporary channel bed; (c) scouring of bridge piers as evidence of channel incision at the Gaula bridge (reach 4) due to sand mining; (d) channel bed degradation as seen from UAV image. The entire channel bed has been excavated, with no geomorphic diversity remaining; (e) on-going sand mining and an armoured riverbed. Approximately, 7500 trucks and other carriers, such as horse carts, supported by 6500 labourers, are involved in this activity; (f) channel bed degradation and bed armouring; (g) the wet channel reappears as baseflow in the reaches of the lower segment, with sparse vegetation on either side of the channel. No sand mining activity is spotted here.

Our findings align with the previous research that suggested a major control of vegetation on channel width and wetted perimeter (Hey and Thorne, 1986), which enhances sediment retention by increasing friction, thereby promoting sedimentation and channel morphodynamics (Sandercock et al., 2007). The Vegetated Bar Difference Index (VBDI) in Gaula follows spatio-temporally strong, similar and low variability patterns (Fig. 2.5c and d). This suggests that the deviation of the vegetated bars from the reference state has surpassed the threshold in the subsequent years, resulting in such distinct spatio-temporal patterns.

2.5.2. Spatio-temporal variability in morphological response

In the upper segment (reaches 1 and 2), the lateral adjustment of in-channel features is limited and the deviation of the VBDI and DCDI from the reference state is not particularly pronounced (Fig. 2.3a, 2.5a, c and d). This is attributed to the inherent behavioural characteristics of the river, which maintains a partly confined channel due to controls such as bedrock, hillslope and terraces (Fig. 2.2). However, the growth of vegetated bars has shifted upstream, as shown by observations in planform images (Fig. 2.3a), resulting in a minor variability in VBDI in reaches 2 and 3 (Fig. 2.5c). This is because mining from reach 3 cleared the vegetated bars and fresh deposits in the middle segment, limiting the deposition of sediments and vegetation growth in the reaches of upper segment only. On the other hand, we note the absence of wet channel area during the non-monsoon period in the upper and middle segments of the Gaula River in the reference year 1976 (Fig. 2.3a and b). Wet channels were only present downstream, where the water table intersected the surface topography. This reflects the ephemeral nature of the Gaula River before the construction of the barrage in the year 1980 and the onset of sand mining activities in 1990. Following the barrage construction, the river flow was regulated, resulting in the emergence of thin wet channels even during the non-monsoon period from 1994 onwards, as evidenced by both planform observations and the WCDI (Fig. 2.3a, 2.3b, 2.5a and 2.5d). Thus, both in the upper and the middle segments, the WCDI values are mostly negative, indicating the presence of wet channels in the subsequent years.

The middle segment (reaches 3 to 13) have experienced the most dramatic effects of sand mining. As already discussed, the maximum channel belt narrowing is documented in these reaches. The positive values of VBDI in the middle segment of reaches 6, 7, 12 and 13 show that the vegetated bars diminished drastically compared to the reference state because of reckless scraping and scooping (Fig. 2.5c and d). The river has entered a new geomorphic regime in these reaches where it behaves like a narrow conduit of water and sediment transfer with significant incision. Like VBDI, the DCDI also shows prominent peaks at reach 5, 6 and 7 (Fig. 2.5b and d). Additionally, reaches 6 and 7 are partly confined, as reflected by the confinement index of 27.73% and 64.61% respectively (Fig. 2.2) by terraces. These terraces were formed by rapid channel narrowing and incision owing to sand mining, and without vegetation, they have developed into potential erosion zones (Fig. 2.10 b and c). The DCDI and VBDI values decrease from Reach 7 to Reach 8, indicating that Reach 7 is highly erosive. This is further supported by the presence of a knickpoint in Reach 7, as the stream power also drops between these reaches (Fig. 2.9). Reaches 8 to 12 show alternate zones of erosion and deposition which suggests that the river is still trying to adjust to the new geomorphic regime. In reach 10, the vegetated bar is absent in all the years, including the reference year, and hence no change is recorded. This implies that reach 10 has always been erosive, flushing the sediments downstream. The absence of vegetation in reach 10, coupled with a substantial decline in dry channel area, suggests that this reach has amplified to be an extremely high erosive reach. Downstream of the elephant corridor, in-channel sand mining recommences at reach 12 (partly) and reach 13, resulting in a drop in bed elevation. This creates a locally steep gradient, forming a knickpoint with high stream power where erosional processes predominate (Fig. 2.9). The lack of vegetated bars coupled with the decline of dry channels and the presence of wet channels also adheres to this, implying erosional processes.

In contrast to the middle segment, the lower segment (reaches 14 to 20) behave moderately analogous to the reference state where all the indices (DCDI, WCDI and VBDI) overlap with slight variability in pattern (Fig. 2.5d). This pattern suggests that the river is not significantly impacted by anthropogenic stress in these reaches. Reaches 14 and 15, situated downstream of the elephant corridor, display the minimum deviation from the reference year in terms of VBDI, DCDI, WCDI, and channel belt width (CBW). In these reaches, the intersection of the water table with

surface topography generates consistent wet channels throughout the years. This inherent characteristic of the river may have contributed to its resilient behaviour. Further downstream, the wet channel area was higher in the reference state and declined in the subsequent years, likely due to channel narrowing and incision. Although sand mining activities are absent in the reaches of the lower segment, the impacts of mining are known to be transferred downstream (Kondolf, 1997). We argue that the excavation from the reaches of the middle segment led to a hollowed and sediment deficit riverbed (Fig. 2.10d, e and f), which trapped the incoming bedload sediment in the upcoming monsoon. This led to the ‘hungry water effect’ downstream and eroded the channel bed and banks in the lower reaches (Kondolf, 1994; Kondolf, 1997; Rinaldi et al., 2005). This is consistent with the WCDI and DCDI trends, both displaying a slight positive deviation from the reference state indicative of channel narrowing associated with incision and channel bed erosion (Liébault and Piégay, 2002; Yanites et al., 2010; Ylla Arbós et al., 2021). The bank erosion is further evidenced by the inter-decadal Thalweg shift, which is higher in the reaches of the lower segment (Fig. 2.7d).

Although the effects of mining are not immediately apparent in the reaches of the lower segment, the planform response to sand mining has been prominent since 2009, with channel narrowing and steady reduction in fresh sediment deposits and vegetated bars (Fig. 2.3c), which have transitioned into active floodplains and terraces, implying riverbed lowering. This signifies a delayed response to sand mining activities in the reaches of the lower segment in recent years. The availability of water with channel narrowing and riverbed lowering, causes less frequent submergence and uprooting of vegetation, allowing for shrub growth (Fig. 2.10g). However, meander and thalweg shifts can lead to erosion and uprooting of vegetation, but they can regrow in the following years.

2.5.3. Controls of thalweg shifts

Thalweg shifts at an inter-decadal scale show alternating periods of high and low changes. Reach 1 displays minimal thalweg shift owing to its bedrock controlled partly confined nature. Conversely, the thalweg shift is considerably high in reaches 2 and 3, and this is attributed to the upstream migration of vegetated bars and the subsequent development of channels across these bars (Fig. 2.7). As the thalweg represents the deepest part of the river, its trajectory is shaped by

the inherent instability of braided river morphology (Ashmore, 2013). Additionally, variations in discharge (from barrage release) and frequent changes in local slope (from river bed mining) cause frequent alteration in the flow regime, leading to the switching of channels across the braided bars. In the reaches of the middle segment, the thalweg shift shows an overall cyclic pattern (Fig. 2.7d), but several reaches (4, 6, 7, 10, and 11) with low average thalweg shift rate and low variability reflect fixing of thalweg because of channel incision (Fig. 2.7c, 2.7d, 2.10a and b). This pattern in the thalweg shifts correlates with other indices (VBDI, WCDI and DCDI), which also indicates channel narrowing and incision. Conversely, the reaches of the lower segment are characterized by unconfined valley bottoms (Fig. 2.2) and, hence, moderate to high thalweg shifts in these reaches. The only exceptions are reach 14 and 18, which show a straight channel with the conversion of vegetated bars and fresh deposits into inactive floodplain (reach 18 shown in Fig. 2.3c), signifying an incised and erosive reach.

In contrast to the long-term response to sediment mining activities, the seasonal or short-term thalweg shifts response can result in quick adjustments in the river's behaviour. Figure 2.7a shows the yearly response as a function of the preceding year's mining activities. At the seasonal scale, reaches 2 to 12 exhibit significant thalweg shifts, reflecting the dynamics of mining operations and sediment deposition. Mining activities vary annually, and thus the spatial distribution of pits also varies. Excavations in the mining season might not get fully replenished in the forthcoming monsoon, and hence, the river follows the locus of the excavated pits. The location of mining pits in the next mining season is guided by sedimentation patterns and concurrent bed topography. Particularly in the middle segment (the mining zone), thalweg shifts are pronounced on a seasonal scale. Large thalweg shifts in reaches 2 and 3 signify extensive mining in the downstream reaches, triggering upstream migration of knickpoints (Kondolf, 1994; Kondolf, 1997; Rinaldi et al., 2005) and prompting the river to seek the most efficient downstream path. Conversely, the impacts of sand mining in the lower segment (reaches 14- 20) on a seasonal scale are negligible with very low variability.

2.6. Connecting the morphological response to evolutionary timelines

Based on the planform dynamics presented above, we have attempted to identify different phases of the geomorphic evolution of the Gaula River under the anthropogenic forcing of sand

mining. In addition to mining activities, the river's channel morphology is also shaped by natural flood events and regulated discharges from the upstream Gaula barrage. Figure 2.11a represents the reference condition of the Gaula River before any major anthropogenic disturbance. We have identified four distinct phases that shaped the river channel morphology (Fig. 2.11b-e).

2.6.1. Start of sand mining: Barren conditions (1976-1995)

The barrage was established in 1980, and mining started in 1990. With the establishment of the barrage (reach 1), the reaches (2 and 3) saw an overall increase in the channel belt area, with an increase in vegetated bars (reach 2 only) and wet channels and a decrease in the dry channel area. This suggests deposition downstream of the barrage due to high sediment supply from active tectonics controlled upper catchment, slope change and controlled flow caused by the barrage (Fig. 2.11b). The controlled flow from the barrage ensured functional connectivity and slope breaks induced from hillslope to plains transition as well as the barrage caused aggradation downstream of the Gaula barrage. A similar increase in bar area suggesting aggradation has also been reported in the Kosi River, attributed to high sediment supply from upstream and slope changes caused by barrage and embankment (Sinha et al., 2014). In the reaches of the middle segment, which is the mining zone, the Gaula river witnessed a major change in morphology e.g. decrease in vegetated bars (Fig. 2.11b) which in turn favoured channel entrenchment and erosion, creating positive feedback on channel narrowing (Bull, 1997; Sandercock et al., 2007). Thus, the overall channel belt area decreased rapidly in this period. There was an increase in wet channels in the reaches of the middle segment too, due to barrage-controlled discharge

(Fig. 2.11b), causing erosion and entrainment from middle segment and deposition downstream. This explains a slight increase in dry channels and fresh deposits in the downstream reaches.

2.6.2. Mobilization (1995 – 1999) followed by incision (1999 -2009)

The mobilization period is marked by a substantial increase in thalweg shift induced by slope changes attributed to sediment deposition and excavation (Fig. 2.11c). In the previous phase, there was a loss of vegetated bars in the reaches of the middle segment, which exacerbated erosional processes and channel narrowing. As a result, the river re-mobilised secondary sediment sources (exposed bars) and re-deposited them in the downstream reaches. A local

increase in gradient due to channel bed excavation also amplified erosion. The incision period is marked by the reduction of the thalweg shift as the river is constrained, which resulted in channel narrowing, as documented earlier. This led to the development of a narrow but continuous wet channel by 2009 but a significant decline in geomorphic diversity (Fig. 2.11c).

2.6.3. Channel belt widening (2009 – 2014)

Despite the reduced geomorphic diversity and a thin, narrow channel, the post-2009 period is characterized by high discharge levels, as depicted in Figure 9. Consequently, the river channel experienced a slight widening in the reaches of the upper and middle segments with an increase in thalweg shift too (Fig. 2.11d). This implies the ability of high floods to recover the channel despite intensive mining activities, as also documented in an ephemeral Mediterranean stream in eastern Spain (Calle et al. 2017). Floods can reactivate sediment transport and fluvial processes, aiding in the restoration of channel morphology to near-reference conditions following extensive gravel mining activities as evidenced in the Palancia River in Spain (Sanchis-Ibor et al., 2017). Dean and Schmidt (2013) also documented instances where floods reversed channel-narrowing trends observed in previous decades and emphasized the geomorphic effectiveness of floods (Wohl, 2020) in modifying and resetting the geomorphology of fluvial systems. However, in the case of the Gaula River, this recovery seems to be short-lived as the sand excavation continued incessantly and eventually degraded the channel geomorphology as evidenced in the next phase.

2.6.4. An underfit channel (2014 – 2021)

In recent years, from 2014-2021, the wet channel is not visible in the upper and middle segments, probably due to the incision, leading to the lowering of the groundwater table (Rinaldi et al., 2005). Notably, the period also happens to include the COVID-19 pandemic year of 2019-20, during which mining operations ceased, facilitating vegetation encroachment on remnant sidebars in the reaches of the upper and middle segments. In these reaches, the river transformed into a low-flow incised channel inset within a macro-channel ('underfit' channel; Dury, 1964), with vegetation growth on river benches shielding them from erosion during low flow (Fig. 2.11e). The mismatch between the size of the incised channel and the valley suggests

that even a high discharge (post-2006) condition is not enough to rejuvenate the river condition to the reference state.

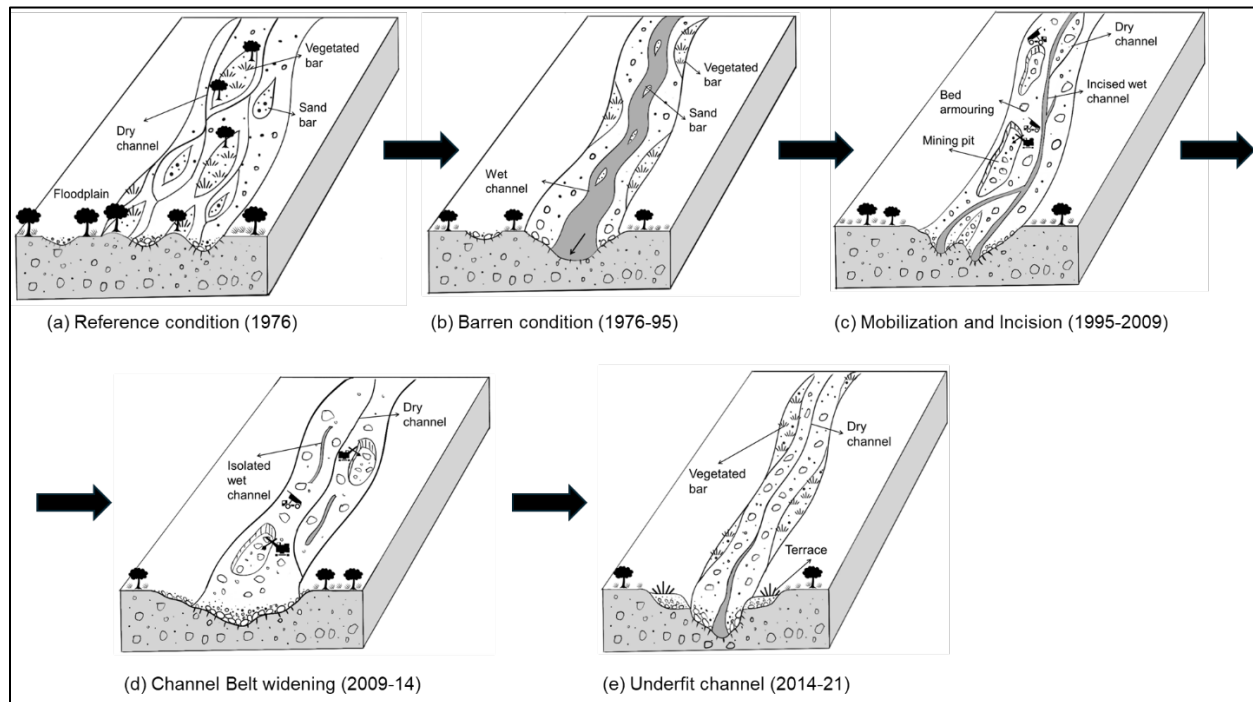


Figure 2.11: Geomorphic evolution of the Gaula River from 1976 to 2021, highlighting key phases of channel alteration due to sand mining and barrage influence. Alteration of the channel from (a) reference condition to (b) barren conditions (1976–1995) with the clearing of vegetated bars, controlled discharge from the upstream Gaula barrage. This was followed by (c) mobilization (1995–1999) and incision (1999–2009) phases, characterized by thalweg shift, sediment mobilization, and narrowing caused by channel incision and then, (d) channel belt widening (2009–2014), driven by high discharge events widening the channel belt. The Gaula River developed (d) underfit channel conditions (2014–2021), marked by bed armouring, low flow incised channel inset a macro-channel with vegetation encroachment on benches during periods of mining cessation (COVID-19).

2.7. Process- Response framework

Sand mining in the Gaula River has significant geomorphic effects, particularly through the loss of vegetated bars, removal of finer grains and subsequent channel erosion. Figure 2.12 shows a process-response framework to illustrate the geomorphic impacts of sand mining based on our understanding of this study. The pronounced effect of sand mining in the reaches of the middle segment can be explained by textural sensitivity, which describes the composition of the materials and their ability to be moved, moulded and reworked by impelling forces (Fryirs, 2017). The longitudinal bars in gravel and sand-bed rivers are more sensitive to recurrent formation and

reworking than fine-grained lateral bars and boulder-based cascades (Fryirs, 2017). The grain size in these reaches of middle segment is mostly gravel and sand, which can be easily mobilized. The removal of vegetated bars degrades the geomorphic diversity and reduces the sediment retention capacity, promoting sediment mobilization and channel erosion, leading to channel incision. Bed armouring occurs as finer sediments are selectively removed, leaving behind a layer of coarser materials that inhibit natural sediment transport and connectivity. The processes of bed armouring and sediment excavation decrease the sediment load within the river system, which exacerbates channel erosion and incision by increasing the stream power because of the 'hungry water effect'. In a similar study, channel incision in several reaches of Drac River, France, accelerated by rapidly cutting through the ancient fluvial-lacustrine clay deposits, increasing scouring rates and reducing gravel supply from bank erosion, highlighting the reach's sensitivity to disturbance (Brousse et al., 2021). Similarly, in the Bernesga River, Spain, an incision was concentrated in narrower segments due to the impact of bedload particles on soft bedrock as a consequence of mining, and further incision (Ferrer-Boix et al., 2023). The Johnsbach Valley in Austria also exhibited enhanced erosion because of the exposure of talus-covered bedrock attributed to gravel mining (Rascher et al., 2018).

In-channel excavation induces slope changes, leading to a drop in the base level, causing the river to concentrate its flow into a single channel. This reduces the wet channel area and further degrades geomorphic diversity. This decline in the wet channel area leads to the fixing of thalweg, leading to further incision. Channel belt narrowing is therefore associated with channel incision, reflecting the river's adjustment to reduced sediment supply and increased erosion. The overall process-response framework is therefore characterized by a positive feedback system.

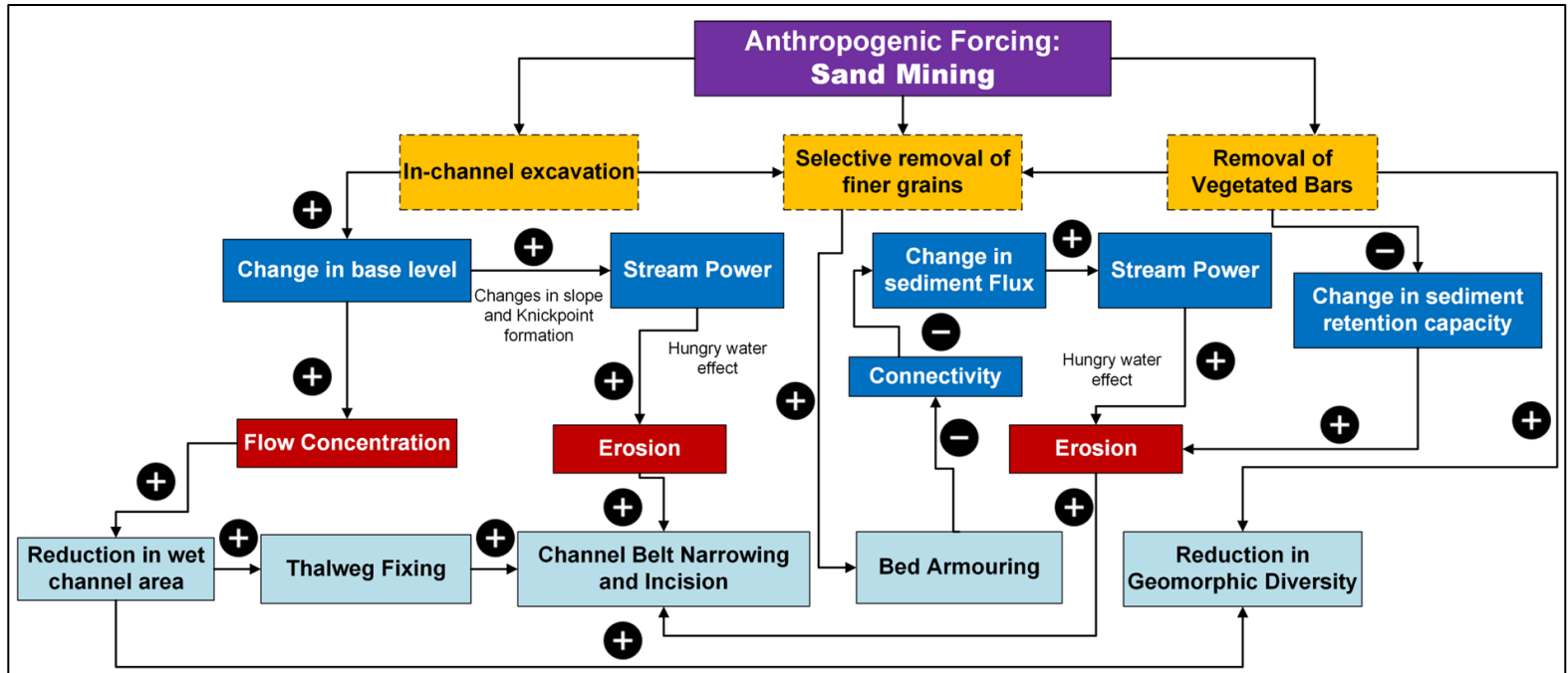


Figure 2.12: A process-response framework of the Gaula River under the anthropogenic forcing of sand mining showcasing a positive feedback system.

2.8. Summary and conclusions

1. In-channel sand mining in the Gaula River has altered the flux boundary conditions, creating an imbalance between driving and resisting forces. For example, the indiscriminate extraction of sand from the channel bed increases the local gradient and generates knickpoints that, in turn, increase the stream power and hence the energy available for sediment transport.
2. We have documented channel narrowing and incision, thalweg fixing, bed armoring and a severe decline in geomorphic diversity as some of the major geomorphic impacts of sand mining in the Gaula River.
3. We have identified four distinct evolutionary phases of the Gaula River at a historical time scale which reveal a fairly rapid degradation of the river in response to sand mining viz. (a) barren conditions (1976–1995), (b) mobilization followed by incision (1995–2009), (c) channel belt widening (2009–2014), and (d) underfit channel (2014–2021).
4. A process-response framework to characterize the geomorphic impacts of sand mining in the Gaula River reveals a positive feedback system. The major hydrogeomorphic processes shaping the channel morphology have been significantly altered by intensive sand mining activities manifested in terms of modified hydrological and sediment transport regimes.

Chapter 3

3. Geomorphic impacts of sand mining: Peninsular River

3.1. General

Riverine sand mining has emerged as a critical driver of fluvial degradation, yet its spatiotemporal distribution and geomorphic implications remain underexplored in many Indian peninsular river systems. This chapter presents an integrative approach to assess the impact of sand mining on river morphology by focusing on the Damodar and Sone Rivers—two heavily mined and regulated systems in India.

Using high-resolution Google Earth imagery, we mapped sand mining sites across 25 reaches of the Damodar River, categorising them into three zones based on the location of barrages and mining activities. Additionally, three severely impacted windows were selected along the Sone River. Each mining site was spatially associated with its morphological class—whether located within the channel belt or on adjacent floodplains—an aspect rarely addressed in prior research. Mining hotspots were also identified and characterised for intensity and spatial growth.

To examine long-term planform dynamics, we utilized Google Earth Engine (GEE) to analyze multi-decadal satellite imagery (1988–2023) and conducted morphometric analysis by calculating Bar area/ channel area, braiding, and sinuosity index using the Python-based RivGraph tool. This automated, reproducible workflow minimizes user bias and enables rapid, large-scale assessment of geomorphic features, including wet channels, sand bars, active river channel, and vegetated bars.

This project fills a major methodological and thematic gap by mapping mining activities in a geomorphological context and linking them to measurable fluvial changes. It contributes to actionable insights for sustainable river management, remote sensing-based monitoring, and evidence-driven mining regulations.

3.2. Mining footprints in high-resolution satellite imagery

Different methods of sand mining are used in the Sone and Damodar rivers. The miners remove sand from wet channels and excavate pits on the river channel and floodplain. They employ bar skimming technique as well. Sand mining pits can be classified into many groups according to the presence of vegetation or water. In this study area, there are different kinds of sand mining pits: vegetated pits, which have developed vegetation after a period of inactivity, wet mining pits, which indicate that they were dug below the water level, and dry mining pits. Bunds, or places where the extracted sand is transported by trucks, are another notable aspect of the sand mining operations that are present at both research sites (Fig. 3.1).

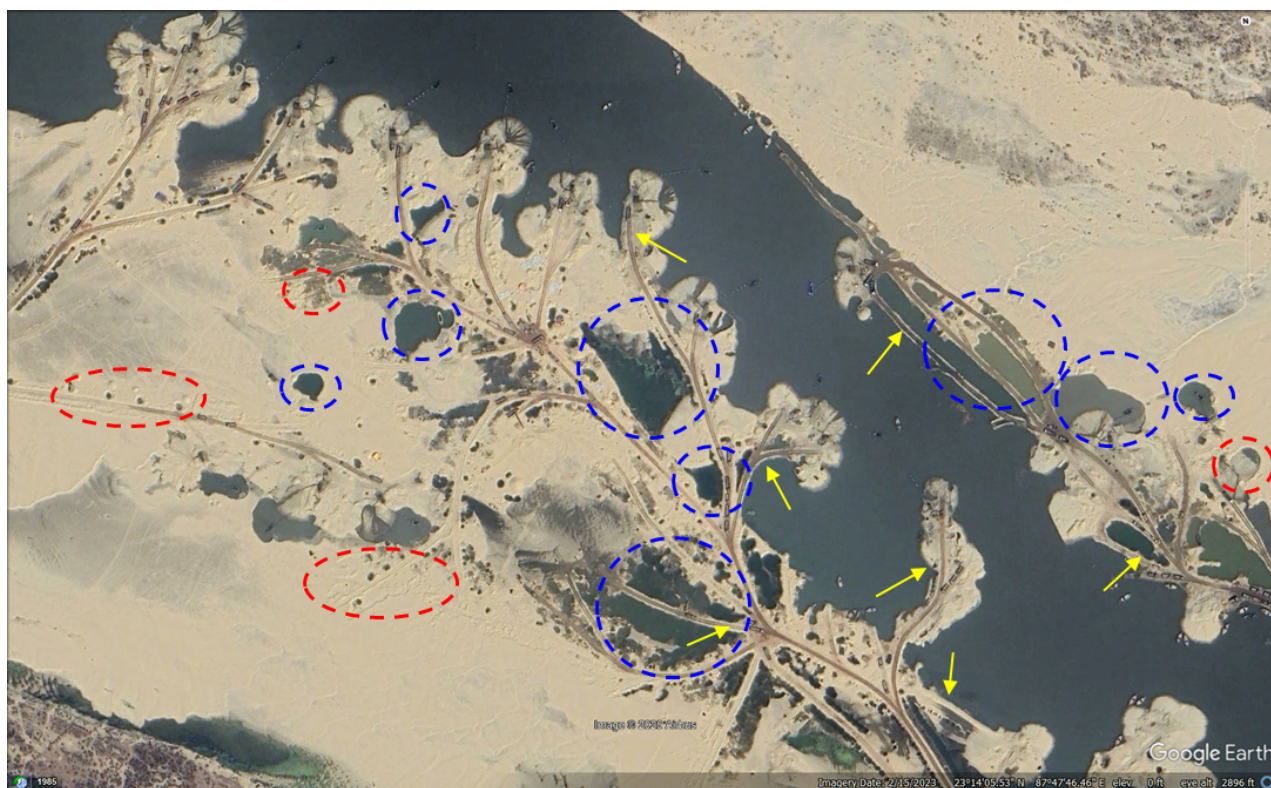


Figure 3.1: Google Earth imagery showing various sand mining features in the Damodar River. Red circles indicate examples of dry mining pits, typically located on exposed sandbars. Blue circles indicate wet mining pits, either situated directly within the wet channel or excavated deep enough for groundwater or channel water to accumulate. Yellow arrows point to bunds, which are temporary earthen roads constructed to facilitate the movement of trucks and equipment for sand transportation.

3.3. Mapping geomorphic impacts of sand mining

3.3.1. Datasets and Methodology

USGS Landsat 5 Level 2, Collection 2, Tier 2: This collection includes atmospherically corrected surface reflectance and land surface temperature data obtained from the Landsat TM sensor. These images include four visible and near-infrared (VNIR) bands, two short-wave infrared (SWIR) bands, and one thermal infrared (TIR) band, all of which have been orthorectified for surface reflectance. They also comprise intermediate bands for calculating ST products, as well as QA bands.

Dataset Availability: 16/03/1984–05/05/2012.

Dataset Provider: USGS.

Revisiting Interval: 16 Days.

Resolution: 30m

Bands Used:

Name	Wavelength	Description
SR_B2	0.52-0.60 μm	Band 2 (green) surface reflectance
SR_B3	0.63-0.69 μm	Band 3 (red) surface reflectance
SR_B4	0.77-0.90 μm	Band 4 (near infrared) surface reflectance
SR_B5	1.55-1.75 μm	Band 5 (shortwave infrared 1) surface reflectance
SR_B7	2.08-2.35 μm	Band 7 (shortwave infrared 2) surface reflectance

USGS Landsat 8 Level 2, Collection 2, Tier 2: This collection provides atmospherically corrected surface reflectance and land surface temperature data obtained from the Landsat 8 OLI/TIRS sensors. These images include five visible and near-infrared (VNIR) bands, two short-wave infrared (SWIR) bands, and one thermal infrared (TIR) band that has been orthorectified for surface temperature. They also comprise intermediate bands for calculating ST products, as well as QA bands.

Dataset Availability: 18/03/2013-30/03/2025.

Dataset Provider: USGS.

Revisiting Interval: 16 Days.

Resolution: 30m.

Bands Used:

Name	Wavelength	Description
SR_B3	0.533-0.590 μm	Band 3 (green) surface reflectance
SR_B4	0.636-0.673 μm	Band 4 (red) surface reflectance
SR_B5	0.851-0.879 μm	Band 5 (near infrared) surface reflectance
SR_B6	1.566-1.651 μm	Band 6 (shortwave infrared 1) surface reflectance

Harmonized Sentinel-2 MSI (Multi Spectral Instrument), Level-2A (SR): The MSI collects data from 13 spectral bands, including visible, near-infrared (NIR), red edge, and short-wave infrared (SWIR), at three different spatial resolutions (10, 20, and 60 meters). Level-2A data items are processed to the surface reflectance level, indicating that atmospheric corrections were applied to the data. The "harmonized" tag indicates that the band-dependent offset that was applied to reflectance bands in processing baseline 04.00 (after January 24th, 2022) has been removed. This provides spectral alignment with the pre-04.00 baseline data.

Dataset Availability: 28/03/2017-05/04/2025.

Dataset Provider: European Union/ESA/Copernicus

Revisiting Interval: 05 Days.

Bands Used:

Name	Pixel Size	Wavelength	Description
B2	10 m	496.6nm (S2A) / 492.1nm (S2B)	Blue
B3	10 m	560nm (S2A) / 559nm (S2B)	Green
B4	10 m	664.5nm (S2A) / 665nm (S2B)	Red

B8	10 m	835.1nm (S2A) / 833nm (S2B)	NIR
B11	20 m	1613.7nm (S2A) / 1610.4nm (S2B)	SWIR 1

SRTM 1 Arc-Second Global Digital Elevation Model (DEM): Elevation data provides global coverage of void-filled data at a precision of 1 arc-second (30 meters) and enables open sharing of this high-resolution global data set.

Projection	Geographic
Horizontal Datum	WGS84
Vertical Datum	EGM96 (Earth Gravitational Model 1996)
Vertical Units	Meters
Spatial Resolution	1 arc-second for global coverage (~30 meters) 3 arc-seconds for global coverage (~90 meters)
Raster Size	1-degree tiles
C-band Wavelength	5.6 cm

Pre-monsoon satellite images were chosen to enhance visibility and accuracy in detecting mining pits and river dynamics, ensuring minimal interference from monsoonal flow, seasonal vegetation growth, and cloud cover. The datasets span multiple years, including:

- Son River: Landsat-5 (2010), Landsat-8 (2016) and Sentinel-2A (2019, 2022, 2023).
- Damodar River: Sentinel-2A (2019, 2020, 2021, 2022, 2023, 2024).

Google Earth imagery of those years was also used to map sand mining sites due to its higher resolution, which enhances accuracy in detecting changes in the channel belt and surrounding floodplains.

Image Processing:

The first step was to delineate the valley bottom margins using the SRTM Digital Elevation Model (DEM) to determine the lateral extent of the area of interest (AOI) from the river channel. Based on this AOI, spatiotemporal filtering was applied in Google Earth Engine (GEE) to extract relevant satellite images of AOI for each year. To enhance data reliability and minimize the influence of cloud cover, a cloud masking algorithm was applied to the satellite imagery. Subsequently,

monthly median composites for April were generated to reduce image noise and improve the clarity of surface features, enabling more accurate identification of geomorphic features.

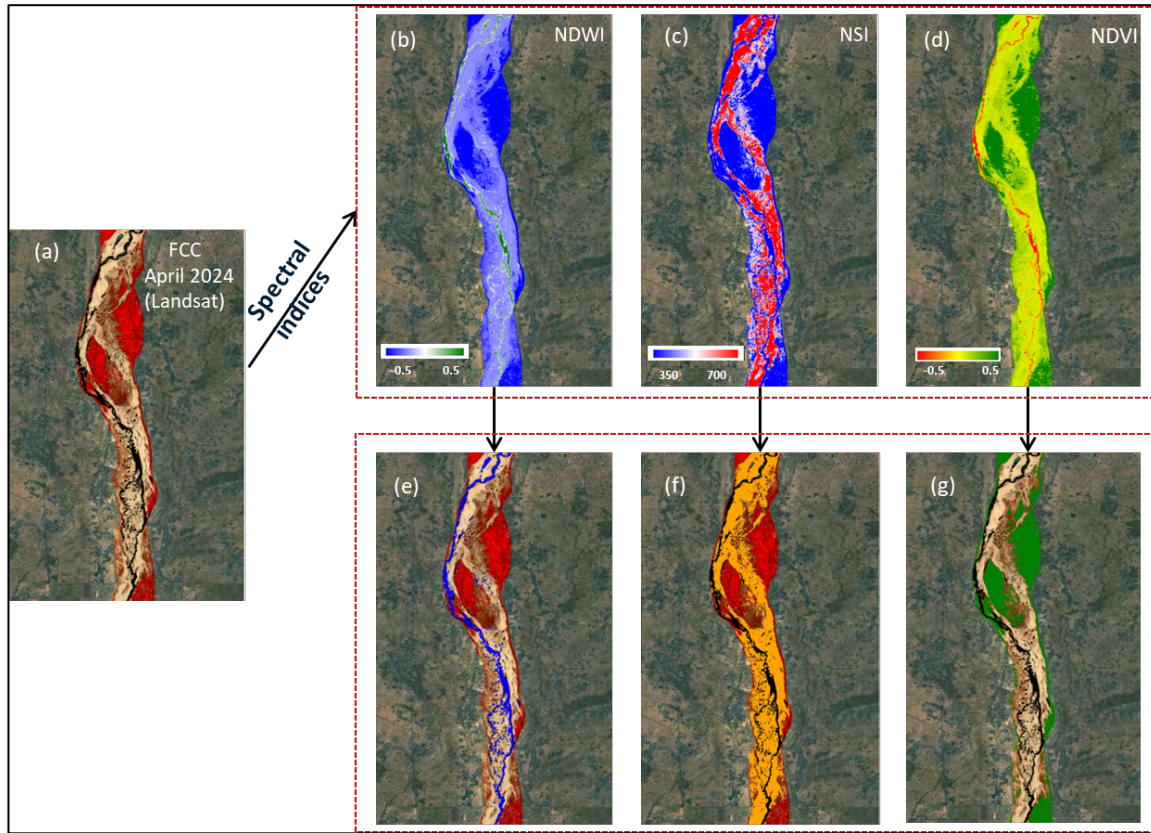


Figure 3.2: Methodology workflow for feature extraction: (a) Pre-monsoon (April) false-color and monthly median composite; (b-d) Derived spectral indices: (b) NDWI (water bodies and wet mining pits), (c) NSI (sand deposits), and (d) NDVI (vegetation cover); (e-g) Threshold-classified geomorphic features: (e) Active wet channel, (f) Sand deposits, and (g) Vegetated bars and floodplains.

Composite images were created using NIR, SWIR, and red bands to enhance the visualization of water, sand, and vegetation (Fig. 3.2). To delineate river geomorphic features, spectral indices were computed in GEE to classify different land cover types (Fig. 3.2). The following indices were applied:

Normalized Water Index (NDWI): Extracted active wet channels and wet mining pits by enhancing water reflectance (McFeeters, 1996).

$$NDWI = \frac{Green - NIR}{Green + NIR}$$

Normalized Vegetation Index (NDVI): Identified vegetated surfaces, including stable vegetated bars and revegetated mining pits (Rouse et al., 1974).

$$NDVI = \frac{NIR - Red}{NIR + Red}$$

Normalized Sand Index (NSI): Identified sand deposits (Secu et al., 2022). Applied only for 2016, 2019, and 2023 due to SWIR band availability.

$$NSI = \frac{(Green + Red)}{(\log(SWIR))}$$

Thresholding techniques were applied to classify these features into discrete land cover categories, including water, fresh sand, sand, vegetation, and barren land (Fig. 3.2). These classified layers formed the basis for further GIS analysis.

Delineation of mining sites and geomorphic mapping

Mining-affected areas were delineated through visual interpretation of high-resolution Google Earth imagery, and corresponding shapefiles were generated via manual digitization using Google Earth Pro. These delineated zones form the basis for subsequent classification into distinct types of mining practices and their association with geomorphic features (Table 3.1).

Table 3.1: Definition and mapping criteria for geomorphic feature

Feature	Definition	Mapping criteria
Channel Belt	The river corridor undergoing periodic adjustments (Active Wet Channel+ Sand Bars + Secondary Wet and Dry Channels + Vegetated Bars)	All geomorphic features were clubbed together, except for floodplains.
Floodplain	Overbank depositional areas subjected to seasonal flooding and sedimentation.	Floodplains were identified using DEM analysis and visual inspection, after removing the channel belt from the valley bottom
Active Wet Channel	The active flow path of the river during the study period	NDWI thresholding
Wet Mining Pits	Sand excavation sites retaining water, identified through NDWI classification.	Mining extents were mapped using Google Earth imagery, and the wet areas within those extents were extracted using NDWI
Dry Mining Pits	Recently mined areas devoid of water, mapped using NSI and Google Earth imagery.	Mining pits were identified through visual inspection using Google Earth imagery, and fresh, non-wet deposits were mapped using the Normalized Sand Index (NSI)
Vegetated Mining Pits	Abandoned excavation sites that have undergone vegetative regrowth, classified using NDVI.	Visual inspection of mining pits was carried out using Google Earth imagery, with NDVI applied to detect vegetated areas associated with these pits
Abandoned Mining Pits	Older mining depressions exhibit no significant vegetation or water	Mining pits were identified through visual inspection using Google Earth imagery, and

	retention, often indicating long-term mining impacts.	older sand deposits were mapped using the Normalized Sand Index (NSI).
--	---	--

To obtain detailed attributes for each feature, the classified raster layers were converted into vector format. This enabled spatial statistics, area calculations, and further GIS-based assessments of mining expansion, morphological changes, and anthropogenic influences.

Spatiotemporal analysis: Identification of hotspots of mining activities

To conduct a spatiotemporal analysis and identify local hotspots of mining, the Damodar River study area was first divided into three zones based on the location and influence of flow regulation structures. Subsequently, the study area was further subdivided into 25 individual reaches to enable a detailed reach-wise assessment of changes and mining activities.

For a comparative analysis, three of the most impacted reaches of the Sone River were also selected. To quantify the intensity of mining activity, the channel belt area and mining-affected area were calculated for each reach. The mining-affected area was then normalized by the corresponding channel belt area of each reach to identify reaches with relatively dense mining activity.

we have also developed a vulnerability index to assess mining activities across 25 reaches of the Damodar River from 2019 to 2024. The methodology combines both mining intensity and annual changes in activity through a weighted scoring system. The calculation process begins with two core metrics: average mining intensity and growth rate. Average intensity represents the mean mining activity over six years, calculated as the sum of annual values (2019-2024) divided by six. The growth rate captures recent changes by subtracting the 2019 value from the 2024 value, highlighting emerging hotspots. Both metrics are normalized to a 0-1 scale to enable comparison across reaches. Normalization divides each reach's average intensity by the maximum average (0.466 at Reach 10) and each growth value by the maximum absolute growth (0.501 at Reach 10). The vulnerability index then combines these normalized scores with a 70:30 weighting, prioritizing average mining intensity while still accounting for changes.

$$\text{AvgIntensity}_i = \frac{1}{6} \sum_{y=2019}^{2024} I_{iy} \dots\dots\dots \text{eq (i)}$$

Where: $I_{i,y}$ = Mining intensity (mining area/channel belt area) for reach i in year y

$$\text{Growth}_i = I_{i,2024} - I_{i,2019} \quad \text{..... eq (ii)}$$

Where, $I_{i,2024}$ and $I_{i,2019}$ are mining intensities of year 2024 and 2019 for reach i

$$\text{Vulnerability Index, } V_i = 0.7 \times \text{NormAvg}_i + 0.3 \times \text{NormGrowth}_i \quad \text{..... eq (iii)}$$

Where:

$$\text{NormAvg}_i = \text{Average Intensity}_i / \text{maximum (AvgIntensity)}$$

$$\text{NormGrowth}_i = \text{Growth}_i / \text{maximum (Growth)}$$

The resulting V (Vulnerability) scores classify reaches into six risk categories. Critical zones ($V \geq 0.8$) show both high intensity and rapid growth, like Reach 10 which scored a perfect 1.0. Protected areas ($V = 0$) had no mining activity, while intermediate categories (Very High to Low) reflect varying combinations of intensity and growth patterns. This approach provides a standardized framework to prioritize reaches needing intervention.

3.3.2. Results

This section presents the spatial distribution and temporal evolution of mining activities and associated morphological features along the Damodar and Sone Rivers. The Damodar River analysis is organized into three geomorphic zones covering 25 reaches, while the Sone River analysis focuses on three selected windows of interest based on the literature review and visual inspection using Google Earth.

3.3.2.1. *Morphological Changes: Damodar River*

Zone 1:

Zone 1 of the Damodar River study area comprises 11 reaches (Fig. 3.3a), extending from Reach 1a (Hijuli, West Bengal, located downstream of Panchet Dam) to Reach 4d, where the Durgapur Barrage is situated at the downstream end. This zone represents a transitional region between rocks of the peninsular shield and Pleistocene to Recent alluvium (Bhattacharyya, 2011) resulting in minimal floodplain development. The geomorphology of this segment is strongly influenced by structural controls, limiting lateral channel migration and floodplain expansion.

The Mining Impacted Channel Belt in Zone 1 showed a steady increase from 4.61% in 2019 to 6.88% in 2024 (Table 3.2), with peak growth occurring between 2022-2023. The Undisturbed Channel Belt exhibited significant fluctuations, decreasing from 78.43% in 2019 to 66.60% in

2024, reaching its lowest point at 45.48% in 2022. Meanwhile, the Active Wet Channel demonstrated considerable variability, expanding from 16.19% in 2019 to a peak of 48.29% in 2022 before contracting to 23.74% in 2024. The Mining Impacted Wet Channel displayed intermittent growth patterns, ranging from 0.78% in 2019 to 4.31% in 2020, then stabilizing between 2.15-2.79% from 2021-2024 (Table 3.2).

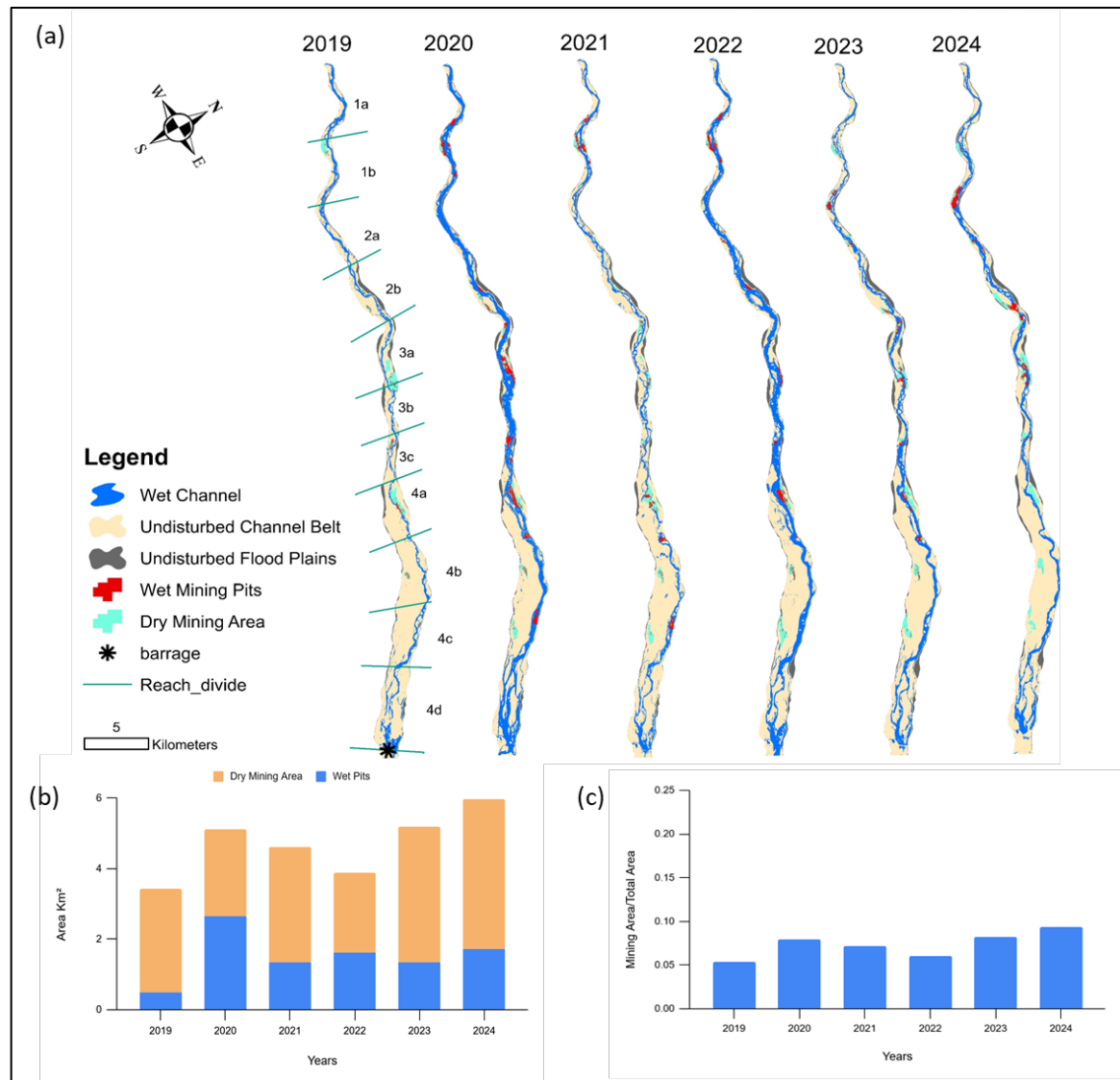


Figure 3.3: (a) Spatiotemporal geomorphic map of the Damodar River (Zone 1) showing variations in morphological features and mining site distributions. (b) Temporal trends in total mining area for Zone 1 (2019-2024). (c) Mining intensity for Zone 1, calculated as the ratio of total mining area to total channel belt area.

Sand mining activity in the Damodar River begins from this zone, with the river flow being heavily regulated by both the upstream Panchet Dam and the downstream Durgapur Barrage. The temporal analysis of mining extent (Fig. 3.3b) indicates a general increasing trend over the study period, except for the years 2020 and 2021. The lowest recorded mining extent was 3.43 km² in 2019, whereas the highest was 5.96 km² in 2024, marking a significant expansion in extraction activity. The decline in mining extent during 2020 and 2021 can likely be attributed to reduced construction activity and lower demand for sand supply during the COVID-19 pandemic and associated lockdown.

In general, Zone 1 exhibits a lower intensity of mining relative to its total channel belt area. When the total mining area is normalized with respect to the total channel belt area of the zone, the highest value of 0.09 was observed in 2024, indicating a growing trend in sand extraction (Fig. 3.3c). The increasing extent of mining in this zone in recent years highlights the necessity of monitoring anthropogenic activities and assessing their long-term impacts on channel stability and sediment transport dynamics.

Table 3.2: Percent distribution of morphological units of Damodar River (zone-normalized to 100%).

	Geomorphic Unit	Area (%)					
		2019	2020	2021	2022	2023	2024
Zone 1	Undisturbed Channel Belt	78.43	52.00	70.55	45.48	67.36	66.60
	Mining Impacted Channel belt	4.60	3.98	5.18	3.61	6.28	6.88
	Active Wet Channel	16.19	39.71	22.16	48.29	24.19	23.74
	Mining Impacted Wet Channel	0.78	4.31	2.15	2.62	2.16	2.796
Zone 2	Undisturbed Channel Belt	80.43	53.562	71.53	42.52	81.18	64.29
	Mining Impacted Channel belt	5.75	6.57	15.02	5.29	12.21	26.85
	Active Wet Channel	12.625	35.83	8.39	49.64	6.03	4.70
	Mining Impacted Wet Channel	1.19	4.04	5.05	2.55	0.57	4.16

Zone 3	Undisturbed Channel Belt	70.54	46.79	57.27	18.86	58.51	55.41
	Mining Impacted Channel belt	11.25	8.80	18.52	11.72	25.03	23.29
	Active Wet Channel	14.69	41.83	20.19	60.80	11.48	15.53
	Mining Impacted Wet Channel	3.51	2.57	4.01	8.62	4.97	5.77

Note: Mining-Impacted Wet Channel, Active Wet Channel, Mining-Affected Channel Belt, and Undisturbed Channel Belt (zone 1–3) showing spatiotemporal changes across three zones (2019–2024).

Zone 2:

Zone 2 of the Damodar River study area comprises three reaches: 5a, 5b, and 6. Unlike Zone 1, this zone exhibits a more pronounced floodplain association. However, all observed mining activities are confined within the active channel belt (Fig. 3.4a), indicating a preference for in-channel sand extraction rather than floodplain mining. This zone is heavily influenced by flow regulation from two major hydraulic structures: the Damodar Barrage at the upstream boundary and the Rondiha Barrage at the downstream end. These barrages play a crucial role in sediment transport, controlling the availability and deposition of extractable sand within the channel.

The Undisturbed Channel Belt exhibited significant fluctuations, decreasing from 80.43% in 2019 to 64.29% in 2024, with a notable low of 42.52% in 2022 (Table 3.2). The Mining Impacted Channel Belt showed a dramatic increase from 5.75% in 2019 to 26.85% in 2024, peaking at the final year of study. Meanwhile, the Active Wet Channel displayed considerable variability, ranging from 4.70% in 2024 to 49.64% in 2022, with an overall decline from its initial 12.63% coverage in 2019. The Mining Impacted Wet Channel varied between 0.57% in 2023 and 5.06% in 2021, ending at 4.16% in 2024. These changes demonstrate substantial geomorphological alterations throughout the study period, with mining activities progressively transforming the river's natural channel characteristics.

Similar to Zone 1, mining extent in Zone 2 has shown a general increasing trend over the study period (Fig. 3.4b), except 2022, when a slight reduction in mining area was observed. The lowest

recorded mining extent was 1.90 km² in 2019, while the highest reached 8.63 km² in 2024. This sharp increase in extraction activity follows a pattern like that of Zone 1, reflecting the growing demand for sand resources over time.

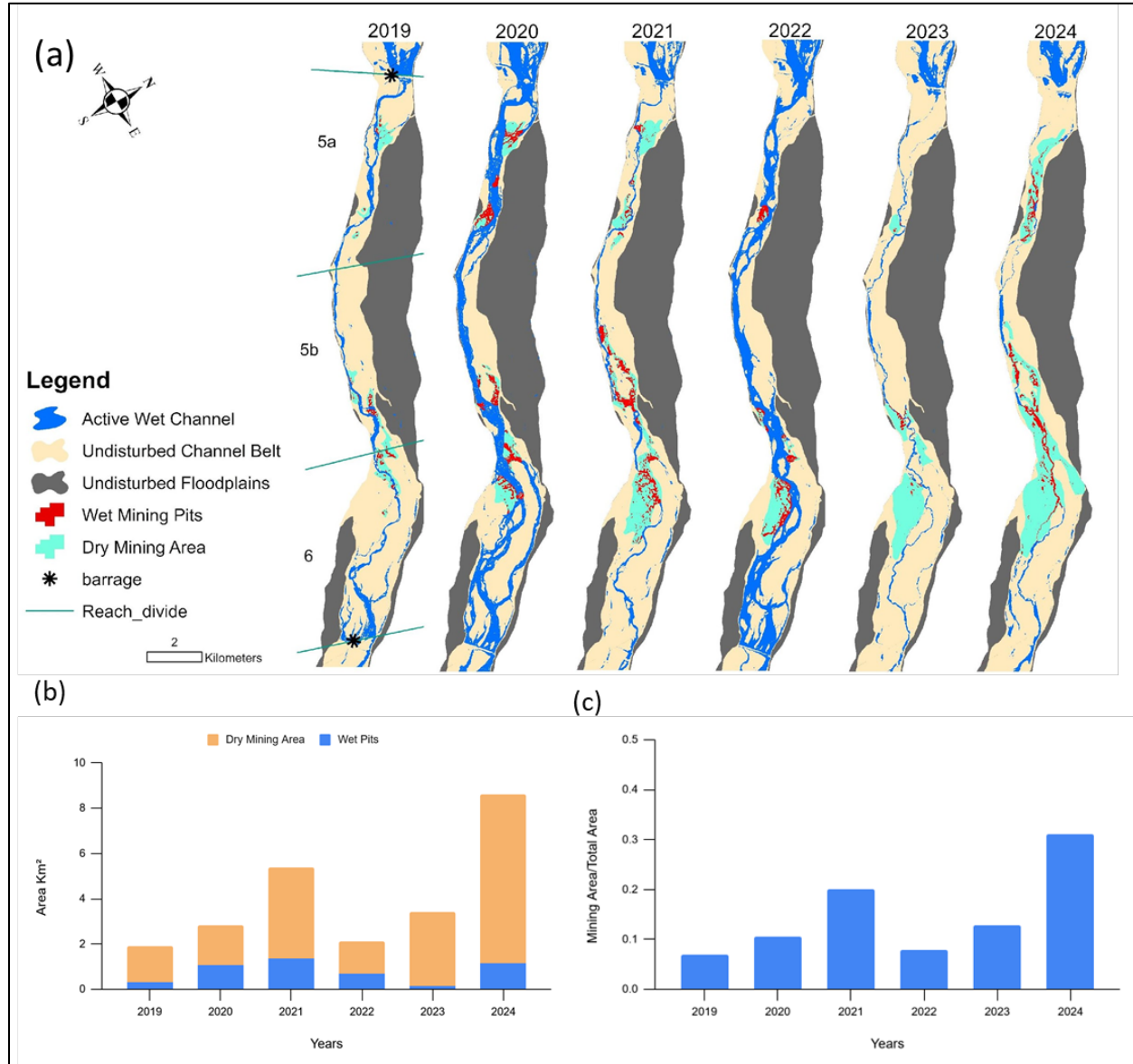


Figure 3.4: (a) Spatiotemporal geomorphic map of the Damodar River (Zone 2) showing variations in morphological features and mining site distributions. (b) Temporal trends in total mining area for Zone 2 (2019-2024). (c) Mining intensity for Zone 2, calculated as the ratio of total mining area to total channel belt area.

Compared to Zone 1, Zone 2 exhibits a significantly higher intensity of mining activities (Fig. 3.4c). When the total mining area of the zone is normalized with respect to the total channel belt area of the zone, the highest value recorded was 0.31 in 2024, indicating a much denser concentration

of mining relative to the available channel space. This intensified extraction pressure suggests that Zone 2 plays a critical role in regional sand supply, with regulated flows from the barrages potentially enhancing sediment deposition and making this zone more favourable for mining operations. The increasing extent of sand mining in this reach underscores the need for stringent monitoring and regulatory measures to prevent excessive geomorphic disturbances and ensure sustainable sediment management.

Zone 3:

Zone 3 of the Damodar River study area comprises the reaches 7a to 14, with Reach 7a located just downstream of the Rondiha Barrage (Fig. 3.5a). Some of the reaches in this zone are affected by flow regulation due to the downstream effect of the Rondiha Barrage, but this zone contains the highest concentration of mining activities.

In Zone 3, the Mining Impacted Wet Channel shows a fluctuating but overall increasing trend from 3.52% in 2019 to a peak of 8.62% in 2022, before slightly decreasing to 4.97% in 2023 (Table 3.2). The Active Wet Channel experiences strong annual variation, expanding sharply from 14.69% in 2019 to 60.80% in 2022, then reducing significantly to 11.48% in 2023, suggesting episodic flow events or intensified mining disruptions during intermediate years. The Mining Impacted Channel Belt displays a consistent upward trajectory, rising from 11.25% in 2019 to 25.03% in 2023, which directly reflects escalating mining activity in this reach. Simultaneously, the Undisturbed Channel Belt declines from 70.54% in 2019 to a low of 18.86% in 2022, recovering slightly to 58.52% in 2023, indicating some resilience or temporary cessation of mining in parts of this zone.

In Zone 1, Reach 3a emerges as the dominant mining location, peaking at 0.336 in 2024 after considerable annual fluctuations. Notably, reach 2a transitioned from complete absence of mining activity in 2019 to significant intensity (0.149) by 2024. The zone also contains several stable reaches, including 4d, which maintained zero mining activity throughout the study period.

Zone 2 is characterized by extremely rapid expansion in Reaches 5b and 6, which grew by 286% and 525%, respectively. A notable temporary decline occurred in 2022, where mining intensity in Reaches 5a and 5b dropped precipitously before rebounding sharply in subsequent years. This

pattern suggests potential short-term regulatory interventions or operational adjustments that temporarily reduced activity.

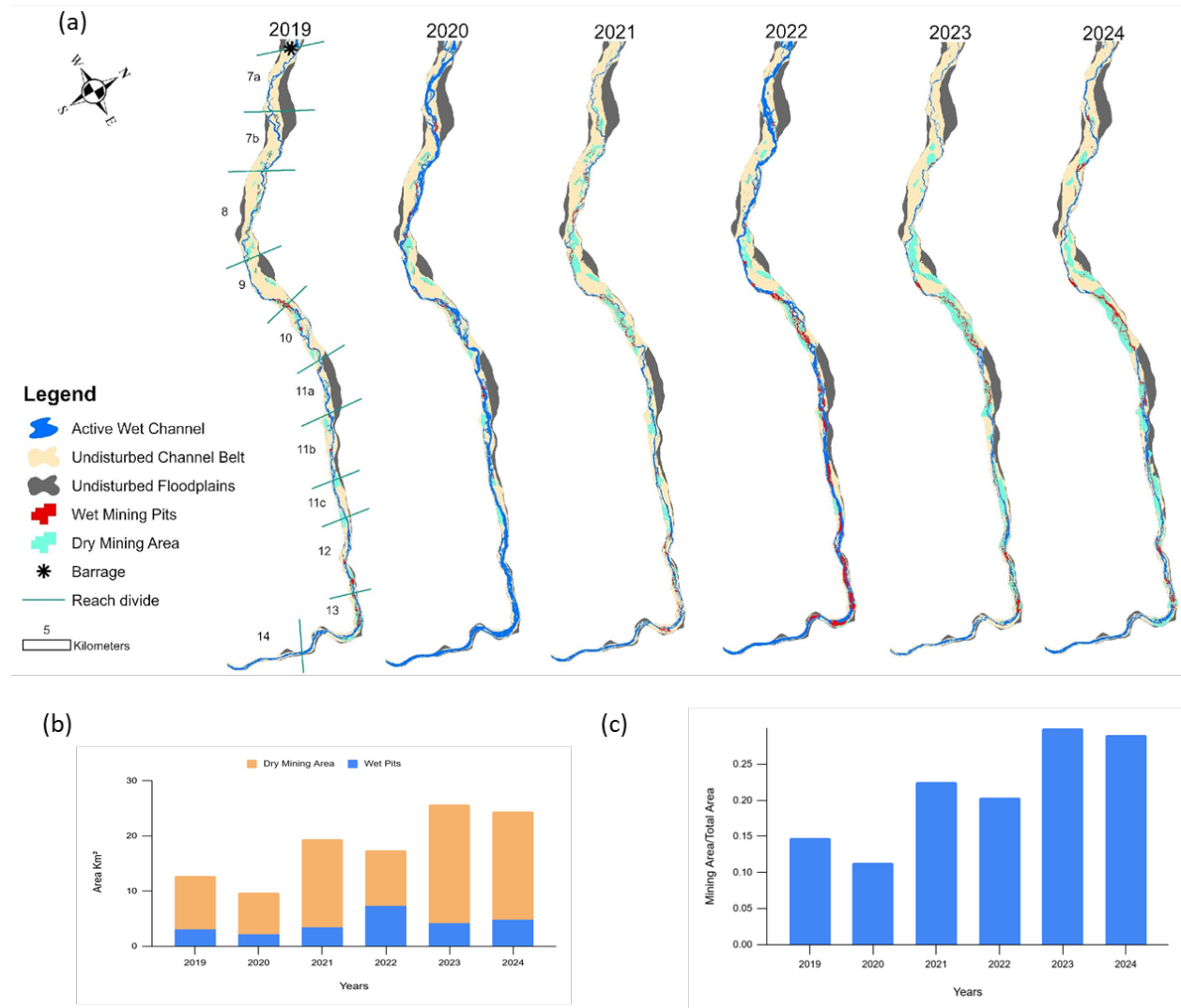


Figure 3.5(a) Spatiotemporal geomorphic map of the Damodar River (Zone 3) showing variations in morphological features and mining site distributions. (b) Temporal trends in total mining area for Zone 3 (2019-2024). (c) Mining intensity for Zone 3, calculated as the ratio of total mining area to total channel belt area.

In contrast to the fluctuations observed in Zones 1 and 2, Zone 3 has seen a consistent increase in the extent of mining over time (Fig. 3.5 b). However, this zone showed a decline in mining activity during the COVID pandemic in 2020, with the lowest extent recorded at 9.79 km². This reduction led to the submergence of mining sites due to the expansion of the active wet channel

during high-flow periods. By 2023, the mining extent increased more than 2-fold, reaching 25.73 km², the highest recorded for this zone.

relative to Zones 1 and 2, Zone 3 exhibits significantly denser mining activities in comparison to its total channel belt area, making it the primary hotspot for mining along the river (Fig. 3.5c). The normalised total area of mining activity relative to the total channel belt area reached its peak at 0.30 in 2023, highlighting the high intensity of mining in this zone. This further emphasises the need for targeted regulatory measures to manage mining in this area, as it is heavily impacted by both natural river dynamics and anthropogenic pressures. Given the scale and intensity of extraction activities, this zone requires immediate attention for sustainable resource management and to mitigate potential geomorphic alterations that could disrupt the river's natural equilibrium.

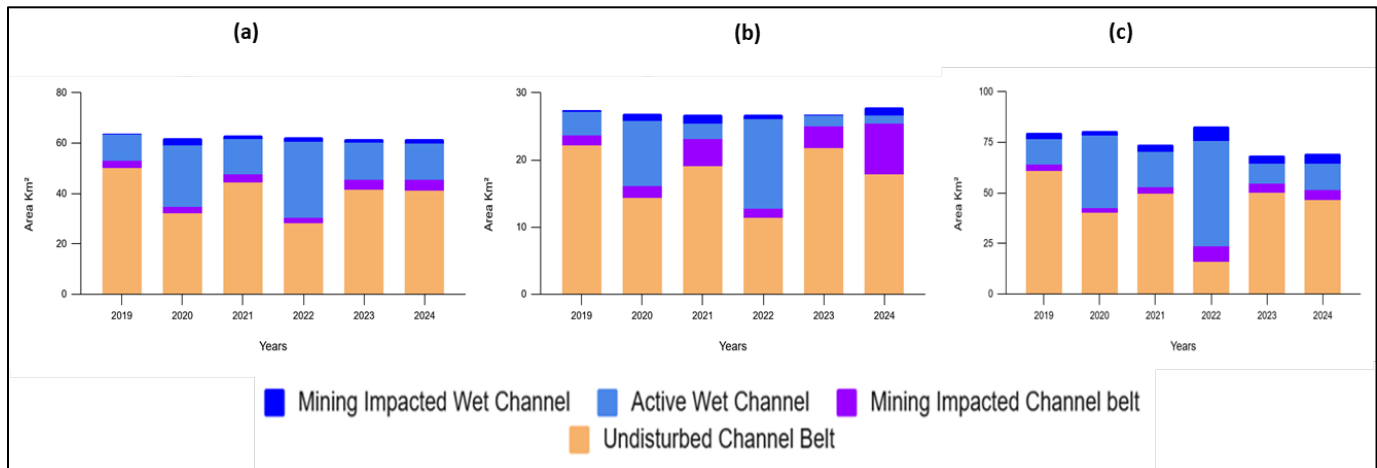


Figure 3.6: Temporal evolution (2019–2024) of morphological features across the Damodar River: (a) Zone 1, (b) Zone 2, and (c) Zone 3

3.3.2.2. Hotspots of Mining Activity (2019-2024)

Statistical analysis of the normalized data yields several important insights. Zone-wide mean of mining densities show clear stratification, with Zone 1 mean 0.089, Zone 2 at 0.154, and Zone 3 significantly higher at 0.209 (Table 3.3). The quantitative analysis of mining intensity across 25 reaches provides precise measurements of mining intensity evolution over the six-year study period.

Zone 3 emerges as the absolute hotspot for mining activity, containing both the highest individual reach values and the greatest concentration of high-intensity operations. Reach 10 stands out as particularly critical, reaching a peak intensity of 0.736 in 2023, the highest value recorded in the study. The spatial distribution reveals clear patterns of concentration in Zone 3 (Fig. 3.7), with certain reaches in each zone accounting for disproportionate shares of total activity. Using reach-wise mining intensity, we were able to identify geographically continuous hotspots of mining activity, primarily in Zone 3. The continuous geographical hotspot includes reaches from 9 to 12.

Table 3.3: Reach-wise temporal variations in mining intensity (mining area/channel belt area ratio) with annual and zonal mean values across Zones 1–3 (2019–2024).

	Year/ Reaches	2019	2020	2021	2022	2023	2024
Zone 1	1a	0.01	0.05	0.05	0.06	0.04	0.06
	1b	0.13	0.16	0.23	0.22	0.13	0.23
	2a	0	0.08	0.02	0.05	0.13	0.15
	2b	0.06	0.10	0.02	0.04	0.07	0.22
	3a	0.22	0.28	0.14	0.05	0.27	0.33
	3b	0.12	0.04	0.06	0.04	0.07	0.09
	3c	0.08	0.12	0.09	0.02	0.10	0.09
	4a	0.12	0.15	0.17	0.11	0.13	0.09
	4b	0.02	0.04	0.05	0.04	0.06	0.04
	4c	0.01	0.08	0.08	0.09	0.07	0.05
	4d	0	0	0	0	0	0
	Annual Mean	0.069	0.093	0.082	0.067	0.098	0.123
	Zonal Mean	0.089					
Zone 2	5a	0.08	0.16	0.19	0.03	0.03	0.26
	5b	0.09	0.12	0.22	0.04	0.11	0.33
	6	0.05	0.07	0.19	0.12	0.18	0.32
	Annual Mean	0.074	0.116	0.203	0.063	0.110	0.304
	Zonal Mean	0.145					
Zone 3	7a	0	0	0.01	0	0	0
	7b	0.09	0.13	0.20	0.06	0.13	0.16

	8	0.17	0.17	0.256	0.11	0.15	0.15
	9	0.15	0.16	0.30	0.29	0.42	0.38
	10	0.21	0.22	0.44	0.47	0.74	0.71
	11a	0.11	0.13	0.16	0.17	0.39	0.33
	11b	0.14	0.09	0.16	0.19	0.23	0.34
	11c	0.15	0.15	0.19	0.21	0.52	0.53
	12	0.24	0.05	0.33	0.31	0.52	0.33
	13	0.27	0	0.20	0.38	0.28	0.33
	14	0	0	0	0	0	0
	Annual Mean	0.141	0.101	0.205	0.200	0.308	0.298
	Zonal Mean	0.209					

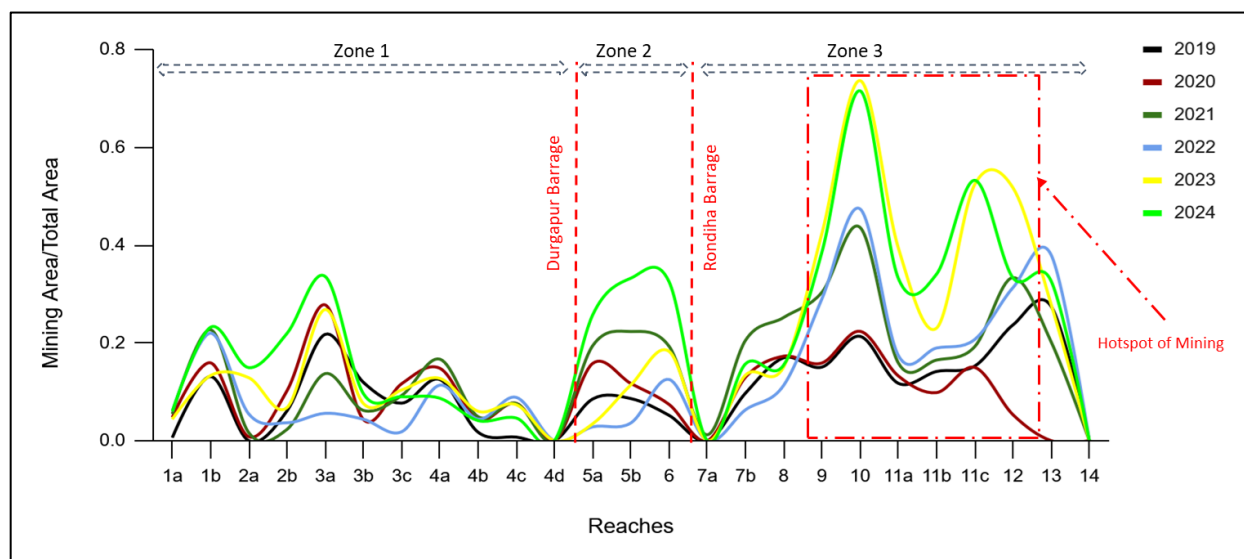


Figure 3.7: Temporal variation in reach-wise mining intensity (mining area/channel belt area ratio) for the Damodar River (2019–2024). Red vertical dashed lines indicate barrage locations (Durgapur, Rondiha) and boundaries between the three zones, while red dashed rectangles highlight mining hotspots.

Table 3.4: Annual mining intensities with vulnerability classification for the Damodar River. Color coding: Critical (red), Very High (orange), High (yellow), Moderate (blue), Low (green), Protected (gray).

Zone	Reach	2019	2020	2021	2022	2023	2024	Avg Intensity	Growth (2019→2024)	V-Score	Category
1	1a	0.007	0.048	0.055	0.061	0.044	0.061	0.046	0.054	0.22	Low
	1b	0.131	0.159	0.227	0.22	0.133	0.232	0.184	0.101	0.47	Moderate
	2a	0	0.008	0.016	0.054	0.129	0.149	0.059	0.149	0.31	Low
	2b	0.061	0.102	0.023	0.037	0.068	0.219	0.085	0.158	0.36	Moderate
	3a	0.218	0.278	0.137	0.056	0.268	0.336	0.216	0.118	0.58	Moderate
	3b	0.119	0.043	0.062	0.044	0.076	0.096	0.073	-0.023	0.19	Low
	3c	0.077	0.116	0.092	0.018	0.104	0.09	0.083	0.013	0.24	Low
	4a	0.125	0.148	0.167	0.113	0.127	0.087	0.128	-0.038	0.32	Low
	4b	0.017	0.044	0.049	0.044	0.06	0.041	0.043	0.024	0.16	Low
	4c	0.008	0.076	0.076	0.088	0.074	0.046	0.062	0.038	0.23	Low
	4d	0	0	0	0	0	0	0	0	0	Protected
2	5a	0.085	0.158	0.194	0.028	0.034	0.257	0.126	0.171	0.45	Moderate
	5b	0.086	0.116	0.223	0.036	0.114	0.332	0.151	0.246	0.49	Moderate
	6	0.052	0.074	0.193	0.125	0.183	0.325	0.158	0.273	0.52	Moderate
	7a	0	0	0.012	0	0	0	0.002	0	0.01	Protected
3	7b	0.097	0.13	0.205	0.063	0.134	0.157	0.131	0.06	0.42	Moderate
	8	0.17	0.173	0.252	0.113	0.151	0.155	0.169	-0.015	0.45	Moderate
	9	0.151	0.159	0.303	0.29	0.423	0.385	0.285	0.234	0.76	Very High
	10	0.214	0.224	0.436	0.474	0.736	0.715	0.466	0.501	1	Critical
	11a	0.118	0.132	0.159	0.174	0.394	0.332	0.218	0.214	0.65	High
	11b	0.142	0.098	0.165	0.189	0.23	0.34	0.194	0.198	0.61	High
	11c	0.153	0.15	0.192	0.207	0.524	0.532	0.293	0.379	0.83	Very High
	12	0.237	0.053	0.334	0.313	0.517	0.333	0.298	0.096	0.69	High
	13	0.275	0	0.202	0.38	0.279	0.326	0.244	0.051	0.55	Moderate
	14	0	0	0	0	0	0	0	0	0	Protected

The mining vulnerability assessment of the Damodar River reveals critical spatial patterns in mining pressure, with Zone 3 emerging as the most severely impacted area (Table 3.4). Reaches 10, 11c, and 9 in Zone 3 represent the highest-priority hotspots, demonstrating both intense mining activity (average intensities of 0.466, 0.293, and 0.285, respectively) and rapid recent

expansion (growth rates exceeding +0.234). These areas face severe risks of channel erosion and sediment disruption, demanding immediate regulatory intervention. Zone 2 shows emerging hotspots, particularly in Reaches 5b and 6, where moderate current intensities (0.151-0.158) combine with alarming growth rates (+0.246 to +0.273), signaling potential future threats if left unmanaged. Zone 1 presents a more variable pattern, with Reach 3a showing volatile but occasionally extreme mining pressure (peaking at 0.336 in 2024). Notably, reaches 4d, 7a, and 14 remain completely protected with no recorded mining activity, serving as valuable ecological benchmarks. The spatial concentration of impacts in Zone 3 suggests systemic mining pressures in this region, while the growth patterns in Zone 2 indicate expanding frontier areas of extraction. These findings enable targeted management strategies, prioritizing immediate action in critical Zone 3 reaches, enhanced monitoring of emerging Zone 2 hotspots, and conservation of the stable reference reaches to maintain ecological balance across the river system. The study underscores the need for zone-specific policies that account for both current intensity levels and growth trajectories to ensure sustainable river management.

3.3.2.3. *Morphological Changes: Sone River*

Window 1

In Window 1, the focus is on the channel belt area, as the floodplain is not significantly affected by mining activities. The geomorphic units are classified as Mining Impacted Wet Channel, Active Wet Channel, Mining Affected Channel Belt, and Undisturbed Channel Belt (Fig. 3.8).

The Mining Impacted Wet Channel has shown a steady increase from 1.17% in 2010 to 9.54% in 2023, peaking at 11.40% in 2019 (Table 3.5). The Active Wet Channel fluctuates slightly, with an overall decline from 15.91% in 2010 to 12.00% in 2023. Meanwhile, the Mining Affected Channel Belt exhibits a significant rise from 1.27% in 2010 to 20.70% in 2023. The Undisturbed Channel Belt has decreased from 81.64% in 2010 to 57.76% in 2023, showing a clear impact of increasing mining activities.

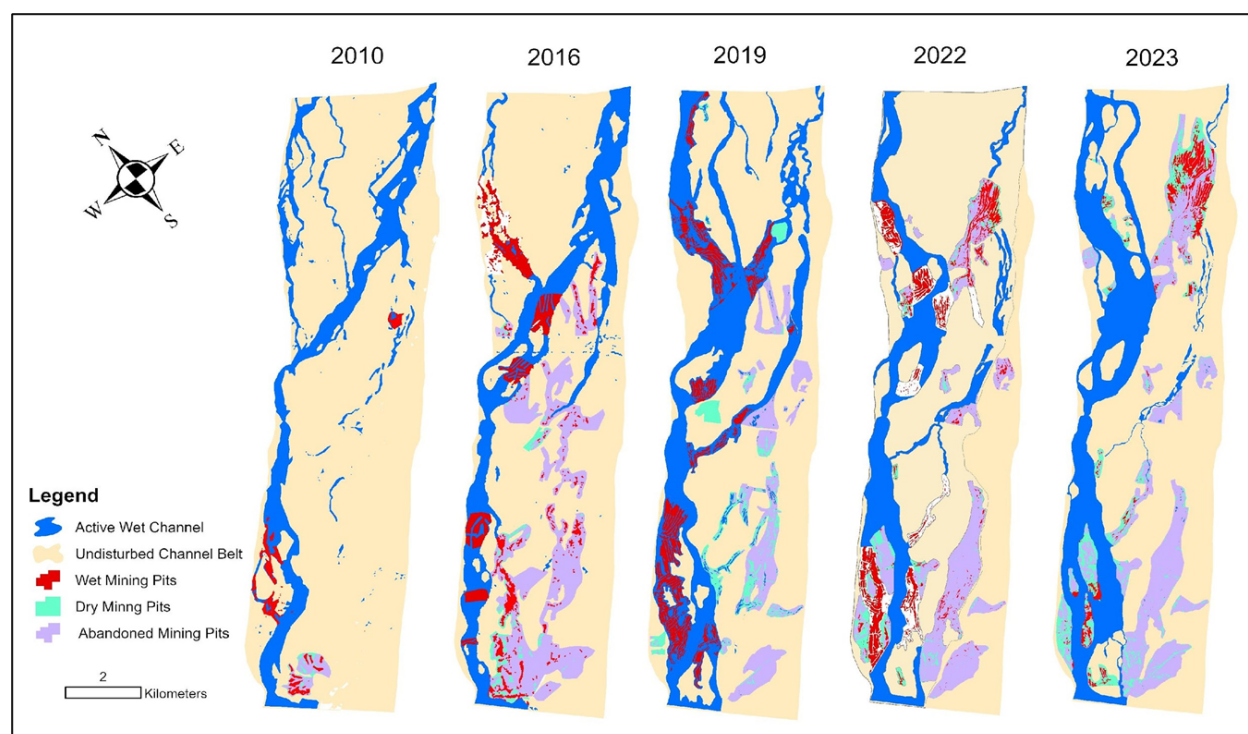


Figure 3.8: Geomorphic maps of the Sone River (Window-1) showing changes in river morphological features and mining pits over time, created using Landsat, Sentinel, and Google Earth imagery

Mining pits in Window-1 have increased considerably (Fig. 3.11). Wet Mining Pits grew from 0.804% in 2010 to 4.657% in 2023. Dry Mining Pits also show a steady rise from 0.132% in 2010 to 3.181% in 2023. Abandoned Mining Pits, which indicate former mining sites, increased from 0.506% in 2010 to 8.723% in 2023. The overall ratio of Mining Impacted Area to Total Area has increased significantly from 0.024 in 2010 to 0.302 in 2023, demonstrating a notable transformation due to mining activities (Figure 3.12).

Window 2

In Window 2, the focus remains on the channel belt area as well (Fig. 3.9). The Mining Impacted Wet Channel rose from 2.98% in 2016 to 29.56% in 2023 (table:3.5), indicating a drastic increase in mining activities. The Active Wet Channel fluctuates, peaking at 19.76% in 2022 before declining to 15.14% in 2023. The Mining Affected Channel Belt increased from 11.08% in 2016 to 25.60% in 2022 before slightly declining to 17.22% in 2023. The Undisturbed Channel Belt has

decreased significantly, from 69.71% in 2016 to 38.08% in 2023, reflecting the growing mining footprint.

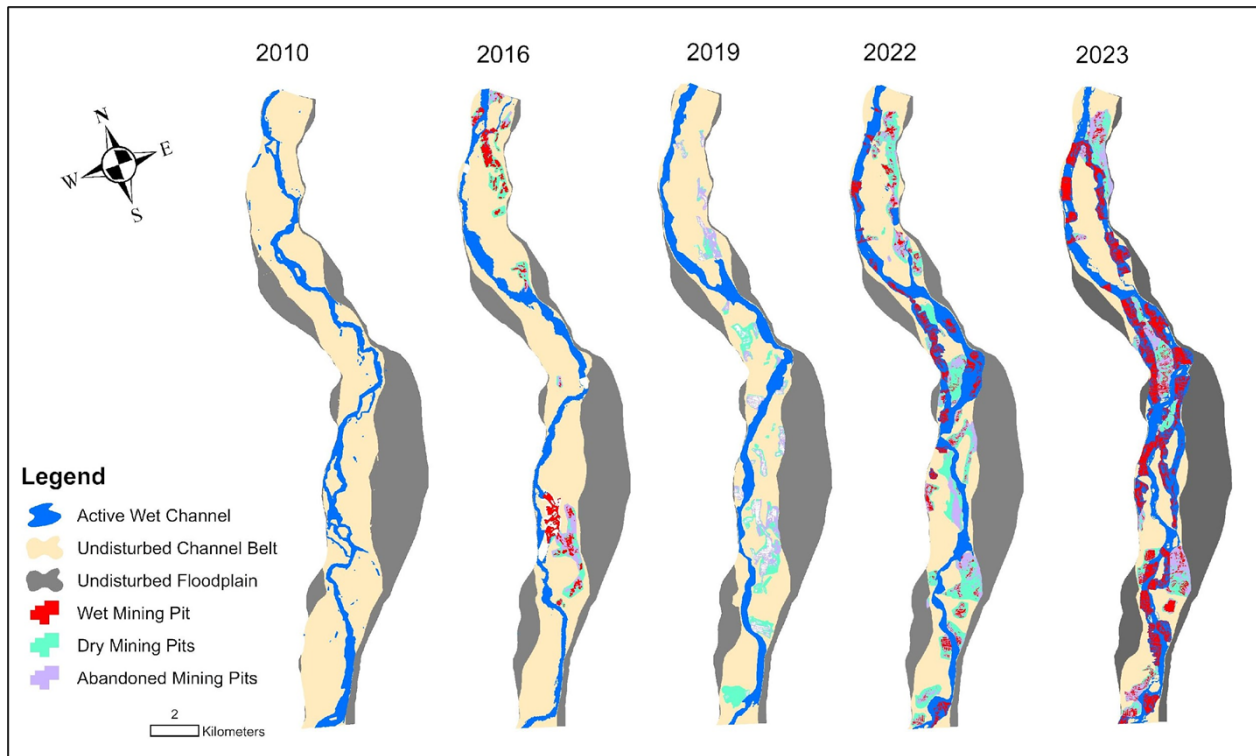


Figure 3.9: Geomorphic maps of the Sone River (Window-2) showing changes in river morphological features and mining pits over time, created using Landsat, Sentinel, and Google Earth imagery.

Mining pits in Window-2 have expanded over the years (Fig. 3.11). Wet Mining Pits increased from 2.635% in 2016 to 9.512% in 2023. Dry Mining Pits also exhibit a sharp rise, from 2.245% in 2016 to 3.041% in 2023. Abandoned Mining Pits, which indicate long-term mining impacts, increased from 1.475% in 2016 to 3.775% in 2023. The ratio of Mining Impacted Area to Total Area rose dramatically from 0.141 in 2016 to 0.468 in 2023 (Fig. 3.12), emphasizing the accelerated impact of mining on the landscape.

Table 3.5: Percent distribution of morphological features of Sone River (window-normalized to 100%): Mining-Impacted Wet Channel, Active Wet Channel, Mining-Affected Channel Belt, and Undisturbed Channel Belt (Windows 1–2); Active Wet Channel, Undisturbed Floodplain, and Mining-Impacted Floodplain (Window 3), showing temporal changes (2010–2023).

Window-Geomorphic features	Area (%)				
	2010	2016	2019	2022	2023
W-1_Mining Impacted Wet channel	1.17	5.02	11.4	7.27	9.54
W-1_Active Wet channel	15.91	14.5	17.07	15.06	12
W-1_Mining affected Channel Belt	1.27	17.45	10.76	14.42	20.7
W-1_Undisturbed Channel Belt	81.64	63.04	60.77	63.25	57.76
W-2_Mining Impacted Wet channel	0	2.98	1.63	8.45	29.56
W-2_Active Wet channel	14.56	16.23	18.31	19.76	15.14
W-2_Mining Impacted Channel Belt	0	11.08	16.93	25.6	17.22
W-2_Undisturbed Channel Belt	85.44	69.71	63.14	46.19	38.08
W-3_Active Wet channel	7.93	9.92	6.05	6.35	5.37
W-3_Undisturbed Floodplain	91.59	72.56	76.43	57.92	48.51
W-3_Mining Impacted Floodplain	0.47	17.52	17.52	35.73	46.12
	100	100	100	100	100

Window 3

Window-3 focuses on the floodplain, which has been predominantly impacted by mining activities (Fig. 3.10). The Active Wet Channel decreased from 7.93% in 2010 to 5.37% in 2023. The Mining Impacted Floodplain has expanded drastically, from 0.47% in 2010 to 46.12% in 2023. Meanwhile, the Undisturbed Floodplain has seen a significant decline from 91.59% in 2010 to 48.51% in 2023, highlighting large-scale mining activity in the floodplain (Table 3.5).

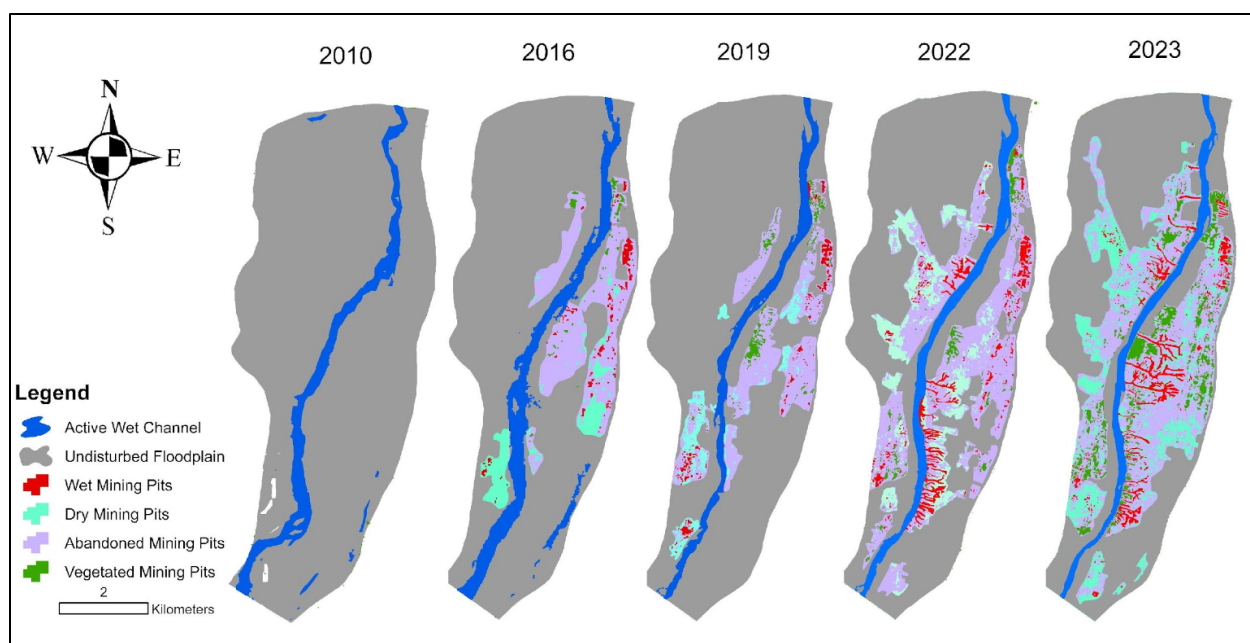


Figure 3.10: Geomorphic maps of the Sone River (Window-3) showing changes in river morphological features and mining pits over time, created using Landsat, Sentinel, and Google Earth imagery.

Mining pits in Window-3 show extensive growth. Wet Mining Pits increased from 0.317% in 2016 to 1.220% in 2023. Dry Mining Pits also exhibit a rising trend, from 1.394% in 2016 to 4.267% in 2023. Abandoned Mining Pits expanded from 4.479% in 2016 to 9.387% in 2023. Additionally, Vegetated Mining Pits, indicating abandoned sites that have undergone vegetation growth, increased from 0.153% in 2016 to 1.846% in 2023 (Fig. 3.11). The ratio of Mining Impacted Area to Total Area surged from 0.005 in 2010 to 0.461 in 2023 (Fig. 3.12), confirming significant floodplain degradation due to mining.

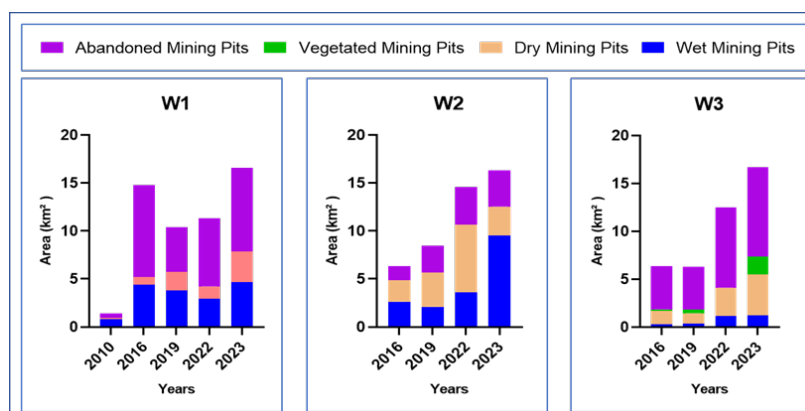


Figure 3.11: Spatiotemporal variation in area of mining pits: (W1) window 1, (W2) window 2, and (W3) window 3.

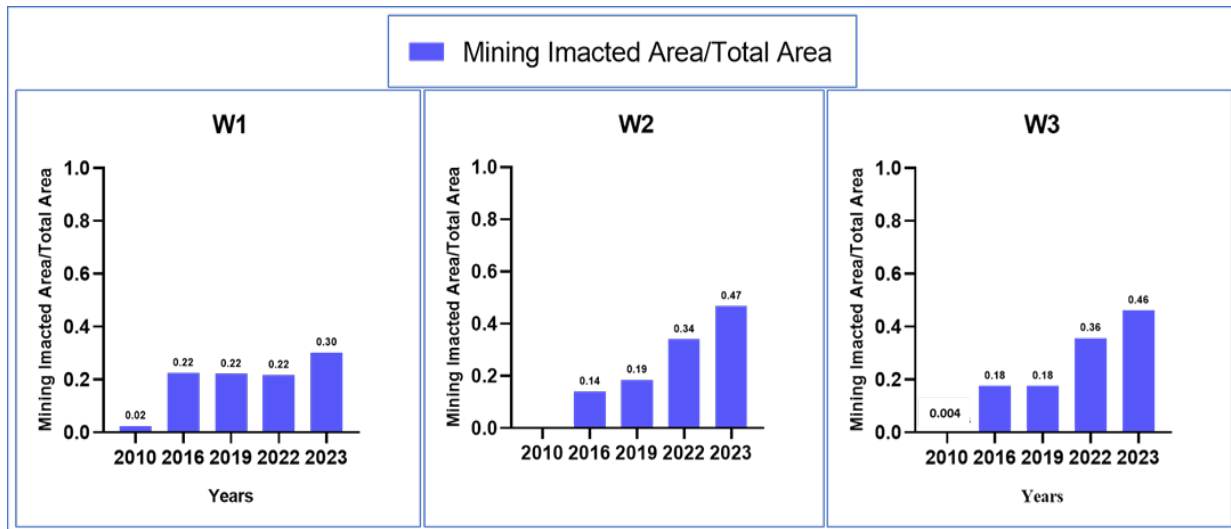


Figure 3.12: Mining intensity three zones calculated as the ratio of total mining area to total channel belt area: (W1) window 1, (W2) window 2, and (W3) window 3.

Across all three windows, mining activities have expanded significantly over time, leading to increased mining-impacted wet channels, mining-affected channel belts, and floodplains. The ratio of Mining Impacted Area to Total Area has risen sharply, particularly post-2016. The reduction in undisturbed geomorphic units across all windows highlights the escalating impact of mining on the Sone River's landscape. These findings underscore the urgent need for sustainable mining practices to mitigate further geomorphic transformations.

This quantitative analysis provides robust evidence for focused policy interventions in the hotspots of mining while identifying potential natural or regulatory constraints in others. The precise measurements enable future monitoring of intervention effectiveness at the individual reach level.

3.4. Sub-decadal Planform analysis using GEE

3.4.1. Datasets and methodology

In my study area, extensive sand extraction from river channels began in the mid-1990s in response to growing urbanisation and industrial development (Ghosh et al., 2016). To see the impacts of anthropogenic activities, we have mapped the river planform from Landsat imagery because of its historical coverage (Fig. 3.13; Nagel et al., 2023). We have used Landsat 5 and 8 datasets having a spatial resolution of 30 m. We have excluded the Landsat 7 data due to its scan

line error. We have taken the years 1988, 1996, 2000, 2005, 2010, 2015, 2020, and 2023 to compare the river planform of pre- and post-mining activities.

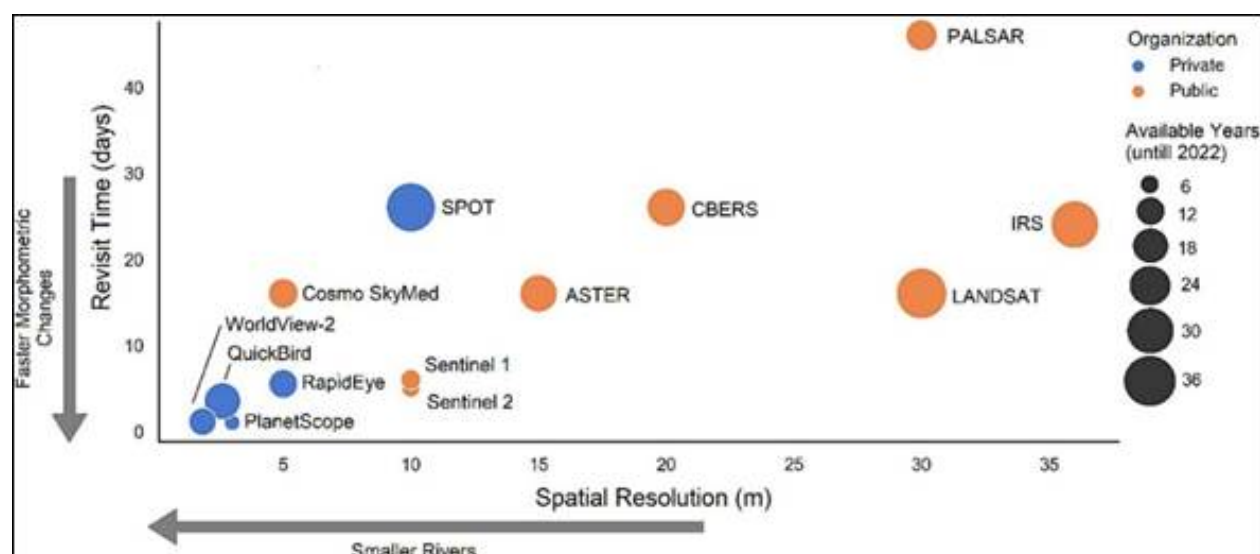


Figure 3.13: Showing the available satellite datasets and their revisit time and spatial resolution (Source: Nagel et al., 2023).

We have selected the Google Earth Engine platform for image processing and river planform feature extraction. Landsat data is open source, making it easily accessible from the Google Earth Engine (GEE) catalogue for seamless processing and analysis.

Dataset	Nominal resolution	Temporal granularity	Temporal coverage	Spatial coverage
Landsat 8 OLI/TIRS	30 m	16 day	2013–Now	Global
Landsat 5 TM	30 m	16 day	1984–2012	Global

USGS Landsat 8 Level 2, Collection 2, Tier 1: This dataset provides atmospherically corrected surface reflectance and land surface temperature data derived from the Landsat 8 OLI/TIRS

sensors. It includes five visible and near-infrared (VNIR) bands, two short-wave infrared (SWIR) bands, and one thermal infrared (TIR) band. The VNIR and SWIR bands are processed to orthorectified surface reflectance, while the TIR band is processed to orthorectified surface temperature. Additionally, the dataset contains intermediate bands used for surface temperature calculations, along with quality assurance (QA) bands. Surface reflectance products for Landsat 8 are generated using the Land Surface Reflectance Code (LaSRC).

Information on used bands:

Name	Wavelength	Description
SR_B1	0.435-0.451 μm	Band 1 (ultra blue, coastal aerosol) surface reflectance
SR_B2	0.452-0.512 μm	Band 2 (blue) surface reflectance
SR_B3	0.533-0.590 μm	Band 3 (green) surface reflectance
SR_B4	0.636-0.673 μm	Band 4 (red) surface reflectance
SR_B5	0.851-0.879 μm	Band 5 (near infrared) surface reflectance
SR_B6	1.566-1.651 μm	Band 6 (shortwave infrared 1) surface reflectance
SR_B7	2.107-2.294 μm	Band 7 (shortwave infrared 2) surface reflectance
QA_PIXEL		Pixel quality attributes generated from the CFMASK algorithm.

USGS Landsat 5 Level 2, Collection 2, Tier 1: This dataset provides atmospherically corrected surface reflectance and land surface temperature data derived from the Landsat TM sensor. It includes four visible and near-infrared (VNIR) bands, two short-wave infrared (SWIR) bands, and one thermal infrared (TIR) band. The VNIR and SWIR bands are processed to orthorectified surface reflectance, while the TIR band is processed to orthorectified surface temperature.

Additionally, the dataset contains intermediate bands used for surface temperature calculations, along with quality assurance (QA) bands.

Surface reflectance products for Landsat 5 are generated using the Landsat Ecosystem Disturbance Adaptive Processing System (LEDAPS) algorithm (version 3.4.0).

Information on used bands:

Name	Wavelength	Description
SR_B1	0.45-0.52 μm	Band 1 (blue) surface reflectance
SR_B2	0.52-0.60 μm	Band 2 (green) surface reflectance
SR_B3	0.63-0.69 μm	Band 3 (red) surface reflectance
SR_B4	0.77-0.90 μm	Band 4 (near infrared) surface reflectance
SR_B5	1.55-1.75 μm	Band 5 (shortwave infrared 1) surface reflectance
SR_B7	2.08-2.35 μm	Band 7 (shortwave infrared 2) surface reflectance
QA_PIXEL		Pixel quality attributes generated from the CFMASK algorithm.

3.4.1.1. Planform Mapping

To accurately map the river's planform, a systematic approach was employed within the Google Earth Engine (GEE) platform to extract binary masks of key geomorphic features, including the wet channel, active river channel, and islands (Fig. 3.14).

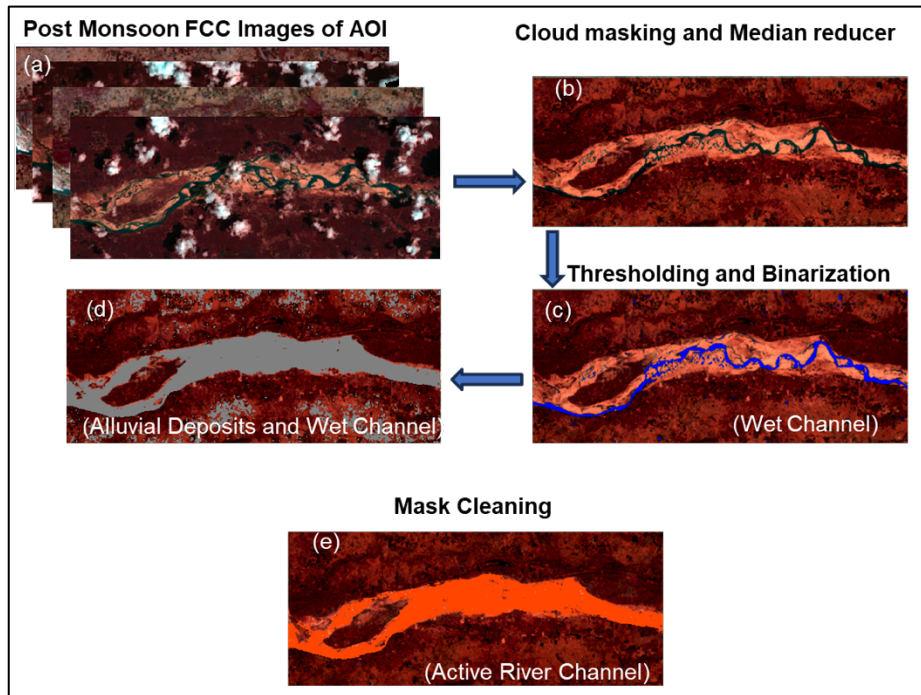


Figure 3.14: Methodology for extracting the binary mask of the active river channel and wet channel using Google Earth Engine.

The active river channel encompassed both the wet channel and alluvial sand deposits, while islands were classified as vegetated bars and assigned zero values in the active river channel binary mask. A previously established methodology by Boothroyd et al. (2020) was adapted and optimised for the study area. Threshold values were carefully adjusted to improve classification accuracy. Furthermore, the algorithm for wet channel extraction was refined, and morphological operations such as dilation and erosion were applied to enhance and clean the resulting binary masks.

The active river channel was delineated based on its physical boundaries, corresponding to the bankfull channel extent, using well-established techniques outlined by Rowland et al. (2016) and Schumann et al. (2009). This ensured the analysis captured only the dynamically active portions of the river system. To comprehensively monitor river migration and morphological transformations over time, a 3-kilometre buffer was generated around the permanent wet channel. This area of interest (AOI) was selected to encompass significant planform shifts, including channel widening, avulsions, and meandering, thus ensuring robust spatial analysis of river evolution.

For consistent active channel extraction, temporal filtering was applied. Image collections were restricted to the post-monsoon period (September to December) to reduce seasonal variability. Surface reflectance datasets from Landsat 5 TM and Landsat 8 OLI/TIRS were used, with atmospheric corrections ensuring accurate spectral comparisons across different time points. Cloud contamination was addressed using the CFMask algorithm (Foga et al., 2017), which automatically removed pixels affected by clouds and shadows, thereby enhancing the reliability of extracted planform features.

To improve the visibility of geomorphic features, annual composite images were created using median (50th percentile) reducers to eliminate outliers and false colour composites to better visualise water and sediment deposits. This aggregation method reduced the influence of transient anomalies and provided a stable and representative depiction of the river planform. Wet channel areas were identified by generating a binary water mask. Several multispectral indices were employed to refine classification accuracy: the Modified Normalised Difference Water Index (MNDWI) for enhancing water features, the Normalised Difference Vegetation Index (NDVI) to eliminate vegetation interference, and the Enhanced Vegetation Index (EVI) for further refinement, as recommended by Zou et al. (2018). Additional validation steps, following Huang et al. (2018), were implemented to increase water detection precision.

The classification of alluvial deposits mirrored the approach used for wetted channels, applying the same multispectral indices (MNDWI, NDVI) and excluding vegetated pixels for a more accurate delineation of sediment deposits. The Shortwave Infrared 2 (SWIR 2) band was intentionally omitted, as it did not enhance the identification of emerging sediment bars (Monegaglia et al., 2018). Active channel pixels were determined using logical operators with thresholds set at $\text{MNDWI} \geq -0.4$ and $\text{NDVI} \leq 0.2$, following criteria established by Bertoldi et al. (2011) for delineating riparian vegetation.

The individual binary masks for wetted channels and alluvial deposits were merged through geometric union operations to produce a comprehensive active river channel mask. To refine the final product and eliminate noise, morphological operations were once again applied: dilation to bridge small gaps between channel segments and erosion to remove isolated noise pixels. These processes resulted in a clean and accurate active channel mask, suitable for detailed morphometric analysis.

The finalized binary masks were exported from GEE as GeoTIFF files to Google Drive. These outputs were then imported into GIS software platforms such as ArcGIS and QGIS for advanced spatial analysis and visualization. This method establishes a consistent, replicable, and scientifically grounded approach for river planform mapping, effectively integrating remote sensing data, advanced classification algorithms, and geospatial analytical tools to assess riverine dynamics over time.

The final active river channel and wet channel masks were imported into ArcGIS for detailed planform classification. The river planform was categorized into distinct classes, including wet channels, active river channels, mid-channel bars, and side bars. Mid-channel bars were identified by detecting zero-value areas within the active river channel binary mask. These mid-channel and side bars were further classified into vegetated and sandy bars based on land cover. This classification facilitated the analysis of spatial distribution patterns and the characteristics of different geomorphic features, contributing to a better understanding of channel dynamics and sediment deposition.

To ensure an accurate representation of morphological changes over time, some vegetated side bars, which later transitioned into active floodplains, were manually digitized. This classification approach provided a comprehensive evaluation of long-term river evolution and planform adjustments.

To assess the influence of sand mining and flow regulation on river morphology, the Damodar River study area was divided into 25 reaches, which were further grouped into three zones based on dominant controlling factors:

- Zone 1 (54.09 km): Located downstream of the Panchet Dam and upstream of the Durgapur Barrage, this zone is moderately affected by sand mining and also experiences regulated flow.
- Zone 2 (22.86 km): Extending from the Durgapur Barrage to the Rondiha Barrage, this reach is predominantly influenced by flow regulation, leading to significant changes in channel morphology.
- Zone 3 (57.37 km): Encompassing reaches that are heavily impacted by sand mining, with the final stretches also affected by excessive sediment extraction downstream.

Additionally, three study windows were identified along the Sone River, all of which are significantly impacted by sand mining:

- Window 1 (16.75 km): Located just downstream of Indrapuri Barrage, this reach experiences the combined influence of flow regulation and sand mining.
- Window 2 (27.4 km): Positioned in the midstream section, this area exhibits the most intense sand mining activity, resulting in major geomorphic alterations.
- Window 3 (11.7 km): Situated in the downstream reaches, this area reflects the cumulative effects of both upstream sediment extraction and natural sediment transport processes.

This zonation and study window approach provided a structured framework for evaluating spatial variations in mining impacts and the resulting morphological changes in both river systems.

3.4.1.2. Spatio-temporal Analysis of River Morphology

To analyse the morphological dynamics of the Damodar and Sone Rivers, the areas of different geomorphic features were measured, including wet channels, sand bars, mid-channel sand bars, mid-channel vegetated bars, and vegetated bars. The active river channel area was computed by summing the wet channel and sand bars while excluding vegetated bars, which are considered more stable features. This active river channel area represents the bankfull stage boundary and corresponds to the riverbanks, providing a reference for assessing channel adjustments over time.

For the Damodar River, area calculations were performed reach-wise across 25 study reaches, while for the Sone River, they were carried out window-wise to evaluate spatial variability.

To visualize these changes, two types of contour maps were generated:

1. Percent change from reference year: Representing the percentage change in the area of each morphological class relative to the reference year (1988), offering insights into long-term trends.
2. Percent change from previous year: Capturing periodic variations in river morphology to identify short-term trends and shifts in sediment deposition and channel adjustments.

3.4.1.3. Braiding and Sinuosity Index Calculation

To evaluate the complexity of river planform configurations, the Braiding Index (BI) and Sinuosity Index (SI) were computed following the methodology outlined by Friend and Sinha (1993). These indices were calculated using a combination of RivGraph—a Python-based automated river network extraction tool—and ArcGIS for detailed spatial processing and visualization. Figure 3.15 shows the workflow for the automated extraction of the wet channel binary mask from satellite imagery. This binary representation of the wetted river surface served as the basis for skeletonization, a process that converts the binary mask into a one-pixel-wide representation of the river's centerline while preserving its connectivity. Using this skeletonized output, RivGraph automatically identified the primary and secondary channels as well as bifurcation points (Schwenk et al., 2021). Subsequent network refinement steps were implemented to remove minor tributaries and any artefacts that could skew the interpretation of channel structure. This refined network highlighted only the active and morphologically significant channel segments. Further spatial processing was conducted in ArcGIS, where the widest continuous channel was clipped and used for index calculation.

The Braiding Index and Sinuosity Index were calculated using the following equations (after Friend and Sinha, 1992):

$$BI = L_{C_{tot}} / L_{C_{max}}$$

$$SI = LC_{\max} / L_r$$

Where:

LC_{tot} : Total length of all channel segments in the network,

LC_{\max} : Length of the widest (dominant) channel segment,

L_r : Valley length or the straight-line distance following the river valley axis.

This combined approach of automated extraction and GIS-based computation significantly minimised manual effort and reduced the potential for user-induced bias. It ensured a consistent, reproducible, and objective framework for evaluating changes in river morphology and planform complexity over time.

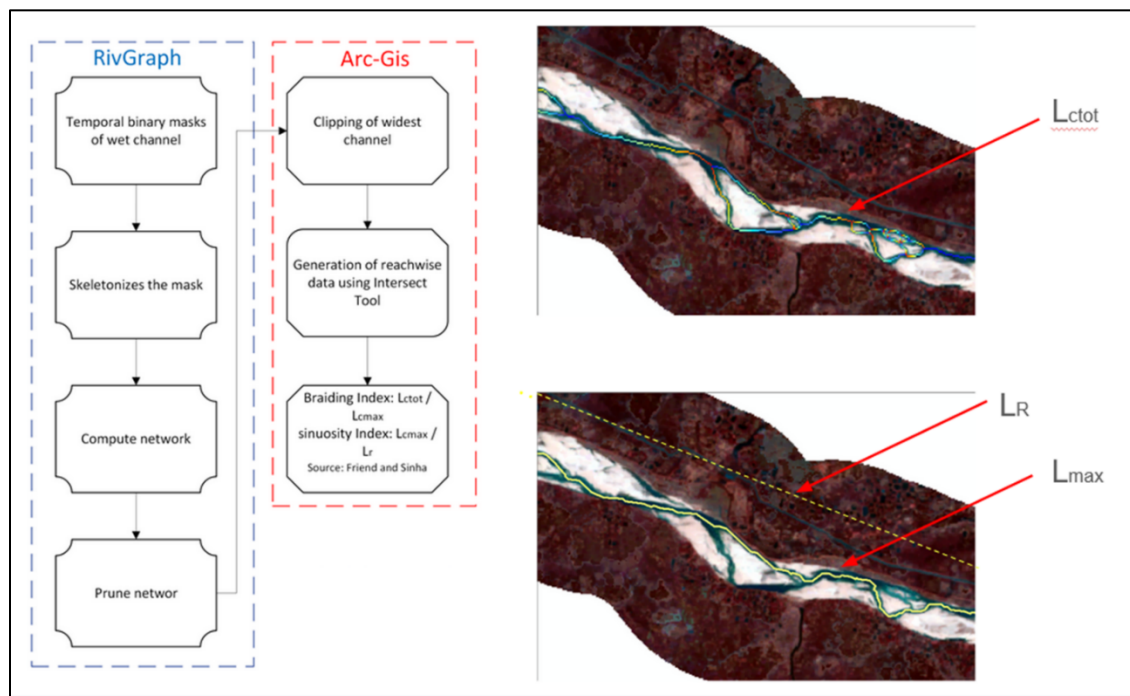


Figure 3.15: Methodology for calculating Braiding and Sinuosity Index using RivGraph.

3.4.1.4. Bar Area and Channel Area Ratio

To quantify sediment deposition within the river corridor, the ratio of bar area to channel area was calculated for each study reach. The bar area consisted of all exposed sand features, including mid-channel bars and channel-margin bars, which were extracted from classified imagery. In parallel, the wet channel area was delineated using NDWI-based classification techniques to capture actively flowing water bodies.

Once both spatial extents were delineated, the total area occupied by bars was divided by the wet channel area to obtain a bar-to-channel area ratio. This ratio serves as an important geomorphic indicator of sediment accumulation and helps in assessing the spatial extent and frequency of deposition zones across the river reaches. The resulting values provide insight into temporal sediment dynamics and potential river stability or instability within each reach.

3.4.2. Results

3.4.2.1. *Spatio-temporal Analysis of Damodar River Morphology*

Figure 3.16a shows that Zone 1 experienced dramatic fluctuations in the sand bar area, which expanded from 6.94 km² in 1988 to a peak of 28.05 km² in 2015, followed by a sharp decline to 7.78 km² in 2023. This trajectory reflects episodic sediment deposition interspersed with phases of erosion or stabilization. A particularly striking transformation was observed in the mid-channel sand bars, which diminished from 10.46 km² in 1988 to just 1.02 km² in 2023. Meanwhile, vegetated bars, which were nearly absent in 1988 (0.01 km²), expanded significantly to 8.22 km² by 2023 (Fig. 3.16b). This pattern indicates a gradual conversion of mid-channel features into vegetated forms, likely due to decreased flow velocities that facilitated vegetation establishment.

Concurrently, the wet channel area contracted from 41.89 km² in 1988 to 31.01 km² in 2023, signalling a broader trend of channel narrowing. In several reaches, specifically 2b, 4a, 4b, and 4c, mid-channel and vegetated bars were reconfigured into bank-attached side bars (Fig. 3.16a). This transformation occurred after 2010 in reach 2b and post-2005 in reaches 4a through 4c. Following 2015, the total sand deposits markedly declined, indicating morphological degradation. While the wet channel area initially showed a declining trend until 2015, it began to expand thereafter, possibly indicating renewed erosion activity.

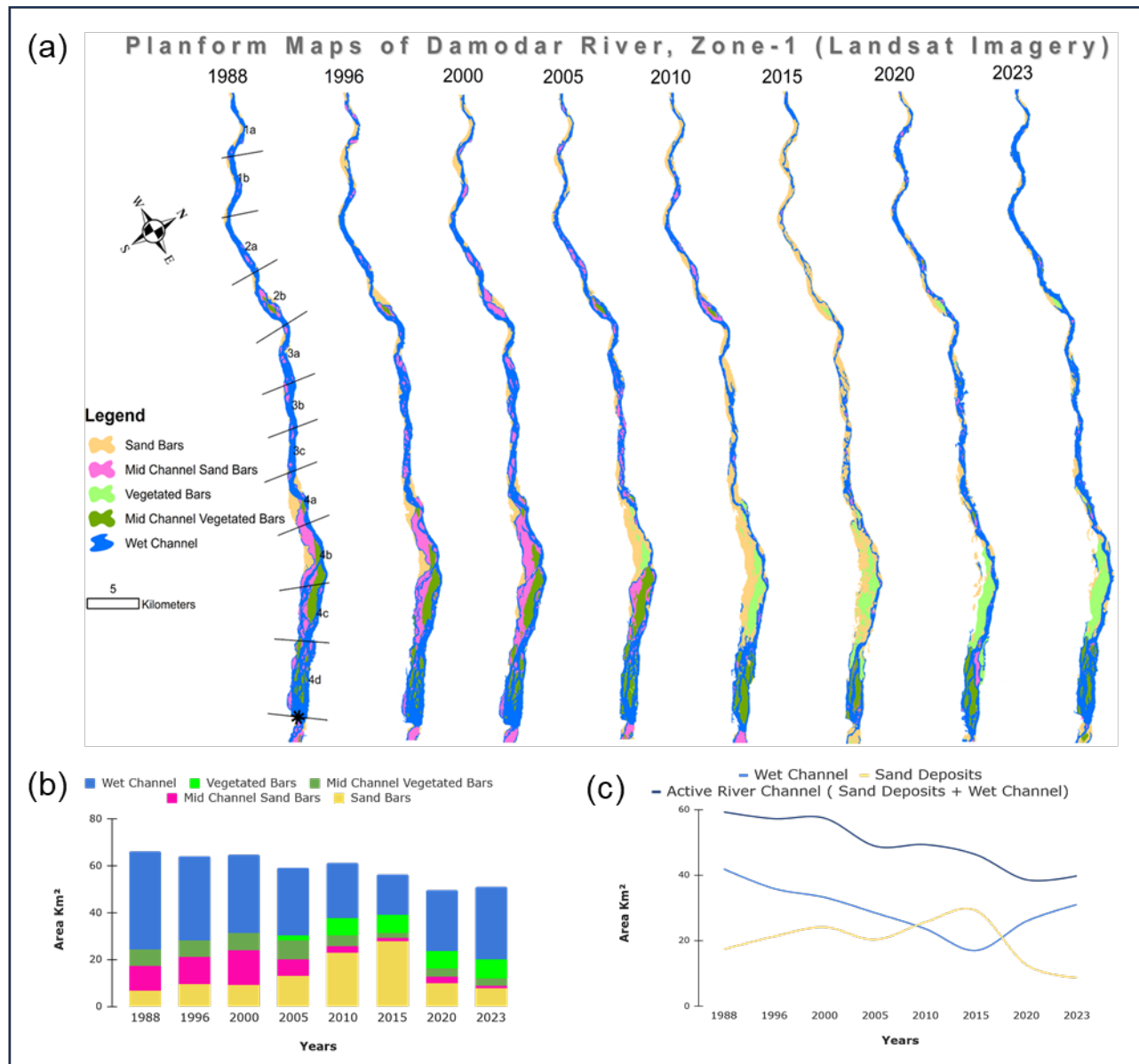


Figure 3.16: (a) Spatiotemporal planform maps of Zone 1 of the Damodar River, derived from Landsat imagery, (b) Changes in morphological classes, and (c) illustrating morphological changes in wet channels, sand deposits, and area of active river channel over time.

An initial decrease in sand deposit area was observed in 2005, with a more pronounced decline after 2015 (Fig. 3.16c). Although flow variations can impact the extent of exposed bars, the combined assessment of wet channel and sand bar areas, termed the active river channel, offers a more comprehensive metric. This active channel area demonstrates a continuous decline,

especially notable in the years 2005 and 2020, pointing to a long-term trend of channel contraction (Fig. 3.16c).

Figure 3.17a shows the morphological dynamics in Zone 2, which are similar to those of Zone 1. Sand bar areas peaked at 14.92 km² in 2015, then declined to 7.79 km² in 2023. The mid-channel sand bars diminished from 13.61 km² in 1988 to 2.50 km² in 2023, while vegetated bars initially

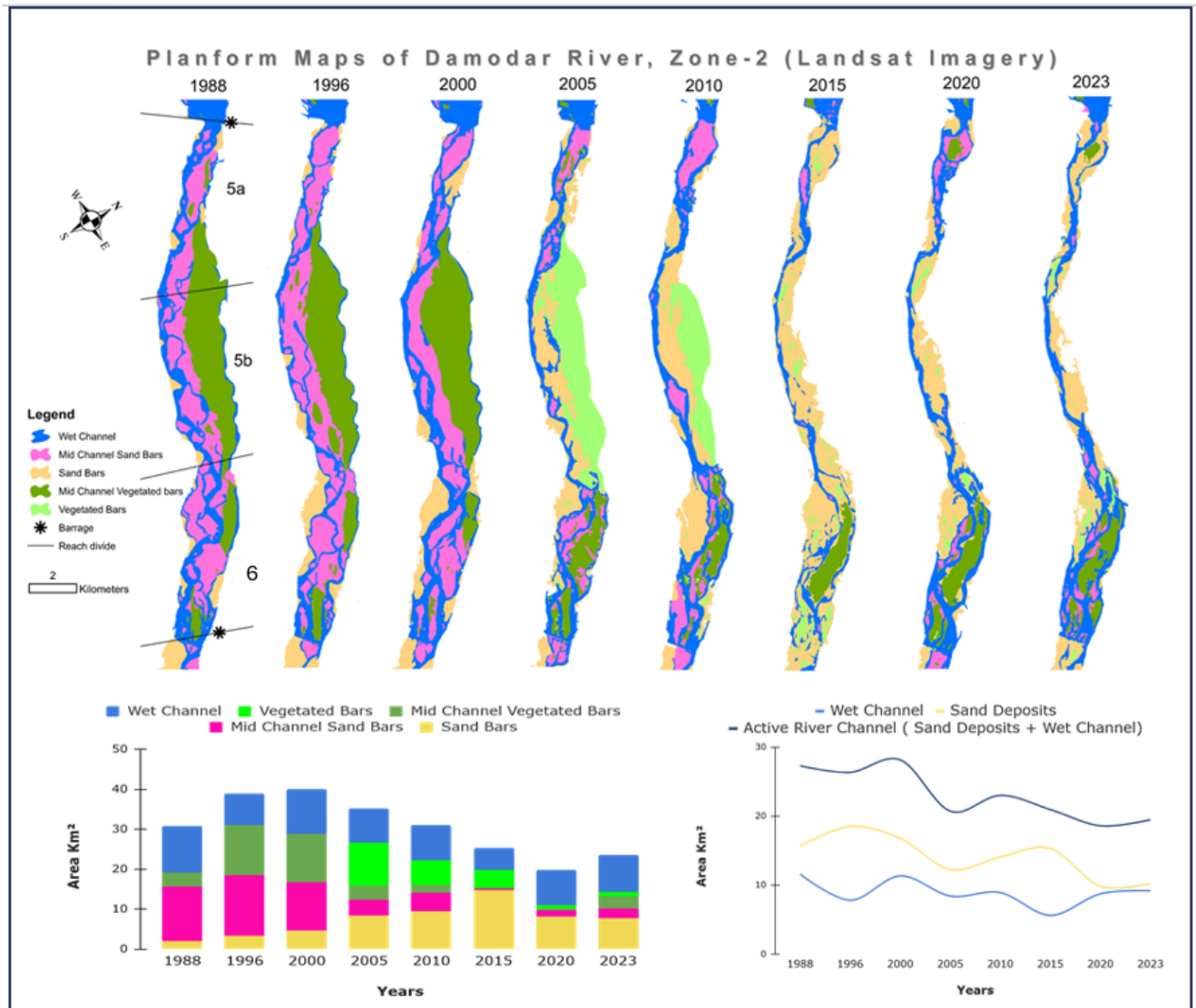


Figure 3.17: (a) Spatiotemporal planform maps of Zone 2 of the Damodar River, derived from Landsat imagery. (b) Changes in morphological classes, and (c) illustrating morphological changes in wet channels, sand deposits, and the area of active river channel over time.

surged from 0.004 km² in 1988 to a peak of 10.82 km² by 2005, before stabilizing at around 1.11 km² by 2023 (Fig. 3.17b). This evolution suggests that mid-channel vegetated features were

converted into more stable bank-attached forms. The wet channel area in this zone shrank from 11.61 km² in 1988 to 9.21 km² in 2023, reflecting an overall trend toward channel stabilization (Fig. 3.17b). Situated between the Durgapur Barrage upstream and Rondiha Barrage downstream, Zone 2 is heavily regulated. Large mid-channel vegetated bars on the river's left flank were transformed into side bars around 2005, eventually merging with the active floodplain by 2015 (Fig. 3.17b). While mid-channel sand bars persisted near the barrage, they nearly disappeared elsewhere. Both the wet channel and sand deposits fluctuated throughout the study period but showed an overall declining trend, with the most significant reductions occurring in 2005. Consequently, the active river channel area also showed marked declines in 2005 and 2020 (Fig. 3.17c).

Zone 3 demonstrated the greatest degree of variability in morphological behaviour (Fig. 3.18a). Sand bar area peaked at 49.33 km² in 2010 before decreasing to 24.82 km² by 2023. Mid-channel sand bars declined substantially from 16.42 km² to 3.55 km², and vegetated bars dropped from 5.63 km² to 0.81 km². These reductions suggest either consolidation into larger bars or gradual vegetation overgrowth. Unlike Zones 1 and 2, the wet channel area in Zone 3 remained relatively stable throughout the study period, hovering around 24 km², which suggests limited hydrological alterations (Fig. 3.18b).

The mid-channel sandbar decline was especially sharp, while vegetated bars in mid-channel positions were eliminated. Although the sand deposit area fluctuated up to 2010, it declined continuously thereafter. Interestingly, the wet channel area began expanding after 2015 and exceeded its initial 1988 extent by 2020 (Fig. 3.18c), an anomalous pattern in contrast to the trends in Zones 1 and 2.

Across the study period, three major transitions in channel behavior were evident. Between 2005 and 2015, all zones experienced a notable expansion in vegetated bars, likely triggered by reduced flow variability or enhanced sediment retention. From 2015 to 2023, a sharp decline in mid-channel features, particularly within Zones 1 and 2, suggested rapid morphological simplification. Meanwhile, Zone 3 displayed a sustained drop in sand bar area from 2010 to 2023, pointing toward either sediment starvation or intensified erosion processes.

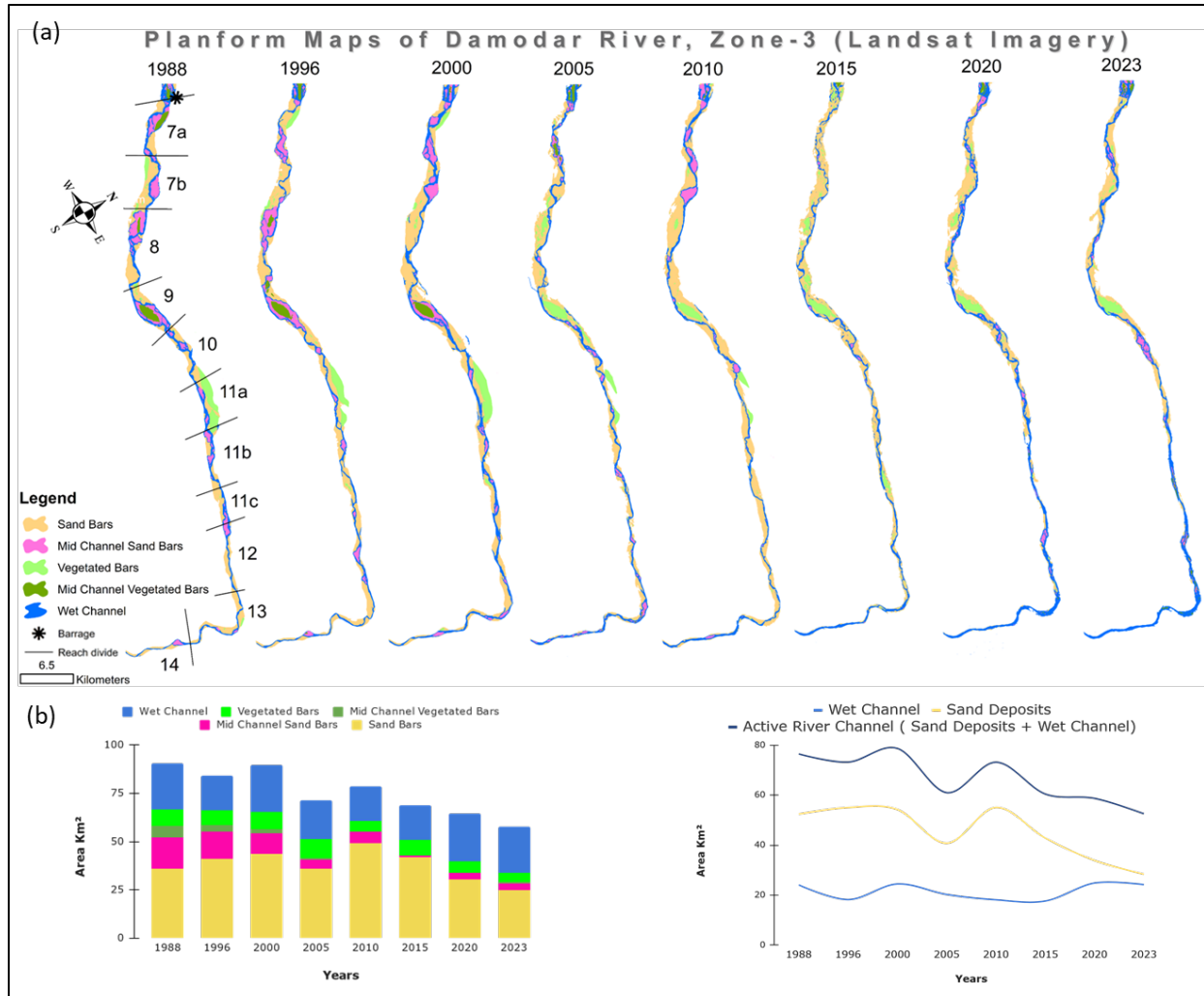


Figure 3.18: (a) Spatiotemporal planform maps of Zone 3 of the Damodar River, derived from Landsat imagery, (b) Changes in morphological classes, and (c) illustrating morphological changes in wet channels, sand deposits, and area of active river channel over time.

3.4.2.1.1. Changes in Wet Channel Area

The wet channel area across the Damodar River's 25 reaches has undergone significant changes between 1988 and 2023, revealing clear spatial and temporal trends. Overall, most reaches experienced a decline in wet channel area, indicating widespread channel narrowing or drying. The period from 2010 to 2015 marked the most severe contraction, with many reaches showing their lowest recorded values. For instance, reach 2a shrank from 3.10 km^2 in 1988 to just 0.88 km^2 in 2015 before partially recovering to 2.66 km^2 by 2023. Similarly, reach 3b declined from 2.96

km² to 1.00 km² during the same period, with only minimal recovery by 2023. These changes suggest long-term sediment deposition or reduced flow in these sections (Fig. 3.19a).

In contrast, some reaches exhibited notable fluctuations or late-stage recovery. Reach 4d, for example, saw a major decline from 9.37 km² in 1988 to 5.26 km² in 2015, followed by a sharp rebound to 7.97 km² by 2023. Reach 6 displayed similar dynamism, peaking at 5.04 km² in 2000, dropping to 2.53 km² in 2015, and then recovering to 4.99 km² by 2023. These variations may reflect the influence of seasonal flows or upstream anthropogenic interventions. Meanwhile, reaches 12 and 13 showed significant recovery; Reach 13 more than doubled its wet area from 2.05 km² to 4.27 km² by 2023, possibly due to flow diversion or localised erosion (Fig. 3.19a).

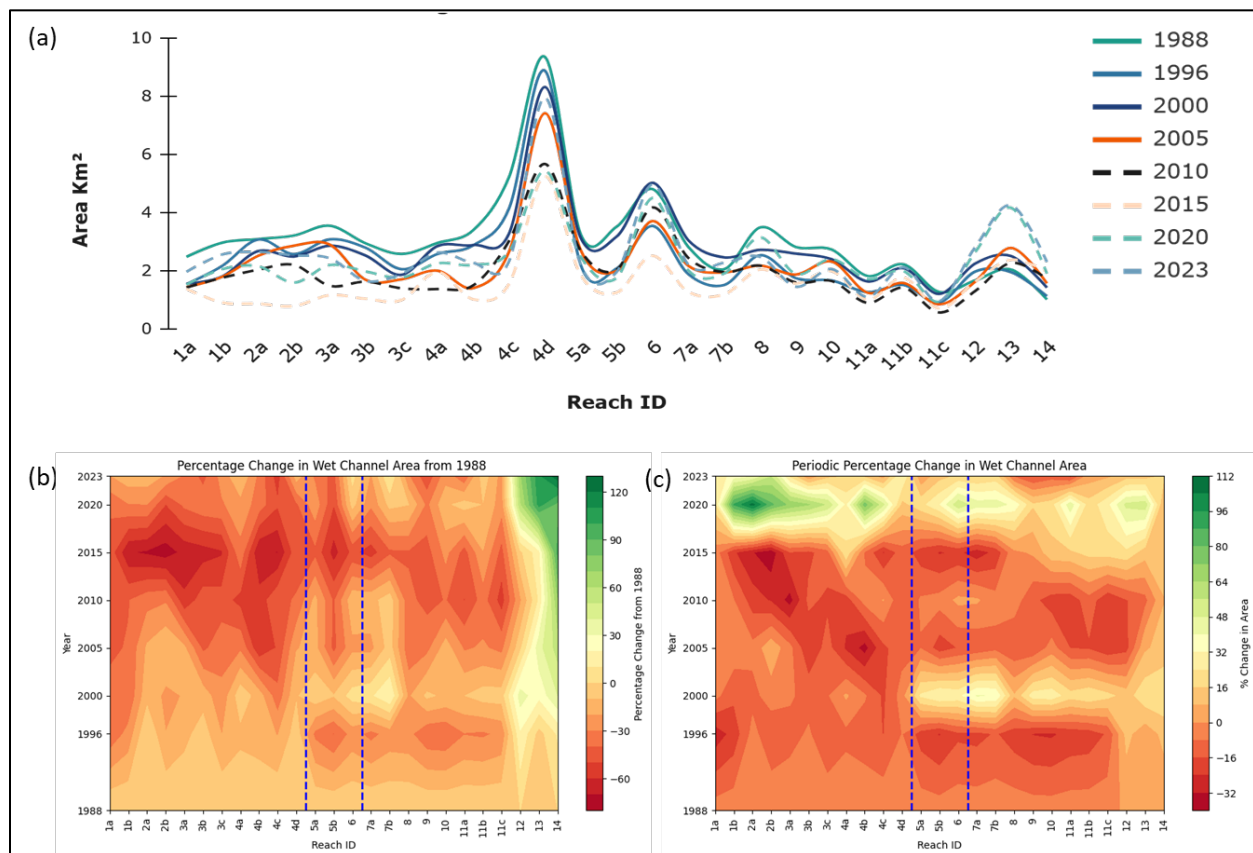


Figure 3.19: (a) Reach-wise line plots depicting changes in wet channel area; (b) Percentage change in wet channel area relative to the reference year (1988); and (c) Percentage change from the previous year, illustrating periodic variability. The blue dashed lines in panels (b) and (c) indicate the locations of the Durgapur and Rondiha barrages.

A few reaches, such as 9 and 11c, have remained relatively stable over the 35-year period, with only minor declines. The observed changes are likely driven by a combination of sediment deposition, dam operations, and climate variability, with the pronounced contraction phase between 2005 and 2015 potentially linked to prolonged dry conditions.

These findings underscore the Damodar River's spatially variable response to environmental and anthropogenic pressures. Reaches like 1a–3c, which show persistent narrowing, may require targeted sediment management, while recovering sections (e.g., 4d, 6, 13) warrant continued monitoring to assess the sustainability of recent improvements.

Figure 3.19b illustrates the contour map showing the percentage change in wet channel area since the baseline year, 1988. Most reaches exhibit a persistent, cumulative decline over time, indicating long-term contraction. However, downstream sections, particularly reaches 7b and reaches 12 to 14, show a positive change, suggesting channel expansion compared to the reference year. The most severe reduction occurred in Zone 1, located upstream of the Durgapur Barrage, marking it as a major area of wet channel degradation. Conversely, the lower reaches, situated downstream of major sand mining hotspots, may have experienced localized erosion leading to channel widening. These spatial patterns highlight the significant role of anthropogenic influences, such as flow regulation and sand mining, on river morphology.

As shown in Figure 3.19c, year-to-year variations in wet channel area reveal distinct temporal patterns and reach-specific responses. The most dramatic fluctuations occurred during 2015–2020, when several reaches experienced extreme, opposing changes. Reach 2a exemplified this volatility, with a 57.15% loss in 2015—the system's maximum single-year decline—followed by a remarkable 146.96% increase in 2020. Similarly, reach 1b shifted from (–) 48.22% change in 2015 to a (+)125.45% gain in 2020, highlighting the impact of flow regulation. The contour visualization identifies 2015 as a critical threshold year, with 18 of 24 reaches showing declines greater than 30% from the previous year, particularly in the upper and middle sections (Reaches 1a–8). This was followed by a system-wide recovery phase (2015–2020), during which 70% of the reaches gained more than 50% area.

In recent years (2020–2023), the system shows signs of stabilization, though exceptions remain. Reach 8 continues to decline (-21.10%), while Reach 4d expands (+46.26%). The spatial distribution of changes indicates that lower reaches (9–14) have maintained more consistent positive trends since 2000, contrasting with the volatility of upstream sections. This pattern suggests differing response mechanisms along the river's longitudinal profile, potentially linked to sediment supply dynamics or anthropogenic interventions. The 2015–2020 oscillation appears especially significant, possibly representing a system-wide adjustment to altered flow regimes or sediment budgets.

3.4.2.1.2. *Changes in Area of Sand Deposits*

Several reaches of the Damodar River have experienced significant reductions in sand deposits between 1988 and 2023, indicating notable geomorphic changes with potential management implications. The most dramatic declines occurred in Reaches 14, 13, and 12, where sand deposits have nearly disappeared by 2023. Reach 14 recorded the most severe reduction, dropping from 3.85 km² in 1988 to just 0.009 km² in 2023—a staggering 99.8% loss. Similarly, reach 13 declined from 5.03 km² to 0.28 km² (94.4% reduction), and Reach 12 decreased from 3.46 km² to 0.69 km² (80% reduction). These lower reaches have shown a consistent pattern of sand depletion since 2000, with accelerated losses after 2015 (Fig. 3.20a).

Other significantly affected reaches include 11c (2.64 km² to 0.51 km², 80.7% loss), 4d (1.49 km² to 0.28 km², 81.4% reduction), and 1a (0.68 km² to 0.59 km², 13.2% reduction). The timing of these declines varies: upper reaches (1a–3c) have undergone gradual reductions, whereas lower reaches (11a–14) experienced more abrupt losses post-2010. These trends likely result from multiple interacting factors, including upstream dam-induced flow regulation, sediment supply alterations, and vegetation encroachment. The loss of sand deposits may lead to reduced sediment connectivity, degraded habitat availability, and potential increases in stream power, possibly intensifying downstream bank erosion. Severely impacted reaches, particularly in the lower stretch, warrant focused sediment management and monitoring to determine whether these transformations are temporary fluctuations or signal a more permanent geomorphic shift.

Figure 3.20b illustrates significant spatial variation in sediment deposition patterns along the river corridor. The upper reaches (1a–3c) demonstrate consistent sediment accumulation, with Reach 3c peaking at +425% in 2015, highlighting substantial deposition. Middle reaches (4a–8) show transitional behavior, with early sediment gains giving way to net losses over time, as seen in Reach 4a's -70% decline by 2023. The most striking trend is evident in the lower reaches (9–14), which experienced severe depletion, particularly Reach 14, where a -99.8% change underscores near-total loss of surface deposits. These sediment reductions could result from physical erosion and downstream transport or the submergence of exposed bars under deepening flow conditions. The spatial progression of losses suggests sediment disconnectivity along the river's longitudinal profile, potentially driven by upstream sediment trapping, decreased transport capacity, or submergence effects from flow regulation. The extreme stress observed in the lower reaches warrants further investigation to distinguish between permanent sediment loss and hydrological submergence. These patterns reflect complex sediment dynamics and emphasise the need for reach-specific strategies that address both erosional and submergence-driven changes.

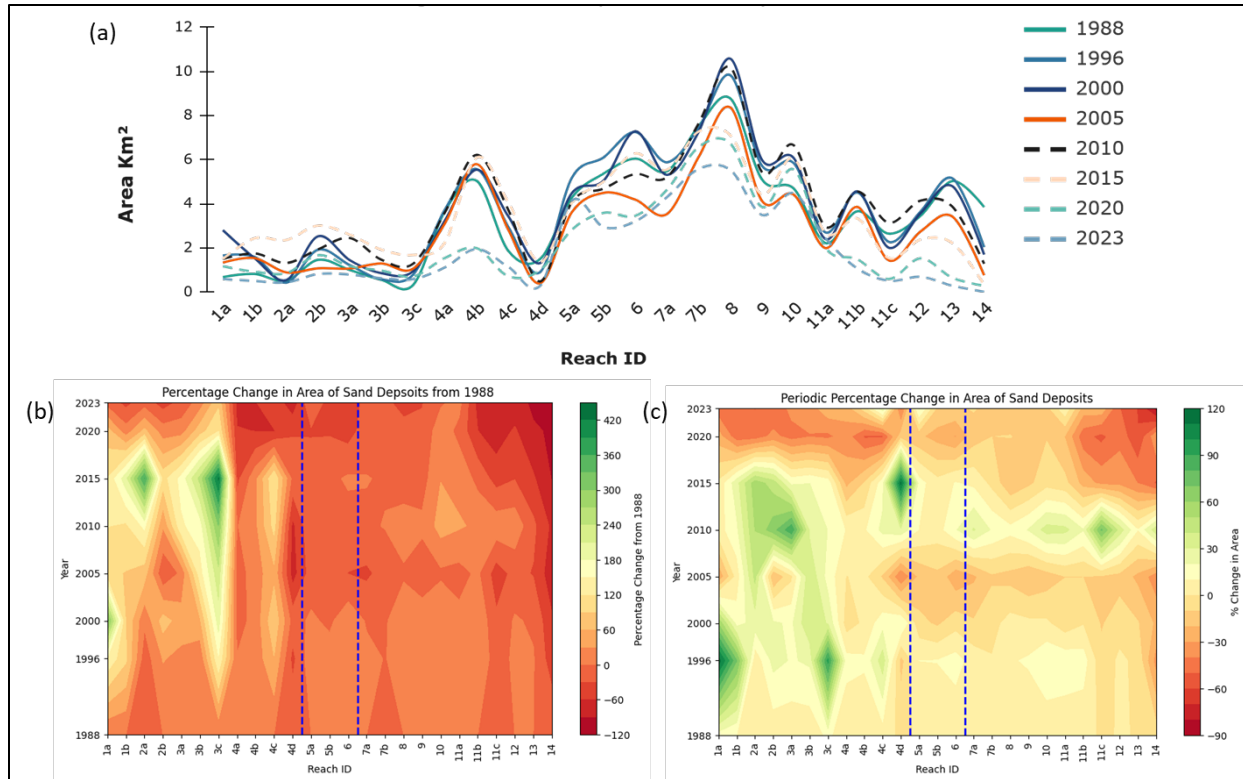


Figure 3.20: (a) Reach-wise line plots depicting changes in Sand deposit area; (b) Percentage change in sand deposit area relative to the reference year (1988); and (c) Percentage change from the previous year, illustrating periodic variability. The blue dashed lines in panels (b) and (c) indicate the locations of the Durgapur and Rondiha barrages.

A periodic analysis highlights critical transitions in geomorphic behavior, especially during the volatile 2015–2020 period (Fig. 20). This phase witnessed abrupt fluctuations: Reach 4d gained +183% in 2015, then declined by -27% in 2020; Reach 2a shifted sharply from +79% to -64% over the same interval. These fluctuations align with concurrent wet channel expansion trends, suggesting a system-wide sediment redistribution event. Lower reaches (11c–14) exhibit persistent erosion, with Reach 14 losing 96.9% in 2023 and Reach 13 undergoing six consecutive years of decline, confirming chronic sediment starvation. Upper reaches reveal more complex trajectories, such as Reach 3c, which peaked with a +147% increase in 1996 before eventually declining to -58% by 2020, indicating depletion of earlier sediment accumulation. The synchronization of mid-reach volatility (4a–8) with lower-reach degradation points to a downstream cascade effect in sediment disconnectivity initiated post-2015. Together, these observations depict a river in rapid transition—from relatively balanced sediment dynamics

before 2015, through chaotic redistribution between 2015–2020, to widespread erosion afterward—with the lower reaches facing the most severe impacts of this disrupted sediment regime.

3.4.2.1.3. *Changes in Active River Channel Area*

The Damodar River's morphological evolution between 1988 and 2023 reveals a complex pattern of active channel adjustments, characterized by alarming contractions in the lower reaches contrasted with relatively stable conditions upstream. The upper reaches (1a–3c) exhibited notable stability, with variations remaining under 20%, while the middle reaches (4a–8) displayed dynamic fluctuations. In stark contrast, the lower reaches (9–14) experienced severe and persistent losses. Reach 14 underwent the most dramatic reduction, losing 52% of its active channel area (4.88 km² to 2.32 km², Fig. 3.21a), followed by Reach 9 with a 37% decline and Reach 13 with a 36% decline, all showing accelerated contractions after 2010.

This downstream degradation is accompanied by significant variability in the middle reaches. For instance, the active channel area in Reach 8 peaked at 13.31 km² in 2000 before dropping to 8.02 km² in 2023 and Reach 6 oscillated between 7.91 km² and 12.33 km² over the study period. Conversely, the upper reaches, such as Reach 1b, maintained consistent stability, with the active channel area ranging from 3.07 km² to 3.79 km² (Fig. 3.21a), indicating a potential buffering capacity against upstream disturbances. The spatial variability in channel morphology from stable headwaters through fluctuating midstream zones to degrading downstream sections suggests increasing sediment disconnectivity, where the river's ability to transport sediment diminishes downstream. These observations portray a river undergoing reach-specific morphological transformations, with the lower reaches experiencing ecologically significant losses that could compromise flood capacity, aquatic habitats, and overall river health. The findings call for differentiated management strategies that address both lower reach degradation and midstream variability across the river's longitudinal profile.

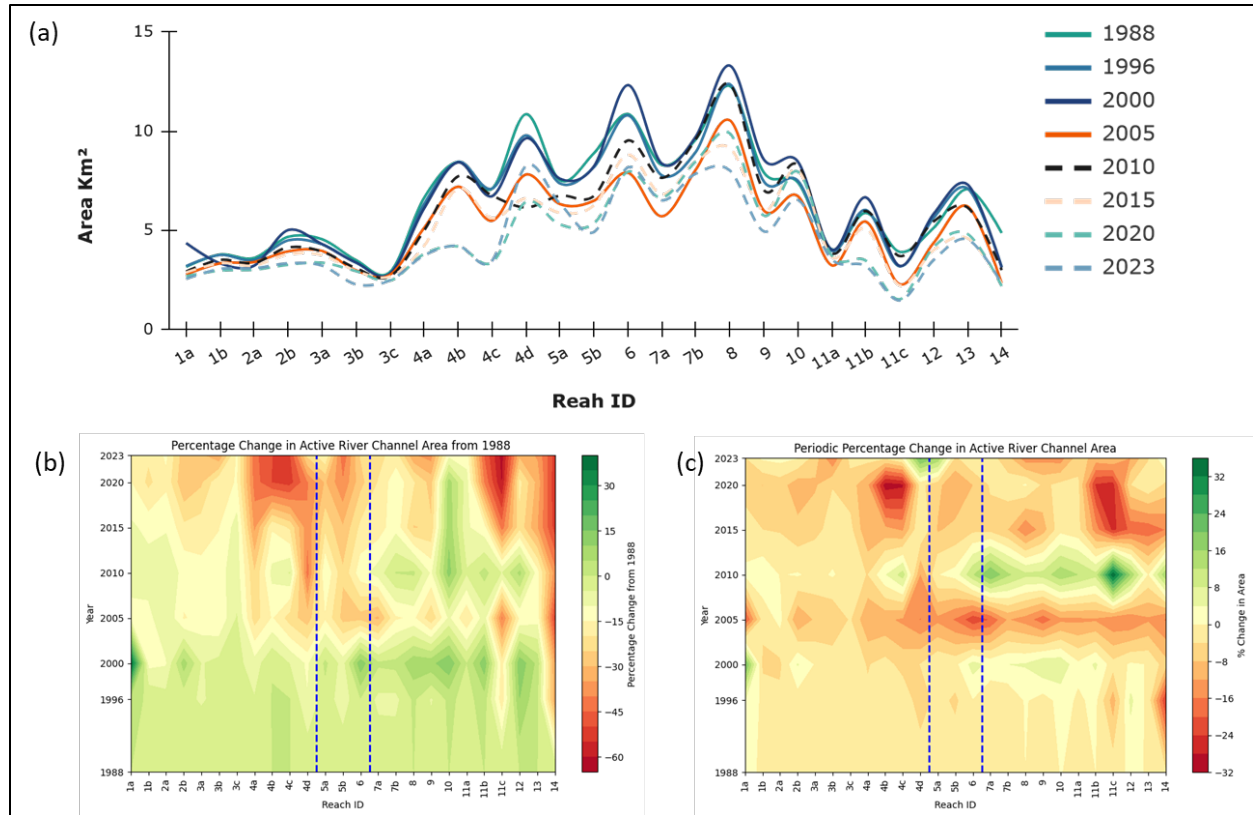


Figure 3.21: (a) Reach-wise line plots depicting changes in active river channel area; (b) Percentage change in active river channel area relative to the reference year (1988); and (c) Percentage change from the previous year, illustrating periodic variability. The blue dashed lines in panels (b) and (c) indicate the locations of the Durgapur and Rondiha barrages.

Further analysis of active channel dynamics highlights critical years of system-wide transformation, underscoring the vulnerability of the lower reaches (9–14) to severe degradation. Reach 11c suffered a catastrophic 62.4% loss in active channel area by 2023, closely followed by Reach 14 with a 52.4% reduction—both indicating near-permanent changes unless restorative interventions are implemented. These persistent losses coincide with periods of dramatic fluctuations, particularly during 2015–2020, a turbulent phase for the entire river system. In 2015, the river's instability was evident: while Reach 4d experienced a massive 183% sediment gain, reach 2a simultaneously saw a 57% loss in active channel area, reflecting the disjointed behavior of the fluvial system (Fig. 3.21b).

The stress continued into the 2020–2023 period, with lower reaches like 11c undergoing consistent annual losses ranging between 30–60%. Meanwhile, upper reaches remained

relatively stable, showing annual changes within $\pm 15\%$. The middle and lower sections, however, exhibited extreme year-to-year fluctuations. For example, reach 6 experienced a 35.8% change in 2005, Reach 2a showed a dramatic +146.9% recovery in 2020, and several reaches exceeded $\pm 50\%$ fluctuations during 2015 (Fig. 3.21c). These intense periodic shifts and chronic long-term reductions, especially in the lower reaches, indicate that degradation has crossed critical recovery thresholds. The active channel metric thus provides vital insight into the dual nature of degradation: chronic loss compounded by acute crashes. This underscores the urgency for targeted sediment management and flow restoration, particularly in the lower reaches, to mitigate irreversible damage and restore the river's geomorphic and ecological balance.

3.4.2.1.4. Braiding Index

This section investigates the spatiotemporal evolution of the Damodar River's braiding index (BI) from 1988 to 2023 across three zones. The analysis reveals significant morphological transformations influenced by sediment-flow disruptions.

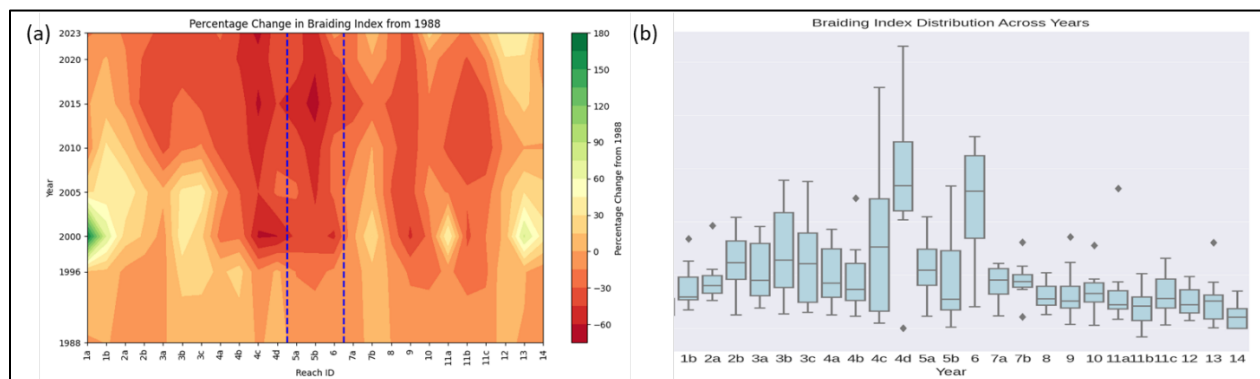


Figure 3.22: (a) Percentage change in Braiding index relative to the reference year 1988; (b) Spatial distribution of the braiding index. The blue dashed lines in panels (b) and (c) mark the locations of the Durgapur and Rondiha Barrages.

Zone 1 (Reaches 1a–4d), located downstream of Panchet Dam and upstream of Durgapur Barrage, exhibits severe braiding degradation. This area shows the most catastrophic loss, particularly in Reach 4c, where the BI dropped from 5.53 in 1988 to 1.28 in 2023, marking a 77% (Fig. 3.22a) decline and indicating a shift toward a single-thread channel system. Two critical degradation phases are evident: between 2000–2005, where acute BI reductions occurred (e.g., an 80% drop

in Reach 4c in 2000, aligning with Durgapur Barrage operations), and between 2015–2020, when widespread simplification took place (e.g., a 48% reduction in Reach 3b by 2020 during extreme flow events). The contour plots highlight high volatility, as seen in Reach 4d, which fluctuated from a 22% increase in 1996 to an 80% loss in 2000. These variations point to complete mid-channel bar erosion and sediment starvation, with most final BI values (2023) clustering between 1.0–1.5, typical of channelized systems.

Zone 2 (Reaches 5a–6), situated between Durgapur and Rondiha Barrages, demonstrates transitional behavior with moderated yet substantial BI declines ranging from 30–63%. For example, Reach 5b experienced a decrease from BI 3.67 to 1.35, while Reach 6 showed some resilience, recording a BI of 4.60 in 2023 after a mid-period decline. The data underscores barrage-induced instability: in 2000, Reach 6 suffered a 68% crash, likely due to sediment trapping by the barrage, whereas by 2023, it exhibited a modest recovery (+4.7%), possibly reflecting partial sediment bypass or redistribution (Fig. 3.22a).

Zone 3 (Reaches 7a–14), downstream of Rondiha Barrage, reflects relative morphological stability. Reach 13 recorded a 56% increase in BI by 2023 (Fig. 3.22a), while Reach 14 remained stable at a BI of approximately 1.0. The overall percentage change in this zone remained within $\pm 40\%$, significantly less volatile than the $\pm 80\%$ seen in Zone 1. These patterns suggest that the geomorphic impact of Rondiha Barrage is less severe than that of Durgapur Barrage.

The key findings highlight an infrastructure gradient in braiding loss severity, with Zone 1 (closest to Durgapur Barrage) showing the greatest degradation, followed by moderate changes in Zone 2, and relative stability in Zone 3. The transitions are nonlinear, characterised by episodic collapses in 2000 and 2015 amidst gradual declines. The results emphasise sediment discontinuity, with complete mid-channel feature loss in Zone 1, while Zone 3 retains its braided character. Overall, the Damodar River's braiding regime has undergone irreversible simplification, especially near major barriers like the Durgapur Barrage. Full braiding index values from 1988 to 2023 for all 25 reaches are presented in Appendix Table A1.

3.4.2.1.5. *Sinuosity Index*

The analysis of the sinuosity index reveals a clear zonal pattern (Fig. 3.23a, b) that both aligns with and complements the findings of the braiding index, offering deeper insight into how the Damodar River's planform geometry has differentially responded to anthropogenic controls.

In Zone 1 (Reaches 1a–4d), located immediately upstream of the Durgapur Barrage, sinuosity trends show moderate increases ranging from 3% to 18%, which contrasts sharply with the severe braiding losses in the same zone. This pattern suggests a compensatory morphological adjustment, wherein the river begins to develop meander bends to maintain energy dissipation in the absence of mid-channel bars. A notable example is Reach 4c, which experienced a sinuosity gain of 15–18% (from 1.15 to 1.36), aligning closely with its 77% loss in braiding index. This inverse relationship underscores how the river attempts to adapt its geometry in response to sediment-flow constraints and channel simplification.

Zone 2 (Reaches 5a–6), situated between the Durgapur and Randiha Barrages, displays transitional behavior. Here, sinuosity changes range from (–) 8% to (+) 7%, reflecting the intermediate nature of braiding reduction in this zone. These modest shifts indicate the influence of both upstream sediment starvation and localized flow reorganisation, resulting in a mixed morphological response. The subtle nature of sinuosity variation in this zone mirrors the balance between imposed constraints and the river's limited capacity for adjustment.

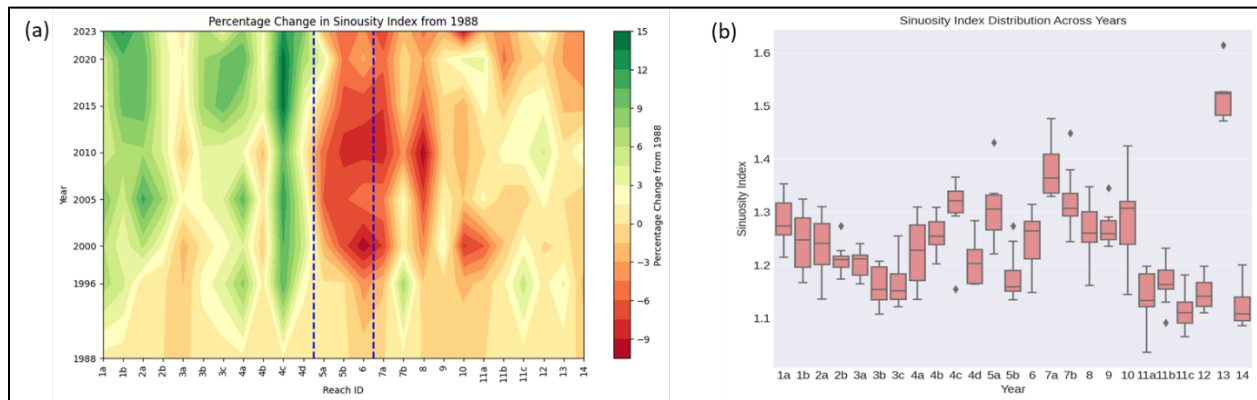


Figure 3.23: (a) Percentage change in sinuosity index relative to the reference year 1988; (b) Spatial distribution of the sinuosity index. The blue dashed lines in panels (b) and (c) mark the locations of the Durgapur and Rondiha Barrages.

In Zone 3 (Reaches 7a–14), downstream of the Rondiha Barrage, the sinuosity index reflects the natural variability expected in less disturbed river systems. Reaches such as 7b display sinuosity gains of up to 11%, while others, like Reach 10, exhibit a 14% decrease, reflecting a tendency toward channel straightening. This heterogeneity corresponds with the relatively preserved, though somewhat reduced, braiding regime in the downstream reaches. The diverse responses in this zone suggest that the river retains greater morphological freedom in the absence of immediate structural constraints.

Importantly, the temporal phasing of sinuosity changes supports the interpretation of barrage-induced impacts. In Zone 1, adjustments in sinuosity typically lagged behind major braiding index collapses by approximately 5–7 years. Peaks in sinuosity change align with periods of operational changes in the barrages, particularly around 2005 and 2020, before the system reached a new equilibrium state.

3.4.2.1.6. Bar Area/Channel Area Ratio

The bar area/channel area (BA/CA) ratio reveals notable spatiotemporal variations across the Damodar River's three management zones, illustrating the distinct morphological responses to flow regulation and sediment dynamics.

In Zone 1 (Reaches 1a–4d), upstream of the Durgapur Barrage, the BA/CA ratio shows dramatic declines, particularly after 2000. Reach 4d experienced the most significant reduction, collapsing from 0.16 in 1988 to 0.03 in 2023, a five-fold decrease, indicating near complete loss of active bars. Reach 4c also demonstrated considerable fluctuation in its ratio, ranging from 0.36 to 2.60 before stabilizing at 0.48 in 2023, suggesting persistent instability (Fig. 3.24).

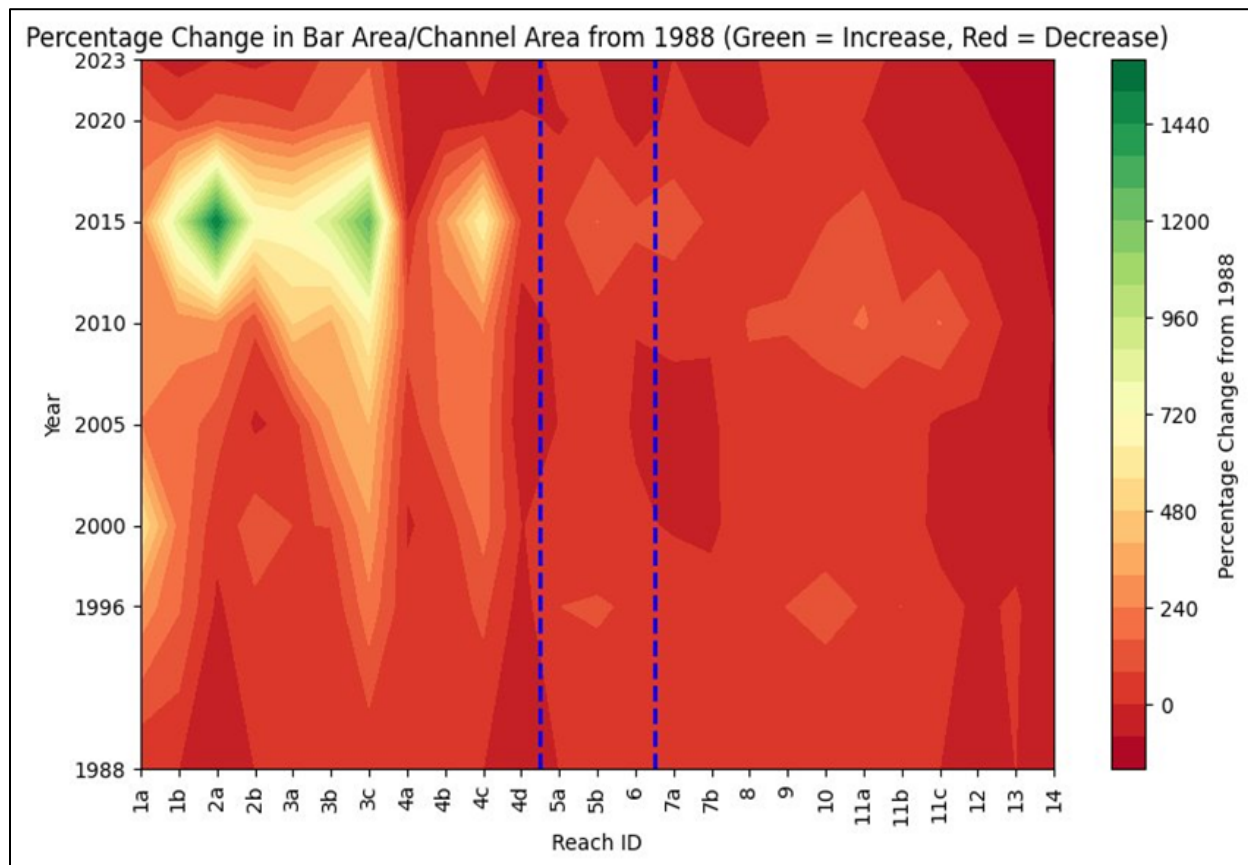


Figure 3.24: Percentage change in BA/CA index relative to the reference year 1988. The blue dashed lines in panels mark the locations of the Durgapur and Rondiha Barrages.

These changes align with the zone's braiding index losses, confirming the channel simplification driven by sediment starvation caused by upstream dam operations. In Zone 2 (Reaches 5a–6), situated between the two barrages, the BA/CA ratio exhibits transitional behavior. Reach 5b's ratio peaked at 3.97 in 2015 before dropping to 1.50 in 2023, while Reach 6 maintained moderate values, ranging from 0.64 to 2.48, indicating intermittent sediment bypass. The 2015 spike in

multiple reaches, such as Reach 4b's increase to 5.91, may be associated with operational changes at the Durgapur Barrage.

In Zone 3 (Reaches 7a–14), downstream of the Rondiha Barrage, the BA/CA ratio remained higher but exhibited a general decline. Reach 7b's ratio halved from 3.64 in 1988 to 2.44 in 2023, while Reach 14 experienced a catastrophic 99% reduction, from 3.76 to 0.004, signaling extreme sediment starvation in the lowest reaches.

Key temporal trends include relative stability in most reaches before 2000, volatile fluctuations between 2000 and 2015 (e.g., Reach 4b's surge to 5.91), and system-wide declines post-2015, especially in Zones 1 and 3. These patterns suggest that the Damodar's active sediment storage capacity has been most severely degraded immediately upstream of the Durgapur Barrage, with impacts diminishing, but not disappearing, downstream. The BA/CA ratios further complement prior findings on braiding and sinuosity, collectively depicting a river transitioning toward a simpler, less dynamic morphology.

3.4.2.2. *Spatio-temporal Analysis of Sone River Morphology*

3.4.2.2.1. *Morphological changes in Window 1: Downstream of Indrapuri Barrage*

The reaches downstream of Indrapuri Barrage experienced significant morphological transformations between 1988 and 2023 (Fig. 3.25a). Sand bars initially expanded from 19.15 km² in 1988 to a peak of 28.02 km² by 2005 (+46%), followed by a sharp decline to 14.95 km² by 2023 (-22%). The most rapid loss occurred between 2005-2010 (-13.07 km²), coinciding with intensified sand mining activity. Mid-channel sand bars showed an even more dramatic reduction, decreasing from 16.47 km² (1988) to just 1.79 km² (-89%) by 2023. The conversion of these mid-channel features into lateral side bars was most pronounced during 2000-2005, when approximately 4.68 km² transformed. Mid-channel vegetated bars initially increased from 5.46 km² (1988) to 8.17 km² (+50%) by 2000, before nearly disappearing (-87%) by 2010, indicating complete loss of vegetated mid-channel features after this period. In contrast, vegetated bars along the channel margins expanded substantially from 3.23 km² to 16.08 km² (+398%), with the most rapid growth occurring between 2005-2010 (+14.17 km²). The wet channel contracted by

47%, from 13.37 km² to 7.05 km², with extreme narrowing during 2005-2010 (-8.34 km²), reflecting reduced flow capacity due to sediment accumulation (Fig. 3.25 b).

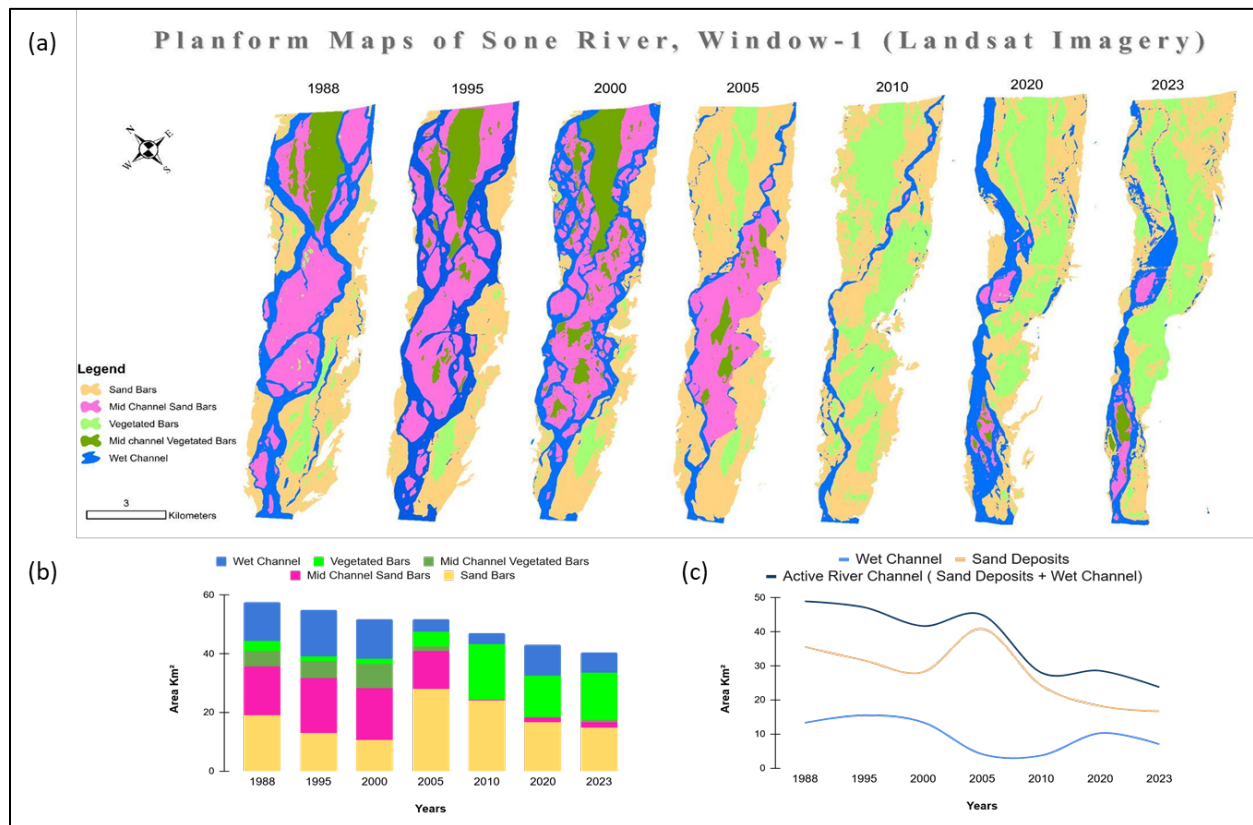


Figure 3.25: (a) Spatiotemporal planform maps of window 1 of the Sone River, derived from Landsat imagery. Zone 1, (b) Changes in morphological classes, and (c) illustrating morphological changes in wet channels, sand deposits, and area of active River channel over time.

When examining sand deposits (sand bars + mid-channel sand bars), the area peaked at 40.86 km² in 2005 before declining to 16.75 km² (-59%) by 2023. This trend inversely correlated with wet channel changes during 2005-2010, when sand deposits increased by 12.62 km² while the wet channel contracted by 8.34 km², demonstrating how sediment accumulation reduces channel capacity. The active channel area, which combines both sand deposits and wet channel, decreased from 48.99 km² to 23.80 km² (-51%), with the most severe reduction (-18.49 km²) occurring during 2005-2010. This confirms significant river degradation, as the active channel's composition shifted from being dominated by dynamic sediment features (67% in 1988) to more stable vegetated margins (70% by 2023). The complete conversion of mid-channel bars to lateral

features by 2015 marks a fundamental change in channel morphology from a braided towards a single-thread system (Fig. 3.25c).

3.4.2.2.2. *Morphological changes in Window 2: Mid-Reach*

The middle section of the Sone River displayed different but equally important morphological changes. Sand bars here fluctuated between 20.53 km² (2020) and 34.01 km² (2010), ultimately decreasing by 12% to 25.05 km² by 2023 (Fig. 3.26a). The 2010 peak coincided with increased sediment supply from upstream mining activities. Mid-channel sand bars reduced from 3.45 km² (1988) to 0.70 km² (-80%) by 2023, with complete conversion to side bars occurring during 2015-2020 (1.50 km² transformed). Mid-channel vegetated bars were completely eliminated after 2005, declining from 0.39 km² to 0 km², while vegetated bars along the banks increased steadily from 2.46 km² to 6.25 km² (+154%). The wet channel showed more stability than Window 1, narrowing by just 17% from 16.10 km² to 13.33 km², but with a notable temporary expansion during 2015-2020 (+9.08 km²) following sediment releases from upstream (Fig. 3.26b).

Sand deposits in this transitional zone remained relatively stable (31.79-36.15 km²) until 2015 before declining to 25.75 km² (-19%) by 2023. The relationship with wet channel area was particularly evident during two periods: (a) 2005-2010, when sand deposits increased (+3.09 km²) as the wet channel contracted (-5.76 km²), and (b) 2015-2020 when sand deposits decreased (-7.52 km²) as the wet channel expanded (+9.08 km²).

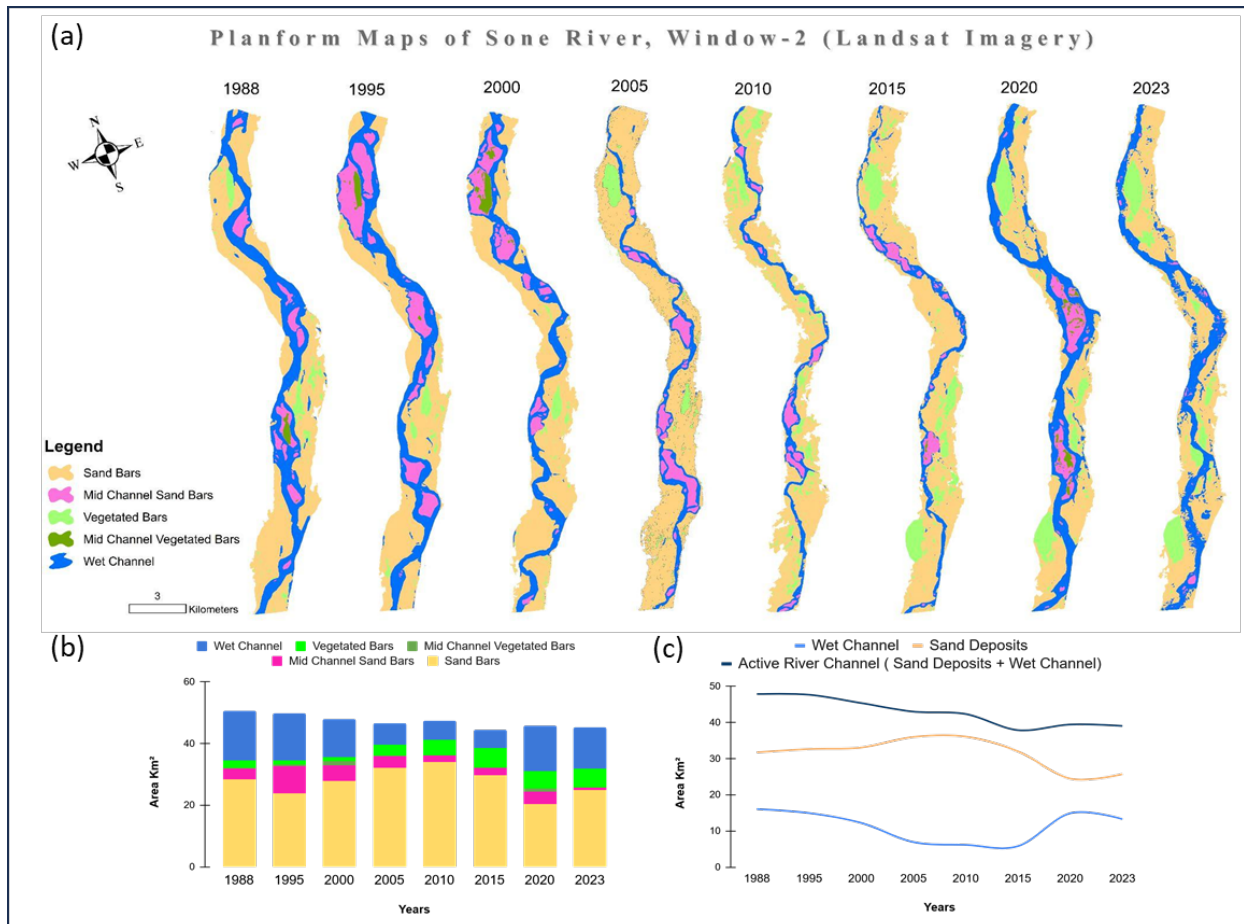


Figure 3.26: (a) Spatiotemporal planform maps of window 2 of the Sone River, derived from Landsat imagery. Zone 1, (b) Changes in morphological classes, and (c) illustrating morphological changes in wet channels, sand deposits, and the area of the active river channel over time.

The active channel area decreased moderately by 18% from 47.89 km² to 39.08 km², with the most significant change (-5.76 km²) during 2015-2020. Unlike Window 1, this reach maintained higher sediment deposit percentages (66-82% of active channel area), indicating better sediment transport continuity. However, the complete transformation of mid-channel features by 2020 and increasing vegetation encroachment suggest growing channel simplification pressures. The delayed response compared to Window 1 (major changes occurring post-2015 rather than 2005-2010) reflects its transitional position in the river system (Fig. 3.26c).

3.4.2.2.3. Morphological changes in Window 3: Lower Reach

The downstream terminus exhibited the most extreme transformations. Sand bars catastrophically declined by 87% from 8.20 km² (1988) to 1.03 km² (2023), with accelerated loss (-7.61 km²) after 2015 (Fig. 3.27a). Mid-channel sand bars nearly vanished (-99.7%), decreasing from 6.68 km² to just 0.02 km², with complete conversion by 2015 - the earliest complete loss among all windows.

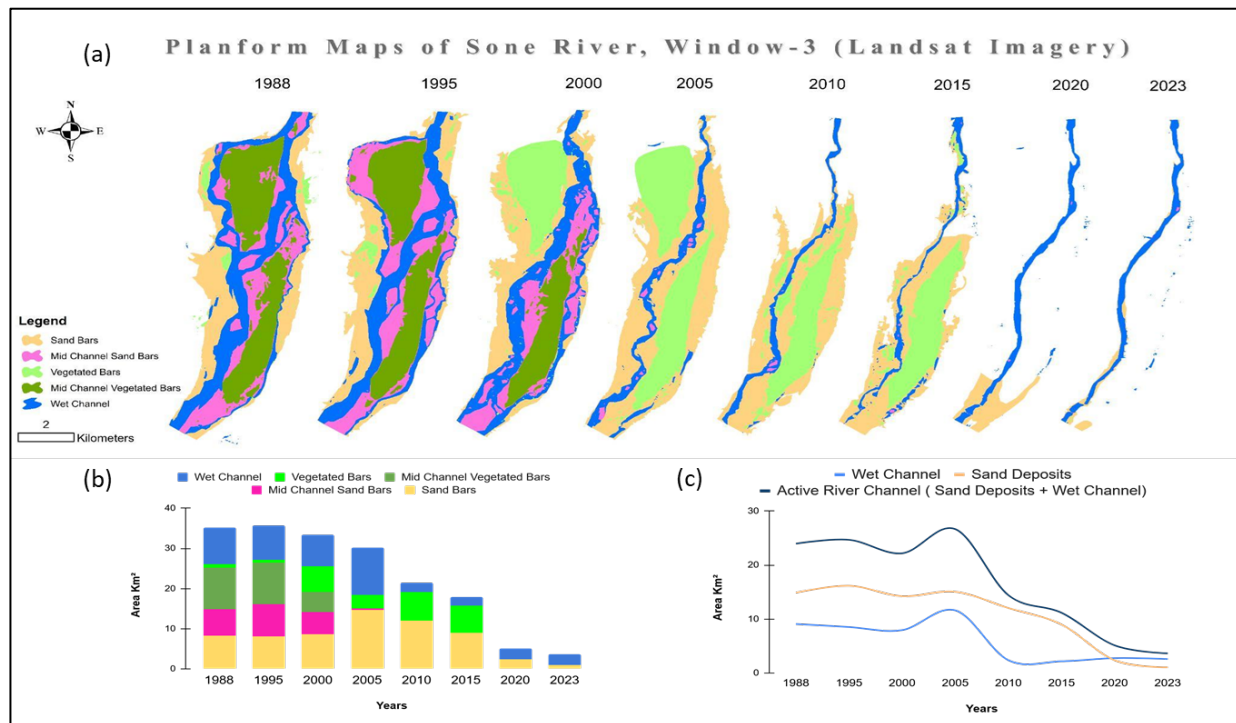


Figure 3.27: (a) Spatiotemporal planform maps of the window 3 of the Sone River, derived from Landsat imagery. Zone 1, (b) Changes in morphological classes, and (c) illustrating morphological changes in wet channels, sand deposits, and the area of the active river channel over time.

Mid-channel vegetated bars were eliminated by 2005 (from 10.34 km² to 0 km²), while vegetated bars along the margins fluctuated before disappearing completely by 2020, unlike the other windows where they expanded. The wet channel collapsed by 72% from 9.09 km² to 2.59 km², with the most severe contraction (-9.24 km²) during 2010-2015 when mining activity intensified (Fig. 3.27b).

Sand deposits decreased by 93% from 14.88 km² to 1.05 km², showing an extreme version of the inverse relationship with wet channel area observed in other windows. During 2005-2010, a temporary 3.67 km² wet channel expansion occurred alongside mining-induced sediment removal, while the 2010-2015 period saw both sediment loss and wet channel contraction. The active channel area suffered devastating 85% reduction from 23.97 km² to 3.64 km², with 67% of this loss (-6.04 km²) occurring during 2015-2023. The most alarming aspect is the complete breakdown of the normal sediment-wet channel relationship - by 2023, sediment deposits comprised only 29% of the active channel (versus 62% in 1988), indicating transformation from a natural sediment-transporting system to an artificial mining-dominated channel (Fig. 3.27c). Unlike Windows 1-2 where some ecological succession occurred, Window 3 shows complete geomorphic disruption with no natural recovery mechanisms remaining.

3.4.2.2.4. *Braiding Index (BI)*

In window 1, the braiding index exhibited dramatic fluctuations, decreasing from 4.16 (1988) to 1.46 (2010) before partial recovery to 2.17 (2023). This 65% reduction in BI correlates strongly with the documented loss of mid-channel bars (-89%) and active channel contraction (-51%). The most severe decline occurred during 2000-2005 (BI dropped from 5.13 to 2.12) (Table 3.6), precisely when satellite imagery shows complete conversion of 4.68 km² of mid-channel bars to lateral features. While BI showed minor recovery post-2010, values remain below half of 1988 levels, confirming the transition from a multi-thread braided system to a predominantly single-thread channel.

The Window 2 displayed more moderate braiding reduction from 2.12 (1988) to 1.58 (2023), consistent with its 18% active channel loss. The BI remained relatively stable until 2015, then fluctuated with mining activity - notably increasing to 2.05 (2020) during peak sediment releases before declining again (Table 3.6). This pattern matches the observed 2015-2020 expansion of wet channel area (+9.08 km²) and temporary mid-channel bar resurgence. However, the 2023 BI value (1.58) confirms the reach has lost 26% of its original braiding complexity.

Window 3 shows the most consistent BI decline, plummeting 64% from 2.87 (1988) to 1.04 (2023). The disappearance of mid-channel bars (-99.7%) directly corresponds to BI reductions,

particularly the steep 2000-2005 drop (3.08→1.67) when mining intensified. Unlike other windows, no recovery occurred post-2015, with BI values stabilizing near 1.0 - indicating complete loss of braiding characteristics and validation of the observed channel simplification to a single-thread system (Fig. 3.28).

Table 3.6: Showing Braiding and Sinuosity Index value across three study windows of the Sone River.

Years	W1		W 2		W 3	
	BI	SI	BI	SI	BI	SI
1988	4.16	1.22	2.12	1.17	2.87	1.16
1995	4.20	1.28	2.21	1.20	2.98	1.11
2000	5.13	1.33	2	1.30	3.08	1.19
2005	2.12	1.31	1.65	1.29	1.67	1.18
2010	1.46	1.30	1.58	1.31	1.05	1.14
2015	NA	NA	1.65	1.32	1.04	1.12
2020	2.32	1.26	2.05	1.24	1.07	1.10
2023	2.17	1.26	1.58	1.30	1.04	1.09

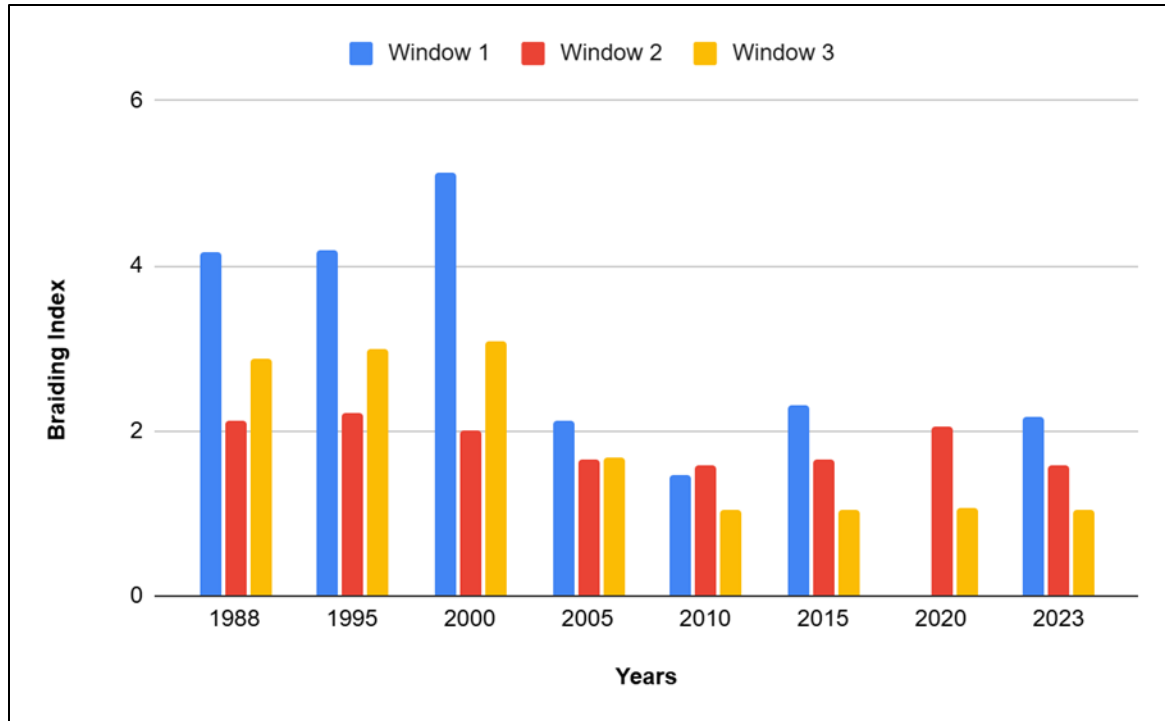


Figure 3.28: Showing Braiding Index value across three study windows of the Sone River.

The Cross-Window Comparison in the Sone River suggests the following:

- All windows show $\geq 64\%$ BI reduction, but timing differs: Window 1 (2000-2005), Window 2 (post-2015), Window 3 (continuous)
- BI declines correlate strongly with mid-channel bar loss.
- Mining impacts are clearest in Window 3 where BI reached near-minimum values (1.0)

3.4.2.2.5. Sinuosity Index (S_i)

Window 1 maintained remarkably stable sinuosity (1.22 ± 0.06), despite massive braiding changes. The 2000 peak (1.33) corresponds with maximum mid-channel vegetated bar extent (8.17 km^2), while the 2023 value (1.26) reflects the balance between forced channel straightening from barrage flows and meander development in stabilized sections (Table 3.6, Fig. 3.29). This stability confirms that while braiding complexity collapsed, the fundamental channel alignment remained constrained by geological controls.

Window 2 exhibited greater sinuosity variability (1.17-1.32), peaking in 2015 (1.32) when mining-induced sediment pulses temporarily reactivated secondary channels. The 2020 dip (1.24) followed channelization efforts, while the 2023 recovery (1.30) suggests natural meander re-establishment in less disturbed sections (Table 3.6, Fig. 3.29). These fluctuations align with observed wet channel expansions/contractions, demonstrating how sediment supply variations affect meander development in transitional zones.

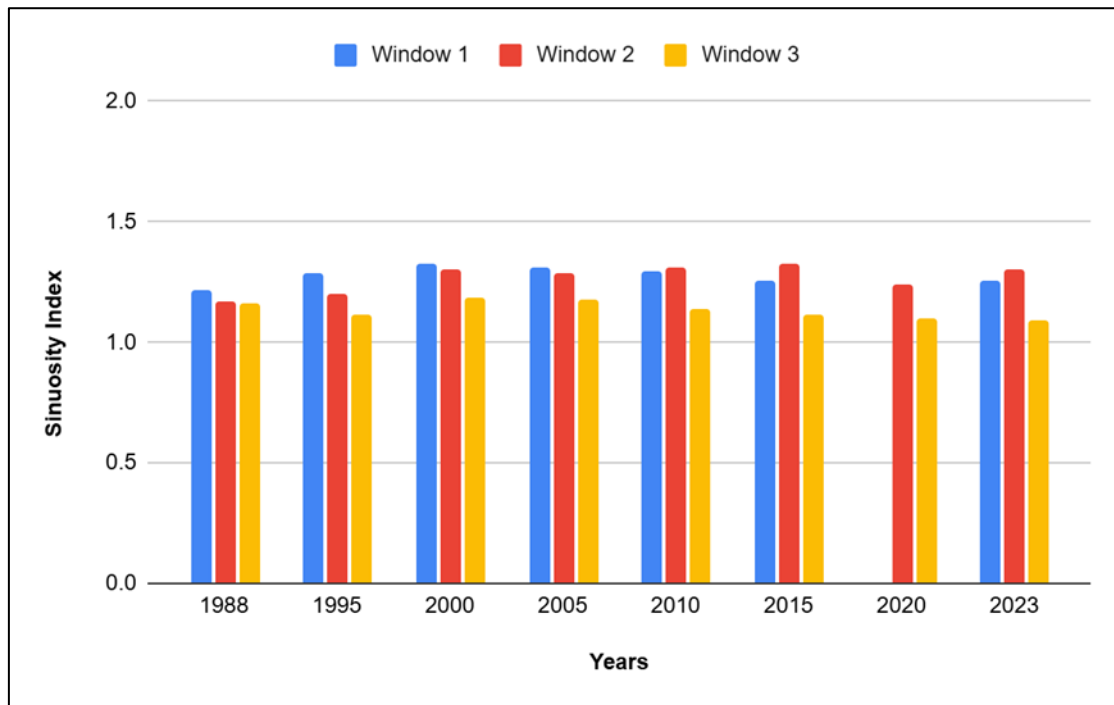


Figure 3.29: Sinuosity Index value across three study windows of the Sone River

Window 3 displayed consistent sinuosity reduction from 1.16 (1988) to 1.09 (2023), directly tracking with mining intensity. The most significant drops occurred during active mining periods: 2000-2005 (1.19→1.18) and 2010-2015 (1.14→1.12). Unlike Windows 1-2, this reach shows no recovery potential, with 2023's record low (1.09) confirming the straightening observed in satellite imagery (Table 3.6, Fig. 3.29).

The main observations, integrating the results from all windows, suggest the following:

- Braiding and sinuosity changes show spatial progression: barrage effects dominate Window 1, transitional dynamics in Window 2, and mining impacts in Window 3.
- BI better indicates system degradation (64-65% reductions), while SI reflects local channel stability.
- The 2015-2020 period emerges as critical for all windows, showing either:
 - Temporary BI recovery (Window 2) from sediment pulses
 - Accelerated decline (Window 3) from mining
 - Stabilization (Window 1)

3.4.2.2.6. *Bar Area/Channel Area Ratio*

The Bar Area to Channel Area (BA/CA) ratio in the Sone River's Window 1 (downstream of Indrapuri Barrage) reveals dramatic morphological changes driven by sediment dynamics (Fig. 3.30). The ratio peaked at 9.84 in 2005, a 270% increase from 1988 levels, reflecting intense sediment deposition and bar formation immediately below the barrage. This was followed by a decrease by 82% to 1.77 by 2020 as mining intensified and the system adjusted, ultimately stabilizing at 2.37 by 2023. These extreme fluctuations (2.03-9.84) demonstrate how barrage operations first enhance then diminish braiding intensity, with the partial recovery indicating limited bar-forming capacity despite significant channel simplification from braided to single-thread morphology.

In Window 2, the transitional mid-reach, BA/CA showed more moderate variation (1.97-5.80), maintaining characteristics of an active braided system. The 2010 peak (5.80) coincided with maximum sand bar extent (34.01 km²) and wet channel contraction, while subsequent declines mirrored mining-induced sediment pulses. Unlike Window 1, this reach preserved greater stability (final BA/CA 1.93 vs 1.97 in 1988) and sediment transport capacity, though the 66% reduction from peak values confirms progressing simplification. The maintained BA/CA >1.5 suggests this zone still functions as a vital sediment conveyor between upstream barrage effects and downstream mining impacts.

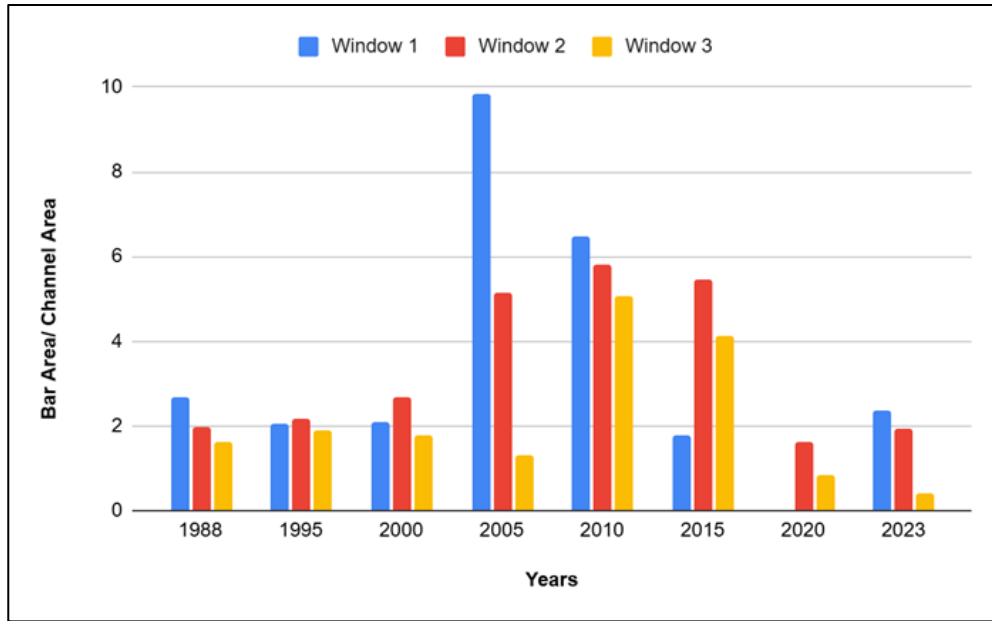


Figure 3.30: Bar area/ channel area Index value across three study windows of the Sone River.

In Window 3, the sharp decline in BA/CA ratio from 1.64 (1988) to 0.40 (2023) marks the most severe degradation, signalling complete braiding loss in this mining-dominated reach. The 2010 spike (5.07) represented temporary bar exposure during peak mining, while the terminal decline to sub-1.0 values confirms irreversible conversion to a non-braided, mining pit morphology. This 76% reduction correlates perfectly with other degradation indicators - 99.7% mid-channel bar loss, 85% active channel contraction, and BI reduction to near-minimum (1.04). The BA/CA <0.5 threshold in Window 3 demands urgent intervention to prevent total loss of fluvial functionality in this critical confluence zone.

3.5. Linking morphological changes to sand mining and flow regulation

3.5.1. Hotspots of mining

The spatiotemporal analysis conducted in this study demonstrates that sand mining is exerting significant pressure on the morphological integrity of river systems, with particularly pronounced impacts in specific hotspot zones. Among the key insights is identifying mining hotspots, where both the intensity and expansion of mining activities are exceptionally high. These hotspots are

not randomly distributed but are strongly associated with certain geomorphic features, especially sand bars, active channel belts, and floodplain zones, which are naturally depositional and hence preferred for extraction. The Damodar River's Zone 3 emerges as the most heavily impacted, particularly Reaches 9 to 12, which collectively form a continuous belt of high-intensity mining. Reach 10, for instance, reached a peak mining intensity of 0.736 in 2023, the highest recorded in the study, and was classified under the “Critical” category in the vulnerability assessment. This is indicative of unsustainable extraction rates and ongoing geomorphic destabilisation.

Similarly, in Zone 2, Reaches 5b and 6 along the Damodar River showed alarming growth rates, exceeding 200% over five years, making them emerging hotspots. Although the current mining intensity in these reaches is moderate compared to Zone 3, the rapid increase in mining footprint indicates that these areas could soon cross critical thresholds, if unregulated. This pattern of sudden surge in mining intensity, followed by brief dips or shifts in spatial focus, may be reflective of variable enforcement, local availability of extractable material, or economic drivers such as construction demand.

The Sone River also displayed notable spatio-temporal variability in mining hotspots. In Window 2, for example, the mining-impacted wet channel grew almost 10-fold between 2016 and 2023, while in Window 3, over 46% of the floodplain area was impacted by mining by 2023. This shift of extraction from mid-channel bars to floodplain areas raises further ecological concerns, as floodplains play a vital role in nutrient cycling, flood mitigation, and groundwater recharge.

The vulnerability index developed in this study offers a nuanced way to categorise and prioritise reaches for intervention. By accounting for both long-term intensity and recent growth rates, the index highlights not just the most degraded zones but also those undergoing rapid change, which are often early warning signs of future degradation. Such zones require proactive attention to prevent irreversible morphological transformation.

From a management perspective, these identified hotspots provide a basis for zoning and regulation. Protected reaches such as 4d, 7a, and 14, where no mining was recorded, can serve as ecological baselines for comparison and could be designated as reference sites or conservation

zones. Meanwhile, critical and very high-risk reaches demand immediate regulatory intervention, possibly including extraction limits, seasonal bans, or active restoration projects. As mining continues to expand in response to infrastructure growth and economic demand, river systems like the Damodar and Sone will require vigilant monitoring. Timely identification and regulation of emerging hotspots are essential to maintaining fluvial stability and ensuring the long-term health of riverine ecosystems.

This study offers several methodological advantages that strengthen the reliability and relevance of its findings. One of the key strengths lies in the integration of manually digitized mining footprints from high-resolution Google Earth imagery with geomorphic features classified through the Google Earth Engine (GEE) platform. This overlay approach allowed for highly accurate identification of the location, type, and geomorphic association of sand mining activities. It enabled a detailed assessment of whether mining occurred within active channel belts or across floodplain areas—information critical to understanding geomorphic vulnerability. Furthermore, the use of multi-temporal and multi-source datasets, including Landsat, Sentinel-2, and Google Earth imagery, ensured broad temporal coverage. The choice of pre-monsoon satellite scenes minimized cloud and vegetation interference, improving the accuracy of feature extraction. Additionally, the methodological workflow, combining cloud-based processing, spectral index classification, and vulnerability scoring, is not only robust but also scalable and reproducible for other river systems undergoing similar pressures.

However, the study is not without limitations. A major constraint was the limited availability of historical high-resolution imagery across the full study area. This restricted the precision of mining footprint mapping for earlier years, particularly before 2010, reducing the temporal depth of the analysis. While public satellite datasets like Landsat and Sentinel are valuable for long-term monitoring, their spatial resolution (10–30 meters) is not sufficient to detect small or dispersed mining sites, especially within narrow or vegetated river corridors.

3.5.2. Impact of sand mining and flow regulation on river planform

The long-term analysis of planform and morphometric changes in the Damodar and Sone Rivers reveals distinct spatial and temporal responses that closely correspond with the location of sand mining hotspots and major flow regulation structures. The use of Google Earth Engine (GEE) and RivGraph has enabled a consistent and objective assessment of channel evolution from 1988 to 2023, providing new insights into the geomorphic consequences of intensified human interventions.

One of the most striking findings is the strong spatial correlation between mining hotspots and zones of significant planform degradation. In particular, Zones 2 and 3 of the Damodar River and Windows 1 and 3 of the Sone River, previously identified as areas of intense sand mining, have experienced the most severe reductions in mid-channel bar area, braiding index, and active river channel area. These reaches also show increasing channel simplification, often transitioning from multi-thread to single-thread morphologies. For instance, Window 3 in the Sone lost over 90% of its mid-channel sand bars, while also recording substantial reductions in active river channel area and braiding complexity.

Interestingly, in recent years, a reversal in wet channel trends has been observed in certain mining-dominated reaches, particularly downstream of mining hotspots. Despite long-term active river channel narrowing, the wet channel area has expanded between 2015 and 2023 in reaches such as 13–14 in Damodar. This widening is not a sign of recovery, but rather a symptom of pit capturing (Fig. 3.31), where the river re-occupied previously mined pits due to increased erosive power. Sand extraction removes in-channel sediment and reduces bed resistance, leaving the river sediment-starved. As a result, flowing water carries more energy and begins to erode banks and pit edges, leading to lateral expansion of the wet channel. These changes are especially visible in the lower reaches of both rivers, where the braided morphology has collapsed and isolated pits now act as preferential flow paths during high discharge.

While wet channel widening might appear to increase flow capacity locally, it is accompanied by a dangerous overall narrowing of the active river channel, which includes all depositional zones

such as sand bars and wet channels. The reduction in active river channel area is especially severe in Reaches 12–14 of the Damodar, where losses exceed 50%, and in Window 3 of the Sone, where over 85% of the active corridor has been lost since 1988. This trend has serious implications for flood management and groundwater sustainability.

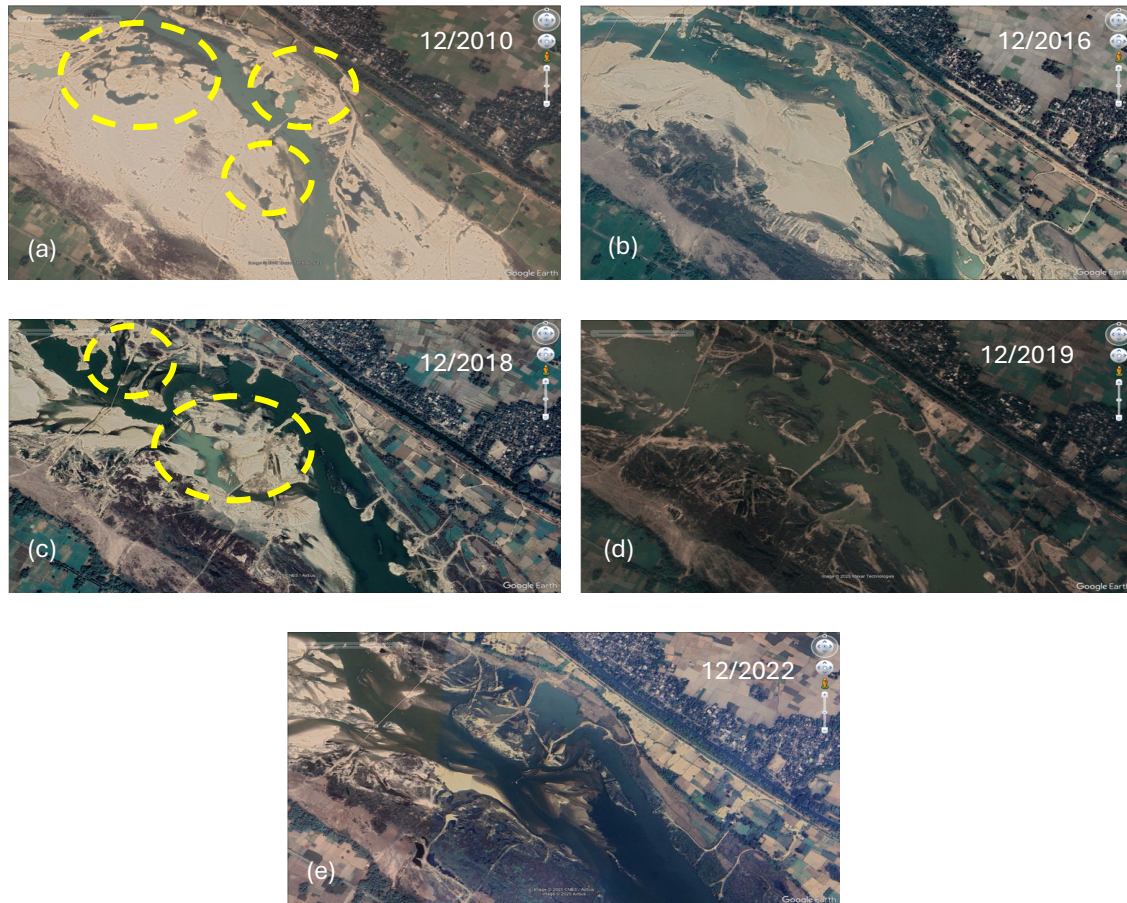


Figure 3.31: High-resolution Google Earth imagery from post-monsoon periods (images a–e; year and month labelled) showing progressive pit capturing by the wet channel in a sand mining-impacted downstream reach of the river. Red circles highlight the location of mining pits being reoccupied by flow in subsequent years. The sequence illustrates how flow gradually reoccupies mining pits due to erosion and channel incision, driven by sediment-starved ("hungry") water. Over time, the wet channel widens laterally, encroaching into the former pit area. This process demonstrates the downstream geomorphic instability induced by intense sand mining activity.

Firstly, the narrowing of the active river channel limits the river's ability to dissipate floodwaters over a wider geomorphic corridor. Previously active bars and floodplains, now abandoned or converted to side bars or vegetated patches, no longer function as overflow buffers. This increases the risk of bank overtopping and unregulated lateral erosion during peak flows, especially in reaches that have lost their natural braiding and meandering capacity. Secondly, the loss of

depositional zones and bar areas reduces the interface between surface water and the floodplain aquifer. These geomorphic features are crucial recharge zones where floodwaters percolate into the subsurface. Their reduction implies a decline in natural groundwater replenishment, further compounded by the channel incision observed in earlier chapters.

These findings are consistent with earlier literature that has identified sand mining and flow regulation as major disruptors of fluvial geomorphology. For example, studies on the Mayurakshi and Yamuna Rivers have highlighted how sand removal and sediment trapping by barrages lead to channel incision, bar disappearance, and increased vulnerability to floods (Islam et al., 2025, Yadav et al., 2023). The present analysis confirms these patterns with long-term, spatially explicit data, while also adding new insights on pit-induced channel reoccupation and active river channel contraction.

Moreover, the morphometric indicators such as braiding index (BI), sinuosity index (SI), and bar-to-channel area ratio (BA/CA) all demonstrate progressive simplification and fragmentation, particularly near the Durgapur and Rondiha Barrages in Damodar and the Indrapuri Barrage in Sone. The upstream barrages restrict sediment flow, exacerbating downstream erosion and promoting bar erosion. In contrast, some middle reaches, like Reach 6 (Damodar) and Window 2 (Sone), show temporary morphological recovery likely due to episodic sediment supply or operational changes in dam release schedules. However, these improvements are limited and not sustained.

In conclusion, this study establishes a clear linkage between observed planform changes and the spatial distribution of mining activity and flow regulation infrastructure. The downstream effects of sediment removal are evident in both the simplification of river geometry and the functional degradation of active corridors. The combination of pit erosion-driven wet channel widening and narrowing of the broader active river channel presents a dual challenge: increasing erosion risk while reducing ecological and hydrological functionality. Addressing this requires a systemic shift in river management—from viewing rivers as extractive landscapes to treating them as dynamic geomorphic systems. Restoration strategies must focus on regulating sediment budgets, protecting mid-channel features, and allowing rivers sufficient lateral space to adjust within safe

geomorphic limits. The methodology adopted in this study represents a significant advancement over earlier approaches that relied heavily on manual digitisation of river planforms. Previous studies on the Damodar and Sone Rivers often used visual interpretation of satellite imagery in GIS environments to delineate river channels and associated features—a process that was not only time-consuming but also subjective, prone to inconsistency across years or interpreters. In contrast, the integration of Google Earth Engine (GEE) with the RivGraph Python library allowed for a more automated, scalable, and objective analysis of planform dynamics. GEE facilitated rapid access to a multi-year archive of Landsat imagery, enabling consistent application of indices like NDWI and NSI for accurate water body and sandbar detection across seasons. These outputs served as standardised inputs for RivGraph, which extracted river centrelines and calculated morphometric metrics (e.g., braiding index and sinuosity index) in a reproducible and statistically robust manner. This automation reduced operator bias and allowed for the analysis of a larger number of reaches—25 in total and 3 windows across both rivers, which would be logistically infeasible using traditional digitization. By leveraging this integrated, semi-automated pipeline, the present study enhances the spatial and temporal resolution of planform change detection and provides a more rigorous foundation for linking morphodynamics with anthropogenic pressures such as sand mining and flow regulation.

3.5.3. Geomorphic impacts of sand mining in peninsular rivers— a process response framework

Sand mining and flow regulation exert significant and interrelated influences on river morphodynamics. Sand mining leads to the direct extraction of sediment from the riverbed, thereby disrupting the river's sediment budget and dynamic equilibrium. Simultaneously, flow regulation structures such as dams and barrages trap sediment upstream, further reducing the downstream sediment supply. The combined reduction in sediment availability initiates the hungry water effect, where sediment-starved flows possess excess stream power. This condition promotes bed degradation through channel incision and enhances lateral erosion along the riverbanks. Consequently, the river's morphological stability is compromised.

As sediment inputs decline, the natural processes of sediment replenishment are hindered, resulting in the progressive loss of key geomorphic features such as active channels and mid-channel or lateral sand bars. Flow regulation further reduces discharge variability, often leading to the stabilization of a single-thread wet channel. The reduction in sediment and flow results in channel simplification and a decrease in the number and complexity of braided channels. Moreover, channel incision leads to a drop in water surface levels, which, combined with bar erosion and channel narrowing, contributes to overall morphological simplification. The impacts are particularly pronounced in downstream reaches. During high-flow depositional events, sediment is preferentially deposited upstream of flow regulation structures, such as barrage pools and mining pits, while downstream reaches experience net sediment deficit. This deficit manifests as increased erosion, widening of the wet channel, and loss of depositional features, in contrast to wet channel contraction observed elsewhere (Fig. 3.32).

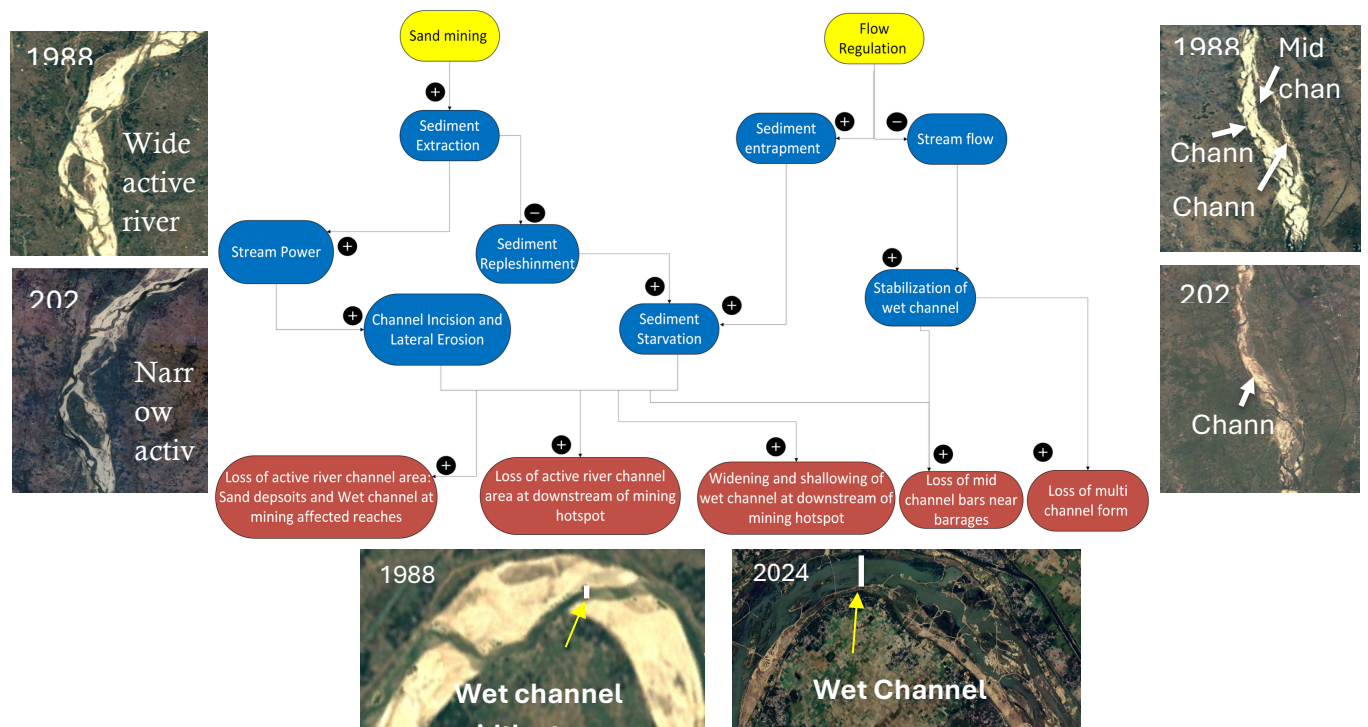


Figure 3.32: The process-response framework of the river demonstrates a positive feedback system under the anthropogenic forcing of sand mining and flow regulation.

3.6. Summary and conclusions

This chapter has involved mapping of sand mining sites in two peninsular river basins, namely Damodar and Sone, using high-resolution Google Earth imagery. Mining areas were classified into dry, wet, and vegetated pits using spectral thresholding techniques (NDVI, NDWI). These classified sites were overlaid on river morphology layers derived from Landsat and Sentinel-2 imagery using Google Earth Engine (GEE) to determine whether mining occurred within channel belts or floodplains. To map sand mining activities, high-resolution Google Earth imagery was interpreted and classified into distinct categories such as dry mining pits, wet mining pits, and vegetated pits using threshold-based classification with spectral indices. Although the manual interpretation process was time-consuming, it provided a high degree of accuracy in detecting mining footprints and their association with river morphology. Based on this mapping, a mining intensity index was calculated for each river reach, representing the proportion of area under mining. To further quantify the pressure and trajectory of mining expansion, a vulnerability index was developed that combines mining intensity and temporal growth rate. This index, scaled from 0 to 1, helped in identifying mining hotspots and reaches at high risk of morphological degradation.

The analysis revealed that most reaches of the Damodar River and windows 1 and 2 of the Sone River are dominated by in-channel mining belt. In contrast, Window 3 of the Sone has been impacted by floodplain mining due to depletion of in-channel sand. Hotspot analysis based on mining intensity identified reaches 9–12 in Damodar and windows 2 and 3 of the Sone River as primary hotspots of mining activities.

The second objective focused on long-term planform change analysis using sub-decadal Landsat data processed through GEE. Efficient and scalable methods were used to extract changes in active river channel, wet channel, and sand deposit areas, as well as bar-to-channel area ratios and metrics such as the sinuosity index and braiding index (using RivGraph). For assessing long-term river planform changes, an automated approach using Google Earth Engine was adopted, enabling efficient and reproducible extraction of river planform features from multi-decadal Landsat imagery. Unlike traditional digitization methods prone to user bias, this approach ensures consistency and scalability across large datasets and extended timeframes. The RivGraph Python library was used to automatically extract the river network from binary water masks, facilitating

the calculation of braiding and sinuosity indices by quantifying centerline length and channel count. Additionally, a custom Python-based algorithm was developed to generate spatiotemporal contour maps of area change, offering a clear visualization of geomorphic hotspots and the progression of planform change over time. These tools collectively provided a robust framework for linking human interventions such as mining and regulation with morphological responses in a spatially explicit and process-informed manner. The analysis showed significant morphological degradation, especially downstream of mining hotspots, with a near-complete loss of sediment bars in Window 3 of the Sone River and severe changes in Zone 3 of the Damodar.

To link these changes with their drivers, a process–response framework was developed, identifying how intensive mining and flow regulation (barrages, reduced sediment supply) lead to channel incision, bar loss, simplification, and changes in wet channel area. This approach provides a reproducible framework to understanding and monitoring the geomorphic impacts of human interventions and supports the development of targeted river restoration strategies.

The major conclusions from this study are as follows:

1. Spatiotemporal sand mining hotspots along with their geomorphological association in both Damodar and Sone rivers suggest that most of the reaches in the identified hotspots have more than 50% of their area occupied by sand mining activities. It emphasizes the urgent need to prioritize these hotspots for monitoring and initiate remediation measures for restoring the river.
2. The severity of impacts from sand mining in both the Damodar and Sone Rivers is evident through extensive morphological degradation observed over time. In some reaches of the Damodar River, a mining intensity as high as 0.8 was documented in recent years (2024) indicating that 80% of its total area was covered by mining activities.
3. A rapid increase on mining activities has been documented in the Damodar River between 2019 and 2024, with several reaches recording 3.5-fold increase in dry mining area and a 2.7-fold increase in wet mining pits, resulting in severe wet channel fragmentation.
4. In the Sone River, major geomorphic impacts of sand mining include loss of channel belt and sand bar areas, and transformation from braided to a single-thread channel system. In some

reaches, nearly 53% of sand bars have been lost, including the near-total disappearance of mid-channel bars.

5. While Windows 1 and 2 in the Sone River exhibit extensive in-channel mining, Window 3 has transitioned to floodplain mining, due to the complete depletion (100%) of sand bars.
6. In both Damodar and Sone Rivers, widespread channel incision, bar erosion, and morphological simplification, which collectively reduce the river's flood buffering capacity, impair floodplain connectivity, and diminish groundwater recharge potential, rendering these reaches highly vulnerable to both hydrological extremes and long-term ecological degradation.
7. The combined effects of sediment extraction through sand mining and sediment entrapment by flow regulation structures significantly reduce the sediment supply downstream. Flow-regulating structures like dams and barrages trap large amounts of sediment upstream, disrupting the natural sediment replenishment process. This sediment deficit is further exacerbated by sand mining, which directly removes sediment from the river system.
8. Sand mining has reduced sediment availability in downstream reaches in two critical ways: firstly, by diminishing the initial sediment supply traveling downstream, and secondly, by creating deep mining pits that act as sediment traps where much of the transported sediment settles and is no longer available to replenish downstream reaches. As a result, downstream reaches become severely sediment-starved.
9. Sediment starvation because of mining triggers the 'hungry water' effect, where sediment-depleted water has increased erosive power, causing channel incision, lowering riverbed levels, and increasing vertical channel space. This has led to significant morphological changes in both Damodar and Sone Rivers, including the loss of sediment bars (lateral erosion) that serve as flood buffers and groundwater aquifers. The loss of these bars and the transformation from multichannel to single-channel morphology reduces channel belt area and degrades floodplain connectivity and ecosystem health.

Chapter 4

4. Impact of sand mining on the sediment dynamics of the Gaula River using CASCADE modelling

4.1. General

Excessive sand and gravel extraction from fluvial systems significantly disrupts sediment transport processes, alters river morphology, degrades aquatic habitats, and lowers groundwater levels. Sediment dynamics are crucial for maintaining nutrient cycles and ensuring morphological and ecological balance in large river systems. When extraction exceeds natural replenishment rates, it disturbs flow regimes and undermines river stability (Hackney et al., 2020), particularly in sensitive environments like ephemeral rivers. Despite growing concern, most existing research is confined to short river stretches, often neglecting catchment-scale sediment connectivity and flux. This oversight is especially critical for rivers such as the Gaula in northwestern India, an ephemeral Himalayan River where approximately 22 km of the channel undergoes annual sand mining. Located in a tectonically active zone, the Gaula experiences intense monsoonal discharges, generating high stream power, causing bed incision and channel narrowing.

To address these challenges, our study adopts an integrated approach that combines SWAT-based hydrological modelling, UAV-derived grain size distribution, and graph-theory-driven CASCADE sediment transport modelling. This framework enables a source-to-sink understanding of sediment connectivity, quantifies spatial variations in sediment flux and highlights geomorphologically vulnerable reaches.

4.2. Approach, data and methodology

The methodological structure of this research comprises three primary elements: (a) river network scale grain size distribution (GSD) analysis, (b) hydrological modelling using SWAT, and (c) sediment transport modelling through CASCADE at the reach scale sediment flux (Fig. 4.1). Sediment response in the upper catchment of the Gaula River is evaluated independently. The lower catchment, characterised by extensive mining activities, is analysed for the impacts of sand

mining. In the hilly upper catchment, the river network was divided into reaches of 1 km in length to account for slope variability in high-altitude (Fig. 4.2a and b).

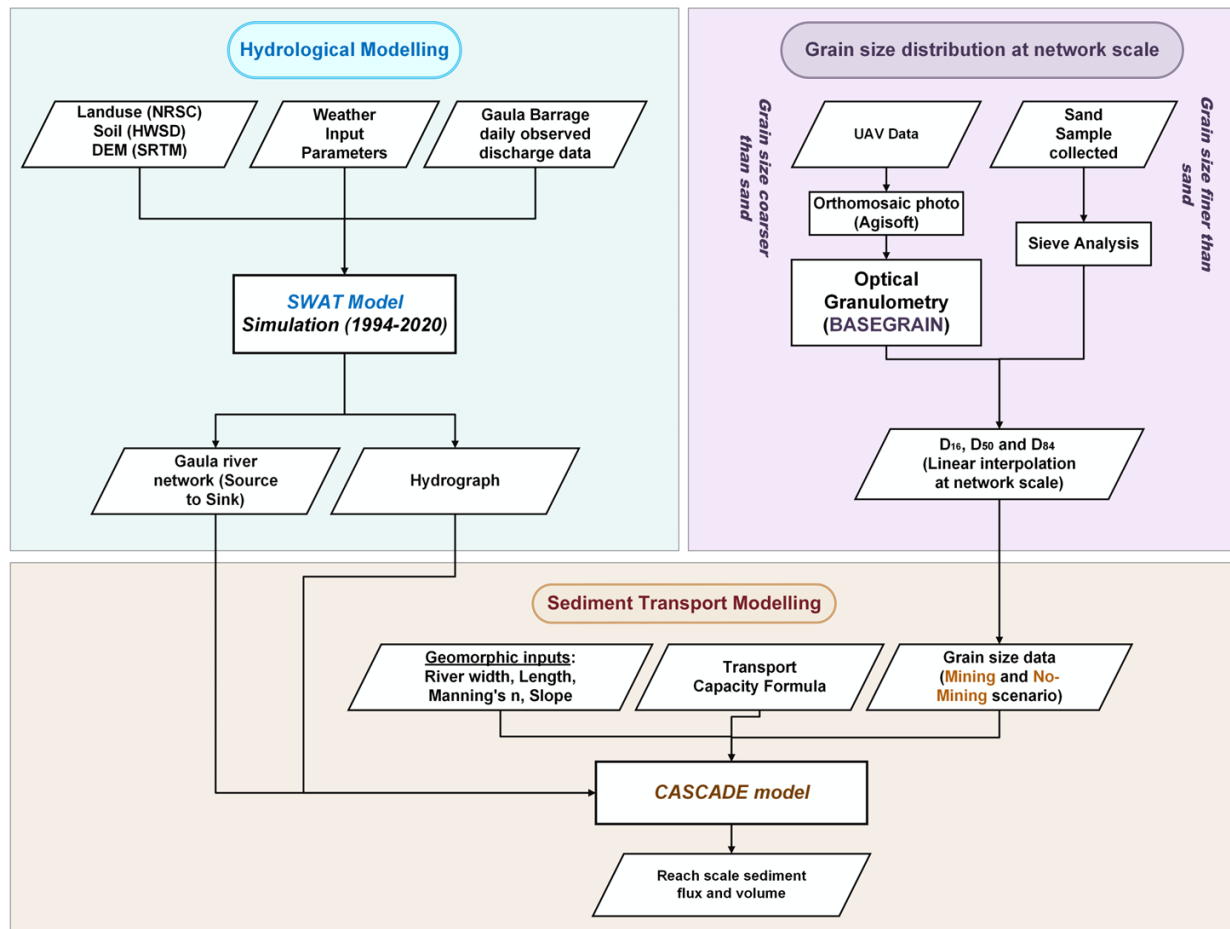


Figure 4.1: Flowchart illustrating an integrated approach of hydrology, GSD size distribution at network scale and their integration with the sediment transport modelling (CASCADE).

zones. In contrast, the lower catchment is divided into 20 reaches of 2 km each, which is appropriate for the foothills and Gaula fan region due to the lower gradient. The hilly upper catchment has an elevation range of 2,557 meters to 530 meters, while the lower catchment, situated in the Gaula fan area, has an elevation range between 530 meters and 139 meters (Fig. 4.2 a, b) (Shukla, 2009). The reach in the upper catchment flows through a narrower valley, whereas the lower catchment features wider valley margins. This geomorphic compartmentalisation significantly influences geomorphic processes, including river dynamics, sediment transport, and evolution (Alexander et al., 2009; Jain et al., 2012; Piégay et al., 2023).

Though the river reach division can influence stream power (Martínez-Fernández et al., 2019), variations in sediment transport and channel morphology further modulate the energy available for erosion and deposition, shaping distinct geomorphic characteristics across different reaches (Wohl et al., 2015).

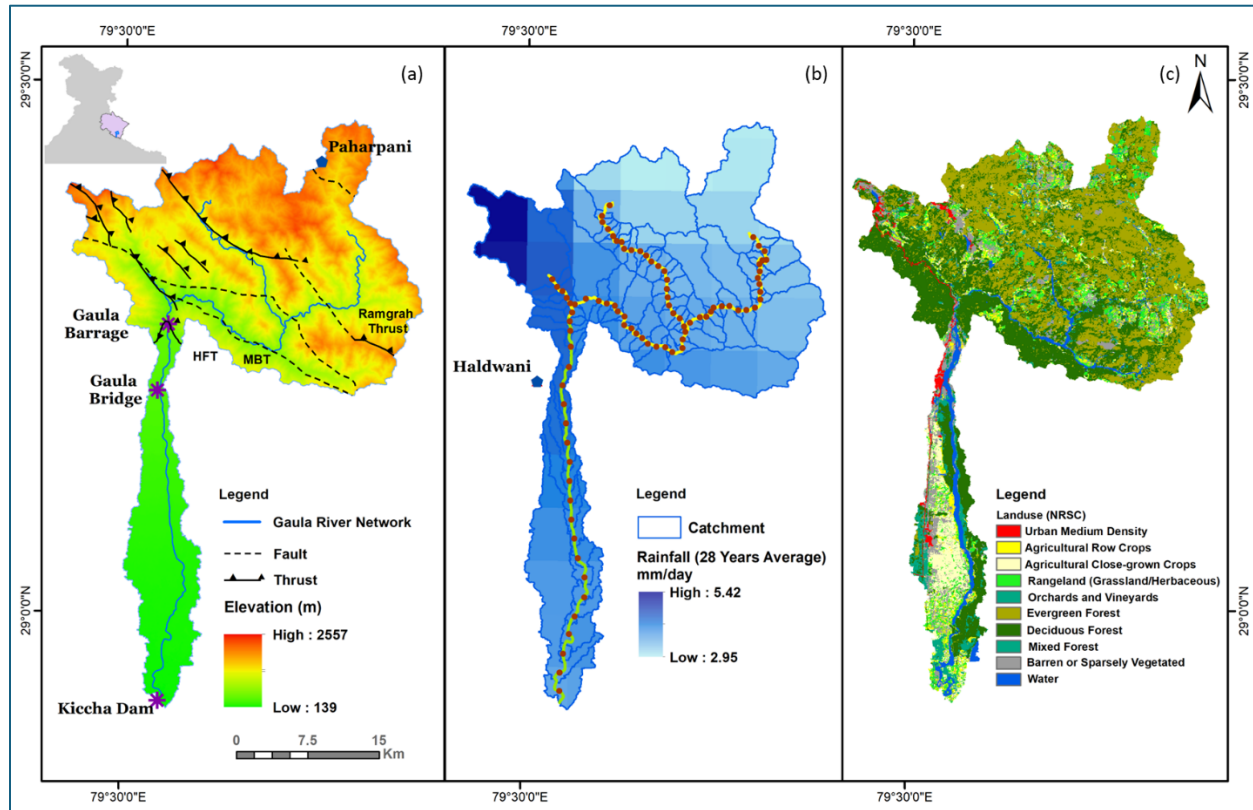


Figure 4.2: Overview of the Gaula River catchment showing key physical and hydrological features (a) Digital Elevation Model (DEM) of the Gaula catchment illustrating terrain variability, river network, and major tectonic structures, including mapped thrusts and faults. (b) Spatial distribution of average rainfall across the catchment with demarcated river reaches divided at 1 km intervals in the upper catchment and 2 km intervals in the lower catchment for hydrological and geomorphic analysis. (c) Land use and land cover map of the Gaula catchment, highlighting forested areas, agricultural zones, urban settlements, and riverine features relevant to sediment source and transport processes.

4.2.1. Drone-based granulometry

The grain size in riverbed materials is crucial in sediment transport dynamics. Larger particles require higher flow velocities for mobilisation, while finer sediments can be suspended at lower velocities. This natural sorting process influences sediment deposition patterns and overall river morphology. Our study examined grain size variations under mining and no-mining conditions to assess the impact of sand mining on sediment flux and connectivity. In March and December

2022, high-resolution drone imagery was captured to document these conditions. The images were processed into orthorectified and scaled formats using Agisoft Metashape (Figure 4.3), enabling precise grain size extraction on hyper-spatial images. Grain size analysis was performed using BASEGRAIN, a MATLAB tool designed for top-view image analysis of non-cohesive riverbed deposits (Detert and Weitbrecht, 2013). The line sampling method proposed by Fehr (1987) was applied to estimate key grain size percentiles (D16, D50, and D84) following the approach of Carboneau et al. (2018). Since BASEGRAIN is limited to coarse-grained sediments, sieving-based grain size distribution (GSD) analysis was conducted in the fine-grained lower reaches of the Gaula River (Reaches 83 and 87). The GSD was categorised into 18 logarithmic scale (ϕ) classes, with the observed distribution serving as a key input for the CASCADE framework. This framework evaluates grain size distributions and estimates grain-specific transport capacity, providing insights into sediment connectivity and transport dynamics.

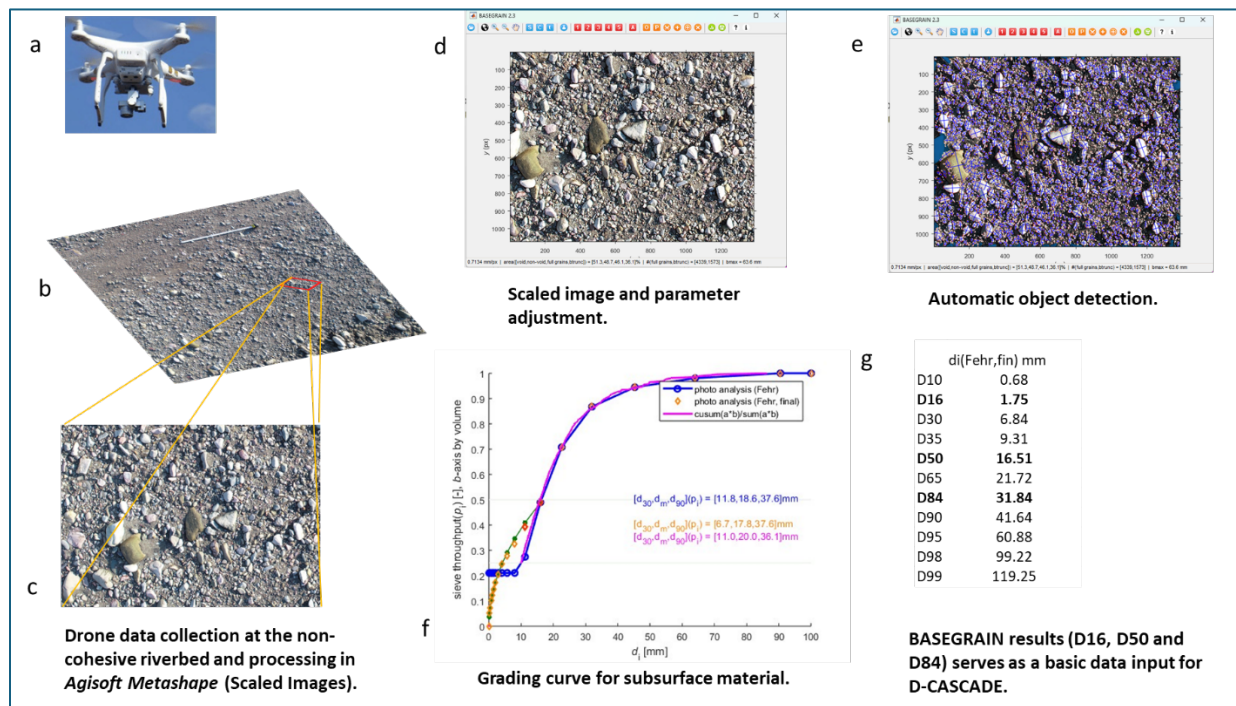


Figure 4.3: Detailed methodology adopted for the GSD data collection using drone images and BASEGRAIN software, a MATLAB-based tool for optical granulometric analysis of top-view images of non-cohesive river deposits to evaluate D16, D50, and D84 grain distribution information.

4.2.2. SWAT modelling

The SWAT model (Arnold et al., 1998; Arnold and Fohrer, 2005) is extensively used to simulate hydrological, environmental, and agricultural processes across diverse watersheds, including non-perennial river systems (Llanos-Paez et al., 2023, 2024; Rath and Hinge, 2024; Leone et al., 2024). Its reliability and adaptability make it a key tool for water resource management and environmental policy development (Baffaut et al., 2015; Liu et al., 2023). In the Gaula River catchment, the SWAT model has been configured to integrate land use, soil characteristics, Digital Elevation Models (DEM), meteorological conditions, and observed streamflow records (Table 4.1).

Table 4.1: Thematic, weather, and discharge data used in the SWAT model setup.

S.No.	Data type	Sources
1	Digital Elevation Model (DEM)	CartoDEM-v3.1, 30m, ISRO (Jain et al., 2018)
2	Landuse	NRSC 2005-06, 1:50,000, (Grekousis et al., 2015)
3	Soil	Harmonised World Soil Database (HWSD) v.1.2 – Food and Agriculture (FAO), (Batjes, 2009)
4	Weather data (Precipitation, Temperature)	IMD Daily Precipitation (1990 – 2022), IMD – Daily Temperature Min, Max (1990 – 2022) (Nandi et al., 2020)
5	River discharge	Observed discharge at the river outlet at Kichha barrage (Source: Uttarakhand Irrigation Department, Haldwani),
6	Weather generator database (Solar radiation, relative humidity, and wind velocity)	https://swat.tamu.edu/data/india-dataset/ (SWAT model official website).

*IMD – Indian Meteorological Department.

The SWAT model was employed to quantify key water balance components, including infiltration, runoff, evapotranspiration, lateral flow, and percolation, at the Hydrologic Response Unit (HRU) level. These components were aggregated at the sub-catchment level, with the resulting flows

routed to the catchment outlet. In the SWAT model setup for the Gaula River, the controlled discharge release data from the Gaula barrage was incorporated into the modelling environment. The model evaluation uses the Kichha Dam data at the outlet for validation. Additionally, essential updates were made to the manning's "n" values of the main channel, tributaries, and overland flow (Chow et al., 1988; Arcement and Schneider, 1989). The model simulated hydrological processes from 1990 to 2021, with the initial four years used as a warm-up period. Thus, the model yielded 28 years of distributed hydrographs for the Gaula River catchment.

The Gaula catchment slope was derived using the Cartosat-1 Digital Elevation Model (DEM) in ArcGIS to assess the topographic variations across the catchment. The SWAT model was used to calculate the average longitudinal slope of the channel (m/m). Total stream power (TSP) represents the energy available for sediment transport and erosion in a river channel (Yang and Stall, 1974). TSP is a function of discharge and channel slope. To quantify TSP, the 28-year average monthly discharge for August, representing peak monsoonal flow, was multiplied by the corresponding slope values for each river reach. This approach provides a spatially distributed representation of energy availability for geomorphic work, particularly sediment transport and channel incision.

The SWAT-derived hydrological data is essential for the CASCADE model, which is used in this study to simulate sediment transport and delivery. Since the CASCADE model relies on external hydrological information, SWAT-simulated hydrographs become crucial inputs. Unlike the continuous simulation of the SWAT model, CASCADE operates instantaneously and requires specific hydrographs for sediment transport modelling. To facilitate integration, SWAT-simulated hydrological data was categorised into eight classes using nine percentile values, spaced one standard deviation apart (-4σ to $+4\sigma$) in a standard normal distribution, providing hydrographs suitable for CASCADE. The associated percentile values correspond to probabilities of 10, 20, 30, 50, 60, 70, 90, 95, and 97. The Gaula River exhibits intermittent flow and irregular sediment transport, with peak discharge occurring during the monsoon months of July and August, while flow remains below average for the rest of the year. Thus, CASCADE sediment transport modelling relies on the 97th percentile discharge to ensure connectivity and effective sediment delivery within the river network. As a predominantly gravel-bed river, the Gaula achieves

maximum sediment connectivity during peak discharge events, producing episodic sediment pulses that shape river geomorphology and sediment dynamics (Emmett and Wolman, 2001; Venditti et al., 2010).

4.2.3. CASCADE model

The CASCADE model is an effective and computationally efficient sediment transport modelling framework that calculates grain-specific sediment flux across a river network (Tangi et al., 2019). It identifies sediment sources and their respective contributions to different river reaches and outlets, providing a detailed representation of entrainment, transportation, and sediment deposition processes. The model simulates sediment movement as cascades representing single transport processes, starting with a specific grain size and flow rate. Cascades gradually deplete as sediment is transported downstream, with deposition occurring along the river profile. Multiple cascades are activated during simulations, allowing for a comprehensive grain-size-specific sediment flux analysis (Tangi et al., 2019).

In this study, we applied the CASCADE model to analyse controls of sediment flux under sand mining conditions. Two modeling scenarios, namely 'Mining' and 'No-mining', were developed, incorporating field-observed grain size distributions (GSD). Other key boundary conditions, including hydrology and the geomorphic characteristic of the river reaches, were kept consistent between the two scenarios. River width was extracted from Google satellite imagery. The river network and hydrograph derived from SWAT were used in the CASCADE model. For both scenarios, the river network included attributes such as river length, slope and Manning's n , obtained from SWAT. The flux estimates were computed using Yang's transport capacity formula (Yang, 1984), which determines total transport capacity. To account for grain-size-dependent transport, the Molinas fractional transport capacity formula (Wu et al., 2003) was applied to derive transport rates for sediment fractions within the ϕ (Φ) range of -9.5 to 7.5. The Molinas fractional transport capacity formula considers sheltering and exposure, where smaller particles are sheltered by larger ones and transported at a lower rate. In contrast, larger particles experience greater fluid dynamic forces. The Molinas transport capacity fraction (TCF) formula enhances the accuracy of predicting fractional transport rates across all sediment size fractions in nonuniform mixtures (Wu et al., 2003, 2004).

The hydraulic characteristics of the river network were estimated using the Manning–Strickler relationship (Manning et al., 1890). For the Gaula River, the net sediment fluxes were calculated as the difference between deposited flux and the sum of transported and entrained fluxes, allowing for an assessment of network-scale connectivity patterns and sediment flux variations between the relatively undisturbed upper catchment and the sand-mining-impacted lower reaches.

4.3. Network Scale GSD establishment with BASEGRAIN

Table 4.2 presents the D50 GSD data obtained through drone-based granulometric analysis using the BASEGRAIN software and sieving method for mining and no-mining scenarios. It illustrates a progressive refinement of the median grain size (D50) along the Gaula River’s reaches. The D50, D16, and D84 values for no-mining and mining scenarios were linearly interpolated to determine the values for the reaches of the river catchment that were not surveyed (Tangi, 2018; Tangi et al., 2022). The D50 grain size was notably larger in the mining scenario than in the no-mining scenario, indicative of bed coarsening (Table 4.2).

Table 4.2: Grain size survey performed along the river for no-mining and mining periods.

Reach ID	D ₅₀ (No-mining scenario)	D ₅₀ (Mining scenario) <i>unit- mm</i>
23	20.74	20.54
33	12.96	*
54	*	27.30
71	*	33.13
72	24.81	*
74	*	20.9
76	16.45	*
77	*	18.38
78	14.49	*
80	*	18.80
83	*	16.55
87	11.28	16.52

** No observation*

4.4. Hydrological response using the SWAT model

Figure 4.4 shows a SWAT-generated 28-year hydrological response at the Gaula catchment outlet at Kichha dam (reach 87) from 1994 to October 2021. Between 1994 and 2005, the hydrological data shows low discharge levels. The Gaula River catchment experienced extreme discharge conditions during the 2005 monsoon. From 2006 onwards, high discharge levels have been observed. The complete hydrograph illustrates distinct peaks during the monsoon seasons, indicating strong flows, with values occasionally exceeding 1000 cubic meters per second in the post-2006 period. Conversely, the river experiences minimal flow during dry seasons, occasionally reaching near-zero levels, underscoring the Gaula River's non-perennial nature in the lower catchment. The observed data at the Kiccha Dam is used for the estimation of model

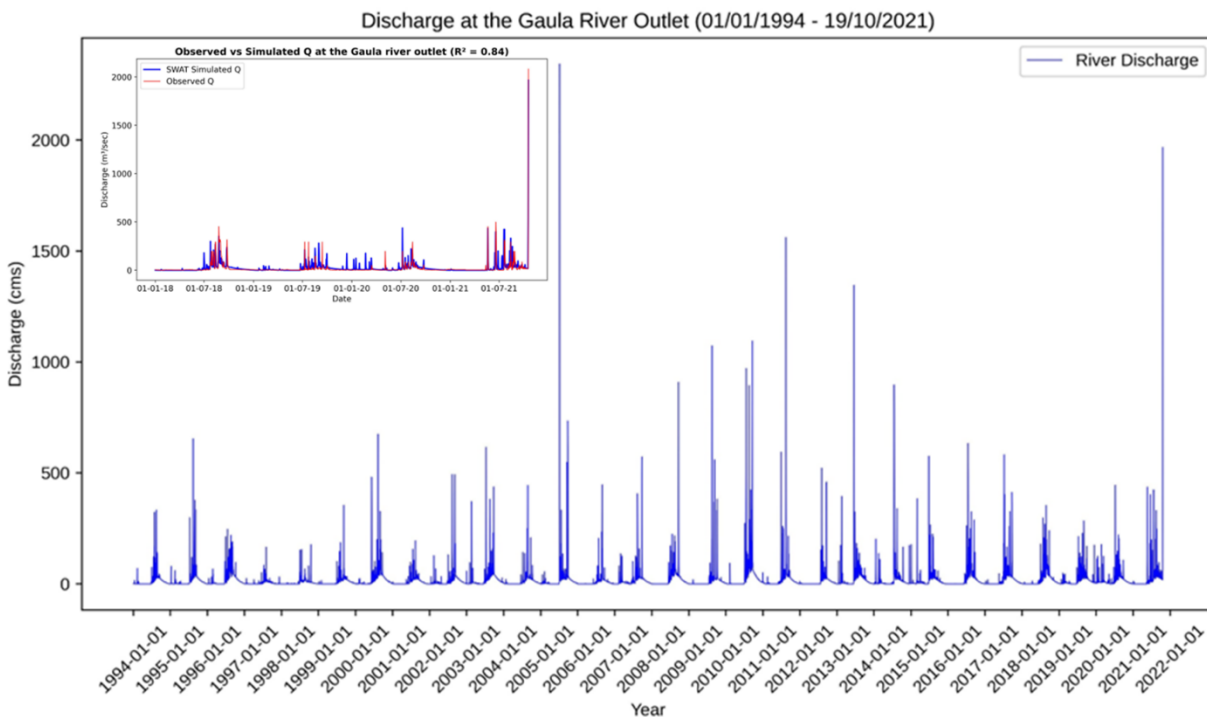


Figure 4.4: SWAT generated 27 years (1994 to 2021) of hydrological simulation response of the Gaula River catchment, and the inset map shows validation for the limited years.

performance and validation from 2018 to October 2021 (Fig. 4.4). The Kichha Dam was breached in October 2021 due to a peak discharge event. Performance metrics between the simulated and observed data included a correlation coefficient (R) of 0.84, Nash-Sutcliffe Efficiency (NSE) of 0.69

and R2 of 0.7, fulfilling the minimum required criteria of NSE > 0.5 and R2 > 0.6 (C. Santhi et al., 2001; D. N. Moriasi et al., 2007; Arnold et al., 2012), suggesting a good predictive capability for the period of 2018–2021. The output of this model shows that the SWAT model can be used to analyse hydrological processes in ungauged river basins where observed data is unavailable or insufficient.

4.5. Hydro-geomorphic controls: catchment slope, channel slope and stream power

Figure 4.5a shows that the Gaula River catchment has two distinct zones in terms of slope variations. The upper catchment area is characterised by its steep slopes (28.64° to 70.88°), indicating rugged topography with high elevation gradients. In contrast, the lower catchment exhibits gentler slopes (0° to 8.62°) with relatively flat terrain. Figures 5b show the channel slope in the Gaula River. The river reaches in the upper catchment show very high (0.047 to 0.088 m/m) to high (0.023 to 0.046 m/m) and moderately high (0.015 to 0.022 m/m) steep slopes (Fig. 4.5b). These steep gradients are associated with mountainous terrain and active tectonic settings. There are also a few reaches with gentle slopes (0.006 to 0.014 m/m) to very gentle slopes (0 to 0.005 m/m), in the southern part of the upper catchment itself (Fig. 5b), where the catchment slope is also low (Fig. 4.5a). The lower catchment of the Gaula River typically has a gentle to very gentle channel slope attributed to the flat terrain. Figure 5c shows the total stream power (TSP) distribution in the Gaula River (Fig. 4.5c). The uppermost northern reach of the upper catchment shows low TSP (0.14 to 0.25 W/m) to very low stream power (0 to 0.13 W/m). These reaches have a high channel slope but low stream power because the discharge in those reaches is not significant enough to produce the stream power necessary for efficient channel transport. Moderate TSP values (0.26 to 0.46 W/m) are observed in the upper catchment's central to lower southern reaches. The highest TSP value (0.72 to 1.26 W/m) is also observed in the upper catchment (Fig. 4.5c), where steep channel slope contributes to increased erosion potential (Fig. 4.5b). The lower catchment has high TSP (0.47 to 0.71 W/m) specifically along the upper and middle segment which transitions into low TSP values in the lower segment indicative of reduced erosive capacity.

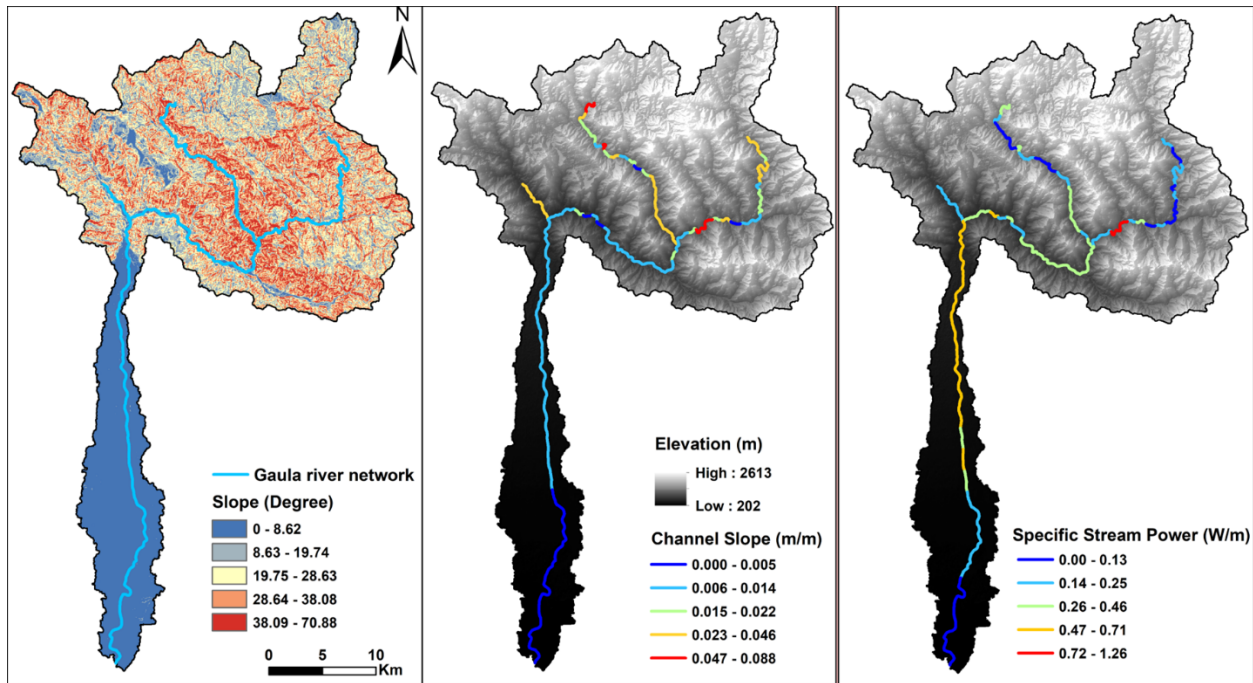


Figure 4.5: (a) Slope map of the Gaula River catchment showing the topographic gradients and delineated river network; (b) Longitudinal variation in channel slope along the Gaula River, highlighting morphological transitions from the upper to lower catchment; and (c) Specific stream power distribution along the Gaula River, indicating zones of high energy and potential erosion linked to geomorphic activity and anthropogenic pressures.

4.6. Sediment Flux estimation from the CASCADE model

Figures 4.6a and b show the Gaula River catchment's sediment flux for the deposition, transportation and entrainment processes under mining and no-mining conditions. The deposited, transported and entrainment flux for both mining and no-mining scenarios in the upper catchment (till reach 49) shows negligible differences, as shown in Figure 4.6. The net sediment fluxes for reach 49 in the mining and no-mining scenarios are 207.15 Kg/sec and 210.56 Kg/sec, respectively. The net sediment delivery of the upper catchment for both scenarios is almost similar, as obtained from the CASCADE model under both scenarios. However, the amount of sediment extracted from the lower catchment is substantial, and it provides the rationale for prioritising lower reaches for the sediment dynamics study utilising the CASCADE model.

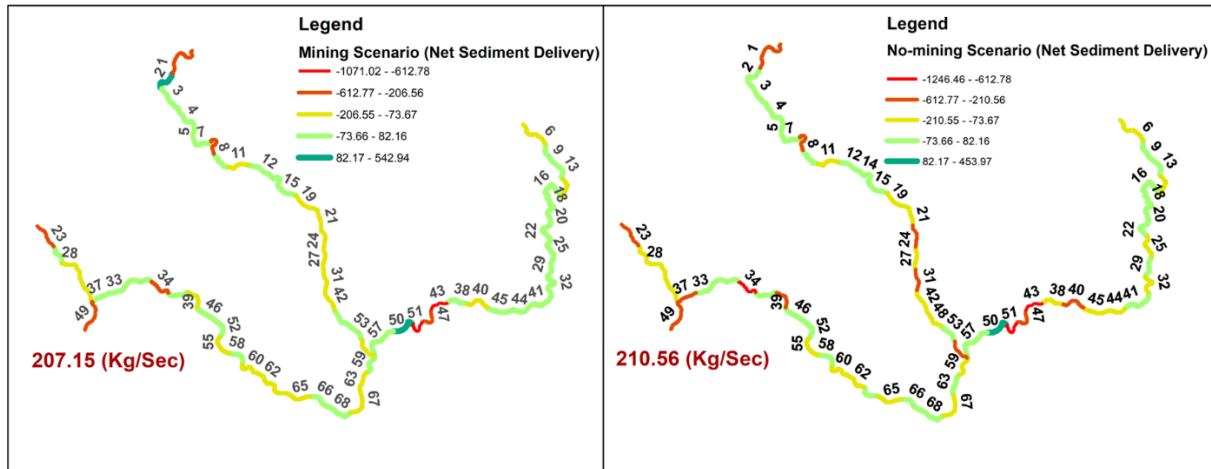


Figure 4.6: Gaula River's pristine upper catchment conditions demonstrate negligible impact on sediment delivery at the foothill zone in (a) mining and (b) no-mining scenarios (Yang's TCF).

4.6.1. Sediment flux under mining scenario

The Gaula River network in the lower catchment is divided into 20 reaches, each 2 km long. Akuria and Sinha (2025) categorised the Lower Gaula catchment into three segments: tectonics- and bedrock-controlled upper segment, the middle segment corresponding to the mining zone, and the unconfined lower segment. We have adopted this terminology here, classifying the upper segment as reaches 61 and 69, the middle segment as reaches 70 to 80, and the lower segment as reaches 81 to 87. In the upper segment, the transported flux is initially high peaking at reach 61 (806 Kg/sec), then decreasing to 245.9 Kg/sec at reach 69 in the mining scenario (Fig. 4.7a). A secondary peak occurs at reach 70 (338.7 Kg/sec), followed by a relatively stable flux across reaches 71 to 78. A sharp decline is observed at reach 79 (94.2 Kg/sec) and 80 (39.5 Kg/sec). Further downstream, the transported flux decreases significantly to reach 83 (19.4 Kg/sec) and remains low thereafter. The entrainment flux mimics the transported flux and shows noticeable peaks at reaches 61 (324.4 Kg/sec) and 70 (92.8 Kg/sec), followed by almost negligible values in the subsequent reaches (Fig. 4.7a). In contrast, deposition flux exhibits peaks where transported flux decreases. Deposition flux shows significant peaks at reaches 69 (278.8 Kg/sec), and 79 (112.3 Kg/sec), and moderate peaks at 71 (90.3 Kg/sec), 75 (41.56 Kg/sec) and 77 (27.65 Kg/sec) where sediment settles more conspicuously (Fig. 4.7a).

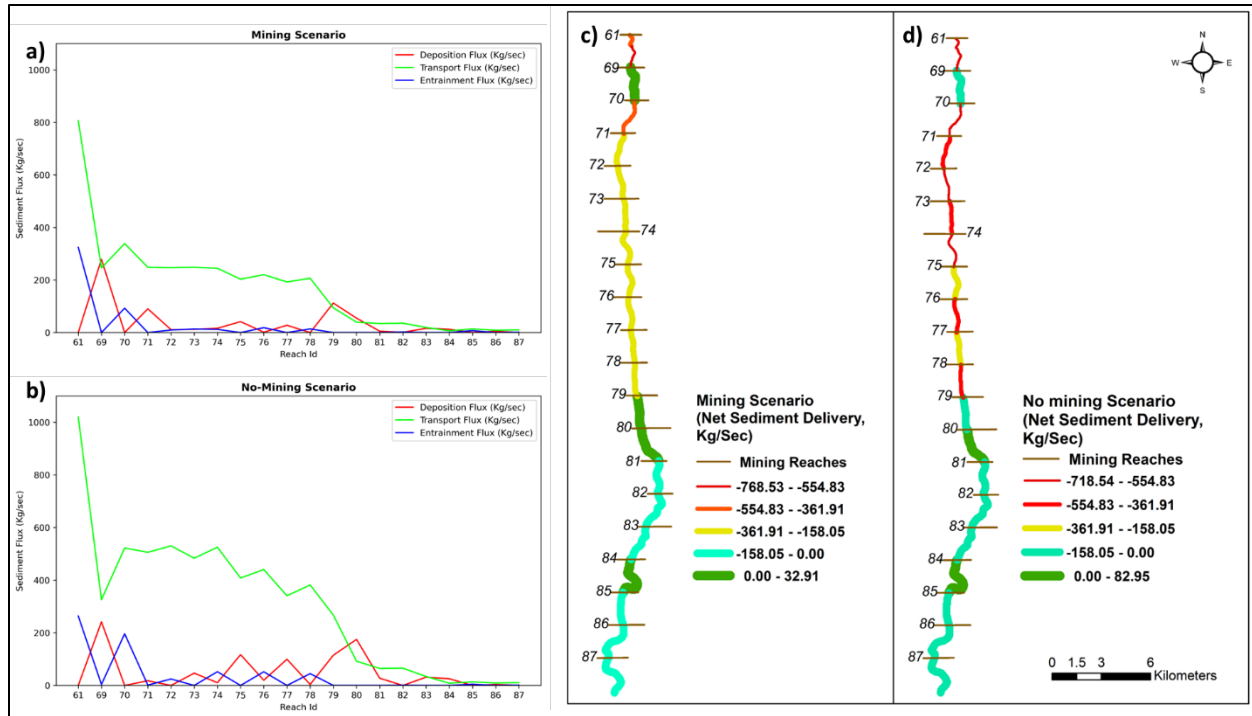


Figure 4.7: Yang's TCF based sediment fluxes (deposited, transported and entrainment) in the lower catchment reaches in a) mining and b) no-mining scenarios. Net sediment delivery highlighting sediment deposition and transport dominant river reaches in c) mining and d) no-mining scenarios.

4.6.2. Sediment flux under no-mining scenario

Conversely, under the no-mining scenario, the transported flux is markedly higher (74.58%) than mining conditions, with notably large values between reaches 70 and 79. The upper segment exhibits a similar pattern in both scenarios. However, with elevated transported flux in the no-mining case, peaking at 1019.9 Kg/sec at reach 61 and 325.8 Kg/sec at reach 69 (Fig. 4.7b). Unlike the stabilised transported flux observed under mining conditions, the no-mining scenario shows alternating high and low flux values between reaches 70 and 78. A sharp decline still occurs from reach 79 (267 Kg/sec) to 80 (92 Kg/sec), followed by minimal transported flux beyond reach 83. The entrainment flux mirrors the transported flux, showing prominent peaks at reaches 61 (263.7 Kg/sec) and 70 (196.3 Kg/sec) and shows moderate values at 74 (52.1 Kg/sec), 76(51.9 Kg/sec) and 78 (44.9 Kg/sec). Figure 7b shows pronounced peaks of deposition flux at reaches 69 (241.5 Kg/sec), 75 (116.9 Kg/sec), 77 (99.5 Kg/sec), 79 (114.8 Kg/sec) and 80 (175.9 Kg/sec), and a minor peak at 73 (46.7 Kg/sec). These values imply that sediment transport, deposition, and entrainment fluxes are all elevated under no-mining conditions, especially in the middle segment

reaches (70 to 80), corresponding to the mining zone. The reaches beyond 81 exhibited equilibrium conditions in both scenarios with negligible change in the three flux values. The mining scenario results in a total transported flux of 3,465.03 Kg/sec, deposition flux of 686.39 Kg/sec, and entrainment flux of 496.25 Kg/sec. In contrast, the no-mining scenario yields significantly higher values, with a total transported flux of 6,049.45 Kg/sec, deposition flux of 934.91 Kg/sec, and entrainment flux of 645.74 Kg/sec.

4.6.3. Net sediment delivery

Figures 4.7c and d show a comparative assessment of net sediment transport along the Gaula River between mining and no-mining scenarios. Negative values signify erosional processes while positive values indicate depositional processes. Figure 4.7c shows a homogenised sediment delivery system in the mining scenario. Bed-rock and tectonics-controlled reach 61 is a remarkably high erosive zone where the sediment delivery is -1130.45 Kg/sec, followed by a depositional zone at reach 69 where sediment delivery is 32.91 Kg/sec (Fig. 4.7c). The middle segment (reaches 70 to 78) corresponding to active mining zones is moderately erosive with reach 70 exhibiting the highest erosion rate (-431.59 Kg/sec). However, a shift toward depositional conditions is observed downstream, as sediment delivery transitions from -220.62 Kg/sec at reach 78 to 18.05 Kg/sec and 15.29 Kg/sec at reaches 79 and 80, respectively. The lower segment (reaches 81–87) shows erosion but with reduced intensity compared to the middle segment, except at reach 84, where a slight deposition of 6.02 Kg/sec is recorded (Fig. 4.7c).

In contrast to the homogenised mining scenario, the no-mining scenario shows a more dynamic sediment delivery system (Fig. 4.7d). Similar to the mining condition, reach 61 remains a highly erosive zone with an increased sediment erosion rate of -1283.7 Kg/sec. However, unlike the mining scenario, reach 69 is mildly erosion-dominated in the no-mining scenario (-88.07 Kg/sec). The reaches of the middle segment are highly erosive to erosive, where the highest erosion occurs in reach 70 (-718.54 Kg/sec), followed by reach 72 (-554.83 Kg/sec) and reach 74 (-556.77 Kg/sec). The exception is reach 80, which is a depositional zone (82.95 Kg/sec). Like the mining scenario, the lower segment (reaches 81–87) exhibits minimal erosion, except for reach 84, where a slight deposition of 16.77 Kg/sec is observed (Fig. 4.7d).

4.7. Reconstruction of hydrology for an ephemeral river

The hydrological response of an ephemeral river in the northwestern Himalayas was analysed, revealing substantial insights into its complex hydrological regime (Qazi et al., 2020), the SWAT analysis indicates a notable increase in discharge levels post-2006 (Fig. 4.4) driven by a slightly increasing trend in rainfall (Banerjee et al., 2020; Kansal and Singh, 2022; Singh and Pandey, 2024). The hydrographs exhibit pronounced peaks during the monsoon season. Intense hydrograph peaks during the monsoon months often trigger flash floods (Fig. 4.4), which frequently trigger flash floods—phenomena influenced by topographic features, climatic conditions, regional geology, and extensive land-use transformations occurring in the NW Himalaya (Ghosh et al., 2019; Sagwal et al., 2024). The Gaula catchment is tectonically active, leading to recurrent landslides in the upper catchment (Bartarya and Valdiya, 1989; Sah et al., 2018; Lal. Kumar et al., 2020), whereas, in the lower catchment, it behaves primarily as an ephemeral river (Akuria and Sinha, 2025). High-intensity precipitation events create conducive conditions for frequent flash floods in these ephemeral streams (Osborn and Lane, 1969; Ortega et al., 2014). In Uttarakhand, notable flash flood incidents have been attributed to extreme rainfall coupled with anthropogenic global warming impacts (Kansal and Singh, 2022; Singh and Pandey, 2024). A catastrophic flood in 2021 destroyed the Kiccha dam on the Gaula River, significantly disrupting both livelihood and property in the surrounding floodplains (Ansari et al., 2023; Rawat et al., 2022). Vegetation loss plays a crucial role in hydrological instability, as reduced cover accelerates sheet flow convergence and channel initiation (Sandercock et al., 2007), in the NW Himalaya (Qazi et al., 2017). Moreover, the removal of vegetated bars from the river in the lower catchment due to sand mining (Akuria and Sinha, 2025) contributed to an increased discharge at the outlet, exacerbating the impacts of floods.

The hydrological results obtained from the SWAT model align closely with the observed Gaula River catchment discharge conditions, as illustrated in the inset plot of Figure 4.4. The level of precision attained with minimal parameterisation emphasizes the effectiveness of SWAT models in examining the hydrology of ephemeral rivers (Gamvroudis et al., 2015; Pulighe et al., 2020; Nabih et al., 2021). Previous investigations have shown that even without calibration, the SWAT model can yield reliable hydrological results (R. Srinivasan et al., 2010; Cho et al., 2013).

Hydrological simulations using the SWAT model closely replicate observed discharge patterns in the Gaula River catchment, successfully capturing the peak flow responsible for the Kiccha dam failure in October 2021 (Fig. 4.4). This high level of accuracy, achieved with minimal parameterisation, highlights the model's suitability for studying ephemeral river hydrology (Gamvroudis et al., 2015; Pulighe et al., 2020; Nabih et al., 2021). It is reported that the SWAT model is an effective tool for managing water resources in the rivers of the Himalayas (Rautela et al., 2023; Swain et al., 2022).

Furthermore, the SWAT model generates river network parameters that inform the input attributes for the CASCADE model. These parameters provided by SWAT include river width, river length, gradient, as well as the elevations and geographic coordinates of the 'to and from' nodes. As a result, the SWAT model offers essential hydrological information and supports the development of an integrated approach, which includes BASEGRAIN-based GSD and CASCADE models, to understand the connectivity in the sand mining-impacted ephemeral Gaula River.

A key challenge in modelling the hydrology of this ephemeral Himalayan River arises from insufficient quantitative information regarding glacier melt contributions, precipitation distribution in the region, a comprehensive discharge gauge network, and challenges associated with accessing the higher hinterland. In ephemeral rivers, the SWAT model provided insights into climate change impacts on hydrology and its suitability for the Indian region (Sharma et al., 2022; Dubey et al., 2023). Nonetheless, the number of studies addressing the ephemeral river hydrology of the NW Himalayas remains limited. This research demonstrates the application of the SWAT model to navigate the complexities introduced by challenging topography, climate variability, and the lack of long-term observational data inherent to ephemeral river systems. Future work should prioritise integrating higher-resolution remote sensing imagery, along with a more robust network of precipitation and river gauge data, which will substantially enhance the understanding and management of these vulnerable Himalayan River systems (Hasan and Pradhanang, 2017; Chiphang et al., 2020; Kumar and Singh, 2023). Ultimately, this will improve our comprehension of sediment transport behaviours and the management of water resources (Ghimire et al., 2024; Quamar et al., 2025).

4.8. River Behaviour with the ‘imposed’ boundary conditions

River systems are dynamic and adjust within the imposed boundary conditions, marked by relief, slope and valley morphology. Flux boundary conditions are inset within the imposed boundary conditions, determining the energy conditions under which rivers behave. Adjustments in river systems are brought about by alterations to the imposed and flux boundary conditions, whether due to ‘natural’ trends or human-induced (anthropogenic) impacts. Understanding the river’s character and behaviour under the imposed and flux boundary conditions is crucial to differentiate between anthropogenic and natural impacts.

Here, we have utilised the nested hierarchical approach (Fryirs, 2017; Fryirs and Brierley, n.d.) to understand the factors that control the imposed boundary conditions. The Gaula catchment is significantly influenced by active tectonics, which plays a significant role in changing the imposed boundary conditions, and the time frame for such adjustments occurs over geologic timescales (105). The Gaula catchment is notably elongated ($Re=0.36$) and has a relief ratio of 18.71, indicating a significant drop in elevation per unit length of the river. This high relief and steep slope render the area more susceptible to headward erosion, ultimately leading to increased sediment production. This phenomenon is attributed to tectonic uplift within the MBT zone (Gururani et al., 2023). Additionally, the Gaula catchment has a low form factor of 0.1361, which suggests that it will exhibit a prolonged, flattened peak flow. Hence, the Gaula catchment can produce a large sediment flux which is transported downstream efficiently through a single channel and an elongated basin. The channel slope map indicates a steep gradient in the upper catchment, transitioning into moderate and low gradients in the lower catchment (Fig. 4.5b). The high slopes in the upstream areas are associated with the tectonically active Himalayan terrain, and the lower reaches exhibit a relatively flat gradient (Fig. 4.5a and b). The TSP follows a similar pattern to the channel slope but does not always directly correlate with channel slope. While some steeply sloped reaches exhibit high TSP, for example, the presence of localised high TSP reaches in the central part of the upper catchment suggests potential areas of increased channel erosion and transport. However, others display only moderate to low values (Fig. 4.5b and c). This discrepancy arises because stream power is influenced not only by slope but also by

discharge. In steep headwater regions, though slopes are high, discharge is relatively low, leading to moderate to low stream power values.

In contrast, upper and middle segments of the lower catchment with higher discharge but lower slopes generate considerable stream power, facilitating sediment transport and channel adjustments. Thus, the river behaves as a sediment transport zone here with high stream power (Fig. 4.5c) with high terraces on either side, which gradually transforms into a laterally unconfined meandering river further downstream (Akuria and Sinha, 2025). The stream power declines in the lower segment of the river in the lower catchment as the catchment and channel slope both are negligible (Fig. 4.5a) indicating reduced erosional capacity, favouring sediment deposition. Moreover, Goswami (2018) highlighted the significant influence of tectonics on the morphology of alluvial fans in the piedmont zone of the Himalayas. Shukla (2009) also suggested that tectonic activity caused the incision of the Gaula River into the deposits of the piedmont fan surface, where the incision in the proximal part of the fan is 8–16 m, while in the middle and distal parts, it is 3–4 m. Therefore, we argue that the imposed boundary conditions in this river are significantly controlled by both tectonics and discharge.

4.9. River response to changes in ‘flux’ boundary conditions

Flux boundary conditions determine the energy conditions under which rivers behave. The geomorphic processes and resulting forms in rivers are driven by a balance between the driving forces, namely, water discharge (Q_w), channel slope (S), and resisting forces, sediment discharge or sediment load (Q_s), and sediment bed grain size or particle diameter (D_s) (Lane 1955). In other words, if any variables are altered, the river will try to maintain its equilibrium by adjusting to other variables. Both natural (climate, tectonics) and/or anthropogenic perturbations can alter the variables and initiate the geomorphic change by altering sediment load and discharge. This impacts the rate and extent of erosional and depositional processes within the channel, leading to changes in channel morphology.

This study examines alterations in grain size distribution based on observed data, highlighting the bed coarsening effect caused by sand mining. While the analysis assumes constant slope and

sediment load, it is acknowledged that these parameters will vary locally under real-world sand mining conditions.

4.9.1. Bed coarsening due to sand mining

Grain size is the primary factor influencing geomorphology, river hydraulics, ecology, and sediment transport dynamics. It also affects riverbed stability and sediment transport rates. Detailed work on different sediment size measurement methods and their implications on the river health interpretations is documented by Kondolf et al. (2003). Sediment flow rate determines the possible change in the river morphology (Best and Rhoads, 2008; Yadav and Yadav, 2021). Variations in sediment grain size affect transport efficiency, influencing how sediment is moved and deposited downstream and affecting river morphology (Friend, 1993). Therefore, sediment size measurements are crucial for the river's hydraulic structure design and ecological health. However, the measurement of sediment transport rates for Indian rivers lacks long-term sediment flux and sediment volume data at the river outlet.

Implementing the BASEGRAIN software for riverbed GSD data development at the network scale has provided valuable insight into both mining scenarios and resulting GSD differences on the riverbed. The data analysed for the mining conditions in the actively mined reaches showed riverbed coarsening. Typically, changes in the refinement of riverbed grain size are influenced by tributaries joining the main river (Rice and Church, 1998). However, no significant tributaries exist in the mining reach section of the Gaula River. Therefore, overexploitation of the sand and gravel from the riverbed has led to the coarsening of D50 values in the reaches impacted by sand mining. The differences observed in mining and no-mining scenarios provide vital information for sediment connectivity modelling. The images shown in figure 2.10 (Chapter 2) stipulate the severity of sand mining actions on the Gaula River's riverbed, and it leaves the riverbed with gravel, cobble and boulder-rich riverbed (Hussain et al., 2022). The BASEGRAIN software has provided ways to document the GSD change in both sand mining scenarios in the actively mined river reaches (Figure 4.3). The GSD differences become river boundary conditions for sediment transport simulation in the CASCADE, producing sediment flux in no-mining and mining conditions (Fig. 4.6 and 4.7).

4.9.2. Sediment connectivity in mining and no-mining scenarios

The challenges and uncertainties in measuring bedload transport have been well documented (Ancey, 2020a, 2020b). Despite these difficulties, advancements in direct measurement techniques for boundary conditions have significantly improved the predictability of bedload transport (Schmitt et al., 2016; Tangi et al., 2019; Lang et al., 2021; Wong et al., 2024). One crucial boundary condition in sediment transport modelling is grain size distribution, which directly influences sediment mobility and connectivity within the river system. It is well documented in the literature that sand mining leads to bed armouring as preferential removal of finer sediment leaves behind a layer of coarser materials that hinder natural sediment transport and connectivity (Mathias Kondolf, 1994; Rinaldi et al., 2005). Our earlier work has documented significant bed armouring in long stretches of the Gaula River (Akuria and Sinha, 2025). The net sediment delivery assessment (Fig. 4.6) indicates that the upper catchment has produced a nearly identical net sediment flux available for the lower catchment in both scenarios. The main reason for this is that the upper catchment has no significant sand mining activity. Secondly, the access to the road from the river network is difficult due to deep and narrow river valley regions, which restricts massive-scale sand mining prospects in the upper catchment. Thirdly, the dominant grain size is boulders, cobbles and pebbles in the upper catchment, which needs to be broken down for use in the aggregate industry. The main changes in the sediment fluxes in the in-channel environment occurred in the actively mined reaches in the lower catchment, as depicted in Figures 4.7a and b.

A no-mining scenario provides a hypothetical baseline to assess the impact of sand mining. Without mining, the river would have maintained a more erosion-dominated regime, particularly in reaches 61 to 79 of the upper and middle segments of the lower catchment, allowing for greater sediment connectivity (Fig. 4.7d). This results in higher transmission sensitivity and lower locational sensitivity. On the contrary, in the mining scenario, the river behaves as a transport-limited system (Khan et al., 2021). The sediment has been excavated from the riverbed, leaving a bed with coarser grains. These coarsened grains act as armour to shield the riverbed from erosion. Bed armour functions as a 'blanket' that prevents the disturbance and reworking of subsurface sediments (Church et al., 1998; Fryirs et al., 2007; Fryirs, 2013). This makes the system

'decoupled' (Khan et al., 2021) and disrupts sediment connectivity (Fryirs, 2017). Therefore, bed armouring reduces transmission sensitivity by limiting the downstream propagation of disturbances while increasing locational sensitivity by localising geomorphic responses (Fig. 4.7c). This disruption in sediment transfer has been likened to a 'jerky conveyor belt' system (Ferguson, 1981), reflecting discontinuous sediment movement. The formation of an armour layer raises the threshold of critical shear stress required for sediment entrainment, necessitating higher flow velocities to initiate particle movement. As a result, entrainment rates decline, particularly during low-flow conditions.

The 69th reach in the no-mining scenario is mildly erosive, but changes to a depositional regime in the mining scenario. This is also reflected in the planform (Akuria and Sinha, 2025), where braided bars form in the same reach in 2021, but the reach was previously a sediment flushing zone in 1976, before the commencement of mining activities (Fig. 4.7c). Similarly, reach 79 changed from a mildly erosive regime in the no-mining scenario to a depositional one in the mining scenario. This is a behavioural change in the river system (Fryirs, 2017). In the no-mining scenario, grain sizes are 22.7 mm in reach 69 and 13.8 mm in reach 79, which coarsen to 32.5 mm and 18.7 mm, respectively under mining conditions. These changes represent critical thresholds that alter the behavioural dynamics of the river system between the no-mining and mining scenarios.

Thus, the poorly sorted gravel on the Gaula requires a critical discharge approach to find the maximum connectivity across the disconnected reaches and rationalise the selection of Q97 percentile discharge scenarios to assess the sediment dynamics, as suggested by (Ferguson, 1994) for gravel-bed rivers. The findings of Lane and Richards (1997) suggest that short space and time scale processes are critical for understanding long-term evolution studies, and numerical modelling can assist in such cases by combining field observations, lab experiments and numerical modelling. It is important to know that the local change in slope and elevation due to sand excavation has not been considered in the modelling environment. There is a high potential for sediment entrainment along the river reaches should they become incised due to sand mining, making these reaches potential hotspots of geomorphic adjustment.

4.10. Summary and conclusions

1. The upper and middle segments of the lower catchment exhibit high stream power due to higher discharge and moderate slopes, enabling active sediment transport and channel adjustments. These reaches function as sediment transport zones. As the river flows downstream, it transitions from a confined, high-energy system to a laterally unconfined meandering form, accompanied by declining stream power and reduced erosional capacity, promoting sediment deposition. Additionally, both discharge and tectonic forces act as dominant imposed boundary conditions shaping the river's form and function across different reaches.
2. Sand mining leads to bed armouring, characterised by coarser surface grains that function as a 'blanket', shielding the riverbed from erosion and disrupting sediment connectivity. This creates a decoupled, transport-limited system, reducing transmission sensitivity and increasing locational sensitivity. This alters the flux boundary conditions.
3. This armour layer increases critical shear stress thresholds, thereby reducing sediment entrainment, especially during low-flow events and contributing to spatially discontinuous sediment transport, akin to a 'jerky conveyor belt'.
4. Reaches 61 to 79 show the maximum impact of sand mining and would have maintained a more erosion-dominated regime in no-mining scenario, allowing for greater sediment connectivity.
5. The integrated method (SWAT-based hydrology, GSD and CASCADE-based sediment transport) provides important insights into sediment flux and dynamics under no-mining and mining scenarios in a data-scarce river catchment.
6. Modelling limitations include the exclusion of local slope and elevation changes due to mining. However, when integrated with field data, numerical models can effectively capture the short-term dynamics essential for understanding long-term river evolution. Mining-induced incision may expose reaches to heightened sediment entrainment, marking them as potential hotspots for geomorphic adjustment.

Chapter 5

5. Measuring Erosion and Deposition in the Gaula River using UAV-based DEM of Difference

5.1. General

Monitoring and quantifying the geomorphic effects of sand mining have traditionally been constrained by the limited spatial resolution of satellite remote sensing. In recent years, Unmanned Aerial Vehicles (UAVs) have emerged as a powerful tool for acquiring high-resolution topographic data in riverine environments (Cucchiaro et al., 2018; La Salandra et al., 2022; Diaconu et al., 2023). When combined with Structure-from-Motion (SfM) photogrammetry, UAV surveys enable the generation of detailed Digital Elevation Models (DEMs) and orthomosaic images, allowing researchers and practitioners to assess landscape change with unprecedented precision (Cucchiaro et al., 2018; Azzoni et al., 2023). A particularly useful application of UAV-derived DEMs is the DEM of Difference (DoD) technique, which involves comparing elevation surfaces from two time periods to quantify vertical changes in terrain (James et al., 2012; Calle et al., 2018; Diaconu et al., 2023). This approach facilitates the spatially explicit detection of erosion and deposition zones, enabling volumetric calculations of material removed or redistributed due to sand mining activities. However, the success of DoD analysis relies heavily on careful error management, including the application of a Level of Detection (LoD) threshold to differentiate real change from noise (Wheaton et al., 2009).

5.2. Approach and Methodology

A practical workflow for using UAV photogrammetry and DoD analysis to detect and quantify the geomorphic impacts of sand mining on riverbeds is presented in Fig. 5.1. It outlines key methodological steps from flight planning and orthomosaic generation to DEM accuracy assessment (Sarkar et al., 2023) thresholding (Wheaton et al., 2009, Williams R. D., 2012) and volume estimation (Diaconu et al., 2023).

5.2.1. UAV survey planning and Data Acquisition

To monitor geomorphic changes associated with sand mining, two UAV-based topographic surveys were conducted over the Gaula River encompassing several reaches of the river (Table 5.1). The first survey was conducted in March 2022, during the pre-monsoon and active mining season, and the second in December 2022, representing a post-monsoon and pre-mining scenario (for the next mining season). A DJI Phantom 4 Pro quadcopter was used for image acquisition, equipped with a high-resolution camera suitable for photogrammetric applications. Flight planning was executed using Drone Deploy, a proprietary software for flight planning. The March flight was done at a height of 200 meters from the launching base, with at least 80% frontal and 70% side overlap to ensure sufficient coverage and redundancy for Structure-from-Motion (SfM) processing. To increase accuracy, the December flight (pre-mining scenario) was done at 120 meters with a similar frontal and side overlap. A total of 1387 images, amounting to approximately 8.73 Gigabytes of data, were captured by the UAV in March 2022, whereas 1777 images, amounting to 12.62 Gigabytes of data, were captured in the December 2022 field survey.

For accurate topographic mapping, Ground Control Points (GCPs) were established before UAV-based surveys using visible target markers composed of high-contrast materials (typically black and white), and identifiable corners of permanent structures that were easily distinguishable in aerial imagery. These points provide known geospatial coordinates (latitude, longitude, and elevation) on the Earth's surface. GCP coordinates were acquired using a Trimble R12 GNSS receiver operating in Real-Time Kinematic (RTK) mode. A GNSS base station was set up on elevated terrain to maximize signal coverage, with the baseline distance maintained under 10 km. In cases where this threshold was exceeded, a daisy-chaining method was employed, establishing a new base using coordinates from the preceding one (Sarkar et al., 2023). During GCP acquisition, the GNSS rover was positioned directly over each target and held stationary for a minimum of 10 seconds to ensure coordinate stability. The GCPs served two key purposes: (1) for ortho-rectification of the UAV-derived imagery and DEMs, and (2) for validating on-ground conditions at key sand mining locations.

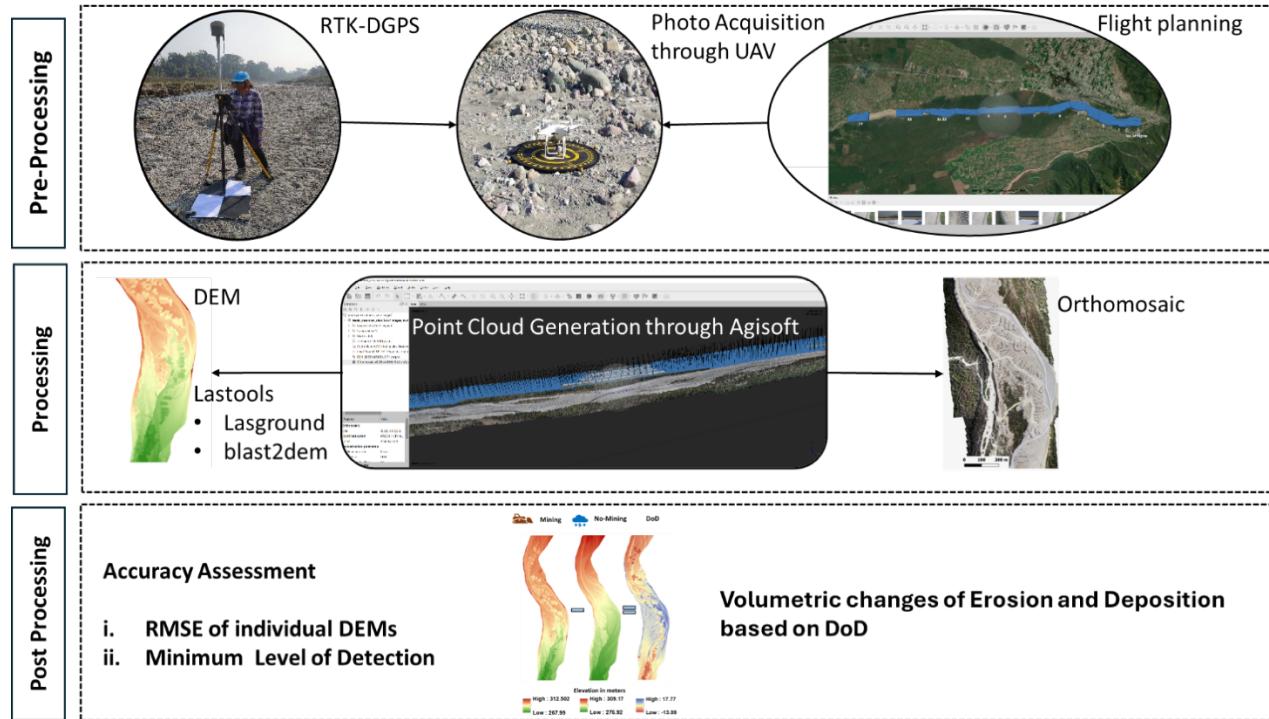


Figure 5.1: Workflow illustrating the practical application of UAV-based photogrammetry and DEM of Difference (DoD) analysis for detecting and quantifying the geomorphic impacts of sand mining on riverbeds.

Table 5.1: UAV image count, data size, and spatial coverage for selected Gaula River reaches (March and December 2022)

Reach	March 2022(Images / Size)	December 2022(Images / Size)	Coverage
2	440 images / 2.77 GB	451 images / 3.23 GB	Full
3	457 images / 2.89 GB	526 images / 3.73 GB	Full
7	255 images / 1.60 GB	406 images / 2.88 GB	Full
12	176 images / 1.10 GB	318 images / 2.25 GB	Half
13	59 images / 0.37 GB	76 images / 0.53 GB	Quarter

5.2.2. Photogrammetric Processing and DEM Generation

Post-flight image processing was mainly conducted in Agisoft Metashape, a proprietary Structure-from-Motion (SfM) photogrammetry platform. The workflow commenced with the removal of blurred and oblique images to ensure precision in the subsequent processing. The integration of Ground Control Points (GCPs) into UAV imagery began with their manual placement, aligning each GCP with the centre pixel of a visible target or the corner of a permanent structure. After accurately marking the GCPs on a few images, the automated marker placement

of the Agisoft Metashape sped up the process by detecting and marking corresponding points in subsequent images. Image alignment was refined with each new Ground Control Point (GCP) added, ensuring that the GCPs served as reliable tie points during image repositioning. In the final stage, after all GCPs had been accurately positioned, the image alignment was reset and recomputed. This recalibration step produced optimised camera parameters and spatial positions, using the GCPs as fixed reference points for geospatial accuracy.

After optimising image alignment, a dense point cloud was built in Agisoft Metashape. Some outlier points were manually removed from the dense point clouds since they were noise. We further refined the dense point cloud by filtering based on “confidence”, which in Agisoft Metashape refers to the number of image pairs used to create each depth point. Points generated from fewer than three image pairs were removed to improve accuracy. The noise-filtered point cloud was then used to generate a Digital Surface Model (DSM). This DSM was utilised to produce orthomosaic images.

To manage large datasets efficiently and minimise memory issues, the point cloud was divided into smaller tiles of 500 meters in size with a buffer overlap of 10 meters. The point cloud was classified into ground and non-ground points using ‘lasground’ in LAStools. The classified tiles were then merged, and only the ground classified point cloud was retained. This ground-classified point cloud served as the basis for generating the Digital Terrain Model (DTM). For surface interpolation, the Adaptive Triangulated Irregular Network (ATIN) method was implemented via Blast2dem in LAStools. This TIN-based approach enables gap-filling through linear interpolation, ensuring smoother and more continuous elevation models. The final DTM achieved a spatial resolution of 25 cm, suitable for detecting topographic changes in the river channel environment. Longitudinal profiles were drawn along the thalweg of the December DEM. The orthomosaic image maintained a resolution of 5 cm. The accuracy of the DEM was assessed by calculating the Root Mean Square Error (RMSE) in the vertical (Z) direction, based on the deviation between UAV-derived elevations and GCP-measured elevations. The RMSE of the first DEM was calculated as follows:

$$\delta z_1 = \sqrt{\frac{\sum (Z_{uav} - Z_{gcp})^2}{n}},$$

where Z_{gcp} is the value of the elevation of a point taken during the DGPS survey, and Z_{uav} is the value of the same point taken from the UAV-based DEM. The δz_1 is found to be 0.155 m i.e. for the March survey. Similarly, the RMSE of the second DEM is calculated as:

$$\delta z_2 = \sqrt{\frac{\sum (Z_{uav} - Z_{gcp})^2}{n}}, \text{ which is found to be 0.062 m for the December survey.}$$

5.2.3. DEM of Difference (DoD) Processing

To detect and quantify changes in terrain elevation, a DEM of Difference (DoD) analysis was conducted in ArcGIS. The DoD was created by subtracting the December 2022 DTM (post-monsoon, pre-mining for the next season) from the March 2022 DTM (mining season), yielding a raster surface of elevation change:

$$\text{DoD} = \text{DTM}_{\text{March 2022}} - \text{DTM}_{\text{December 2022}}$$

To ensure that only significant elevation changes were interpreted as actual geomorphic change from the DoD, a threshold known as the vertical Level of Detection (LoD) ± 0.16 m was applied. This threshold value accounts for the vertical uncertainty inherent in both input DEMs. The combined uncertainty of the DoD, denoted as δU_{DoD} is calculated as:

$$\delta U_{\text{DoD}} = \sqrt{(\delta z_1^2 + \delta z_2^2)},$$

where δz_1 and δz_2 are the RMSE errors associated with DEM 1 and DEM 2, respectively. All changes within this ± 0.16 m range were excluded from further analysis to eliminate noise and uncertainty. This thresholding step resulted in a filtered DoD raster, isolating zones of deposition (negative values beyond -0.16 m) and erosion (positive values beyond $+0.16$ m).

5.2.4. Volume Calculation of Erosion and Deposition

Following the generation of a thresholded Digital Elevation Model (DEM) of Difference (DoD), volumetric analysis was performed to quantify the spatial extent and magnitude of erosion and deposition linked to geomorphic changes after the mining season. The thresholded DoD raster,

which retained only elevation changes exceeding the vertical Level of Detection (LoD) of ± 0.16 m, was classified into two categories: positive DoD values indicated erosion, while negative values represented deposition. These changes were classified using raster calculator operations in ArcGIS to generate separate erosion and deposition rasters. For each pixel, the volume change was calculated by multiplying the elevation change by the pixel area (0.25 m^2 for a 25 cm resolution DEM). Total volumes of erosion and deposition were derived using the "Zonal Statistics as Table" tool, which aggregated pixel-wise values for each designated analysis zone.

5.3. Results

5.3.1. Seasonal changes in planform morphology and bed topography as revealed from high-resolution UAV images

High-resolution UAV-based orthomosaics from March 2022 (active mining phase) and December 2022 (post-monsoon phase) were analyzed to assess short-term geomorphic changes in selected reaches of the Gaula River (see Table 5.1). These comparative visuals offer insights into the dynamics of one-time seasonal recovery, including bar recovery, vegetation regeneration, visible mining scars, and thalweg shifts. We have selected a few reaches from our UAV surveys to illustrate these seasonal changes.

Reach 2 exhibits limited seasonal recovery in the post-monsoon, as observed in the December orthomosaic (Fig. 5.2a and b). While remnants of extraction pits and scars remain visible in the December orthomosaic (inset images 2a and 2b in Fig. 5.2a and b), some pits have undergone partial sediment deposition. The thalweg remained relatively stable, showing minimal displacement. The longitudinal profile also shows partial infilling of previously mined pits, though the reach mainly exhibits signs of erosion (Fig. 5.2g). There has been up to 6m incision in reach 2 between March and December, as can be seen in the longitudinal profile in the downstream of the reach (Fig. 5.2g). Lateral erosion was evident along the floodplains (inset images 1a and 1b in Fig. 5.2a and b) and as can be seen on the western bank along the cross-sections (Fig. 5.2f).

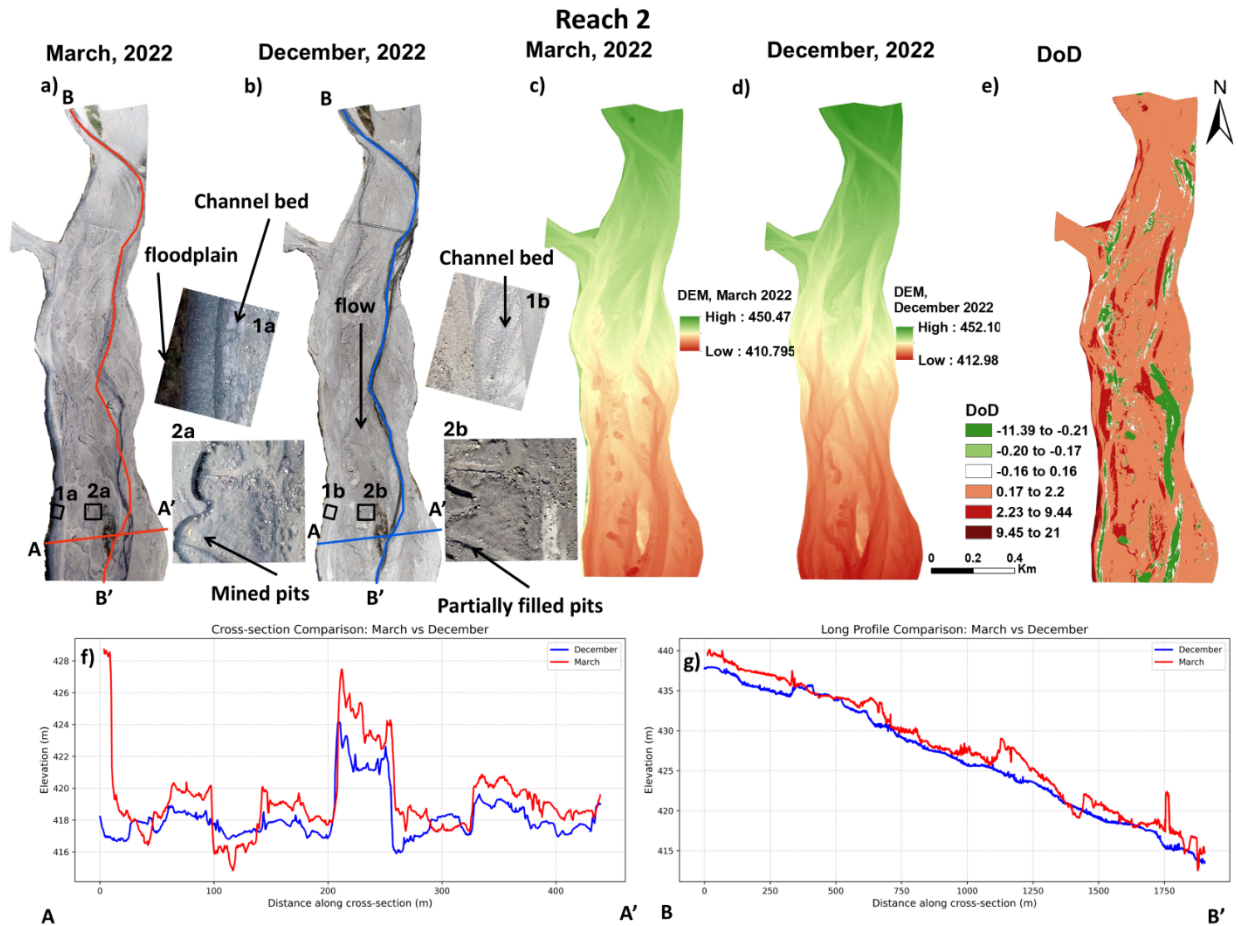


Figure 5.2: a) Orthomosaic image of Reach 2 in March (active mining period) and b) December (post-monsoon period). Inset images 1a and 1b from both the orthomosaics shows lateral erosion and inset images 2a and 2b shows remnant mining scars prevalent even after the monsoon; c) DTM of Reach 2 in March 2022 and d) December 2022; e) DEM of Difference (March DEM – December DEM), where positive values indicate erosion and negative values indicate deposition, and -0.16 to 0.16 indicates vertical uncertainty calculated from vertical Level of detection (LoD); f) Cross-sectional profile along AA' in Reach 2 derived from December and March DTM. Red indicates March profile, while blue indicates December profile; g) Longitudinal profile along BB' in reach 2 derived from December and March DTM. Red indicates the March profile, while blue indicates the December profile.

Similarly, **reach 3** also showed limited signs of recovery as seen in the December orthomosaic. Mined pits and extraction scars visible in the March imagery were partially infilled by December (Fig. 5.3a and b). Vegetation regrowth emerged along the mined zones (inset images 1a and 1b in Fig. 5.3a and b). Cross-section profiles show up to 4m incision between March and December (Fig. 5.3f). The longitudinal profile reveals partial sediment accumulation in previously excavated pits but also shows that this reach remains erosional overall (Fig. 5.3g). A slight lateral shift of the thalweg was also observed. Evidence of lateral erosion was also noted along the floodplains (inset images 2a and 2b in Fig. 5.3a and b). The spike in the March longitudinal profile shows that it was

a part of the floodplain in the pre-monsoon, which got eroded and is now a part of the channel belt in post-monsoon (inset images 2a and 2b in Fig. 5.3a, b and Fig. 5.3g).

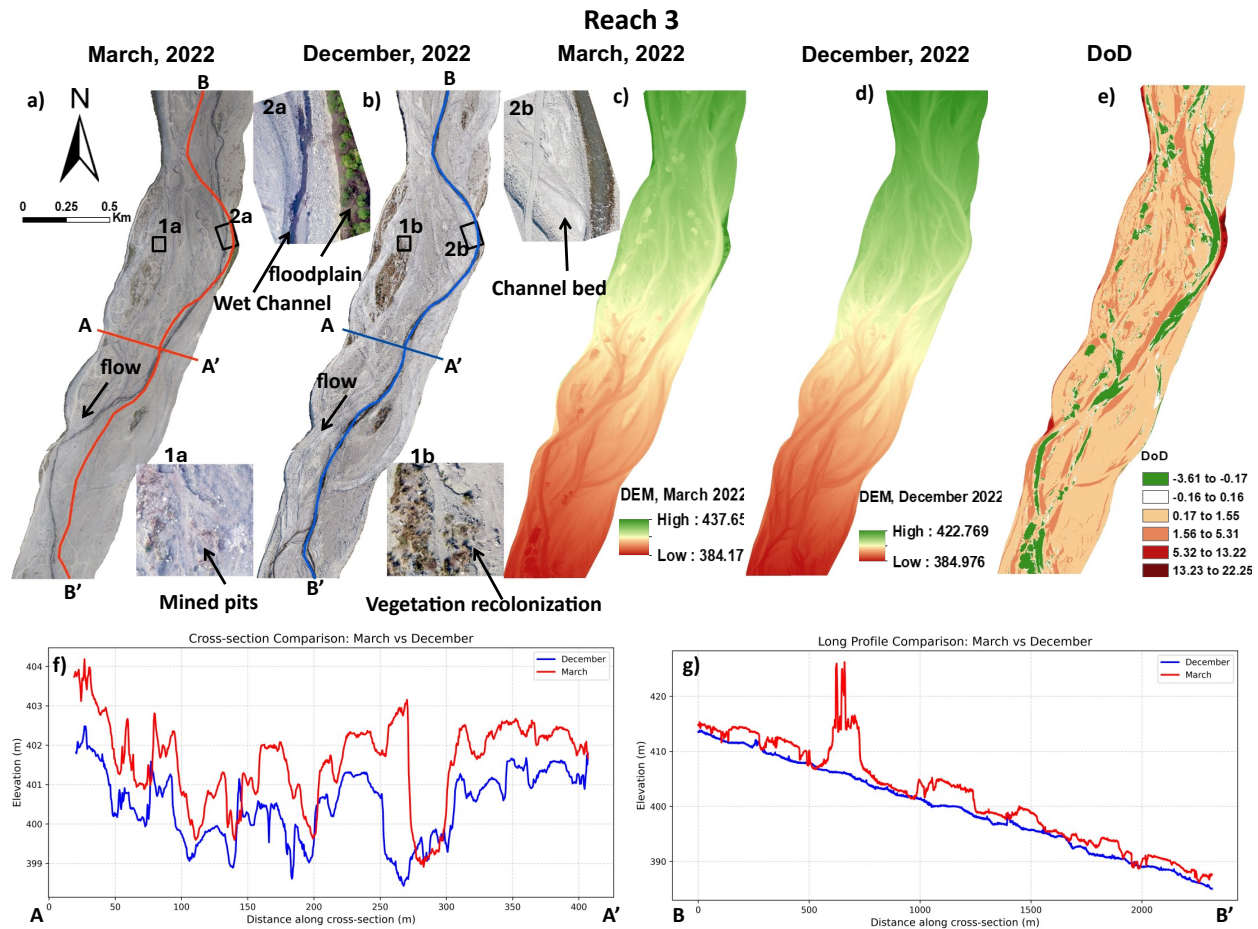


Figure 5.3: a) Orthomosaic image of Reach 3 in March (active mining period) and b) December (post-monsoon period). Inset image 1 from both the orthomosaics shows vegetation regrowth post monsoon and inset image 2 shows lateral erosion along floodplain; c) DTM of Reach 3 in March 2022 and d) December 2022; e) DEM of Difference (March DEM – December DEM), where positive values indicate erosion and negative values indicate deposition, and -0.16 to 0.16 indicates vertical uncertainty calculated from vertical Level of detection (LoD); f) Cross-sectional profile along AA' in Reach 3 derived from December and March DTM. Red indicates March profile, while blue indicates December profile; g) Longitudinal profile along BB' in reach 3 derived from December and March DTM. Red indicates the March profile, while blue indicates the December profile.

Reach 7 showed distinct geomorphic activity and signs of seasonal adjustment (Fig. 5.4). The post-monsoon orthomosaic showed bar reshaping (inset images 1a and 1b in Fig. 5.4a and b) and minor vegetation recolonization (inset images 2a and 2b in Fig. 5.4a and b). However, there was a noticeable shift in the thalweg with lateral erosion along the eastern bank (along the AA' cross-section line in Fig. 5.4f). Some mined scars that occurred on the vegetated bars were still visible,

but the reach demonstrated a relatively dynamic recovery response from March 2022 to December 2022. Deposition up to 8m was observed in the longitudinal profile (Fig. 5.4 g).

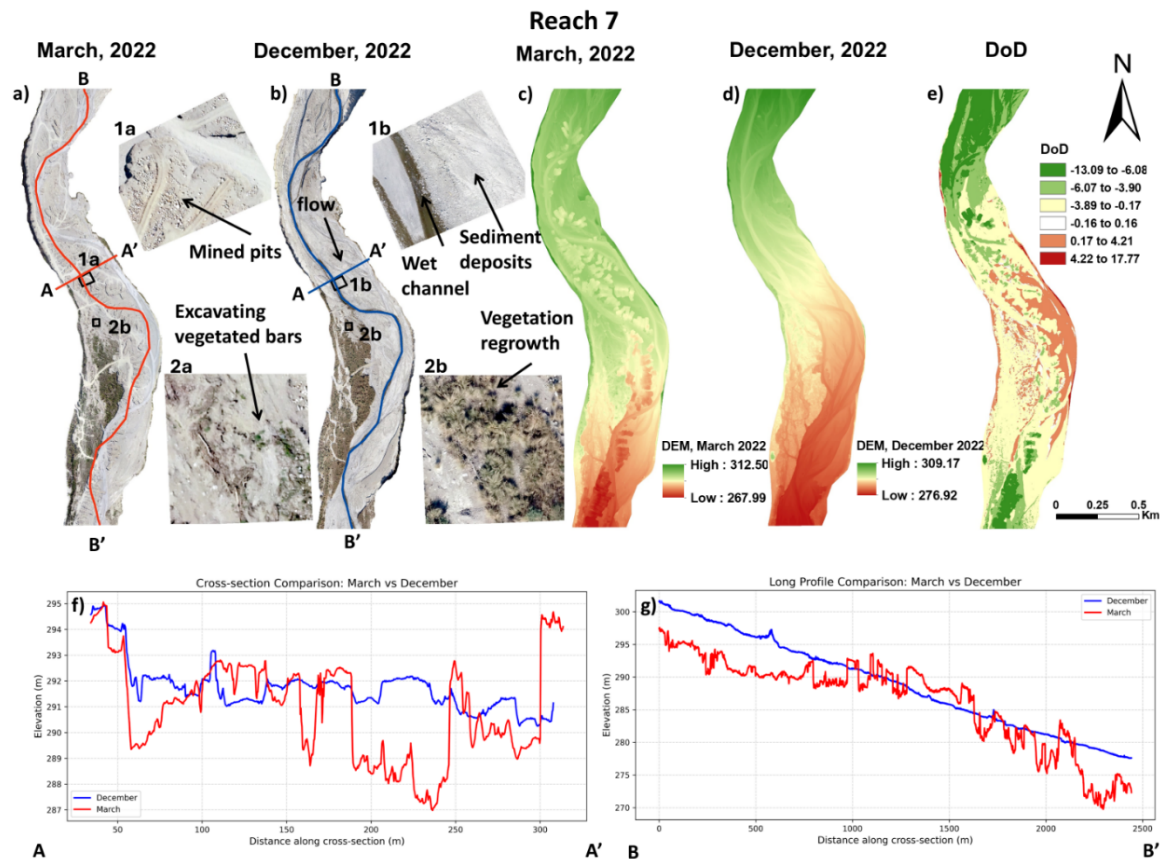


Figure 5.4: a) Orthomosaic image of Reach 7 in March (active mining period) and b) December (post-monsoon period). Inset image 1 from both the orthomosaics shows filling of mined pits and bar reshaping and inset image 2 shows vegetation recolonization; c) DTM of Reach 7 in March 2022 and d) December 2022; e) DEM of Difference (March DEM – December DEM), where positive values indicate erosion and negative values indicate deposition, and -0.16 to 0.16 indicates vertical uncertainty calculated from vertical Level of detection (LoD); f) Cross-sectional profile along AA' in Reach 7 derived from December and March DTM. Red indicates March profile, while blue indicates December profile; g) Longitudinal profile along BB' in reach 7 derived from December and March DTM. Red indicates the March profile, while blue indicates the December profile.

Reach 12 also showed post-mining recovery following the monsoon. The orthomosaic of March showed scattered mining pits with tailing ponds and disconnected and isolated wet channels (Fig. 5.5). While in the December orthomosaic, the pits and scars recovered completely with fresh sediment deposits (Fig. 5.5a and b). The reach also showed micro-braiding with narrow, connected wet channels. Deposition upto 2.5m was observed from the cross-sectional and longitudinal profiles (Fig. 5.5f and g).

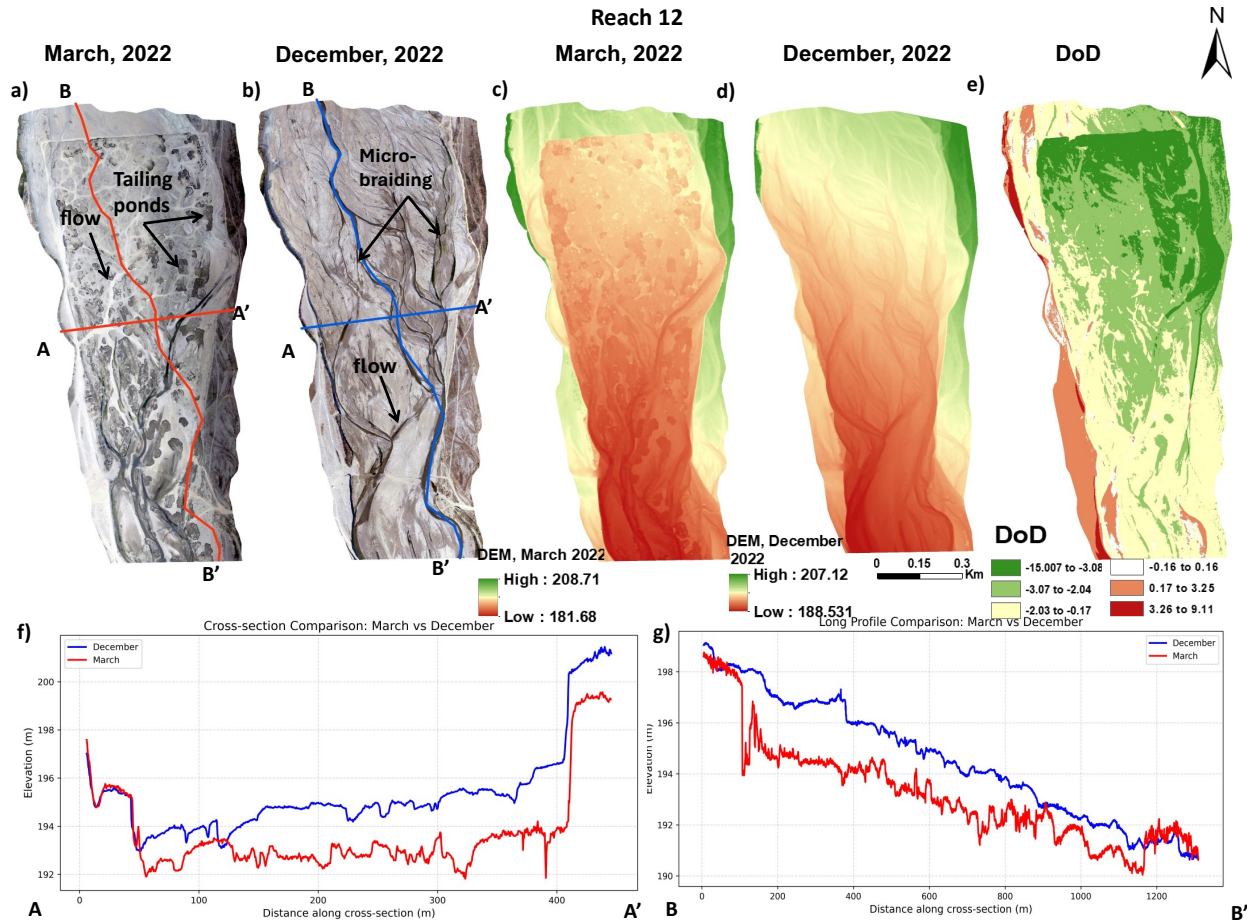


Figure 5.5: a) Orthomosaic image of Reach 12 in March (active mining period) and b) December (post-monsoon period); c) DTM of Reach 12 in March 2022 and d) December 2022; e) DEM of Difference (March DEM – December DEM), where positive values indicate erosion and negative values indicate deposition, and -0.16 to 0.16 indicates vertical uncertainty calculated from vertical Level of detection (LoD); f) Cross-sectional profile along AA' in Reach 12 derived from December and March DTM. Red indicates March profile, while blue indicates December profile; g) Longitudinal profile along BB' in reach 12 derived from December and March DTM. Red indicates the March profile, while blue indicates the December profile.

Reach 13 was only partially covered in our UAV surveys where we documented post-monsoon infilling of previously mined pits (Fig. 5.6a and b, inset images 1a and 1b in Fig. 5.6). However, there was notable lateral erosion along the floodplains (Fig. 5.6a and b, inset images 2a and 2b in Fig. 5.6). The cross-sectional profile shows erosion up to 2.5 m along the western and eastern banks (Fig. 5.6f). The longitudinal profile along the BB' line shows incision up to 2m and

deposition up to 1.5 m in previously mined pits (Fig. 5.6g). A summary of the key observations has been provided in Table 5.2.

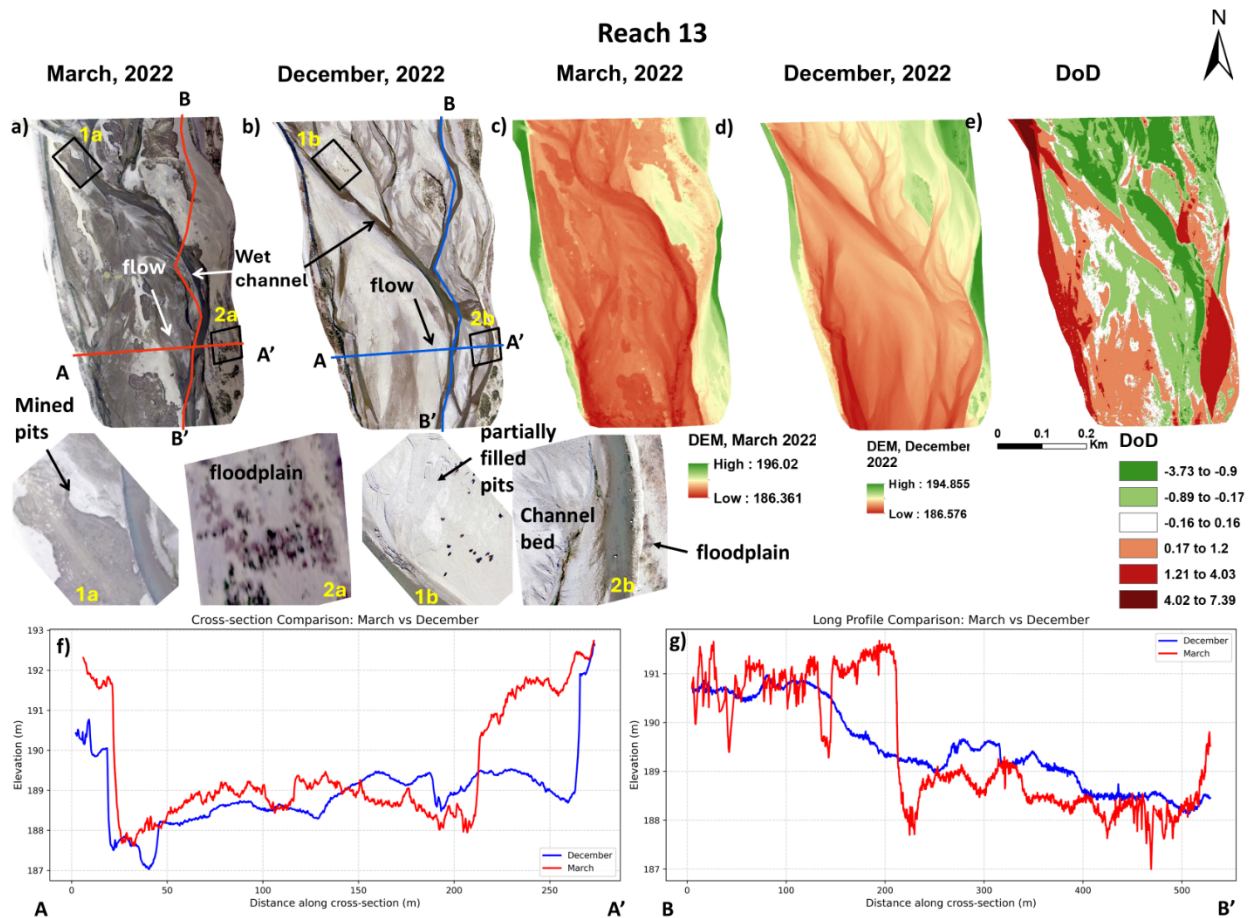


Figure 5.6: a) Orthomosaic image of Reach 13 in March (active mining period) and b) December (post-monsoon period). Inset images 1a and 1b from both the orthomosaics shows filling of mined pits and inset images 2a and 2b shows lateral erosion along the floodplain; c) DTM of Reach 13 in March 2022 and d) December 2022; e) DEM of Difference (March DEM – December DEM), where positive values indicate erosion and negative values indicate deposition, and -0.16 to 0.16 indicates vertical uncertainty calculated from vertical Level of detection (LoD); f) Cross-sectional profile along AA' in Reach 13 derived from December and March DTM. Red indicates March profile, while blue indicates December profile; g) Longitudinal profile along BB' in reach 13 derived from December and March DTM. Red indicates the March profile, while blue indicates the December profile.

Table 5.2: Summary of seasonal geomorphic changes between pre-monsoon (March 2022) and post-monsoon (December 2022) in selected Gaula River reaches, based on UAV-derived orthomosaics and topographic profiles.

Reach	Seasonal Recovery (Dec 2022 vs. Mar 2022)	Key Observations from Orthomosaics	Thalweg shift/wet channel	Profile Analysis (Cross-Section / Longitudinal)
2	Limited recovery	Partial infilling of mined pits; remnants of scars visible; lateral erosion along floodplains	Minimal thalweg shift	Up to 6 m incision downstream; erosion dominant; partial pit infilling in longitudinal profile
3	Limited recovery	Partial infilling of pits; vegetation regrowth in mined zones; lateral erosion	Slight thalweg shift; floodplain erosion	Up to 4 m incision; erosion dominant; spike in March profile linked to floodplain erosion and channel belt expansion
7	Moderate recovery	Bar reshaping; fresh bar deposits; minor vegetation recolonization;	Noticeable thalweg shift; lateral erosion along eastern bank	Deposition up to 8m in longitudinal profile
12	High recovery	Complete infilling of pits; fresh sediment deposits; disconnected channels to micro-braiding observed with narrow wet channels	Micro-braiding observed	Deposition up to 2.5 m in both cross-section and longitudinal profiles
13	Partial recovery	Infilling of pits; notable lateral erosion along floodplains	Micro-braiding; slight thalweg shift observed	Erosion up to 2.5 m (banks) observed in X-section; erosion up to 2 m and deposition up to 1.5 m in pits observed in long profile

5.3.2. Volumetric Analysis of Erosion and Deposition in the Gaula River

The UAV-derived Digital Elevation Models of Difference (DoD) facilitated a spatially explicit assessment of geomorphic change along the monitored stretches of the Gaula River. This specifically captured elevation differences between the end of the mining season (March 2022) and the post-monsoon, pre-mining phase for the subsequent mining season (December 2022).

These variations mainly indicate natural fluvial responses like erosion and deposition during the intervening monsoon period.

Positive elevation changes in the DoD were interpreted as erosion from further lowering or widening of the channel in the monsoon, while negative changes were seen as deposition from sediment accumulation that partially or completely filled the mined depressions in the monsoon. To evaluate the extent of geomorphic recovery or continued degradation, the estimated volumetric deposition across each reach was compared with the officially reported volumes of sand extraction obtained from the Forest Department. This comparison allowed us to assess whether monsoonal sediment inputs were sufficient to replenish the material removed during mining. Reaches where extraction volumes significantly exceeded post-monsoon deposition were flagged as potential zones of unsustainable sediment removal, with implications for channel stability and sediment budgeting.

5.3.2.1. Erosional reaches

Figure 5.2e shows that in Reach 2, the net volume change was approximately $646,498.91 \text{ m}^3$, with erosion ($695,079.97 \text{ m}^3$) significantly exceeding deposition ($48,581.06 \text{ m}^3$). Reach 3 exhibited a similarly dominant erosional signature, with $878,375.93 \text{ m}^3$ of erosion and $83,678.10 \text{ m}^3$ of deposition, resulting in a net loss of $794,697.83 \text{ m}^3$ (Fig. 5.3e). Reach 13 also presented a case of net degradation. While the deposition was $45,955.05 \text{ m}^3$, erosion exceeded that at $66,255.27 \text{ m}^3$, resulting in a net loss of $20,300.22 \text{ m}^3$ (Fig. 5.6e). It should be noted that a small area was only covered by the UAV in reach 13. Additionally, the corresponding reported sand extraction volumes for the mining season 2022-2023 were $223,606.97 \text{ m}^3$ in Reach 2, $109,085.57 \text{ m}^3$ in Reach 3, and $121,550.48 \text{ m}^3$ in Reach 13. These extraction records pertain to the following mining season and are presented here to indicate the removal volumes after the 2022 monsoonal period (Table 5.3). So, even though these reaches were eroded during the previous monsoon season, significant volumes of sand were extracted from these reaches.

5.3.2.2. Depositional Reaches

Reaches 7 and 12 displayed net deposition based on the UAV-based DEM of Difference (DoD) analysis. In Reach 7, net deposition amounted to $1,620,995.07 \text{ m}^3$, with $1,763,760.33 \text{ m}^3$ deposited and $142,765.26 \text{ m}^3$ eroded (Fig. 5.4e). The corresponding reported extraction volume

was 500,401.35 m³, indicating that mining in this reach remained below the volume replenished during the monsoon. Reach 12 showed 864,172.92 m³ of deposition and 78,494.17 m³ of erosion, leading to a net gain of 785,678.75 m³ (Fig. 5.5e), compared to a reported extraction of 281815.81 m³ (Table 5.3). It should also be noted that reach 12 was partially covered by the UAV.

5.4. Synthesis of results

The DoD-based volumetric analysis reveals spatial variability in sediment dynamics across the monitored river reaches following the 2022 monsoon. The results underscore the natural replenishment capacity of the river system after sediment removal through mining.

Reaches 2, 3, and 13 exhibited net erosion, where monsoonal flows failed to replenish volumes lost during the preceding mining season. Reaches 2 and 3 experienced high-flow-induced lateral erosion, likely driven by floodplain undercutting and bank collapse during peak discharge events (see orthomosaics, inset images and cross-sectional images in Fig. 5.2 and Fig. 5.3). Despite this lack of replenishment, further extraction was carried out in 2023, as indicated by the reported mining. In other words, these reaches suffered erosion from the monsoon and were subjected to further sediment depletion by mining, leading to severe degradation. Similar patterns were also observed in reach 13, which experienced net erosion following the 2022 monsoon. Although reach 13 was only partially covered by UAV surveys, the DoD analysis revealed an erosional trend in this particular season. Reach 13 also recorded degradation primarily from lateral erosion and floodplain scouring during peak discharge (see orthomosaics, inset images and cross-sectional images in Fig. 5.6). The decision to permit mining from the reaches 2, 3, and 13 which had not yet recovered from monsoon-induced erosion, points to a lack of process understanding leading to mismatch between natural replenishment patterns and annual licensing practices (Table 5.3).

In contrast to the erosion-dominated segments, reaches 7 and 12 demonstrated clear signals of monsoonal sediment replenishment, with net aggradation occurring across the monitored areas (Fig. 5.4 and 5.5). This pattern indicates that during the post-monsoon period, high flows effectively contributed to infilling and channel restoration, offsetting prior extraction and erosional losses. These observed depositions align with expectations for mined reaches that possess channel morphologies like mined pits, which are conducive to sediment trapping during

flood recession. Notably, the volumetric gains in these reaches were sufficient to accommodate the subsequent season's authorized extraction, implying that mining activities occurred within the limits of natural replenishment (Table 5.3). This correspondence between replenishment potential and mining volume suggests a more sustainable sediment budget in these segments where natural fluvial processes appear capable of maintaining geomorphic equilibrium under current extraction intensities.

Table 5.3: Net aggradation/degradation, reported extraction volumes, and drone coverage for selected monitored reaches of the Gaula River.

Reach	Net Aggradation / Degradation (m³)	Reported Volume extracted (m³)	Drone Coverage
2	-646,498.91	270,220.21	Full
3	-794,697.83	128,245.41	Full
7	1,620,995.07	621,832.21	Full
12	785,678.73	391,134.40	Partial (Half)
13	-20,300.22	145,604.12	Partial (Quarter)

5.5. Episodic Recovery and Sustainable Mining Limits

While the results from the UAV-derived DoD analysis provide important insights into post-monsoonal sediment dynamics, it is crucial to recognise that the findings are based on a single temporal scale and may not reflect long-term replenishment trends. The 2022 monsoon followed a high-discharge year in 2021 (see Fig. 4.4, Chapter 4), which is linked to a return period of roughly 10–15 years. This likely contributed to increased sediment delivery and improved channel recovery in certain reaches. This unusually high flow event may have temporarily filled mined pits and caused lateral redistribution of sediment across the active channel and floodplain. However, such events are episodic, and assuming that similar replenishment will occur every year is inherently flawed. The apparent balance between monsoonal deposition and mining extraction

observed in several reaches may not be sustainable under average or below-average flow conditions, especially in an ephemeral river system that only becomes actively functional during the monsoon.

Long-term observations already point to this risk. As shown in Chapter 2 (section 2.6.3 and Figure 2.11d), the high floods of 2009-2014 led to significant channel widening and sediment redistribution, offering short-term geomorphic recovery. Yet, continued and probably unregulated sand mining in the following years reversed these gains, pushing the river toward incision and loss of connectivity. This historical trajectory reinforces the idea that replenishment observed in a short time cannot be interpreted as evidence of sustainable sediment balance.

To avoid repeating this cycle of temporary recovery followed by cumulative degradation, a regulated and monitored mining strategy must be adopted. This includes integrating UAV-based DoD assessments into annual pre-licensing evaluations, accounting for interannual variability in discharge, and setting extraction thresholds based on both channel response and replenishment capacity. With appropriate feedback mechanisms, rotational or zonal mining could allow certain reaches to recover naturally.

5.6. Summary, conclusions and limitations

The heterogeneity in erosion and deposition across reaches underscores the need for reach-specific assessments rather than uniform extraction guidelines. While some segments (e.g., Reaches 7 and 12) act as sediment sinks during high-flow periods, others (e.g., Reaches 2,3 and 13) appear more vulnerable to lateral erosion and geomorphic instability. These patterns likely reflect variations in channel planform, confinement, sediment availability, and hydraulic energy distribution during flood events. These findings reinforce the importance of using volumetric change detection not only to assess degradation but also to identify zones with sufficient natural resilience, where regulated, rotational mining could be continued with minimal long-term geomorphic disruption.

While UAV-based DoD provides a powerful tool for high-resolution monitoring, certain limitations must be acknowledged. Incomplete UAV coverage in certain areas may lead to an underestimation of the actual volumetric change. Additionally, the temporal gap between UAV

surveys must be carefully aligned with mining activities to attribute erosion or deposition directly to anthropogenic causes. Furthermore, minor geomorphic changes below the vertical LoD threshold (± 0.16 m) were excluded from the analysis to maintain reliability.

Chapter 6

6. 'Hotspots' of sand mining and Policy recommendations

Sand mining in alluvial river systems, while economically vital, poses significant geomorphic and ecological risks when left unregulated or poorly monitored. In rivers subjected to sustained extraction, these risks manifest as channel incision, bank instability, sediment starvation, and habitat degradation. Traditional licensing frameworks rarely account for spatial-temporal variability in river response. To address this, a Hotspot Index was developed for the Himalayan River (Gaula River) and peninsular rivers (Damodar and Sone), integrating geomorphic indicators across multiple temporal and spatial scales to identify segments of the channel most vulnerable to degradation.

6.1. Himalayan River: The Gaula River

The Hotspot Index of the Gaula River in Uttarakhand serves as a comprehensive, reach-scale evaluative metric of mining impacts, integrating multiple indicators: (a) long-term planform dynamics, capturing decadal channel behaviour patterns; (b) sediment connectivity dynamics; and (c) short-term seasonal variations, including monsoonal sediment erosion and replenishment.

By combining these tiers into a weighted index, this approach enables evidence-based zoning for riverbed mining, highlighting areas requiring restriction, restoration, or close monitoring. The methodology is designed to be transferable and adaptable for annual survey-based licensing and long-term river governance.

6.1.1. Methodology

The Hotspot Index for the Gaula River was developed as a multi-tiered decision-support framework, combining parameters derived from spatial analysis, modelling, and field observations. Each tier reflects a distinct temporal and geomorphic perspective, allowing both chronic and episodic vulnerabilities to be captured.

For the Gaula River we have used different parameters namely, (a) Channel belt width (CBW) variability, (b) Average Dry Channel Difference Index (DCDI), (c) Average Vegetated Bar Difference Index (VBDI), and (d) Average Wet Channel Difference Index (WCDI), and (e) Inter-decadal thalweg shifts of each reach to generate a hotspot index. For each of these parameters, we determined thresholds for different classes using Jenks classification and divided them into four classes (1, 2, 3, and 4), where 1 represents the least degraded or stable and 4 represents the most geomorphologically degraded (see Table 6.1). And then the final classes of the hotspot index were computed by integrating them using a relative weightage scheme. The relative weightage scheme was based on our understanding of geomorphic processes, sediment dynamics, field observations and drone surveys. The hotspot Index shows geomorphologically degraded reaches of the Gaula River.

6.1.1.1. Tier 1: Long-term Planform Dynamics

This tier captures decadal-scale channel behavior using remote sensing and spatial metrics that reflect historical changes (Table 6.1). Three main indicators were used:

- a) Channel Belt Width Variability (CBW): Assessed from multi-decadal satellite imagery, indicating lateral mobility and channel narrowing trends, which is a proxy for incision.
- b) Average Difference Indices (DCDI, VBDI, WCDI): Quantify deviations in wet channels, dry channel bars, and vegetated bar areas compared to a reference state.
- c) Thalweg Shift Variability (Inter-decadal): Fixed thalwegs indicate an incised river channel.

Each parameter was normalized and weighted based on geomorphic significance, with the composite Tier 1 score reflecting long-term degradation. The weights were decided based on our geomorphic understanding of the area and were calculated as:

$$\text{Long term Geomorphic Impact (LGI)} = 0.25 * \text{CBW} + 0.25 * \text{DCDI} + 0.25 * \text{VBDI} + 0.10 * \text{WCDI} + 0.15 * \text{Thalweg shift variability}$$

Table 6.1: Tier-1 Long-term Geomorphic Impact(LGI) using planform dynamics indicators.

Parameter	Description	Data Source	Indicator Type	Interpretation
Channel Belt Width Variability (CBW)	Change in lateral extent of active channel belt over multi-decadal period	Historical satellite imagery (1976–2021)	Quantitative	Reduced variability indicates erosion and incision
Vegetated Bar Difference Index (VBDI)	Change in vegetated bar area from reference year	Remote sensing classification (1976-2021)	Quantitative	Decrease suggests habitat loss or sediment extraction impacts
Dry Channel Difference Index (DCDI)	Change in exposed channel surface/fresh deposits from the reference year	Remote sensing classification (1976-2021)	Quantitative	Reduced dry bar area suggests sediment removal or incision
Wet Channel Difference Index (WCDI)	Change in wetted area of the river channel from the reference year	Remote sensing classification (1976-2021)	Quantitative	Shrinkage may indicate hydrologic change or incision
Inter-decadal Thalweg Shift	Displacement of river thalweg over decadal intervals	Channel centerline mapping (multi-year)	Quantitative	Low variability reflects thalweg fixation, typically due to deepening

6.1.1.2. Tier 2: Connectivity and Sediment Transport Disruption

Tier 2 evaluates the impact of sand mining on the river’s sediment transport connectivity, emphasizing how mining activities disrupt the natural delivery of sediment along the channel network. This tier is informed by outputs from the CASCADE sediment transport model, which simulates sediment flux under two scenarios: one representing a no-mining condition and another reflecting an active mining condition. The primary parameter used in this tier is the sediment delivery difference. This is calculated as the absolute difference in sediment flux between the no-mining and mining scenarios for each reach (Table 6.2). A larger absolute flux

drop indicates greater disruption of sediment continuity caused by mining-induced bed armouring. Armoured beds suggest reduced mobility and sediment transport.

Unlike Tier 1, which captures long-term planform change, Tier 2 focuses on process-based, functional degradation, specifically the river's reduced capacity to transport sediment effectively due to anthropogenic interference. This simplification, using the absolute flux drop, provides a quantifiable and scalable metric for comparing sediment delivery disruptions across reaches.

Table 6.2: Tier-2 Connectivity Disruption Index (CDI) using CASCADE model.

Parameter	Description	Data Source	Indicator Type	Interpretation
Connectivity disruption Index (CDI)	Absolute reduction in modeled sediment flux due to mining (CASCADE model)	CASCADE model output (Q97 input)	Quantitative	Greater flux drop indicates stronger connectivity disruption due to mining

6.1.1.3. Tier 3: Short-Term (Seasonal) Morphodynamic Change

Tier 3 incorporates UAV-based, satellite and field-based observations to evaluate seasonal channel response, particularly to monsoonal flows, and their capacity to replenish mined sediments (Table 6.3). Together, Tier 3 captures short-term system resilience or sensitivity to mining-induced changes and hydrological variability.

- a) Seasonal Thalweg Shift and Channel Belt Change (CBW seasonal): Calculated across 5 seasonal periods (e.g., 1995–1994, 1999–1998, 2009–2008, 2014–2013, 2021–2020), indicating anthropogenic disturbance and altered flow paths.
- b) Visual Field Score: Integrated where UAV coverage was unavailable, based on visual signatures (e.g., persistent sand pits, bar scouring, thalweg shifts, and vegetated bar recovery) on Google Earth imagery and field visits.
- c) Replenishment Ratio (RR): Calculated as the ratio of UAV-based Dem of Difference (DoD) derived deposition volume to reported extraction. Negative or low values indicate poor recovery.

Each parameter was normalized and weighed based on geomorphic significance. The weights were decided based on our geomorphic understanding and were calculated as:

**Tier 3 = 0.3 * Seasonal Thalweg shift + 0.3 * Seasonal Channel Belt Width + 0.4 *
Replenishment ratio and Visual Field score**

Table 6.3: Tier-3 Short-Term / Seasonal Indicators.

Parameter	Description	Data Source	Indicator Type	Interpretation
Replenishment Ratio (RR)	Ratio of monsoonal deposition (DoD) to reported extraction volume	UAV-based DoD + Forest Dept. records (2022-2023)	Quantitative	Lower or negative RR indicates limited recovery; high RR suggests replenishment
Seasonal Thalweg Shift	Change in thalweg position between pre-mining and post-mining periods (5 intervals)	Satellite imagery (e.g., Landsat)	Quantitative	Larger shift implies dynamic response
Seasonal Channel Belt Width	Difference in CBW between pre-mining and post-mining (5 years)	Satellite imagery (e.g., Landsat)	Quantitative	Greater width change indicates instability due to mining
Visual Score (Field/Imagery)	Presence of visible mining scars, unrecovered sand pits, or bar degradation	UAV-based orthomosaic /Field visits/ Google Earth	Qualitative (scored)	Higher visual impact score = more disturbance and less natural replenishment

6.1.1.4. Hotspot Index Integration

Each tier was independently normalized and scored, and the final Hotspot Index was derived using a weighted linear combination:

$$\text{Hotspot Index} = 0.5 \times \text{Tier 1} + 0.3 \times \text{Tier 2} + 0.2 \times \text{Tier 3}$$

Weights were assigned based on our geomorphic understanding, indicator robustness, and data confidence. Reaches were then classified using Jenks Natural Breaks into four categories: Stable, Low, Moderate, and High.

6.1.2. Results

The Hotspot Index was calculated for each reach of the Gaula River by integrating normalized scores from Tier 1 (Table 6.4), Tier 2 (Table 6.5), and Tier 3 (Table 6.6). The final scores ranged from 0.15 to 0.80, reflecting varying degrees of geomorphic degradation across the study area (Table 6.7). Using Jenks Natural Breaks classification, the reaches were categorized into four classes (Table 6.7):

- a) Stable: Hotspot Index ≤ 0.298
- b) Low Degradation: 0.299–0.467
- c) Moderate Degradation: 0.468–0.562
- d) High Degradation: > 0.562

Table 6.4: Computation of Long-term Geomorphic Impact (LGI) for tier 1 using morphometric indices from satellite-based planform dynamics (46 years data).

Reach	Average CBW	Average DCDI	Average VBDI	Average WCDI	Thalweg fixing	LGI
1	0.00	0.11	0.14	0.32	0.96	0.24
2	0.24	0.14	0.00	0.14	0.00	0.11
3	0.27	0.21	0.13	0.07	0.03	0.17
4	0.28	0.56	0.11	0.26	0.97	0.41
5	0.68	0.97	0.44	0.38	0.81	0.68
6	1.00	1.00	1.00	0.30	0.98	0.93
7	0.89	1.00	0.74	0.34	1.00	0.84
8	0.47	0.39	0.53	0.39	0.79	0.50
9	0.54	0.59	0.35	0.43	0.84	0.54
10	0.47	0.87	0.12	0.39	0.95	0.55
11	0.36	0.54	0.31	0.40	0.93	0.48
12	0.39	0.54	0.44	0.26	0.74	0.48
13	0.24	0.15	0.54	0.00	0.93	0.37
14	0.09	0.00	0.11	0.59	0.95	0.25
15	0.07	0.04	0.13	0.51	0.95	0.25
16	0.24	0.07	0.11	1.00	0.91	0.34
17	0.20	0.08	0.09	0.71	0.98	0.31
18	0.21	0.17	0.14	0.88	0.90	0.35
19	0.36	0.07	0.07	0.95	0.56	0.30
20	0.15	0.01	0.12	0.88	0.56	0.24

Table 6.5: Computation of Connectivity Disruption Index(CDI) for tier 2 using absolute difference in sediment flux between the no-mining and mining scenarios

Reach	Sediment Delivery (Kg/sec) No Mining	Sediment Delivery (Kg/sec) No Mining	Absolute Flux Difference	Normalized CDI
1	-1283.70	-1130.46	153.24	0.46
2	-88.07	32.91	120.99	0.36
3	-718.54	-431.60	286.94	0.87
4	-489.34	-158.06	331.28	1.00
5	-554.84	-245.91	308.92	0.93
6	-436.78	-249.88	186.90	0.56
7	-566.77	-240.74	326.04	0.98
8	-291.19	-161.49	129.70	0.39
9	-472.49	-237.51	234.98	0.71
10	-241.17	-164.97	76.21	0.23
11	-423.02	-220.63	202.39	0.61
12	-152.15	18.05	170.20	0.51
13	82.96	15.29	67.67	0.20
14	-37.26	-29.04	8.22	0.02
15	-66.46	-37.14	29.32	0.09
16	-2.65	-3.08	0.43	0.00
17	16.77	6.03	10.74	0.03
18	-18.21	-21.31	3.10	0.01
19	-5.59	-3.76	1.83	0.00
20	-11.79	-11.58	0.21	0.00

Table 6.5: Computation of Tier 3 using Seasonal or short-term indicators.

Reach	Normalized Seasonal Thalweg Shift	Normalized Seasonal CBW	Replenishment Ratio + Visual Score (Field/Imagery)	Tier 3
1	0.09	0.00	0.00	0.03
2	0.67	0.05	0.65	0.48
3	1.00	0.00	0.66	0.56
4	0.25	0.30	0.31	0.29
5	0.24	0.58	0.28	0.36
6	0.14	0.58	0.33	0.35
7	0.18	0.41	0.65	0.44
8	0.20	0.26	0.50	0.34
9	0.19	0.56	0.30	0.35
10	0.13	0.36	0.29	0.26
11	0.29	0.41	0.00	0.21
12	0.18	0.07	0.32	0.20
13	0.15	0.18	0.41	0.26
14	0.01	0.16	0.16	0.12
15	0.02	0.31	0.16	0.16
16	0.01	0.68	0.00	0.21
17	0.00	0.39	0.87	0.46
18	0.01	0.28	0.00	0.09
19	0.01	1.00	0.00	0.30
20	0.03	0.17	0.25	0.16

6.1.3. Discussion

The Hotspot Index provided a multi-dimensional assessment of sand mining vulnerability across the Gaula River, drawing upon indicators from long-term channel adjustment (Tier 1), sediment connectivity disruption (Tier 2), and seasonal geomorphic response (Tier 3). The resulting classification revealed clear spatial patterns of degradation and recovery potential that can inform more adaptive, evidence-based sand mining governance. Out of the 20 reaches, 3 were classified as high degradation, 2 as moderate degradation, 5 as low degradation, and 10 as stable.

Reaches such as 5, 6, and 7 are highly degraded reaches, as seen from long-term planform indicators such as narrowed channel belts, loss of fresh deposits and vegetated bars, fixed thalwegs, and sharp reductions in sediment delivery under mining scenarios. Despite the one-time seasonal replenishment or recovery, these reaches represent geomorphic hotspots where continued unsustainable extraction risks severe degradation. As indicated by their scores, these

reaches require the adoption of rotational mining practices (alternate years), allowing for natural recovery.

Although reaches 4 and 9 exhibit some degree of seasonal recovery, they are classified as moderately degraded due to significant sediment delivery disruption and noticeable planform alteration. Notably, the Gaula bridge is located within reach 4, where active scour around bridge piers has been observed (see Figure 2.10c of Chapter 2). To mitigate the risk of structural failure and ensure the long-term stability of the bridge, it is critical to establish a 1 km no-mining buffer zone both upstream and downstream of the barrage. Meanwhile, reach 9 will be better managed through a rotational mining strategy to allow for periodic recovery and sediment rebalancing.

In contrast to the highly and moderately degraded segments, reaches 3, 8, 10, 11 and 12 are marked as low degraded reaches, allowing for regulated extraction within replenishment limits. It is to be noted that pilot channels must be dug out in the elephant corridor (located across reach 11 and partly reach 12) to allow free flow of water during the monsoon. And the aggraded bar of the elephant corridor must be skimmed strategically so that the elevation remains lower than the adjacent bank heights to avoid overbank flow diversion and habitat disturbance. Reaches 1 and 2, both classified as stable, consistently exhibited low Hotspot Index scores across all tiers. These upstream segments lie closer to the mountain front and are characterized by bedrock-controlled, partly confined valley morphology, limiting lateral channel activity and geomorphic degradation. Mining is currently absent in Reach 1, which also contains the Gaula Barrage, and this reach should remain undisturbed to preserve its fluvial stability. In Reach 2, mining is permitted from downstream areas and may continue, provided it remains within natural replenishment thresholds. Downstream reaches 13 to 20, which were not part of historical mining operations, generally reflect lower geomorphic degradation. However, recent observations suggest the emergence of channel and floodplain mining activity, raising concerns about potential habitat loss and morphological disturbance. These lower reaches host perennial surface water, contributing significantly to ecological integrity and supporting aquatic biodiversity. Given their environmental sensitivity, these segments should be excluded from future mining activities to prevent long-term ecological degradation and loss of riverine function.

This synthesis has been summarized in Table 6.7 and shows that vulnerability cannot be inferred from single-year deposition volumes alone, as process-based disruptions (Tier 2) and long-term morphological degradation (Tier 1) reveal cumulative risks. The tiered approach ensures that reaches with different types of vulnerabilities, whether long-term, functional, or seasonal, are all identified. By aligning annual licensing with geomorphic resilience and sediment delivery thresholds, the Hotspot Index (Table 6.7 and Figure 6.1) offers a practical, scalable tool for sustainable riverbed mining governance.

Table 6.6: Computation of Hotspot Index for the Gaula River

Reach	LGI (Tier1)	CDI (Tier2)	Tier3	Hotspot	Degradation Class	Drivers and impacts	Recommendations
1	0.24	0.46	0.03	0.26	Stable	These reaches are closer to the mountain front, and show bedrock and tectonics controlled partly confined valley bottom. Hence, these reaches show minimal geomorphic degradation. Stream power is high in reach 1 but drops in reach 2, suggesting aggradation in reach 2.	Mining in reach 1 does not occur and should be left as such. The Gaula barrage is also located in reach 1. The mining starts from the downstream areas of reach 2 and can continue, but within the replenishment limit.
2	0.11	0.36	0.48	0.26			
3	0.17	0.87	0.56	0.46	Low	The long-term planform impacts (Tier 1) are not that high, but the connectivity has been disrupted, and recently in 2023 it's been subjected to bank and bed erosion. The stream power is also relatively high, suggesting erosive reach.	Mining can be permitted, but within the replenishment limit.
4	0.41	1.00	0.29	0.56	Moderate	This reach shows significant sediment delivery disruption in the mining scenario. This reach also exhibits moderate long-term geomorphic degradation (Tier 1). The monsoonal sediment recovery for 2023 has been low, and the reach shows visible degradation (mining scars) even after the monsoon.	Rotational mining (alternate years to allow the river to rejuvenate or replenish) is recommended, and mining should be left out at least 1 Km upstream and downstream of the Bridge.
5	0.68	0.93	0.36	0.69	High	These reaches show severe degradation in long-term planform dynamics, including channel belt narrowing, loss of vegetated bars, and fresh deposits, and a fixed thalweg indicating incision (Tier 1). These reaches also show significant sediment delivery disruption	Rotational Mining can occur (alternate years to allow the river to rejuvenate or replenish), and mining must occur within the replenishment limit.
6	0.93	0.56	0.35	0.70			

7	0.84	0.98	0.44	0.80		(Tier 2). They represent the most geomorphologically sensitive zones. But recently, in 2023, there has been monsoonal replenishment, and mining has been within limits.	
8	0.50	0.39	0.34	0.44	Low	This reach exhibits moderate long-term geomorphic degradation, as reflected in Tier 1 indicators such as narrowed channel belt width, loss of vegetated and fresh deposited bars, and a fixed thalweg. In contrast, the impact on connectivity (Tier 2) is lower, and the extent of seasonal recovery (Tier 3) for 2023 is higher. The stream power is also relatively low, suggesting a slightly aggrading reach.	Mining can be permitted, but within the replenishment limit.
9	0.54	0.71	0.35	0.55	Moderate	This reach shows very high Tier 2 scores, indicating significant sediment delivery disruption. This reach also exhibits moderate to high long-term geomorphic degradation (Tier 1). In contrast, monsoonal sediment recovery for 2023 has been modest.	Rotational Mining can occur (alternate years to allow the river to rejuvenate or replenish), and mining must occur within the replenishment limit.
10	0.55	0.23	0.26	0.39	Low	These reaches exhibit moderate long-term geomorphic degradation, as reflected in Tier 1 indicators such as narrowed channel belt width, loss of vegetated and fresh depositional features, and a fixed thalweg. The impact on connectivity (Tier 2) is low in reach 10 but higher in reach 11 and 12. But the extent of seasonal recovery (Tier 3) for 2023 is higher in all these reaches.	Mining can be permitted, but within the replenishment limit. Pilot channels must be dug out in the elephant corridor to allow free flow of water. The aggraded bar of the elephant corridor must be skimmed (as a river training measure) so that the elevation remains lower than the elevation of adjacent bank heights to avoid the risk of flooding.
11	0.48	0.61	0.21	0.47			
12	0.48	0.51	0.20	0.43			
13	0.37	0.20	0.26	0.30	Stable	The downstream reaches have not been subjected to historical mining; hence these	The lower reaches are where the surface water is seen, and the river has perennial
14	0.25	0.02	0.12	0.16			

15	0.25	0.09	0.16	0.19		reaches show lower geomorphic degradation. But recently, there have been signs of floodplain and channel mining in these reaches, which could potentially degrade the riverine habitat.	water. These areas are of high ecological importance and should be left out of mining.
16	0.34	0.00	0.21	0.21			
17	0.31	0.03	0.46	0.26			
18	0.35	0.01	0.09	0.20			
19	0.30	0.00	0.30	0.21			
20	0.24	0.00	0.16	0.15			

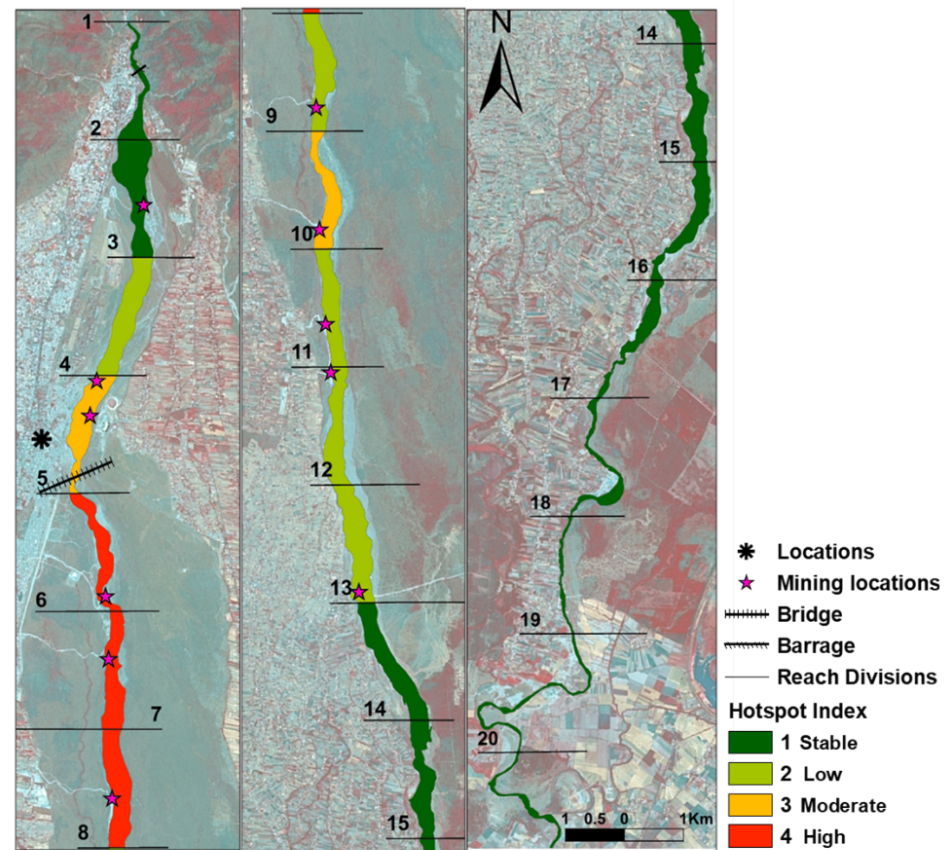


Figure 6.1: Hotspot Index for the Gaula River

6.2. Peninsular Rivers: Damodar and Sone

The Damodar and Sone rivers, major peninsular tributaries of the Ganga, have experienced extensive sand mining over the past decades. Unlike Himalayan rivers such as the Gaula, which have high sediment supply and more seasonal variability, these rivers are not sediment-rich. Due to the lack of detailed sediment transport data, this study aims to identify the most degraded reaches of the Damodar and Sone based on long-term planform dynamics reconstructed from temporal satellite images. A Hotspot Index was developed using changes in key morphometric indicators derived from spatio-temporal data. This index incorporates channel-scale variables that reflect changes in the river planform.

6.2.1. Methodology

In the absence of high-resolution temporal datasets and a field data-based sediment transport model, the hotspot index for the Sone and Damodar rivers was developed using only Tier 1 indicators, focused on evaluating long-term planform dynamics. This approach aligns with the methodology applied in the Gaula River, offering a robust, spatially consistent means to assess geomorphic instability associated with sand mining. Five geomorphic parameters were selected to capture key aspects of planform change:

- a) WCC: Wet Channel Change in Area from Initial Year
- b) DCC: Dry Channel Change in Area from Initial Year
- c) ARCC: Active River Channel Change in Area from the Initial Year
- d) BA/CA: Changes in Bar Area/ Channel Area from the Initial Year
- e) BI: Braiding Index Change from Initial Year

Each of these parameters was first normalized using min-max normalization to a common scale (0 to 1) to allow for cross-comparison and unbiased weighting. The final Hotspot Index was then calculated using a weighted linear combination of the normalized values:

$$\text{Hotspot Index} = (0.4 \times \text{ARCC_norm}) + (0.3 \times \text{BA/CA_norm}) + (0.3 \times \text{BI_norm})$$

Table 6.7: Tier-1 parameters used for calculating the Hotspot Index for the Damodar and Sone rivers.

Parameter	Description	Data Source	Indicator Type	Interpretation
Active River Corridor Change (ARCC)	Change in the total active corridor, combining wet and dry channel areas	Multi-year satellite imagery	Quantitative	Reduction implies incision; expansion indicates aggradation
Bar Area to Channel Area Ratio Change (BA/CA)	Variation in the ratio of bar surface to total channel area	Classified satellite imagery	Quantitative	Lower values imply bar loss or degradation; higher values reflect aggradation
Braiding Index Change (BI)	Change in number and arrangement of channel threads from the initial year	Multi-year satellite imagery	Quantitative	A decrease indicates reduced sedimentation; increase implies higher sedimentation

6.2.2. Results

Damodar River

The Hotspot Index was calculated for each reach of the Damodar by incorporating normalized planform parameters derived from spatio-temporal satellite imagery (Tables 6.8 and 6.9). The final scores ranged from 0.07 to 0.69, reflecting varying degrees of geomorphic degradation across the assessed reaches (Table 6.9 and Figure 6.2). Using Jenks Natural Breaks classification, the reaches were grouped into four classes:

- a) Stable: Hotspot Index ≤ 0.15
- b) Low Degradation: 0.16 to 0.30
- c) Moderate Degradation: 0.31 to 0.43
- d) High Degradation: > 0.44

This classification highlights the spatial variation in geomorphic response, with several reaches showing pronounced changes in channel morphology based solely on long-term planform indicators. The resulting Hotspot Index values provide a quantitative basis for identifying areas most affected by or susceptible to degradation due to sand mining and associated pressures.

Table 6.8: Computation of Hotspot Indices for Damodar River

Reach	ARCC normalized	BA/CA normalized	BI normalized	Hotspot Index	Degradation Class	Drivers and Impacts	Recommendations
1a	0.05	0.20	0.21	0.14	Stable	These reaches fall in the zone of granite gneiss bedrock. Hence, sediment availability is poor.	These reaches are bedrock-controlled and, hence, are not aggradational zones and should be excluded from mining.
1b	0.08	0.22	0.18	0.15	Stable		
2a	0.03	0.21	0.21	0.14	Stable		
2b	0.24	0.23	0.25	0.24	Low	These reaches fall in the zone of granite gneiss bedrock. Hence, sediment availability is poor. Despite the river not having sufficient sand deposits, mining activities started recently. The wet channel declined slightly from the reference year, suggesting possible incision.	These reaches are bedrock-controlled and hence are not aggradational zones and should be left out of mining.
3a	0.24	0.20	0.36	0.26	Low		
3b	0.21	0.17	0.32	0.23	Low		
3c	0.00	0.17	0.33	0.15	Stable	The wet channel declined slightly from the reference year, suggesting possible incision.	Rotational mining can occur, providing sufficient time for the river to replenish during the monsoon. Mining should be left for at least 3 years in the peninsular rivers.
4a	0.64	0.38	0.26	0.45	Moderate	There is a significant reduction in the active river channel width, with severe degradation in bar area.	Mining should be halted for the river to replenish itself close to the reference year. Bar skimming should be enforced without altering the riverbed slope.
4b	0.99	0.34	0.36	0.61	High	The river has significantly degraded here in terms of the bar area,	Mining should not occur here till near reference conditions have been restored.

4c	0.84	0.18	1.00	0.69	High	braiding bars, active river channel width and wet channel.	
4d	0.57	0.23	0.44	0.43	Moderate	The river dynamics are significantly controlled by the Durgapur barrage. Despite being upstream of the barrage, the active river area has declined.	Mining should not occur here till near reference conditions have been restored.
5a	0.20	0.09	0.40	0.23	Low	This is downstream of Durgapur Barrage.	Rotational mining can occur. But a minimum of 500 m should be left from the critical structures.
5b	0.93	0.21	0.61	0.62	High	The river has significantly degraded here in terms of the bar area, braiding bars, active river channel width and wet channel.	Mining should not occur here.
6	0.59	0.34	0.10	0.37	Moderate	There has been a significant reduction in wet channel and sand deposits in recent years.	Rotational mining can occur, providing sufficient time for the river to replenish during the monsoon. Mining should be left for at least 3 years.
7a	0.36	0.21	0.30	0.29	Low	There is a slight reduction in the wet channel and sand bars.	Rotational mining can occur.
7b	0.34	0.46	0.06	0.29	Low		
8	1.00	0.27	0.25	0.55	High	The river has significantly degraded here in terms of the bar area, braiding bars, active river channel width and wet channel.	Mining should not occur here.

9	0.66	0.08	0.43	0.42	Moderate	The river has degraded here in terms of the bar area, braiding bars, and wet channel.	Rotational mining can occur, providing sufficient time for the river to replenish during the monsoon. Mining should be left for at least 3 years.
10	0.12	0.11	0.00	0.08	Stable	Reach 10 was degraded earlier but has recovered in recent years. Reach 11 hasn't degraded much except loss of few vegetated bars which turned into floodplain.	Rotational mining can occur.
11a	0.02	0.00	0.19	0.07	Stable		
11b	0.59	0.45	0.24	0.44	Moderate	The river has significantly degraded here in terms of the mid-channel bars and reduced braiding bars.	Rotational mining can occur, providing sufficient time for the river to replenish during the monsoon. Mining should be left for at least 3 years.
11c	0.53	0.53	0.09	0.40			
12	0.32	0.59	0.02	0.31			
13	0.55	0.71	0.01	0.44	High	The river has significantly degraded here in terms of the bar area and lateral erosion. It shows the downstream impact of sand mining.	Mining should not occur here.
14	0.56	1.00	0.20	0.58	High		

6.2.2.1. Sone River

The Hotspot Index for the Sone River was computed for three windows using normalized planform metrics extracted from multi-temporal satellite imagery (refer to Tables 6.8 and 6.10). The resulting index values ranged from 0.11 to 0.84, indicating a broad spectrum of geomorphic degradation across the studied reaches and windows (Table 6.10 and Figure 6.3). The reaches were categorized into four degradation classes:

- a) Stable: Hotspot Index ≤ 0.19
- b) Low Degradation: 0.20 to 0.42
- c) Moderate Degradation: 0.43 to 0.67
- d) High Degradation: > 0.68

This classification highlights the spatial variation in geomorphic response, with several reaches showing pronounced changes in channel morphology based solely on long-term planform indicators.

Table 6.9: Computation of Hotspot Index for Sone River

Reach	Window	ARCC normalized	BA/CA normalized	BI normalized	Hotspot Index	Degradation Class	Drivers and Impacts	Recommendations
1	1	0.30	0.00	1.00	0.42	Low	The river transformed from braiding to sinous to straight to disconnected.	Rotational mining can occur. Bar skimming should be enforced, and wet pit mining should be strictly avoided.
2	1	1.00	0.74	0.74	0.84	High	The river transformed from braiding to sinous to straight to disconnected. There has been significant loss in bar area.	Mining should not occur here.
3	1	0.47	0.66	0.92	0.66	Moderate	There has been significant loss in bar area.	Rotational mining can occur. Bar skimming should be enforced, and wet pit mining should be strictly avoided.
4	2	0.05	0.28	0.00	0.11	Stable	There has not been much change in terms of sand bars and wet channel.	Rotational mining can occur. Bar skimming should be enforced.
5	2	0.02	0.43	0.08	0.16			
6	2	0.00	0.67	0.03	0.21			
7	2	0.05	0.36	0.05	0.14			
8	2	0.10	0.52	0.04	0.21			
9	3	0.75	1.00	0.28	0.69	High	There has been severe floodplain and in-channel mining leading to complete loss of bars and wet channel.	Mining should not occur here.
10	3	0.79	0.95	0.29	0.69			

6.2.3. Discussion

The hotspot index analysis has helped identify the most degraded reaches in the Damodar and Sone Rivers, enabling a targeted understanding of regions requiring urgent management and intervention. A key insight from this study is the pronounced downstream impact of sand mining, which is a distinctive feature observed in Peninsular rivers, in contrast to Himalayan rivers, where degradation is typically localized to mining sites.

6.2.3.1. Damodar River

The Damodar River presents striking evidence of downstream geomorphic impact. Reaches 12, 13, and 14 (Fig. 6.2), which are located downstream and show minimal or no direct mining activity, are among the most degraded in the entire study area. This strongly suggests that mining activity upstream is triggering sediment starvation downstream, weakening sediment replenishment processes and destabilising the river morphology.

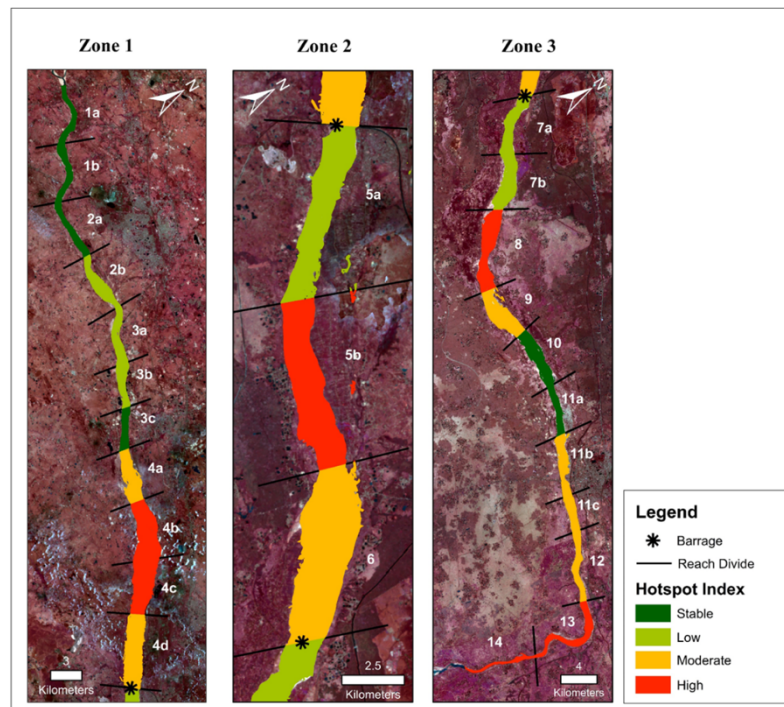


Figure 6.2: Hotspot Index of Damodar River.

Upstream reaches like 4b, 4d, 5b, and 6 also show high degradation, resulting from the cumulative effects of onsite mining and regulated flow. These factors act together to disrupt sediment transport continuity, particularly in Zone 3, the most active mining zone. Within zone3, while most

reaches are moderately or highly degraded, reaches 7a, 9, 10, and 11a remain stable or less affected, possibly due to site-specific resilience, channel width, or sediment source variability. The recommendations based on each reach are presented in Table 6.9.

6.2.3.2. *Sone River*

In the Sone River, three study windows were further divided into ten sub-reaches to assess spatial variability (Fig. 6.3). Reaches 9 and 10 in Window 3 emerged as high degradation zones, impacted not only by direct sand mining but also by significant downstream effects. The depletion of sediment due to upstream mining reduces sediment supply to downstream sections, leading to sediment starvation, loss of sediment bars, and progressive morphological degradation.

Similarly, Window 1 also shows signs of compound degradation from both mining and flow regulation. Reach 2 is highly degraded, while Reaches 1 and 3 show low and moderate changes. On the other hand, Window 2 remains relatively stable, despite ongoing mining in certain sections. This is probably due to rotational mining being practised. The recommendations based on each reach are presented in Table 6.10.

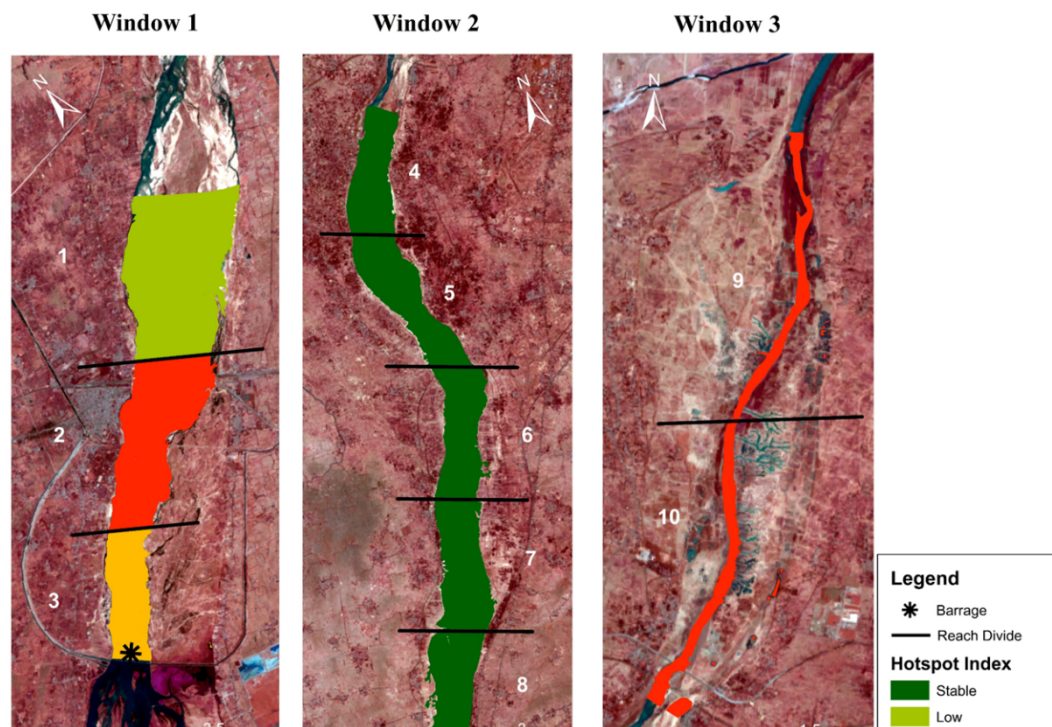


Figure 6.3: Hotspot Index of the Sone River

6.3. Policy Implications for Sustainable Sand Mining in Himalayan and Peninsular Rivers

Rivers are a major source of sand and gravel for numerous reasons: (a) cities tend to be located near rivers so transport costs are low; (b) river energy grinds rocks into gravels and sands, thus eliminating the cost of mining, grinding, and sorting rocks; and (c) the material produced by rivers tends to consist of resilient minerals of angular shape that are preferred for construction (whereas wind-blown deposits in deserts are rounder and less suitable) (Koehnken et al., 2020). The term “sand mining” is used as a generic term to encompass the extraction of riverine aggregates, regardless of particle size. Sand mining activities are among the numerous recognised pressures affecting riverine ecosystems, where biodiversity is already in rapid decline (World Wildlife Fund, 2018). Increasingly, there are media reports about the negative environmental and social impacts of sand mining, and as calls grow for stronger regulation of mining (Schandl et al., 2016), there is a need to understand the scientific evidence of mining impacts to underpin management.

In recent times, the concern about the impacts of sand mining has arisen globally due to several factors, and the most important of these include the lack of reliable data on sand mining and extraction rates, as much of the sand mining activity is unregulated and unmonitored (Hackney et al., 2020). There is also a lack of sediment transport data, which makes the estimates of replenishment unreliable and uncertain. However, the availability of modern technologies, such as high-resolution remote sensing from drones and sediment transport models like CASCADE, can overcome some of these problems and offer reliable solutions. Further, it is also important to understand the impacts of sand mining, which could be direct as well as indirect (Koehnken et al., 2020). Direct impacts are those in which the extraction of material is directly responsible for the ecosystem impact, such as due to the removal of floodplain habitat. Indirect impacts are related to ecosystem changes that are propagated through the system due to physical changes in the river system resulting from sand extraction. For example, the removal of material from a river can alter the channel, river hydraulics, or sediment budget, which in turn can alter the distribution of habitats and ecosystem functioning. These types of impacts can be difficult to attribute to sand mining, as they may require long time frames to emerge, and other interventions can result in similar changes. The situation is further complicated by the existence of geomorphic thresholds

in river systems (Schumm, 1979). Alterations linked to the removal of sand from rivers may not be gradual and/or linear, and only limited changes may be observed for an extended period, but once a threshold is reached, change may become rapid and irreversible. Whether the impacts of sand mining are positive, neutral, or negative depends on the situation and perceptions of different stakeholders. For example, river incision could be perceived as positive by stakeholders if it reduces flood risk; however, it can also be considered a change from natural or a decline in geomorphic or ecosystem characteristics as negative.

In India, unsustainable sand mining has been rampant despite the 2016 guidelines issued by the Ministry of Environment, Forests and Climate Change (MoEFCC), Government of India. To strengthen the existing system and to curb illegal and unsustainable mining, the MoEFCC released the 'Enforcement and Monitoring Guidelines for Sand Mining 2020' with the following objectives:

- a) Identification and quantification, and efficient use of Mineral Assets.
- b) To control sand and gravel mining in the Country from its recognition by consumers and the general public to its final end-use.
- c) Use of IT-enabled systems and the latest sand mining monitoring technologies at every phase.
- d) Reduced demand & shortages in supply.
- e) Development of a Sand replenishment process.
- f) Monitoring post-Environmental Clearance.
- g) Environmental Assessment Protocol
- h) Monitor illegal mining instances.

The MoEFCC sand mining policy 2020 is a very comprehensive document, and among other things, it suggests the use of technologies like drones with night vision for surveillance of sand mining sites, steps to identify sources of sand, procedures for replenishment of sand, post-environmental clearance monitoring of sand mining sites, a procedure for environmental audit of such areas and steps to control the instances of illegal mining. The salient points of this document are as follows:

- a) A comprehensive District Survey Report and Mining Plan must be developed in which all potential river mining zones/areas should be identified. Table 6.11 shows the typical structure and content of the DSR and Mining Report
- b) The latitude and longitude of each mining lease shall be mentioned in the Letter of Intent issued to the potential mining lease.
- c) Environmental Clearance must be obtained for all mining sites.
- d) No riverbed mining in monsoon, as defined by IMD (typically after 30th June), should be permitted.
- e) Replenishment studies should be conducted regularly for which the following protocols are prescribed:
 - i. 1st Survey: To be done in April to estimate the level of mining lease before monsoon.
 - ii. 2nd Survey: Closing of the mines for the monsoon season for quantification of the materials excavated before the onset of monsoon.
 - iii. 3rd Survey in the post-monsoon period to estimate the material deposited/replenished.
 - iv. 4th Survey at the end of March of the subsequent year to quantify how much material is excavated.
 - v. The areas of deposition and erosion for each cross-section should be determined.
 - vi. Estimation of the bed load transport should be done with analytical models for replenishment estimation
 - vii. Iso-pluvial maps should be acquired from the Meteorological Department for the estimation of rainfall.
 - viii. Runoff coefficient measurement should be carried out.
 - ix. Peak flood discharge estimation should be done every year.

Table 6.10: Structure of the District Survey Report and Mining Plan

District Survey Report (DSR)	Mining Plan
<ul style="list-style-type: none"> • Inventory of RBM • Defining the sources of sand • Channelization of river bed on a map showing areas of aggradation and degradation, zones of bank protection and 'no mining zone' (use of UAVs encouraged for surveys) • Permanent boundary pillars • Mining lease to be selected in the depositional areas • Mining outside the river bed only if there is enough replenishment • Potential impacts on forest, protected area, habitation, bridges to be avoided (necessary certificates required) 	<ul style="list-style-type: none"> • Original ground level recorded at an interval not more than 10M x 10M along & across the length of the river • Mapping of the deposition or aggradation reaches in the river • Sediment rating curve for the potential sites (to be checked against the extracted RBM) • Extraction across the active channel in dry season – dry and abandoned channels to be preferred (no diversion allowed) • No extraction in erosional reaches • Extent of lateral migration to be identified (extraction within the zone) • Mining depth < 3 m and distance from bank 1/4th of river width • Piedmont zone – mining away from channel banks

6.3.1. **Himalayan River: Gaula**

This case study on the Gaula River above utilized historical remote sensing data, drone technology and field-data-based sediment transport model CASCADE, which have provided important insights about the geomorphic processes operating in this region. Based on this, we would like to offer a few additional guidelines with specific reference to the Himalayan rivers:

- a) A particular stretch of the river is characterized by aggradation or degradation (sediment deposition or erosion) depending upon (a) stream power and (b) sediment supply. While the stream power is a function of water discharge and slope, the sediment supply is influenced by upstream/hinterland characteristics. The stream power determines the **imposed boundary conditions** within which the river performs its geomorphic activities. Therefore, the first criterion is to identify the imposed boundary conditions of the river. Valley bottom confinement also serves as a tool to identify imposed boundary conditions.
- b) After identifying the imposed boundary conditions, a historical analysis of satellite images and available maps must be done. The focus should be on the long-term trend

- rather than one-time mapping. The decision regarding sand mining in a river should not be governed on its present state or morphology, but on defining a **‘reference state’**, which is a minimum acceptable or agreed upon morphological and ecological state of the river. The reference state does not need to be the pristine state of the river but should be based on the dynamic behaviour of the river and an understanding of its processes and forms. All mapping and calculations must assess how much deviation has occurred relative to the reference condition.
- c) Next, all mining should be located around the aggradational stretches, or where the rivers are stable and least degradation has happened. To map the hotspots of aggradation/degradation, the associated processes, such as in-channel dynamics (vegetated bars, wet channel, dry channel and bars) and bank erosion, should also be investigated. The causal factors (natural vs anthropogenic) should be established.
 - d) While the spatial distribution of aggradational areas may be crucial, it is also important to understand the depth of permissible mining at these locations. Depth of mining should be determined based on the rates of accumulation (sand budget) at these locations, and it should not alter the general slope of the stretch in a major way. This requires site-specific topographic, hydrologic and hydraulic information and some measurements. Modern technologies such as UAV-based DEM of Difference and empirical sediment transport models can be employed. Such data is used to determine the amount and depth of sand that can be removed from a site. In general, the extractable volume of sand should never exceed the volume that can be replenished by normal hydraulic transport. Therefore, bar skimming or scraping is considered the most sustainable way of sand mining.
 - e) Riverbed mining in selected areas should always be taken up in patches to maintain the riffle-pool structure of the river longitudinally. This is an important ecological criterion and must be followed. A sudden change in slope due to mining can create a ‘knick-point’ and this can induce downstream degradation, thereby damaging bridge piers and buried pipelines, if any. Uniform mining all along the river also alters the slope and increases the runoff in high flow periods, leading to increased flood risk.

Therefore, the maintenance of a desired slope in a river is the key to maintaining the river form, and this must be established through field/modelling studies before commencing the mining.

- f) A minimum 1 km no-mining buffer zone upstream and downstream of key structures such as bridges, barrages, and piers should be enforced to prevent scour, bank collapse, and structural instability. This rule should be applied proactively in geomorphologically unstable reaches, where bridge foundation exposure has already been recorded.
- g) Cutting of river banks and widening of river channels must be avoided during sand mining. This will disturb the hydrologic regime of the river significantly and will also harm the riparian vegetation and soil. Therefore, management measures must be taken up in areas earmarked for sand mining, such as river stabilization, revegetation of buffer strips and impacts of the linked floodplain.
- h) Several river systems or several reaches in a river are naturally aggrading due to exceptionally large sediment flux from the source areas. These rivers or specific reaches pose serious threats to the existing infrastructure and also enhance the flood risk due to large-scale channel aggradation. At the same time, they offer potential areas for sand mining or dredging. It is therefore crucial to have a sediment management strategy for these rivers. It may be extremely beneficial to integrate river training works with sand mining activities, and the concerned departments should work in tandem. However, precautions should be taken not to change the form and slope of the river in a major way.
- i) Limited mining of the filled paleochannels away from the active channels is a good option but again some caution is required as they also serve as important areas for groundwater recharge. Lowering of the riverbed results in a corresponding lowering of the water table, causing the wells in the vicinity of the river to dry out, thereby increasing the chances of the local communities losing their sources of drinking water. Excessive mining from these areas may, therefore, impact the groundwater potential

of the region, and therefore, a minimum of 3-4 m sand layer (undisturbed unsaturated zone) should be left for the protection of the aquifer.

- j) In areas where mining has been done before or is being carried out, continuous monitoring of the river form and position both upstream and downstream of the sand mining areas must be carried out regularly to avoid any undesirable impacts. Alluvial rivers often transmit the disturbance upstream and downstream and such responses are governed by geomorphic thresholds, feedback and lags. Continuous monitoring can help detect such responses and take necessary action.
- k) All ecological hotspots along the river should be avoided for sand mining, irrespective of their regime. The first level zoning of all such habitats must be carried out before planning the sand mining activities, and these areas should be excluded from the plans.
- l) The most fundamental point about sand mining is that if undertaken at all, the extraction of riverbed sand should be conducted at rates that are less than the rate at which sand is redeposited from either bedload or suspended load transported from upstream. Therefore, **rotational mining** is suggested in these cases where enough time should be provided to the river to replenish its sediments in a stretch, and therefore, mining areas should shift regularly along the river. In Himalayan rivers, where the sediment supply is high, we recommend mining in alternate years.

6.3.2. **Peninsular Rivers: Damodar and Sone**

Unlike Himalayan River systems, peninsular rivers such as the Damodar and Sone are characterized by less dynamic fluvial behaviour and are not driven by active tectonic processes. Hence, these rivers receive limited sediment supply, making them more sensitive to sediment extraction pressures. As a result, sand mining policies must be adapted to reflect these distinct geomorphic and sedimentary contexts. Drawing from our analysis of long-term satellite-derived data for the Damodar and Sone rivers, we propose the following additional policy recommendations tailored to the specific conditions of Peninsular River systems:

- a) In Himalayan rivers, imposed boundary conditions are largely governed by steep gradients and active tectonics. Hence, stream power can be used to understand the imposed boundary conditions. In contrast, Peninsular rivers flow through relatively flat terrains and are typically sediment-supply-limited, making lithology a more reliable indicator for **imposed boundary conditions**. Bedrock-dominated stretches, characterized by minimal sediment availability, contrast with alluvial segments, which contain extractable deposits and therefore serve as more appropriate targets for mining. This serves as a key step in identifying suitable zones (aggradation or sediment accumulation and degradation, or erosion) for riverbed mining along the river corridor. Mining activities should be concentrated only in aggradational zones. Valley bottom confinement can also be used to delineate the area within which the river performs its geomorphic work.
- b) After identifying the imposed boundary conditions, a historical analysis of satellite images and available maps must be done. The focus should be on the long-term trend rather than one-time mapping. The decision regarding sand mining in a river should not be governed by its present state or morphology, but on defining a '**reference state**', which is a minimum acceptable or agreed upon morphological and ecological state of the river. The reference state does not need to be the pristine state of the river, but should be based on the dynamic behaviour of the river and an understanding of its processes and forms. All mapping and calculations must assess how much deviation has occurred relative to the reference condition.
- c) Next, all mining should be located around the aggradational stretches, or where the rivers are stable and least degradation has happened. To map the hotspots of aggradation/degradation, the associated processes, such as in-channel dynamics (vegetated bars, wet channel, dry channel and bars) and bank erosion, should also be investigated. The causal factors (natural vs anthropogenic) should be established.
- d) While the spatial distribution of aggradational areas may be crucial, it is also important to understand the depth of permissible mining at these locations. Depth of mining should be determined based on the rates of accumulation (sand budget) at these

- locations, and it should not alter the general slope of the stretch in a major way. This requires site-specific topographic, hydrologic and hydraulic information and some measurements. Such data is used to determine the amount and depth of sand that can be removed from a site. In general, the extractable volume of sand should never exceed the volume that can be replenished by normal hydraulic transport. Therefore, **bar skimming or scraping** is considered the most sustainable way of sand mining.
- e) Riverbed mining in selected areas should always be taken up in patches to maintain the riffle-pool structure of the river longitudinally. This is an important ecological criterion and must be followed. A sudden change in slope due to mining can create a 'knick-point' and this can induce downstream degradation, thereby damaging bridge piers and buried pipelines, if any. Uniform mining all along the river also alters the slope and increases the runoff in high flow periods, leading to increased flood risk. Therefore, the maintenance of a desired slope in a river is the key to maintaining the river form, and this must be established through field/modelling studies before commencing the mining.
 - f) Cutting of river banks and widening of river channels must be avoided during sand mining. This will disturb the hydrologic regime of the river significantly and will also harm the riparian vegetation and soil. Therefore, management measures must be taken up in areas earmarked for sand mining, such as river stabilisation, revegetation of buffer strips and impacts of the linked floodplain.
 - g) A minimum 500 m no-mining buffer zone upstream and downstream of key structures such as bridges, barrages, and piers should be enforced to prevent scour, bank collapse, and structural instability in peninsular rivers. This rule should be applied proactively in geomorphologically unstable reaches, where bridge foundation exposure has already been recorded.
 - h) Sediment accumulation often occurs upstream of dams and barrages. They offer potential areas for sand mining or dredging. Hence, to avoid overbank flow time to time-to-time monitoring should be done. It is therefore crucial to have a sediment management strategy for these rivers. It may be extremely beneficial to integrate river

training works with sand mining activities, and the concerned departments should work in tandem. However, precautions should be taken not to change the form and slope of the river in a major way.

- i) Limited mining of the filled paleochannels away from the active channels is a good option, but again, some caution is required, as they also serve as important areas for groundwater recharge. Lowering of the riverbed results in a corresponding lowering of the water table, causing the wells in the vicinity of the river to dry out, thereby increasing the chances of the local communities losing their sources of drinking water. Excessive mining from these areas may, therefore, impact the groundwater potential of the region, and therefore, a minimum of 3-4 m sand layer (undisturbed unsaturated zone) should be left for the protection of the aquifer.
- j) In areas where mining has been done before or is being carried out, continuous monitoring of the river form and position both upstream and downstream of the sand mining areas must be carried out regularly to avoid any undesirable impacts. Alluvial rivers often transmit the disturbance upstream and downstream, and such responses are governed by geomorphic thresholds, feedback and lags. Continuous monitoring can help detect such responses and take necessary action.
- k) All ecological hotspots along the river should be avoided for sand mining, irrespective of their regime. The first level zoning of all such habitats must be carried out before planning the sand mining activities, and these areas should be excluded from the plans.
- l) The most fundamental point about sand mining is that if undertaken at all, the extraction of riverbed sand should be conducted at rates that are less than the rate at which sand is redeposited from either bedload or suspended load transported from upstream. Therefore, **rotational mining** is suggested in these cases where enough time should be provided to the river to replenish its sediments in a stretch, and therefore, mining areas should shift regularly along the river. In peninsular rivers, where the sediment supply is low, we recommend a replenishment time of 3-4 years.

In summary, it is important to note that the geomorphic impacts of sand mining are quite different in the Himalayan and peninsular rivers, and therefore, the strategy for sustainable mining as well as the guiding policies need to be designed differently. Table 6.12 highlights the major differences in the policy drives for these two different settings.

Table 6.11: Policy recommendations for sand mining: Himalayan vs Peninsular rivers

Policy Driver	Himalayan Rivers (e.g., Ganga)	Peninsular Rivers (e.g., Damodar, Sone)
Dominant Controls	High stream power, tectonic activity, steep slopes	Lithology, limited sediment supply, flat terrain
Imposed Boundary Condition Indicators	Stream power, slope, valley bottom confinement	Lithology (bedrock vs alluvial), valley bottom confinement
Sediment Availability	High (episodic, monsoonal), dynamic	Low, often supply-limited
Reference State Approach	Required for long-term monitoring with focus on deviation from reference geomorphic state	Same as Himalayan river
Suitable Zones for Mining	Aggradational/stable stretches; avoid degraded areas	Alluvial and aggradational stretches; avoid bedrock or degraded zones
Extraction Method	Bar skimming, rotational mining in alternate years	Bar skimming, rotational mining every 3–4 years
Depth Control	Based on sediment budget, maintain slope, supported by UAV/field models	Based on accumulation rates and channel slope; no alteration of general gradient
Ecological Integrity	Exclude ecological hotspots	Same as Himalayan; sensitive riparian zones (floodplain mining) must be excluded
Buffer Zones Near Infrastructure	Minimum 1 km upstream & downstream of bridges, barrages, etc.	Minimum 500 m near critical structures
Paleochannel Mining	Limited; ensure 3–4 m of unsaturated sand remains for groundwater protection	Similar caution; prioritize recharge protection and avoid excessive lowering of water table
Monitoring Requirement	Continuous upstream & downstream monitoring to detect morphological thresholds and responses	Same; especially needed due to lagged response in alluvial, low-energy systems

Policy Driver	Himalayan Rivers (e.g., Gaula)	Peninsular Rivers (e.g., Damodar, Sone)
Integration with River Training Works	Recommended in aggrading rivers; avoid drastic channel slope change	Dredging possible upstream of barrages; integrated with sediment management strategy
Flood Risk Mitigation	Avoid continuous mining; maintain slope and channel geometry	Similar approach; mining-induced slope alteration must be minimized

6.4. Final remarks

Instream sand mining, driven by rapid urbanization and economic growth, has surged in recent years, causing significant ecological and geomorphological damage to rivers. Unregulated extraction leads to channel incision, endangering infrastructure such as bridges and lowering water tables, while also triggering lateral instability, bank erosion, and channel shifts that increase flood risks. The loss of channel form and sediment balance disrupts aquatic and riparian habitats, degrades fisheries, and undermines biodiversity. In India, both Himalayan and peninsular rivers have been severely impacted, with the Damodar River experiencing lowered water levels, habitat loss, and chemical pollution, and the Sone River suffering from altered flow, habitat degradation, and groundwater decline. For the Himalayan setting, the Gaula river in Uttarakhand was selected as a prominent Himalayan river to document and analyse the impacts of sand mining. To understand and manage these impacts, the CASCADE (Catchment Sediment Connectivity And Delivery) modelling framework was also set up for the Gaula river, which integrates graph theory with sediment transport equations to estimate grain-specific sediment flux and assess habitat availability. Given their differing geomorphic settings—Himalayan rivers with high sediment loads driven by tectonic activity and monsoons, and sediment-limited peninsular rivers—management strategies must be river-specific: for Himalayan rivers, regulating extraction based on dynamic sediment budgets and maintaining connectivity; for peninsular rivers, restricting mining to low-sensitivity zones and favoring controlled, non-mechanized methods. Overall, science-based, data-driven policies, continuous monitoring, strict enforcement, and community engagement are essential to safeguard riverine ecosystems and preserve their ecological and societal benefits.

Finally, this project resulted in capacity building and the dissemination of the science of sand mining in a major way (see Appendix 1). One PhD and one Master's student worked full-time on this project, and they have delivered excellent theses. Several project staff were also hired from time to time, who contributed significantly to the project, and also got trained in various aspects, such as UAV data analysis and modelling. We also presented several papers in national and international conferences and workshops, which included the datasets generated from this project. One major research paper was published in an international journal and a book chapter was also published, which was partly based on our previous project funded by NMCG. Several papers are in the pipeline for publication and will be reported to NMCG as and when they are published. Overall, this project was a very successful project and has provided a very satisfying experience.

While working on this project, we have developed several new ideas that can be taken up quickly as a new project utilising the results of the ongoing project. We are currently formulating such a project to develop a Sand Mining Monitoring Module (SaMM) using machine learning tools to provide insights into the temporal variations of a designated sand mine over a specified time interval and enable illicit sand mine monitoring and analysis. We believe that such a platform for the assessment of sand mining-impacted areas would be very useful. Once developed for a few pilot areas, this module can be upscaled to several basins across the country and will serve as an excellent platform to monitor sand mining activities across the country. This project will also align with the activities of the Ganga Knowledge Centre at NMCG, and we will be able to create several online modules as well as policy briefs for this centre.

S&T benefits accrued from this project

1. List of Research Publications

- Akuria, M. and Sinha, R. (2025). Spatiotemporal morphodynamics of an ephemeral Himalayan River impacted by sand mining: a process-response framework. *Science of the Total Environment*, 964, 178526. <https://doi.org/10.1016/j.scitotenv.2025.178526>
- Sinha, R., Moumita Akuria, Kanchan Mishra and Dipro Sarkar (in press). River Sand mining: a developing geohazard in the Himalaya. In: Sandipan Ghosh (editor). *The Himalaya Dilemma: Navigating Risk, Vulnerability, and Resilience in Geohazard-Prone Regions*. Springer.
- Moumita Akuria, Shobhit Pipil and Rajiv Sinha (2023). Anthropogenic impacts of sand mining on channel form and sediment transport in a Himalayan River, NW India: a hydrogeomorphic approach. *International Fluvial Sedimentology Conference*, Padova, Italy.
- Moumita Akuria, Shobhit Pipil, Rajiv Sinha (2023). River channel morphodynamics and sediment flux modeling in the Gaula River, NW India in consequence to sand mining. *American Geophysical Union Annual meeting*, San Francisco, USA.
- Moumita Akuria and Rajiv Sinha (2025). Spatio-temporal Morphodynamics of Himalayan River in Consequence of Sand Mining Using Satellite and UAV Remote Sensing. *European Geosciences Union General Assembly*, Vienna, Austria.
- Shobhit Pipil, Moumita Akuria, Rajiv Sinha (2025). Sediment transport modelling in a mining impacted ephemeral Himalayan River, *International Association of Hydrological Sciences Conference*, IIT Roorkee.
- Moumita Akuria and Rajiv Sinha (2026). Assessing the Geomorphic Impacts of Sand Mining in the Gaula River Using UAV-based DEMs, Remote Sensing, and Sediment Transport Modelling. *International Association of Geomorphologists Conference*, New Zealand. (to be presented).

2. Manpower trained on the project

No. of Ph.D. produced: One

Moumita Akuria: Spatio-temporal morphodynamics and sediment dynamics of a Himalayan River in consequence of sand mining (likely to submit in December 2025).

No. of Master's thesis produced: One

Aayush Tiwari: Morphodynamics of large Peninsular Rivers in consequence to sand mining using Google Earth Engine (GEE) (completed in June 2025).

Student interns

Ankit Yadav

Shreyansh Dewangan

Ansh Dwivedi

Rakshita Chauhan

Priyanshi Agarwal

Other Technical Personnel supported

Dr. Kanchan Mishra

Dr. Shobhit Pipil

Dr. Dipro Sarkar

Dr. Ashwini Agnihotri

Dr. Sandeep Kumar Madhesia

Mr. Girish Chandra Pandey

Dr. Prinsi Singh

Mr. Naresh Kumar

Mr. Vishal Agnihotri

Mr. Rammurat Rathore

Mr. Chandrasekhar

3. Multiplier effects and future directions

- Apart from the research carried out through this project, a number of multiplier effects may be highlighted here:
- Policy briefs for the development of protocols for sand mining.

- Presentations at several national and international workshops to highlight the results of the project.
- Several invited lectures across the country to propagate the impacts of sand mining on rivers.
- Participation in a capacity-building workshop on sand mining at IISER Bhopal in January 2025.
- Preparing a proposal on the development of a web GIS module for the detection and monitoring of sand mining (to be submitted to NMCG).

References

- Aithani, D., Kushawaha, J., Sreerama Naik, S.R., 2021. Water Quality of Himalayan Rivers in Uttarakhand, in: Taloor, A.K., Kotlia, B.S., Kumar, K. (Eds.), *Water, Cryosphere, and Climate Change in the Himalayas: A Geospatial Approach*. Springer International Publishing, Cham, pp. 247–258. https://doi.org/10.1007/978-3-030-67932-3_15
- Akuria, M., Sinha, R., 2025. Spatiotemporal morphodynamics of an ephemeral Himalayan River impacted by sand mining: A process-response framework. *Science of The Total Environment* 964, 178526. <https://doi.org/10.1016/j.scitotenv.2025.178526>
- Alexander, J.S., Zelt, R.B., Schaepe, N.J., 2009. Geomorphic segmentation, hydraulic geometry, and hydraulic microhabitats of the Niobrara River, Nebraska—Methods and initial results.
- Ancey, C., 2020. Bedload transport: a walk between randomness and determinism. Part 1. The state of the art. *Journal of Hydraulic Research* 58, 1–17. <https://doi.org/10.1080/00221686.2019.1702594>
- Ansari, A.A., Shah, P., Punera, A., 2023. Flood disaster and its management in Terai region with special reference to Udham Singh Nagar district of Uttarakhand, India. *Khoj: An International Peer Reviewed Journal of Geography* 10, 18–28. <https://doi.org/10.5958/2455-6963.2023.00002.4>
- Arcement, G.J., Schneider, V.R., 1989. Guide for selecting Manning's roughness coefficients for natural channels and flood plains. US Government Printing Office Washington, DC.
- Arnold, J.G., Fohrer, N., 2005. SWAT2000: current capabilities and research opportunities in applied watershed modelling. *Hydrological Processes* 19, 563–572. <https://doi.org/10.1002/hyp.5611>
- Arnold, J.G., Moriasi, D.N., Gassman, P.W., Abbaspour, K.C., White, M.J., n.d. SWAT: Model use, calibration, and validation.
- Arnold, J.G., Srinivasan, R., Muttiah, R.S., Williams, J.R., 1998. LARGE AREA HYDROLOGIC MODELING AND ASSESSMENT PART I: MODEL DEVELOPMENT 1. *J American Water Resour Assoc* 34, 73–89. <https://doi.org/10.1111/j.1752-1688.1998.tb05961.x>
- Arróspide, F., Mao, L., Escauriaza, C., 2018. Morphological evolution of the Maipo River in central Chile: Influence of instream gravel mining. *Geomorphology* 306, 182–197. <https://doi.org/10.1016/j.geomorph.2018.01.019>
- Arun, P.R., Sreeja, R., Sreebha, S., Maya, K. and Padmalal, D., 2006. River sand mining and its impact on physical and biological environments of Kerala Rivers, Southwest Coast of India. *Ecochronicle*, 1, pp.1-6.

- Ashmore, P., 2013. 9.17 Morphology and Dynamics of Braided Rivers, in: *Treatise on Geomorphology*. Elsevier, pp. 289–312. <https://doi.org/10.1016/B978-0-12-374739-6.00242-6>
- Baffaut, C., Dabney, S., Smolen, M., Youssef, M., Bonta, J., Chu, Guzman, J., Shedekar, V., Jha, M., Arnold, J., 2015. Hydrologic and Water Quality Modeling: Spatial and Temporal Considerations. *Transactions of the ASABE (American Society of Agricultural and Biological Engineers)* 58. <https://doi.org/10.13031/trans.58.10714>
- Banerjee, A., Chen, R., E. Meadows, M., Singh, R.B., Mal, S., Sengupta, D., 2020. An Analysis of Long-Term Rainfall Trends and Variability in the Uttarakhand Himalaya Using Google Earth Engine. *Remote Sensing* 12, 709. <https://doi.org/10.3390/rs12040709>
- Bartarya, S.K., Valdiya, K.S., 1989. Landslides and Erosion in the Catchment of the Gaula River, Kumaun Lesser Himalaya, India. *Mountain Research and Development* 9, 405–419. <https://doi.org/10.2307/3673588>
- Bathrellos, G., Skilodimou, H., 2022. Estimation of sand and gravel extraction sites. *Zeitschrift für Geomorphologie Supplementary Issues* 63, 313–328. <https://doi.org/10.1127/zfg/2021/0674>
- Batjes, N.H., 2009. Harmonized soil profile data for applications at global and continental scales: updates to the WISE database. *Soil Use and Management* 25, 124–127. <https://doi.org/10.1111/j.1475-2743.2009.00202.x>
- Benda, L., Dunne, T., 1997. Stochastic forcing of sediment routing and storage in channel networks. *Water Resources Research* 33, 2865–2880. <https://doi.org/10.1029/97WR02387>
- Bendixen, M., Iversen, L.L., Best, J., Franks, D.M., Hackney, C.R., Latrubesse, E.M., Tusting, L.S., 2021. Sand, gravel, and UN Sustainable Development Goals: Conflicts, synergies, and pathways forward. *One Earth* 4, 1095–1111. <https://doi.org/10.1016/j.oneear.2021.07.008>
- Bendixen, M., Best, J., Hackney, C., Iversen, L.L., 2019. Time is running out for sand. *Nature* 571, 29–31. <https://doi.org/10.1038/d41586-019-02042-4>
- Bertoldi, W., Drake, N. A., & Gurnell, A. M. (2011). 'Interactions between river flows and colonizing vegetation on a braided river: Exploring spatial and temporal dynamics in riparian vegetation cover using satellite data'. *Earth Surface Processes and Landforms*, *36*(11), 1474–1486.
- Best, J.L., Rhoads, B.L., 2008. Sediment transport, bed morphology and the sedimentology of river channel confluences. *River confluences, tributaries and the fluvial network* 45–72.
- Bhatawdekar, R.M., Singh, T.N., Tonnizam Mohamad, E., Armaghani, D.J., Binti Abang Hasbollah, D.Z., 2021. River sand mining vis a vis manufactured sand for sustainability, in: *Proceedings of the International Conference on Innovations for Sustainable and Responsible Mining: ISRM 2020-Volume 1*. Springer, pp. 143–169.

Bhattacharya, R., Dolui, G., Das Chatterjee, N., 2019a. Effect of instream sand mining on hydraulic variables of bedload transport and channel planform: an alluvial stream in South Bengal basin, India. *Environ Earth Sci* 78, 303. <https://doi.org/10.1007/s12665-019-8267-3>

Bhattacharya, R.K., Das Chatterjee, N., Das, K., 2019b. Geomorphic response to riverine land cover dynamics in a quarried alluvial river Kangsabati, South Bengal, India. *Environ Earth Sci* 78, 633. <https://doi.org/10.1007/s12665-019-8652-y>

Bhattacharya, R.K., Chatterjee, N.D., 2021. River Sand Mining Modelling and Sustainable Practice: The Kangsabati River, India, Environmental Science and Engineering. Springer International Publishing, Cham. <https://doi.org/10.1007/978-3-030-72296-8>

Binh, D.V., Kantoush, S.A., Sumi, T., Mai, N.P., Ngoc, T.A., Trung, L.V., An, T.D., 2021. Effects of riverbed incision on the hydrology of the Vietnamese Mekong Delta. *Hydrological Processes* 35, e14030. <https://doi.org/10.1002/hyp.14030>

Bisht, A., 2021. Conceptualizing sand extractivism: Deconstructing an emerging resource frontier. *The Extractive Industries and Society*, 8(2), p.100904. <https://doi.org/10.1016/j.exis.2021.100904>

Bizzi, S., Demarchi, L., Weissteiner, C., Van de Bund, W., Piégay, H., 2015. The use of remote sensing data for regional hydromorphological characterization, in: *Conférence Internationale IsRivers 2015*.

Boon, P.J., 1998. River restoration in five dimensions. *Aquatic Conserv: Mar. Freshw. Ecosyst.* 8, 257–264. [https://doi.org/10.1002/\(SICI\)1099-0755\(199801/02\)8:1<257::AID-AQC281>3.0.CO;2-C](https://doi.org/10.1002/(SICI)1099-0755(199801/02)8:1<257::AID-AQC281>3.0.CO;2-C)

Boothroyd, R. J., Williams, R. D., Barrett, B., Hoey, T. B., Tolentino, P. L. M., Perez, J. E., Guardian, E., David, C. P., & Yang, X. (2020). ‘Detecting and quantifying morphological change in tropical rivers using Google Earth Engine and image analysis techniques’. In *River Flow 2020: 10th Conference on Fluvial Hydraulics* (pp. 1013–1021). CRC Press.

Bracken, L.J., Turnbull, L., Wainwright, J., Bogaart, P., 2015. Sediment connectivity: a framework for understanding sediment transfer at multiple scales: SEDIMENT CONNECTIVITY: SEDIMENT TRANSFER AT MULTIPLE SCALES. *Earth Surf. Process. Landforms* 40, 177–188. <https://doi.org/10.1002/esp.3635>

Brasington, J., Langham, J., Rumsby, B., 2003. Methodological sensitivity of morphometric estimates of coarse fluvial sediment transport. *Geomorphology* 53, 299–316. [https://doi.org/10.1016/S0169-555X\(02\)00320-3](https://doi.org/10.1016/S0169-555X(02)00320-3)

Brenna, A., Surian, N., Mao, L., 2021. Alteration of gravel-bed river morphodynamics in response to multiple anthropogenic disturbances: Insights from the sediment-starved Parma River

(northern Italy). *Geomorphology* 389, 107845.
<https://doi.org/10.1016/j.geomorph.2021.107845>

Brierley, G., Fryirs, K., 2022. Truths of the Riverscape: Moving beyond command-and-control to geomorphologically informed nature-based river management. *Geoscience Letters* 9, 14.
<https://doi.org/10.1186/s40562-022-00223-0>

Brierley, G.J., Fryirs, K., 2005. *Geomorphology and River Management: Applications of the River Styles Framework*. Blackwell Publishing, Oxford, UK.

Brousse, G., Liébault, F., Arnaud-Fassetta, G., Breilh, B., Tacon, S., 2021. Gravel replenishment and active-channel widening for braided-river restoration: The case of the Upper Drac River (France). *Sci. Total Environ.* 766, 142517. <https://doi.org/10.1016/j.scitotenv.2020.142517>

Brunier, G., Anthony, E.J., Goichot, M., Provansal, M., Dussouillez, P., 2014. Recent morphological changes in the Mekong and Bassac river channels, Mekong delta: The marked impact of river-bed mining and implications for delta destabilisation. *Geomorphology* 224, 177–191.
<https://doi.org/10.1016/j.geomorph.2014.07.009>

Bull, W.B., 1997. Discontinuous ephemeral streams. *Geomorphology* 19, 227–276.
[https://doi.org/10.1016/S0169-555X\(97\)00016-0](https://doi.org/10.1016/S0169-555X(97)00016-0)

C. Santhi, J. G. Arnold, J. R. Williams, L. M. Hauck, W. A. Dugas, 2001. APPLICATION OF A WATERSHED MODEL TO EVALUATE MANAGEMENT EFFECTS ON POINT AND NONPOINT SOURCE POLLUTION. *Transactions of the ASAE* 44. <https://doi.org/10.13031/2013.7041>

Calle, M., Alho, P., Benito, G., 2017. Channel dynamics and geomorphic resilience in an ephemeral Mediterranean river affected by gravel mining. *Geomorphology* 285, 333–346.
<https://doi.org/10.1016/j.geomorph.2017.02.026>

Calle, M., Alho, P., Benito, G., 2018. Monitoring ephemeral river changes during floods with SfM photogrammetry. *J Iber Geol* 44, 355–373.

Chiari, M., Rickenmann, D., 2011. Back-calculation of bedload transport in steep channels with a numerical model. *Earth Surface Processes and Landforms* 36, 805–815.
<https://doi.org/10.1002/esp.2108>

Chiphang, N., Bandyopadhyay, A., Bhadra, A., 2020. Assessing the Effects of Snowmelt Dynamics on Streamflow and Water Balance Components in an Eastern Himalayan River Basin Using SWAT Model. *Environ Model Assess* 25, 861–883. <https://doi.org/10.1007/s10666-020-09716-8>

Cho, J., Bosch, D., Vellidis, G., Lowrance, R., Strickland, T., 2013. Multi-site evaluation of hydrology component of SWAT in the coastal plain of southwest Georgia. *Hydrological Processes* 27, 1691–1700. <https://doi.org/10.1002/hyp.9341>

- Chow, V.T., Maidment, D.R., Larry, W., 1988. Applied Hydrology. MacGraw-Hill Book Co.
- Church, M., Hassan, M.A., Wolcott, J.F., 1998. Stabilizing self-organized structures in gravel-bed stream channels: Field and experimental observations. *Water Resources Research* 34, 3169–3179. <https://doi.org/10.1029/98WR00484>
- Comiti, F., Da Canal, M., Surian, N., Mao, L., Picco, L., Lenzi, M.A., 2011. Channel adjustments and vegetation cover dynamics in a large gravel bed river over the last 200 years. *Geomorphology* 125, 147–159. <https://doi.org/10.1016/j.geomorph.2010.09.011>
- Copernicus Digital Elevation Model - Copernicus Contributing Missions Online [WWW Document], n.d. URL <https://spacedata.copernicus.eu/collections/copernicus-digital-elevation-model> (accessed 6.13.24).
- Costea, M., 2018. Impact of floodplain gravel mining on landforms and processes: a study case in Orlat gravel pit (Romania). *Environ Earth Sci* 77, 119. <https://doi.org/10.1007/s12665-018-7320-y>
- Crook, D.A., Lowe, W.H., Allendorf, F.W., Erős, T., Finn, D.S., Gillanders, B.M., Hadwen, W.L., Harrod, C., Hermoso, V., Jennings, S., Kilada, R.W., Nagelkerken, I., Hansen, M.M., Page, T.J., Riginos, C., Fry, B., Hughes, J.M., 2015. Human effects on ecological connectivity in aquatic ecosystems: Integrating scientific approaches to support management and mitigation. *Science of The Total Environment* 534, 52–64. <https://doi.org/10.1016/j.scitotenv.2015.04.034>
- Cucchiaro, S., Cavalli, M., Vericat, D., Crema, S., Llena, M., Beinat, A., Marchi, L., Cazorzi, F., 2018. Monitoring topographic changes through 4D-structure-from-motion photogrammetry: application to a debris-flow channel. *Environ Earth Sci* 77, 632.
- Czuba, J.A., 2018. A Lagrangian framework for exploring complexities of mixed-size sediment transport in gravel-bedded river networks. *Geomorphology* 321, 146–152. <https://doi.org/10.1016/j.geomorph.2018.08.031>
- D. N. Moriasi, J. G. Arnold, M. W. Van Liew, R. L. Bingner, R. D. Harmel, T. L. Veith, 2007. Model Evaluation Guidelines for Systematic Quantification of Accuracy in Watershed Simulations. *Transactions of the ASABE* 50, 885–900. <https://doi.org/10.13031/2013.23153>
- Dar, S.A., Ganie, D.H., Teeli, J.I., Bhat, S.U., 2023. A policy approach for sustainable governance of sand mining activities in NW Kashmir Himalayas. *The Extractive Industries and Society* 13, 101204. <https://doi.org/10.1016/j.exis.2022.101204>
- Dean, D.J., Schmidt, J.C., 2013. The geomorphic effectiveness of a large flood on the Rio Grande in the Big Bend region: Insights on geomorphic controls and post-flood geomorphic response. *Geomorphology* 201, 183–198. <https://doi.org/10.1016/j.geomorph.2013.06.020>

- Detert, M., Weitbrecht, V., n.d. User guide to gravelometric image analysis by BASEGRAIN.
- Diaconu, D.C., Koutalakis, P.D., Gkiatas, G.T., Dascalu, G.V., Zaimes, G.N., 2023. River Sand and Gravel Mining Monitoring Using Remote Sensing and UAVs. *Sustainability* 15, 1944.
- Downs, P.W., Dusterhoff, S.R., Sears, W.A., 2013. Reach-scale channel sensitivity to multiple human activities and natural events: Lower Santa Clara River, California, USA. *Geomorphology* 189, 121–134. <https://doi.org/10.1016/j.geomorph.2013.01.023>
- Duan, H., Cao, Z., Shen, M., Liu, D., Xiao, Q., 2019. Detection of illicit sand mining and the associated environmental effects in China's fourth largest freshwater lake using daytime and nighttime satellite images. *Sci. Total Environ.* 647, 606–618. <https://doi.org/10.1016/j.scitotenv.2018.07.359>
- Dubey, S.K., Kim, J., Her, Y., Sharma, D., Jeong, H., 2023. Hydroclimatic Impact Assessment Using the SWAT Model in India—State of the Art Review. *Sustainability* 15, 15779. <https://doi.org/10.3390/su152215779>
- Dufour, S., Rinaldi, M., Piégay, H., Michalon, A., 2015. How do river dynamics and human influences affect the landscape pattern of fluvial corridors? Lessons from the Magra River, Central–Northern Italy. *Landscape. Urban Plan.* 134, 107–118. <https://doi.org/10.1016/j.landurbplan.2014.10.007>
- Dujardin, E., Vercruysse, K., Cohen, S., Poesen, J., Vanmaercke, M., 2024. Mapping and modeling riverine sand and gravel mining at the sub-continental scale: A case study for India. *Sci. Total Environ.* 912, 169200. <https://doi.org/10.1016/j.scitotenv.2023.169200>
- Dury, G.H., 1964. *Principles of Underfit Streams*. U.S. Government Printing Office.
- Emmett, W.W., Wolman, M.G., 2001. Effective discharge and gravel-bed rivers. *Earth Surf. Process. Landf.* 26, 1369–1380. <https://doi.org/10.1002/esp.303>
- Ferdowsi, B., Ortiz, C.P., Houssais, M., Jerolmack, D.J., 2017. River-bed armouring as a granular segregation phenomenon. *Nat Commun* 8, 1363. <https://doi.org/10.1038/s41467-017-01681-3>
- Ferguson, R.I., 1994. Critical discharge for entrainment of poorly sorted gravel. *Earth Surface Processes and Landforms* 19, 179–186. <https://doi.org/10.1002/esp.3290190208>
- Ferrer-Boix, C., Scorpio, V., Martín-Vide, J.P., Núñez-González, F., Mora, D., 2023. Massive incision and outcropping of bedrock in a former braided river attributed to mining and training. *Geomorphology* 436, 108774. <https://doi.org/10.1016/j.geomorph.2023.108774>

Foga, S., Scaramuzza, P. L., Guo, S., Zhu, Z., Dilley, R. D., Beckmann, T., & Laue, B. (2017). 'Cloud detection algorithm comparison and validation for operational Landsat data products'. *Remote Sensing of Environment*, *194*, 379–390.

Freedman, J.A., Carline, R.F., Stauffer, J.R., 2013. Gravel dredging alters diversity and structure of riverine fish assemblages. *Freshwater Biology* 58, 261–274. <https://doi.org/10.1111/fwb.12056>

Friend, P. F., & Sinha, R. (1993). 'Braiding and meandering parameters'. Geological Society, London, Special Publications, *75*(1), 105–111.

Friend, P.F., 1993. Control of river morphology by the grain-size of sediment supplied. *Sedimentary Geology* 85, 171–177. [https://doi.org/10.1016/0037-0738\(93\)90081-F](https://doi.org/10.1016/0037-0738(93)90081-F)

Fryirs, K.A., 2017. River sensitivity: a lost foundation concept in fluvial geomorphology: River sensitivity: A lost foundation concept in fluvial geomorphology. *Earth Surf. Process. Landforms* 42, 55–70. <https://doi.org/10.1002/esp.3940>

Fryirs, K.A., Brierley, G.J., 2005. *Geomorphic analysis of river systems: an approach to reading the landscape*. John Wiley & Sons.

Fryirs, K., Brierley, G.J., 2010. Antecedent controls on river character and behaviour in partly confined valley settings: Upper Hunter catchment, NSW, Australia. *Geomorphology* 117, 106–120. <https://doi.org/10.1016/j.geomorph.2009.11.015>

Fryirs, K.A., 2017. River sensitivity: a lost foundation concept in fluvial geomorphology: River sensitivity: A lost foundation concept in fluvial geomorphology. *Earth Surf. Process. Landf.* 42, 55–70. <https://doi.org/10.1002/esp.3940>

Fryirs, K.A., 2015. Developing and using geomorphic condition assessments for river rehabilitation planning, implementation and monitoring. *WIREs Water* 2, 649–667. <https://doi.org/10.1002/wat2.1100>

Fryirs, K.A., Brierley, G.J., 2013. *Geomorphic analysis of river systems: an approach to reading the landscape*. John Wiley & Sons.

Fryirs, K.A., Wheaton, J.M., Brierley, G.J., 2016. An approach for measuring confinement and assessing the influence of valley setting on river forms and processes: Measuring Confinement along Fluvial Corridors. *Earth Surf. Process. Landf.* 41, 701–710. <https://doi.org/10.1002/esp.3893>

Fryirs, K., 2013. (Dis)Connectivity in catchment sediment cascades: a fresh look at the sediment delivery problem: (DIS)CONNECTIVITY IN CATCHMENT SEDIMENT CASCADES. *Earth Surf. Process. Landforms* 38, 30–46. <https://doi.org/10.1002/esp.3242>

Fryirs, K.A., Brierley, G.J., Preston, N.J., Kasai, M., 2007. Buffers, barriers and blankets: The (dis)connectivity of catchment-scale sediment cascades. *CATENA* 70, 49–67. <https://doi.org/10.1016/j.catena.2006.07.007>

Gallagher, L., Peduzzi, P., 2019. Sand and sustainability: Finding new solutions for environmental governance of global sand resources.

Gamvroudis, C., Nikolaidis, N.P., Tzoraki, O., Papadoulakis, V., Karalemas, N., 2015. Water and sediment transport modeling of a large temporary river basin in Greece. *Science of The Total Environment* 508, 354–365. <https://doi.org/10.1016/j.scitotenv.2014.12.005>

Gavriletea, M., 2017. Environmental Impacts of Sand Exploitation. *Analysis of Sand Market. Sustainability* 9, 1118. <https://doi.org/10.3390/su9071118>

Ghimire, S., Singh, U., Panthi, K.K., Bhattarai, P.K., 2024. Suspended Sediment Source and Transport Mechanisms in a Himalayan River. *Water* 16, 1063. <https://doi.org/10.3390/w16071063>

Ghosh, A., Maiti, R., 2021. Development of new Ecological Susceptibility Index (ESI) for monitoring ecological risk of river corridor using F-AHP and AHP and its application on the Mayurakshi river of Eastern India. *Ecological Informatics* 63, 101318. <https://doi.org/10.1016/j.ecoinf.2021.101318>

Ghosh, B., 2024. Assessing the effects of human interventions on the morphodynamics and health of a lowland tropical river: A case study of the river Dwarkeswar, India. *Geosystems and Geoenvironment* 3, 100234. <https://doi.org/10.1016/j.geogeo.2023.100234>

Ghosh, P.K., Bandyopadhyay, S., Jana, N.C., Mukhopadhyay, R., 2016. Sand quarrying activities in an alluvial reach of Damodar River, Eastern India: towards a geomorphic assessment. *International Journal of River Basin Management* 14, 477–489. <https://doi.org/10.1080/15715124.2016.1209509>

Ghosh, P.K., Jana, N.C., 2021. Study of river sensitivity for sustainable management of sand quarrying activities in Damodar river, West Bengal, India. *Current Science* 121, 810. <https://doi.org/10.18520/cs/v121/i6/810-822>

Ghosh, P.K., Bandyopadhyay, S., Jana, N.C., and Mukhopadhyay, R. 2016. Sand quarrying activities in an alluvial reach of Damodar River, Eastern India: towards a geomorphic assessment. *International Journal of River Basin Management*, 14(4): 477–489.

Ghosh, P. K., & Jana, N. C., 2021. ‘Study of river sensitivity for sustainable management of sand quarrying activities in Damodar River, West Bengal, India’. *Current Science*, *121*(6), 810–822.

Ghosh, T.K., Jakobsen, F., Joshi, M., Pareta, K., 2019. Extreme rainfall and vulnerability assessment: case study of Uttarakhand rivers. *Nat Hazards* 99, 665–687. <https://doi.org/10.1007/s11069-019-03765-3>

Goswami, P.K., 2018. Controls of basin margin tectonics on the morphology of alluvial fans in the western Ganga foreland basin's piedmont zone, India. *Geological Journal* 53, 1840–1853. <https://doi.org/10.1002/gj.3010>

Graf, W.L., 1978. 1978. Fluvial adjustments to the spread of tamarisk in the Colorado Plateau region, *Geological Society of American Bulletin* 89, 1491-501.

Grekousis, G., Mountrakis, G., Kavouras, M., 2015. An overview of 21 global and 43 regional land-cover mapping products. *International Journal of Remote Sensing* 36, 5309–5335.

Gumiero, B., Rinaldi, M., Belletti, B., Lenzi, D., Puppi, G., 2015. Riparian vegetation as indicator of channel adjustments and environmental conditions: the case of the Panaro River (Northern Italy). *Aquat Sci* 77, 563–582. <https://doi.org/10.1007/s00027-015-0403-x>

Gururani, K., Kothiyari, G.C., Kotlia, B.S., 2023. Morphotectonic assessment of the Gaula river basin, Kumaun lesser Himalaya, Uttarakhand. *Quaternary Science Advances* 12, 100115. <https://doi.org/10.1016/j.qsa.2023.100115>

Hackney, C.R., Darby, S.E., Parsons, D.R., Leyland, J., Best, J.L., Aalto, R., Nicholas, A.P., Houseago, R.C., 2020. River bank instability from unsustainable sand mining in the lower Mekong River. *Nat Sustain* 3, 217–225. <https://doi.org/10.1038/s41893-019-0455-3>

Hackney, C.R., Vasilopoulos, G., Heng, S., Darbari, V., Walker, S., Parsons, D.R., 2021. Sand mining far outpaces natural supply in a large alluvial river. *Earth Surf. Dynam.* 9, 1323–1334. <https://doi.org/10.5194/esurf-9-1323-2021>

Hasan, M.A., Pradhanang, S.M., 2017. Estimation of flow regime for a spatially varied Himalayan watershed using improved multi-site calibration of the Soil and Water Assessment Tool (SWAT) model. *Environ Earth Sci* 76, 787. <https://doi.org/10.1007/s12665-017-7134-3>

Hauer, C., Leitner, P., Unfer, G., Pulg, U., Habersack, H., Graf, W., 2018. The Role of Sediment and Sediment Dynamics in the Aquatic Environment, in: Schmutz, S., Sendzimir, J. (Eds.), *Riverine Ecosystem Management*. Springer International Publishing, Cham, pp. 151–169. https://doi.org/10.1007/978-3-319-73250-3_8

Heckmann, T., Haas, F., Abel, J., Rimböck, A., Becht, M., 2017. Feeding the hungry river: Fluvial morphodynamics and the entrainment of artificially inserted sediment at the dammed river Isar, Eastern Alps, Germany. *Geomorphology* 291, 128–142. <https://doi.org/10.1016/j.geomorph.2017.01.025>

Heckmann, T., Schwanghart, W., Phillips, J.D., 2015. Graph theory—Recent developments of its application in geomorphology. *Geomorphology* 243, 130–146. <https://doi.org/10.1016/j.geomorph.2014.12.024>

Hey, R.D. and Thorne, C.R., 1986. Stable channels with mobile gravel beds. *J. Hydraul. Eng.*, 112(8), pp.671-689.

Hohensinner, S., Habersack, H., Jungwirth, M., Zauner, G., 2004. Reconstruction of the characteristics of a natural alluvial river–floodplain system and hydromorphological changes following human modifications: the Danube River (1812–1991). *River Research & Apps* 20, 25–41. <https://doi.org/10.1002/rra.719>

Hovius, N., 1998. Controls on Sediment Supply by Large Rivers, in: Kocurek, G. (Ed.), *Relative Role of Eustacy, Climate, and Tectonism in Continental Rocks*. SEPM Society for Sedimentary Geology, p. 0. <https://doi.org/10.2110/pec.98.59.0002>

Huang, C., Chen, Y., Zhang, S., & Wu, J., 2018. ‘Detecting, extracting, and monitoring surface water from space using optical sensors: A review’. *Reviews of Geophysics*, *56*(2), 333–360.

Hussain, J., Rashid, G., Singh, R., 2022. Impacts of Sand Mining on Riverine Ecosystems: A Short Review. *Inventum Biologicum: An International Journal of Biological Research* 2, 105–108.

Isik, S., Dogan, E., Kalin, L., Sasal, M., Agiralioglu, N., 2008. Effects of anthropogenic activities on the Lower Sakarya River. *CATENA* 75, 172–181. <https://doi.org/10.1016/j.catena.2008.06.001>

Islam, A., & Guchhait, S. K., 2017. ‘Analysing the influence of Farakka Barrage Project on channel dynamics and meander geometry of Bhagirathi River of West Bengal, India’. *Arabian Journal of Geosciences*, *10*(1), 1–18.

Jain, A.O., Thaker, T., Chaurasia, A., Patel, P., Singh, A.K., 2018. Vertical accuracy evaluation of SRTM-GL1, GDEM-V2, AW3D30 and CartoDEM-V3.1 of 30-m resolution with dual frequency GNSS for lower Tapi Basin India. *Geocarto International* 33, 1237–1256. <https://doi.org/10.1080/10106049.2017.1343392>

Jain, V., Tandon, S.K., Sinha, R., 2012. Application of modern geomorphic concepts for understanding the spatio-temporal complexity of the large Ganga river dispersal system. *Current Science* 1300–1319.

James, L.A., Hodgson, M.E., Ghoshal, S., Latiolais, M.M., 2012. Geomorphic change detection using historic maps and DEM differencing: The temporal dimension of geospatial analysis. *Geomorphology* 137, 181–198.

Jordan, C., Tiede, J., Lojek, O., Visscher, J., Apel, H., Nguyen, H.Q., Quang, C.N.X., Schlurmann, T., 2019. Sand mining in the Mekong Delta revisited - current scales of local sediment deficits. *Sci. Rep.* 9, 17823. <https://doi.org/10.1038/s41598-019-53804-z>

Kamboj, N., Kamboj, V., 2019. Riverbed mining as a threat to in-stream agricultural floodplain and biodiversity of Ganges River, India, in: *Contaminants in Agriculture and Environment: Health Risks and Remediation*. Agro Environ Media - Agriculture and Environmental Science Academy, Haridwar, India, pp. 250–263. <https://doi.org/10.26832/AESA-2019-CAE-0151-019>

Kansal, M.L., Singh, S., 2022. Flood Management Issues in Hilly Regions of Uttarakhand (India) under Changing Climatic Conditions. *Water* 14, 1879. <https://doi.org/10.3390/w14121879>

Kaushal, R.K., Sarkar, A., Mishra, K., Sinha, R., Nepal, S., Jain, V., 2020. Spatio-temporal variability in stream power distribution in the Upper Kosi River basin, Central Himalaya: Controls and geomorphic implications. *Geomorphology* 350, 106888. <https://doi.org/10.1016/j.geomorph.2019.106888>

Khan, S., Fryirs, K., Bizzi, S., 2021. Modelling sediment (dis)connectivity across a river network to understand locational-transmission-filter sensitivity for identifying hotspots of potential geomorphic adjustment. *Earth Surface Processes and Landforms* 46, 2856–2869. <https://doi.org/10.1002/esp.5213>

King, C.A.M., 1970. Feedback Relationships in Geomorphology. *Geografiska Annaler: Series A, Physical Geography* 52, 147–159. <https://doi.org/10.1080/04353676.1970.11879820>

Knutson, C.Y., 2023. Sand and Gravel (Industrial). U.S. Geological Survey.

Koehnken, L., Rintoul, M.S., Goichot, M., Tickner, D., Loftus, A., Acreman, M.C., 2020. Impacts of riverine sand mining on freshwater ecosystems: A review of the scientific evidence and guidance for future research. *River Res Applic* 36, 362–370. <https://doi.org/10.1002/rra.3586>

Kondolf, G.M., 1994. Geomorphic and environmental effects of instream gravel mining. *Landscape and Urban Planning* 28, 225–243. [https://doi.org/10.1016/0169-2046\(94\)90010-8](https://doi.org/10.1016/0169-2046(94)90010-8).

Kondolf, G.M., 1997. PROFILE: Hungry Water: Effects of Dams and Gravel Mining on River Channels. *Environmental Management* 21, 533–551. <https://doi.org/10.1007/s002679900048>

Kondolf, G.M., Piégay, H., Landon, N., 2007. Changes in the riparian zone of the lower Eygues River, France, since 1830. *Landscape Ecol* 22, 367–384. <https://doi.org/10.1007/s10980-006-9033-y>

Kondolf, G.M., Boulton, A.J., O'Daniel, S., Poole, G.C., Rahel, F.J., Stanley, E.H., Wohl, E., Bång, A., Carlstrom, J., Cristoni, C., Huber, H., Koljonen, S., Louhi, P., Nakamura, K., 2006. Process-Based

Ecological River Restoration: Visualizing Three-Dimensional Connectivity and Dynamic Vectors to Recover Lost Linkages. *E&S* 11, art5. <https://doi.org/10.5751/ES-01747-110205>

Kondolf, G.M., Lisle, T.E., Wolman, G.M., 2003. Bed sediment measurement. *Tools in fluvial geomorphology* 347, 395.

Kumar, U., Singh, D.K., 2023. Simulating hydrological responses using high resolution satellite inputs for a forest dominated hilly catchment of Uttarakhand Himalayas. *Arab J Geosci* 16, 401. <https://doi.org/10.1007/s12517-023-11505-y>

La Salandra, M., Roseto, R., Mele, D., Dellino, P., Capolongo, D., 2022. Probabilistic hydro-geomorphological hazard assessment based on UAV-derived high-resolution topographic data: The case of Basento river (Southern Italy). *Science of The Total Environment* 842, 156736.

Lal. Kumar, Joshi, G., Agarwal, K.K., 2020. Morphometry and Morphostructural Studies of the Parts of Gola River and Kalsa River Basins, Chanphi-Okhalkanda Region, Kumaun Lesser Himalaya, India. *Geotecton.* 54, 410–427. <https://doi.org/10.1134/S0016852120030048>

Lane, E.W., 1955. Design of stable channels. *Transactions of the American society of Civil Engineers* 120, 1234–1260.

Lane, S.N., Richards, K.S., 1997. Linking river channel form and process: time, space and causality revisited. *Earth Surface Processes and Landforms* 22, 249–260.

Lang, N., Irniger, A., Rozniak, A., Hunziker, R., Wegner, J.D., Schindler, K., 2021. GRAINet: mapping grain size distributions in river beds from UAV images with convolutional neural networks. *Hydrology and Earth System Sciences* 25, 2567–2597. <https://doi.org/10.5194/hess-25-2567-2021>

Lau, R.Y.S., Park, E., Koh, Y.Q., Tran, D.D., Kantoush, S.A., Binh, D.V., Loc, H.H., 2024. Recurrence interval of riverbed sand mining hotspots in the Mekong delta: Potential indications of unsustainable replenishment rates. *J. Environ. Manage.* 370, 122435. <https://doi.org/10.1016/j.jenvman.2024.122435>

Leal Filho, W., Hunt, J., Lingos, A., Platje, J., Vieira, L., Will, M., Gavriletea, M., 2021. The Unsustainable Use of Sand: Reporting on a Global Problem. *Sustainability* 13, 3356. <https://doi.org/10.3390/su13063356>

Leone, M., Gentile, F., Lo Porto, A., Ricci, G.F., Schürz, C., Strauch, M., Volk, M., De Girolamo, A.M., 2024. Setting an environmental flow regime under climate change in a data-limited Mediterranean basin with temporary river. *Journal of Hydrology: Regional Studies* 52, 101698. <https://doi.org/10.1016/j.ejrh.2024.101698>

- Lisenby, P.E., Fryirs, K.A., Thompson, C.J., 2020. River sensitivity and sediment connectivity as tools for assessing future geomorphic channel behavior. *International Journal of River Basin Management* 18, 279–293. <https://doi.org/10.1080/15715124.2019.1672705>
- Liu, D., Wang, X., Aminjafari, S., Yang, W., Cui, B., Yan, S., Zhang, Y., Zhu, J., Jaramillo, F., 2020. Using INSAR to identify hydrological connectivity and barriers in a highly fragmented wetland. *Hydrological Processes* 34, 4417–4430. <https://doi.org/10.1002/hyp.13899>
- Liu, Z., Rong, L., Wei, W., 2023. Impacts of land use/cover change on water balance by using the SWAT model in a typical loess hilly watershed of China. *Geography and Sustainability* 4, 19–28. <https://doi.org/10.1016/j.geosus.2022.11.006>
- Liébault, F., Piégay, H., 2002. Causes of 20th century channel narrowing in mountain and piedmont rivers of southeastern France. *Earth Surf. Process. Landf.* 27, 425–444. <https://doi.org/10.1002/esp.328>
- Llanos-Paez, O., Estrada, L., Pastén-Zapata, E., Boithias, L., Jorda-Capdevila, D., Sabater, S., Acuña, V., 2023. Spatial and temporal patterns of flow intermittency in a Mediterranean basin using the SWAT+ model. *Hydrological Sciences Journal* 68, 276–289. <https://doi.org/10.1080/02626667.2022.2155523>
- Llanos-Paez, O., Qi, J., Gutierrez, N., Colls, M., Sabater, S., Acuña, V., 2024. Dynamics of Organic Matter Transport, Storage, and Processing in a Non-perennial Mediterranean River Network. *Ecosystems* 27, 636–654. <https://doi.org/10.1007/s10021-024-00910-3>
- Lu, X.X., Zhang, S.R., Xie, S.P., Ma, P.K., 2007. Rapid channel incision of the lower Pearl River (China) since the 1990s as a consequence of sediment depletion. *Hydrol. Earth Syst. Sci.* 11, 1897–1906. <https://doi.org/10.5194/hess-11-1897-2007>
- Luirei, K., Bhakuni, S.S., Longkumer, L., Kumar, V., Jamir, I., 2021. Geomorphic assessment of the factors contributing to the evolution of landforms in Ukhalhunga area, Kosi River valley, Kumaun Himalaya, Uttarakhand. *Geosci J* 25, 465–478. <https://doi.org/10.1007/s12303-020-0034-7>
- Mahadevan, P., 2019. Sand mafias in India. *Disorganized Crime in a Growing Economy*, pp.1-27.
- Mandarino, A., 2022. Morphological adjustments of the lower Orba River (NW Italy) since the mid-nineteenth century. *Geomorphology* 410, 108280. <https://doi.org/10.1016/j.geomorph.2022.108280>
- Manning, R., Griffith, J.P., Pigot, T.F., Vernon-Harcourt, L.F., 1890. On the flow of water in open channels and pipes.

Martín-Vide, J.P., Ferrer-Boix, C., Ollero, A., 2010. Incision due to gravel mining: Modeling a case study from the Gállego River, Spain. *Geomorphology* 117, 261–271. <https://doi.org/10.1016/j.geomorph.2009.01.019>

Martínez-Fernández, V., González del Tánago, M., García de Jalón, D., 2019. Selecting geomorphic variables for automatic river segmentation: Trade-offs between information gained and effort required. *Geomorphology* 329, 248–258. <https://doi.org/10.1016/j.geomorph.2019.01.005>

McFeeters, S. K. (1996). 'The use of the Normalized Difference Water Index (NDWI) in the delineation of open water features'. *International Journal of Remote Sensing*, *17*(7), 1425–1432.

Meadows, P.S., Anderson, J.G., 1966. Micro-organisms attached to marine and freshwater sand grains. *Nature* 212, 1059–1060.

Mingist, M., Gebremedhin, S., 2016. Could sand mining be a major threat for the declining endemic *Labeobarbus* species of Lake Tana, Ethiopia? *Singapore Journal of Tropical Geography* 37, 195–208. <https://doi.org/10.1111/sjtg.12150>

Mitra, S., Mondal, M., Datta, D., Tamang, L., 2023. Planform adjustments of sub-Himalayan Mahananda-Balason River over five decades in response to anthropogenic interventions. *Arab J Geosci* 16, 676. <https://doi.org/10.1007/s12517-023-11809-z>

Monegaglia, F., Zolezzi, G., Güneralp, I., Henshaw, A. J., & Tubino, M. (2018). 'Automated extraction of meandering river morphodynamics from multitemporal remotely sensed data'. *Earth Surface Processes and Landforms*, *43*(11), 2401–2419.

Mossa, J., McLean, M., 1997. Channel planform and land cover changes on a mined river floodplain. *Applied Geography* 17, 43–54. [https://doi.org/10.1016/S0143-6228\(96\)00026-4](https://doi.org/10.1016/S0143-6228(96)00026-4)

Moudgil, M., 2018. How sand mining impacts ecosystem [WWW Document]. India Water Portal Hindi. URL <https://www.indiawaterportal.org/articles/how-sand-mining-impacts-ecosystem> (accessed 8.5.23).

Nabih, S., Tzoraki, O., Zanis, P., Tsikerdekis, T., Akritidis, D., Kontogeorgos, I., Benaabidate, L., 2021. Alteration of the Ecohydrological Status of the Intermittent Flow Rivers and Ephemeral Streams due to the Climate Change Impact (Case Study: Tsiknias River). *Hydrology* 8, 43. <https://doi.org/10.3390/hydrology8010043>

Nagel, G. W., Darby, S. E., & Leyland, J. (2023). 'The use of satellite remote sensing for exploring river meander migration'. *Remote Sensing of Environment*, *285*, 113402.

Ndehedehe, C., 2022. Remote Sensing Hydrology, in: *Satellite Remote Sensing of Terrestrial Hydrology*. Springer, pp. 3–17.

Ng, W.X., Park, E., 2021. Shrinking Tonlé Sap and the recent intensification of sand mining in the Cambodian Mekong River. *Science of The Total Environment* 777, 146180. <https://doi.org/10.1016/j.scitotenv.2021.146180>

Ortega, J.A., Razola, L., Garzón, G., 2014. Recent human impacts and change in dynamics and morphology of ephemeral rivers. *Natural Hazards and Earth System Sciences* 14, 713–730. <https://doi.org/10.5194/nhess-14-713-2014>

Osborn, H.B., Lane, L., 1969. Precipitation-runoff relations for very small semiarid rangeland watersheds. *Water Resources Research* 5, 419–425. <https://doi.org/10.1029/WR005i002p00419>

O'Brien, G.R., Wheaton, J.M., Fryirs, K., Macfarlane, W.W., Brierley, G., Whitehead, K., Gilbert, J., Volk, C., 2019. Mapping valley bottom confinement at the network scale. *Earth Surf. Process. Landf.* 44, 1828–1845. <https://doi.org/10.1002/esp.4615>

Padmalal, D., Maya, K., 2014. *Sand Mining: Environmental Impacts and Selected Case Studies*, Environmental Science and Engineering. Springer Netherlands, Dordrecht. <https://doi.org/10.1007/978-94-017-9144-1>

Padmalal, D., Maya, K., Sreebha, S., Sreeja, R., 2008. Environmental effects of river sand mining: a case from the river catchments of Vembanad lake, Southwest coast of India. *Environ Geol* 54, 879–889. <https://doi.org/10.1007/s00254-007-0870-z>

Park, E., 2024. Sand mining in the Mekong Delta: Extent and compounded impacts. *Science of The Total Environment* 924, 171620. <https://doi.org/10.1016/j.scitotenv.2024.171620>

Park, E., Ho, H.L., Tran, D.D., Yang, X., Alcantara, E., Merino, E., Son, V.H., 2020. Dramatic decrease of flood frequency in the Mekong Delta due to river-bed mining and dyke construction. *Science of The Total Environment* 723, 138066. <https://doi.org/10.1016/j.scitotenv.2020.138066>

Peduzzi, P., 2014. Sand, rarer than one thinks. *Environmental Development* 11, 682.

Pipil, S., Akuria, M., Sinha, R., Assessing Sand Mining Impacts in an Ephemeral Himalayan River Catchment: A CASCADE Modeling Approach, (in prep).

Piégay, H., Arnaud, F., Belletti, B., Cassel, M., Marteau, B., Riquier, J., Rousson, C., Vazquez-Tarrio, D., 2023. Why Consider Geomorphology in River Rehabilitation? *Land* 12, 1491. <https://doi.org/10.3390/land12081491>

Poepl, R.E., Keesstra, S.D., Maroulis, J., 2017. A conceptual connectivity framework for understanding geomorphic change in human-impacted fluvial systems. *Geomorphology* 277, 237–250. <https://doi.org/10.1016/j.geomorph.2016.07.033>

Prabhakar, R., Kumari, A., Sinha, R.K., 2019. Impact of Sand Mining on Zooplankton of River Ganga in and Around Patna, Bihar, India.

Pringle, C., 2003. What is hydrologic connectivity and why is it ecologically important? *Hydrol. Process.* 17, 2685–2689. <https://doi.org/10.1002/hyp.5145>

Pringle, C.M., 2001. HYDROLOGIC CONNECTIVITY AND THE MANAGEMENT OF BIOLOGICAL RESERVES: A GLOBAL PERSPECTIVE. *Ecological Applications* 11.

Pulighe, G., Bonati, G., Colangeli, M., Traverso, L., Lupia, F., Altobelli, F., Dalla Marta, A., Napoli, M., 2020. Predicting Streamflow and Nutrient Loadings in a Semi-Arid Mediterranean Watershed with Ephemeral Streams Using the SWAT Model. *Agronomy* 10, 2. <https://doi.org/10.3390/agronomy10010002>

Qazi, N.Q., Bruijnzeel, L. Adrian, Rai, Shive Prakash, and Ghimire, C.P., 2017. Impact of forest degradation on streamflow regime and runoff response to rainfall in the Garhwal Himalaya, Northwest India. *Hydrological Sciences Journal* 62, 1114–1130. <https://doi.org/10.1080/02626667.2017.1308637>

Qazi, N.Q., Jain, S.K., Thayyen, R.J., Patil, P.R., Singh, M.K., 2020. Hydrology of the Himalayas, in: Dimri, A.P., Bookhagen, B., Stoffel, M., Yasunari, T. (Eds.), *Himalayan Weather and Climate and Their Impact on the Environment*. Springer International Publishing, Cham, pp. 419–450. https://doi.org/10.1007/978-3-030-29684-1_21

Quamar, S., Kumar, P., Singh, H.P., 2025. Streamflow and sediment simulation in the Song River basin using the SWAT model. *Front. Water* 7, 1500086. <https://doi.org/10.3389/frwa.2025.1500086>

R. Srinivasan, X. Zhang, J. Arnold, 2010. SWAT Ungauged: Hydrological Budget and Crop Yield Predictions in the Upper Mississippi River Basin. *Transactions of the ASABE* 53, 1533–1546. <https://doi.org/10.13031/2013.34903>

Rascher, E., Rindler, R., Habersack, H., Sass, O., 2018. Impacts of gravel mining and renaturation measures on the sediment flux and budget in an alpine catchment (Johnsbach Valley, Austria). *Geomorphology* 318, 404–420. <https://doi.org/10.1016/j.geomorph.2018.07.009>

Rath, S., Hinge, G., 2024. Groundwater sustainability mapping for managed aquifer recharge in Dwarkeswar River basin: Integration of watershed modeling, multi-criteria decision analysis, and constraint mapping. *Groundwater for Sustainable Development* 26, 101279. <https://doi.org/10.1016/j.gsd.2024.101279>

Rautela, K.S., Kumar, D., Gandhi, B.G.R., Kumar, A., Dubey, A.K., 2023. Long-term hydrological simulation for the estimation of snowmelt contribution of Alaknanda River Basin, Uttarakhand

using SWAT. *AQUA - Water Infrastructure, Ecosystems and Society* 72, 139–159. <https://doi.org/10.2166/aqua.2023.176>

Rawat, K.S., Sahu, S.R., Singh, S.K., Mishra, A.K., 2022. Cloudburst analysis in the Nainital district, Himalayan Region, 2021. *Discov Water* 2, 12. <https://doi.org/10.1007/s43832-022-00020-y>

Rege, A., 2016. Not biting the dust: using a tripartite model of organized crime to examine India's Sand Mafia. *International Journal of Comparative and Applied Criminal Justice* 40, 101–121. <https://doi.org/10.1080/01924036.2015.1082486>

Rentier, E.S., Cammeraat, L.H., 2022. The environmental impacts of river sand mining. *Sci. Total Environ.* 838, 155877. <https://doi.org/10.1016/j.scitotenv.2022.155877>

Rice, S., Church, M., 1998. Grain size along two gravel-bed rivers: statistical variation, spatial pattern and sedimentary links. *Earth Surface Processes and Landforms* 23, 345–363. [https://doi.org/10.1002/\(SICI\)1096-9837\(199804\)23:4<345::AID-ESP850>3.0.CO;2-B](https://doi.org/10.1002/(SICI)1096-9837(199804)23:4<345::AID-ESP850>3.0.CO;2-B)

Rinaldi, M., Simoncini, C., Piégay, H., 2009. Scientific design strategy for promoting sustainable sediment management: the case of the Magra River (Central-Northern Italy). *River Res. Applic.* 25, 607–625. <https://doi.org/10.1002/rra.1243>

Rinaldi, M., Wyzga, B., Surian, N., 2005. Sediment mining in alluvial channels: physical effects and management perspectives. *River Res. Applic.* 21, 805–828. <https://doi.org/10.1002/rra.884>

Rinaldi, M., Surian, N., Comiti, F., Bussettini, M., 2013. A method for the assessment and analysis of the hydromorphological condition of Italian streams: The Morphological Quality Index (MQI). *Geomorphology* 180–181, 96–108. <https://doi.org/10.1016/j.geomorph.2012.09.009>

Robinson, D.M., Pearson, O.N., 2013. Was Himalayan normal faulting triggered by initiation of the Ramgarh–Munsiari thrust and development of the Lesser Himalayan duplex? *Int J Earth Sci (Geol Rundsch)* 102, 1773–1790. <https://doi.org/10.1007/s00531-013-0895-3>

Rouse, J. W., Haas, R. H., Schell, J. A., & Deering, D. W. (1974). 'Monitoring vegetation systems in the Great Plains with ERTS'. *NASA SP-351*, *1*, 309–317.

Roux, C., Alber, A., Bertrand, M., Vaudor, L., Piégay, H., 2015. "FluvialCorridor": A new ArcGIS toolbox package for multiscale riverscape exploration. *Geomorphology* 242, 29–37. <https://doi.org/10.1016/j.geomorph.2014.04.018>

Rovira, A., Batalla, R.J., Sala, M., 2005. Response of a river sediment budget after historical gravel mining (the lower Tordera, NE Spain). *River Res. Applic.* 21, 829–847. <https://doi.org/10.1002/rra.885>

Rowland, J. C., Shelef, E., Pope, P. A., Muss, J., Gangodagamage, C., & Wilson, C. J. (2016). 'A morphology-independent methodology for quantifying planview river change and characteristics from remotely sensed imagery'. *Water Resources Research*, *52*(1), 370–392.

S., Pelfini, M., Zerboni, A., 2023. Estimating the Evolution of a Post-Little Ice Age Deglaciated Alpine Valley through the DEM of Difference (DoD). *Remote Sensing* 15, 3190.

Sagwal, S., Panda, S., Sengupta, D., Shahrukh, M., Kumar, S., Kumar, A., Dutt, S., 2024. Flash flood dynamics in the foothills of the NW Himalayas: insights into hydrological and morphological controls. *Environ Monit Assess* 197, 81. <https://doi.org/10.1007/s10661-024-13541-x>

Sah, N., Kumar, M., Upadhyay, R., Dutt, S., 2018. Hill slope instability of Nainital City, Kumaun Lesser Himalaya, Uttarakhand, India. *Journal of Rock Mechanics and Geotechnical Engineering* 10, 280–289. <https://doi.org/10.1016/j.jrmge.2017.09.011>

Sanchis-Ibor, C., Segura-Beltrán, F., Almonacid-Caballer, J., 2017. Channel forms recovery in an ephemeral river after gravel mining (Palancia River, Eastern Spain). *CATENA* 158, 357–370. <https://doi.org/10.1016/j.catena.2017.07.012>

Sandercock, P.J., Hooke, J.M., Mant, J.M., 2007. Vegetation in dryland river channels and its interaction with fluvial processes. *Progress in Physical Geography: Earth and Environment* 31, 107–129. <https://doi.org/10.1177/0309133307076106>

Sarkar, D., Sinha, R., 2024. Integrating UAV -Based Topographic and Geomorphic Analysis for the Development of River Rehabilitation Plans in Semi-Urban Settings. *River Res. Appl.* rra.4371. <https://doi.org/10.1002/rra.4371>

Sarkar, D., Sinha, R., Bookhagen, B., 2023. Towards a Guideline for UAV-Based Data Acquisition for Geomorphic Applications. *Remote Sensing* 15, 3692.

Schandl, H., Hatfield-Dodds, S., Wiedmann, T., Geschke, A., Cai, Y., West, J., Newth, D., Baynes, T., Lenzen, M., Owen, A., 2016. Decoupling global environmental pressure and economic growth: scenarios for energy use, materials use and carbon emissions. *Journal of Cleaner Production* 132, 45–56. <https://doi.org/10.1016/j.jclepro.2015.06.100>

Schmitt, R.J.P., Bizzi, S., Castelletti, A., 2016. Tracking multiple sediment cascades at the river network scale identifies controls and emerging patterns of sediment connectivity: TRACKING MULTIPLE SEDIMENT CASCADES AT RIVER NETWORK SCALE. *Water Resour. Res.* 52, 3941–3965. <https://doi.org/10.1002/2015WR018097>

Schumann, G., Bates, P. D., Horritt, M. S., Matgen, P., & Pappenberger, F. (2009). 'Progress in integration of remote sensing-derived flood extent and stage data and hydraulic models'. *Reviews of Geophysics*, *47*(4), RG4001.

- Schumm, S.A., 1979. Geomorphic Thresholds: The Concept and Its Applications. *Transactions of the Institute of British Geographers* 4, 485. <https://doi.org/10.2307/622211>
- Schwenk, J., & Hariharan, J., 2021. 'RivGraph: Automatic extraction and analysis of river and delta channel network topology'. *Journal of Open Source Software*, *6*(59), 2952.
- Secu, C., Nistor, M. M., Stoleriu, C. C., & Munteanu, I., 2022. 'Remote sensing analysis for the identification and monitoring of sand mining areas using NSI and other spectral indices'. *Remote Sensing*, *14*(18), 4491.
- Sharma, A., Patel, P.L., Sharma, P.J., 2022. Influence of climate and land-use changes on the sensitivity of SWAT model parameters and water availability in a semi-arid river basin. *CATENA* 215, 106298. <https://doi.org/10.1016/j.catena.2022.106298>
- Shukla, U.K., 2009. Sedimentation model of gravel-dominated alluvial piedmont fan, Ganga Plain, India. *Int J Earth Sci (Geol Rundsch)* 98, 443–459. <https://doi.org/10.1007/s00531-007-0261-4>
- Shymbin, B.W., Nongbri, G., 2022. Impact of Sand Mining on the Physical Health of the River and the Livelihood of the People: A Case Study of Umtyngngar River, Meghalaya. *Anthropogeomorphology: A Geospatial Technology Based Approach*.
- Singh, H., Rao, R.J., 2017. Status, threats and conservation challenges to key aquatic fauna (Crocodile and Dolphin) in National Chambal Sanctuary, India. *Aquatic Ecosystem Health & Management* 20, 59–70. <https://doi.org/10.1080/14634988.2017.1298964>
- Singh, R., Sidhu, M.S., 2016. An overview of environmental impacts of riverbed mining in Himalayan terrain of Himachal Pradesh. *Journal of applied geochemistry* 18, 473–479.
- Singh, G., Pandey, A., 2024. Climate change induced disasters and highly vulnerable infrastructure in Uttarakhand, India: current status and way forward towards resilience and long-term sustainability. *Sustainable and Resilient Infrastructure* 9, 145–167. <https://doi.org/10.1080/23789689.2023.2253409>
- Singh, M., Sinha, R., Tandon, S.K., 2021. Geomorphic connectivity and its application for understanding landscape complexities: a focus on the hydro-geomorphic systems of India. *Earth Surf Processes Landf* 46, 110–130. <https://doi.org/10.1002/esp.4945>
- Singh, M., Tandon, S.K., Sinha, R., 2017. Assessment of connectivity in a water-stressed wetland (Kaabar Tal) of Kosi-Gandak interfan, north Bihar Plains, India: CONNECTIVITY RESPONSE UNITS IN A WETLAND. *Earth Surf. Process. Landforms* 42, 1982–1996. <https://doi.org/10.1002/esp.4156>
- Sinha, R., 2018. Sediment Management of The Himalayan Rivers: A Challenge for River Managers. *Current Science* 115, 367. <https://doi.org/10.18520/cs/v115/i3/367-368>

Sinha, R., Friend, P.F., 1994. River systems and their sediment flux, Indo-Gangetic plains, Northern Bihar, India. *Sedimentology* 41, 825–845. <https://doi.org/10.1111/j.1365-3091.1994.tb01426.x>

Sinha, R., Gupta, A., Mishra, K., Tripathi, S., Nepal, S., Wahid, S.M., Swarnkar, S., 2019. Basin-scale hydrology and sediment dynamics of the Kosi river in the Himalayan foreland. *Journal of Hydrology* 570, 156–166. <https://doi.org/10.1016/j.jhydrol.2018.12.051>

Sinha, R., Sripriyanka, K., Jain, V., Mukul, M., 2014. Avulsion threshold and planform dynamics of the Kosi River in north Bihar (India) and Nepal: A GIS framework. *Geomorphology* 216, 157–170.

Skalski, T., Kędzior, R., Wyżga, B., Radecki-Pawlik, A., Plesiński, K., Zawiejska, J., 2016. Impact of Incision of Gravel-bed Rivers on Ground Beetle Assemblages: Ground Beetles of Mountain River Incised Channel. *River Res. Applic.* 32, 1968–1977. <https://doi.org/10.1002/rra.3027>

Sonak, S., Pangam, P., Sonak, M., Mayekar, D., 2006. Impact of sand mining on local ecology. Multiple dimensions of global environmental change. Teri Press, New Delhi 101–121.

Sreebha, S., Padmalal, D., 2011. Environmental Impact Assessment of Sand Mining from the Small Catchment Rivers in the Southwestern Coast of India: A Case Study. *Environmental Management* 47, 130–140. <https://doi.org/10.1007/s00267-010-9571-6>

Surian, N., Cisotto, A., 2007. Channel adjustments, bedload transport and sediment sources in a gravel-bed river, Brenta River, Italy. *Earth Surface Processes and Landforms* 32, 1641–1656. <https://doi.org/10.1002/esp.1591>

Surian, N., Rinaldi, M., Pellegrini, L., Audisio, C., Maraga, F., Teruggi, L., Turitto, O. and Ziliani, L., 2009. Channel adjustments in northern and central Italy over the last 200 years. *Management and Restoration of Fluvial Systems with Broad Historical Changes and Human Impacts*, James LA, Rathburn SL, Whitecar GR(eds)., Geological Society of America Special Paper, 451, pp.83-95.

Sverdrup, H.U., Koca, D., Schlyter, P., 2017. A Simple System Dynamics Model for the Global Production Rate of Sand, Gravel, Crushed Rock and Stone, Market Prices and Long-Term Supply Embedded into the WORLD6 Model. *Biophys Econ Resour Qual* 2, 8. <https://doi.org/10.1007/s41247-017-0023-2>

Swain, S., Mishra, S.K., Pandey, A., Pandey, A.C., Jain, A., Chauhan, S.K., Badoni, A.K., 2022. Hydrological modelling through SWAT over a Himalayan catchment using high-resolution geospatial inputs. *Environmental Challenges* 8, 100579. <https://doi.org/10.1016/j.envc.2022.100579>

Tamang, L., Mandal, D.K., 2015. Bed material extraction and its effects on the forms and processes of the lower Balason River in the Darjeeling Himalayas, India. *Geogr. Pol.* 88. <https://doi.org/10.7163/GPol.2015.3>

Tandon, S.K., Sinha, R., 2007. Geology of Large River Systems, in: Large Rivers. John Wiley & Sons, Ltd, pp. 7–28. <https://doi.org/10.1002/9780470723722.ch2>

Tangi, M., 2018. Balancing sediment stravation and hydropower production, The case study of Vjosa River. Politecnico di Milano, Italy.

Tangi, M., Bizzi, S., Fryirs, K., Castelletti, A., 2022. A Dynamic, Network Scale Sediment (Dis)Connectivity Model to Reconstruct Historical Sediment Transfer and River Reach Sediment Budgets. *Water Resources Research* 58, e2021WR030784. <https://doi.org/10.1029/2021WR030784>

Tangi, M., Schmitt, R., Bizzi, S., Castelletti, A., 2019. The CASCADE toolbox for analyzing river sediment connectivity and management. *Environmental Modelling & Software* 119, 400–406. <https://doi.org/10.1016/j.envsoft.2019.07.008>

Valdiya, K.S., Bartarya, S.K., 1991. Hydrogeological Studies of Springs in the Catchment of the Gaula River, Kumaun Lesser Himalaya, India. *Mountain Research and Development* 11, 239–258. <https://doi.org/10.2307/3673618>

Venditti, J.G., Dietrich, W.E., Nelson, P.A., Wydzga, M.A., Fadde, J., Sklar, L., 2010. Effect of sediment pulse grain size on sediment transport rates and bed mobility in gravel bed rivers. *Journal of Geophysical Research: Earth Surface* 115. <https://doi.org/10.1029/2009JF001418>

Vercruysse, K., Grabowski, R.C., 2021. Human impact on river planform within the context of multi-timescale river channel dynamics in a Himalayan river system. *Geomorphology* 381, 107659. <https://doi.org/10.1016/j.geomorph.2021.107659>

Vericat, D., Batalla, R.J., Garcia, C., 2006. Breakup and reestablishment of the armour layer in a large gravel-bed river below dams: The lower Ebro. *Geomorphology* 76, 122–136. <https://doi.org/10.1016/j.geomorph.2005.10.005>

Vázquez-Tarrío, D., Piégay, H., Menéndez-Duarte, R., 2020. Textural signatures of sediment supply in gravel-bed rivers: Revisiting the armour ratio. *Earth-Science Reviews* 207, 103211. <https://doi.org/10.1016/j.earscirev.2020.103211>

Ward, J.V., 1989. The Four-Dimensional Nature of Lotic Ecosystems. *Journal of the North American Benthological Society* 8, 2–8. <https://doi.org/10.2307/1467397>

Ward, J.V., Stanford, J.A., 1995. Ecological connectivity in alluvial river ecosystems and its disruption by flow regulation. *Regul. Rivers: Res. Mgmt.* 11, 105–119. <https://doi.org/10.1002/rrr.3450110109>

- Wheaton, J.M., Fryirs, K.A., Brierley, G., Bangen, S.G., Bouwes, N., O'Brien, G., 2015. Geomorphic mapping and taxonomy of fluvial landforms. *Geomorphology* 248, 273–295. <https://doi.org/10.1016/j.geomorph.2015.07.010>
- Wheaton, J.M., Brasington, J., Darby, S.E., Sear, D.A., 2009. Accounting for uncertainty in DEMs from repeat topographic surveys: improved sediment budgets. *Earth Surf. Process. Landforms* n/a-n/a.
- Wiejaczka, Ł., Tamang, L., Piróg, D., Prokop, P., 2018. Socioenvironmental issues of river bed material extraction in the Himalayan piedmont (India). *Environ Earth Sci* 77, 718. <https://doi.org/10.1007/s12665-018-7897-1>
- Wohl, E.E., 2020. *Rivers in the landscape*, Second edition. ed. Wiley/Blackwell, Hoboken, NJ.
- Wohl, E., Bledsoe, B.P., Jacobson, R.B., Poff, N.L., Rathburn, S.L., Walters, D.M., Wilcox, A.C., 2015. The Natural Sediment Regime in Rivers: Broadening the Foundation for Ecosystem Management. *BioScience* 65, 358–371. <https://doi.org/10.1093/biosci/biv002>
- Wohl, E., Magilligan, F.J., Rathburn, S.L., 2017. Introduction to the special issue: Connectivity in Geomorphology. *Geomorphology* 277, 1–5. <https://doi.org/10.1016/j.geomorph.2016.11.005>
- Wong, T., Khanal, S., Zhao, K., Lyon, S.W., 2024. Grain size estimation in fluvial gravel bars using uncrewed aerial vehicles: A comparison between methods based on imagery and topography. *Earth Surface Processes and Landforms* 49, 374–392. <https://doi.org/10.1002/esp.5709>
- World Wildlife Fund. (2018). *Living planet report (2018) risk and resilience in a new era*. Gland, Switzerland: WWF International.
- Wright, S.A., Minear, J.T., 2019. Dam effects on bedload transport on the upper Santa Ana River, California, and implications for native fish habitat. *River Research & Apps* 35, 632–645. <https://doi.org/10.1002/rra.3443>
- Wu, B., Molinas, A., Shu, A., 2003. Fractional transport of sediment mixtures. *International Journal of Sediment Research* 18.
- Wu, W., Vieira, D.A., Wang, S.S.Y., 2004. One-Dimensional Numerical Model for Nonuniform Sediment Transport under Unsteady Flows in Channel Networks. *J. Hydraul. Eng.* 130, 914–923. [https://doi.org/10.1061/\(ASCE\)0733-9429\(2004\)130:9\(914\)](https://doi.org/10.1061/(ASCE)0733-9429(2004)130:9(914))
- Yadav, A., Boothroyd, R. J., Smith, G. H. S., Sen, S., 2023. 'Morphological adjustments of the Yamuna River in the Himalayan foothills in response to natural and anthropogenic stresses'. *Hydrological Processes*, *37*(11), e14771.

Yadav, V., Yadav, S.M., 2021. Evaluation of Selected Bed Load Transport Equation for Different Representative Sediment Sizes in Mountain Rivers, in: International Conference on Hydraulics, Water Resources and Coastal Engineering. Springer, pp. 37–47.

Yang, C.T., 1984. Unit stream power equation for gravel. *Journal of Hydraulic Engineering* 110, 1783–1797.

Yanites, B.J., Tucker, G.E., Mueller, K.J., Chen, Y.-G., Wilcox, T., Huang, S.-Y., Shi, K.-W., 2010. Incision and channel morphology across active structures along the Peikang River, central Taiwan: Implications for the importance of channel width. *Geol. Soc. Am. Bull.* 122, 1192–1208. <https://doi.org/10.1130/B30035.1>

Ylla Arbós, C., Blom, A., Viparelli, E., Reneerkens, M., Frings, R.M., Schielen, R.M.J., 2021. River Response to Anthropogenic Modification: Channel Steepening and Gravel Front Fading in an Incising River. *Geophys. Res. Lett.* 48, e2020GL091338. <https://doi.org/10.1029/2020GL091338>

Yuen, K.W., Park, E., Tran, D.D., Loc, H.H., Feng, L., Wang, J., Gruel, C.-R., Switzer, A.D., 2024. Extent of illegal sand mining in the Mekong Delta. *Commun. Earth Environ.* 5, 31. <https://doi.org/10.1038/s43247-023-01161-1>

Ziliani, L., Surian, N., 2016. Reconstructing temporal changes and prediction of channel evolution in a large Alpine river: the Tagliamento river, Italy. *Aquat Sci* 78, 83–94. <https://doi.org/10.1007/s00027-015-0431-6>

Zou, W., Tolonen, K.T., Zhu, G., Qin, B., Zhang, Y., Cao, Z., Peng, K., Cai, Y., Gong, Z., 2019. Catastrophic effects of sand mining on macroinvertebrates in a large shallow lake with implications for management. *Science of The Total Environment* 695, 133706. <https://doi.org/10.1016/j.scitotenv.2019.133706>

Zou, Z., Xiao, X., Dong, J., Qin, Y., Doughty, R. B., Menarguez, M. A., & Wang, J. (2018). ‘Divergent trends of open-surface water body area in the contiguous United States from 1984 to 2016’. *Proceedings of the National Academy of Sciences*, *115*(15), 3810–3815.

